A.D. MDLXII

UNIVERSITY OF SASSARI

Department of Chemistry and Pharmacy

PhD School in Chemical Sciences and Technologies

Curriculum Chemical Sciences

Design, synthesis and investigation of the photosensitive properties of mesoporous titania powders and donor-acceptor chromophores

PhD Thesis of
Dr. Elisabetta Masolo

Supervisor	Coordinator
Dr. Maria I. Pilo	Prof. Stefano Enzo

CYCLE XXVII, 2011-2014

CONTENTS

3.2.1 Chromophores bearing one ethynyl group on the bithiophene backbone

3.2.2 Chromophores bearing two ethynyl groups on the bithiophene backbone

Introduction

The thirst for energy, due to the increase in population and the rising demand from developing countries, together with the big challenge of replacing fossil fuel with renewable energy sources, are leading the actual energetic scenario and, consequently, the scientific research is moving in that direction by studying novel promising materials. The Sun is a clean energy source already used by nature to sustain life on earth; therefore, the use of this natural energetic reservoir seems to be one of the most promising way to answer to the actual energy challenge.

Commercially available photovoltaic devices are based on high cost, and sometimes even toxic, inorganic materials. Organic photovoltaic can avoid these problems although efficiencies for these devices are still lower than the inorganic counterpart. A material for organic photovoltaic devices should possess both good light harvesting and carriers transporting properties, but this is a no trivial task to achieve. On the other hand, in the so-called Dye Sensitised Solar Cells (DSSCs) the charge generation is done at a semiconductor-dye interface and the charge transport is performed by the semiconductor and the electrolyte; as a consequence, spectral properties can be tuned by modifying the dye, while carriers transport can be improved acting on the semiconductor and the electrolyte.

This thesis starts from these assumptions and experimental work was done moving in two main directions: the synthesis and characterisation of mesoporous titanium dioxide as semiconductor and the design, synthesis and characterisation of organic chromophores for possible light harvesting applications.

The idea of synthesising low cost materials leads to the choice of focusing the research on mesoporous titanium dioxide, that is a widely studied photocatalyst that offers large surface areas together with a nanocrystalline structure. In particular, Evaporation-Induced Self-Assembly method (EISA) was selected as synthetic way to the obtainment of mesoporous powders.

As a matter of fact, EISA is a low cost sol-gel method largely applied for the synthesis of ordered mesoporous titania thin films, but only few papers can be found concerning the preparation of crystalline ordered powders [1, 2].

Experimental effort was then spent in this direction, and two sets of TiO_2 mesoporous crystalline powders were synthesised with the aim of understanding the influence of different synthetic parameters on the structural and morphological properties of the products and on their photocatalytic performances.

On the other side, novel chromophores were designed and synthesised during this thesis starting from previous work by the group where this thesis was done. In particular, a series of terthiophene derivatives fuctionalised in their 3' position with chelating units and various spacers were previously synthesised and studied (Fig. 1) [3, 4, 5, 6, 7].

All the derivatives, excepr for TAF5, were also electropolymerised on the 5,5'' terthiophene positions. Some of these compounds were also used as ligands to coordinate Ru and the corresponding hybrid organic/inorganic products were electropolymerised leading to 'outer-sphere' metallopolymers [8, 9, 10].

In particular, TAT (Fig. 1) ligand was used to synthesise a heteroleptic Ru(II)-terpyridine complex (Fig. 2) that was preliminary tested as a dye in DSSCs [11]. The compound showed poor performances due to the limited light harvesting and fast deactivation of the excited state.

---

[1] L. Chen, B. Yao, Y. Cao, K. Fan, *Journal of Physical Chemistry C* **2007**, 111, 11849

[2] H. Li, J. Shi, J. Liang, X. Li, L. Li, M. Ruan, *Materials Letters* **2008**, 62, 1410-1413

[3] C. Zanardi, R. Scanu, L. Pigani, M.I. Pilo, G. Sanna, R. Seeber, N. Spano, F. Terzi, A. Zucca, *Electrochimica Acta* **2006**, 51, 4859

[4] C. Zanardi, R. Scanu, L. Pigani, M.I. Pilo, G. Sanna, R. Seeber, N. Spano, F. Terzi, A. Zucca, *Synthetic Metals* **2006**, 156, 984

[5] P. Manca, M.I. Pilo, G. Casu, S. Gladiali, G. Sanna, R. Scanu, N. Spano, A. Zucca, C. Zanardi, D. Bagnis, L. Valentini, *Journal of Polymer Science A: Polymer Chemistry* **2011**, 49, 3513

[6] G. Bergamini, L. Boselli, P. Ceroni, P. Manca, G. Sanna, M.I. Pilo, *European Journal of Inorganic Chemistry* **2011**, 4590

[7] P. Manca, S. Gladiali, D. Cozzula, A. Zucca, G. Sanna, N. Spano, M.I. Pilo, *Polymer* **2015**, 56, 123

[8] P. Manca, M.I. Pilo, G. Sanna, A. Zucca, G. Bergamini, P. Ceroni, *Chemical Communications* **2011**, 47, 3413

[9] P. Manca, R. Scanu, A. Zucca, G. Sanna, N. Spano, M.I. Pilo, *Polymer* **2013**, 54, 3504

[10] R. Scanu, P. Manca, A. Zucca, G. Sanna, N. Spano, R. Seeber, C. Zanardi, M.I. Pilo, *Polyhedron*, **2013**, 49, 24

[11] P. Manca, M.I. Pilo, G. Sanna, G. Bergamini, P. Ceroni, R. Boaretto, S. Caramori, *Synthetic Metals* **2015**, 200, 109

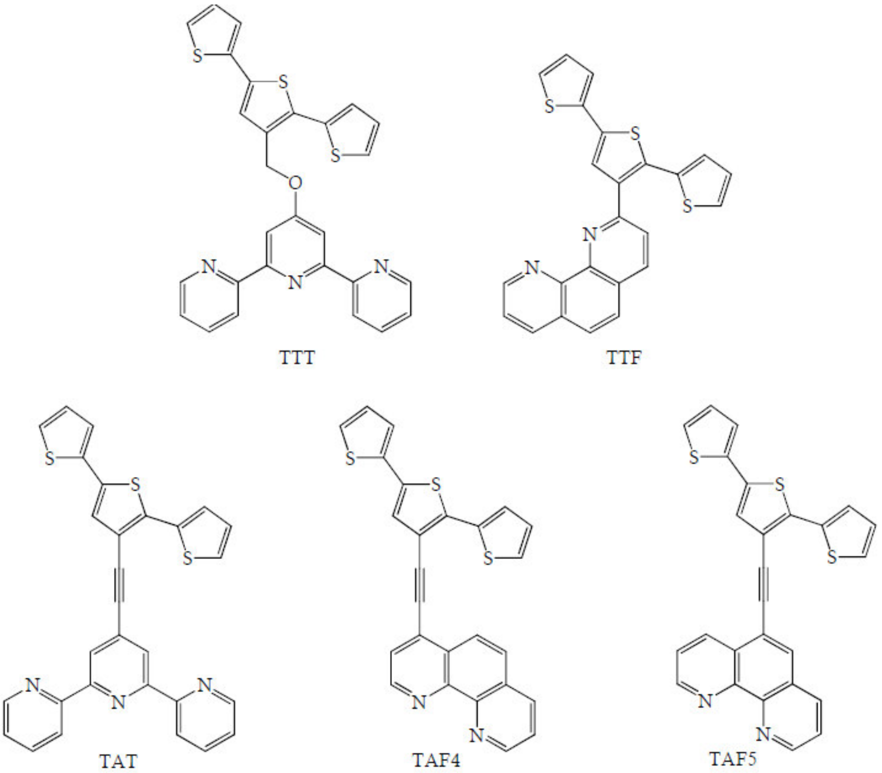
TTT TTF
TAT TAF4 TAF5

Fig. 1: thiophene-based compounds previously synthesised by the research group where this thesis was done.

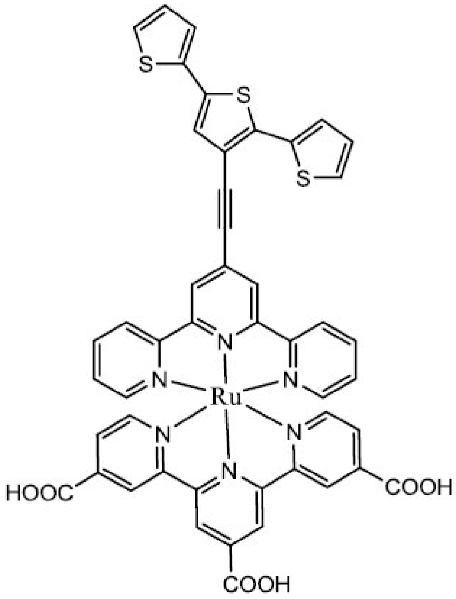

Fig. 2: heteroleptic [Ru(TAT)(tpy-COOH)]$^{2+}$ previously synthesised in the research group where this thesis was done

In the field of chromophores for titania sensitisation for DSSCs applications, two classes of sensitizers can be found in literature: Ru-based polypyridine complexes and metal free organic dyes. Organic dyes usually possess a donor-spacer-acceptor (D-π-A) structure, and among the spacers thiophene units are the most common because of their excellent charge-transport properties.

Basing on the aforementioned concepts, and with the intent of obtaining chromophores with promising light-sensitive properties, two compounds with a D-π-A structure were synthesised and characterised during this thesis (Fig. 3).

Triphenylamine (TPA) was chosen as donor fragment because of its non-planar structure that suppress dye aggregation and also because it is characterised by a high extinction coefficients. Moreover the presence of nitrogen as a redox-active centre suppress electron-hole recombination. Bithiophene was chosen as a spacer because it increases the conjugation of the system, lowers the steric hindrance between aromatic rings and increases the planarity of the dye. Moreover also one or two ethynyl groups were added as spacers to further improve planarity and charge transport and also for their electron withdrawing properties. The terpyridine was chosen as acceptor for two important reasons: i) it has been demonstrated that the nitrogen of a pyridine ring can form coordination bonding between the lone pair on the nitrogen and the Lewis acid sites of titania, giving electron injection efficiencies comparable to or higher than similar dyes where the pyridine ring is replaced with carboxyphenyl group [12] , and ii) terpyridine can also bind to Ru to give hybrid organic/inorganic dyes.

Thiophene units that act as spacers in organic dyes are usually functionalised in the α position in respect to sulphur.

The decision of functionalising the bithiophene moiety in its 4,4’ position was taken because of the possibility of electropolymerising all the chromophores, through the free α position of the bithiophene, obtained during the synthetic steps.

---

[12] Y. Ooyama, S. Inoue, T. Nagano, K. Kushimoto, J. Oshita, I. Imae, K. Komaguchi, Y. Harima, *Angewandte Chemie International Edition* **2011**, 50, 7429

The resulting electropolymers are, as well, potential chromophores for DSSCs. As a matter of fact, polymers with D-π-A structure have been investigated as promising sensitisers in Gratzel cells (see par. 1.2.3).

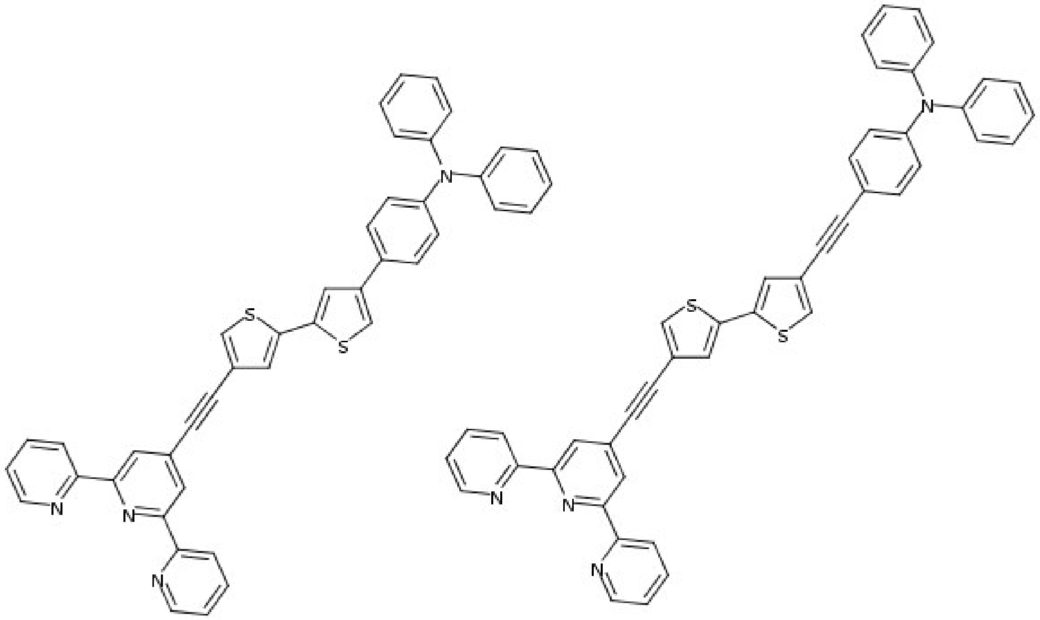

Tpy-Et-BT-TPA

Tpy-Et-BT-Et-TP

Fig. 3: D-π-A molecules synthesised in this thesis

The experimental work was, as explained, divided into two main parts:

- synthesis and characterisation, by means of X-Ray Powder Diffraction, N_2 Physisorption measurement, Transmission Electron Microscopy, UV-Vis spectrophotometry and Linear Scan voltammetry, of mesoporous titania powders with the intent of evaluating the role of synthetic parameters on their structure, morphology and photoelectrochemical performances. EISA was chosen with the intent of giving new additional information on the use of this technique for the synthesis of porous powders and not ordered thin films;
- design, synthesis and electrochemical (cyclic voltammetry and chronoamperometry) and optical (UV-Vis spectrophotometry) characterisation of monomers and corresponding electro-generated polymers with a D-π-A structure, with the intent of understanding the

role of donor (TPA), spacer (one or two ethynyl groups) and acceptor (terpyridine) moieties on a bithiophene backbone. The influence of the introduction of each substituent on bithiophene was studied by characterising each intermediate compound, and the corresponding polymer, obtained in the synthetic steps that finally led to the chromophores in Fig. 3.

Chapter 1

State of the Art

1.1 Titanium Dioxide

1.1.1 Titanium Dioxide: structure and properties

Since its commercial production in the early twentieth century, titanium dioxide (titania) has been used as a white pigment [13], in sunscreens [14], in toothpastes [15] etc…
Moreover, TiO_2 finds many application in areas ranging from photovoltaics and photocatalysis to photo-electrochromics and sensors [16]. These applications can be generally divided into 'energy' and 'environmental' categories, many of which depend both on the properties and modifications of a TiO_2 material host (e.g. sensitisation with dyes, see paragraph 1.1.3.2).
New physical and chemical properties emerge when the size of titania, and of a general material, becomes smaller and down to the nanometer scale. The surface area and surface-to-volume ratio increases dramatically when the size of a material decreases [17]. The high surface area is beneficial to many titania-based devices as it facilitates reaction/interaction between devices and the interacting media, that mainly occurs on the surface or at the interface of the material. Thus, the performances of titania-baed devices are widely influenced by the sizes of TiO_2 building units.
As often described, there are three main types of TiO_2 structures: rutile, anatase and brookite. The size dependence of the stability of these phases has recently been reported

---

[13] G. Pfeff, P. Reynders, *Chemical Reviews* **1999**, 99, 1963
[14] R. Zallen, M.P. Moret, *Silid State Communications* **2006**, 137, 154
[15] S. Yuan, W,H, Chen, S. Hu, *Material Science and Engineering C* **2005**, 25, 479
[16] A. Hegfeldt, M. Gratzel, *Chemical Reviews* **1995**, 95, 49
[17] A.P. Alivisatos, *Science* **1996**, 271, 933

[18] and rutile is the most stable phase for particles above 35 nm in size, anatase for particles below 11 nm while brookite for particles in the 11-35 range. Another structure, cotunnite, has been obtained at elevated pressures [19]. The attention is usually devoted to anatase and rutile polymorphs because of their role in photocatalytic applications. Both structures present an octahedral $(TiO_6)^{2-}$ coordination around Ti atom and the difference lies in the distortion of this configuration: in anatase each octahedral is strongly distorted and near to other eight octahedra, with four of them sharing the vertex and with the other four the edges (Fig. 1.1). In rutile octahedral are less distorted and are near to other ten octahedra (Fig. 1.1).

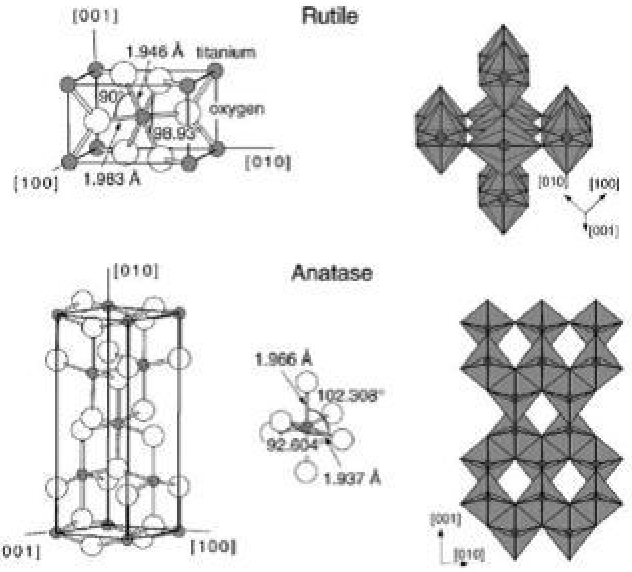

Fig. 1.1: anatase and rutile structures

TiO_2 features predominantly in past and present work on semiconductor photocatalysis and in the following part a brief description of the basic of photocatalysis will be given.

---

[18] H. Zhang, J.F. Barfield, *Journal of Physical Chemistry B* **2000**, 104, 3481

[19] B.A. Goodman, J.B. Raynor, *Advances in Inorganic Chemistry and Radiochemistry* **1970**

1.1.2 Principles of TiO_2 photocatalysis

For many compounds, as the number N of atomic units in a particle increases, the energy necessary to photoexcite the particle decreases. When N >> 2000 it is possible to end up with a particle that has the electronic structure of semiconductor, as illustrated in Fig. 1.2, in which the highest occupied molecular orbital (HOMO) and the lowest unoccupied molecular orbital (LUMO) are separated by a Band Gap ΔE [20].

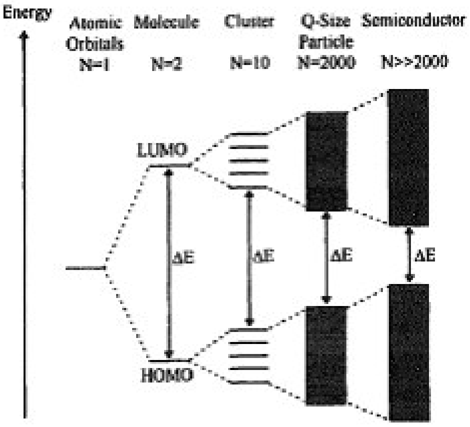

Fig. 1.2: changes in the electronic structures of a semiconductor

As indicated in Fig. 1.3, activation of a semiconductor photocatalyst for reaction is achieved through the absorption of a photon with an energy equal to the Band Gap value of the semiconductor; an electron e^- is promoted from the VB to the CB, with a concomitant generation of a hole h^+ in the VB. Upon excitation several processes can occur: electron-hole recombination can take place either at the surface (a) or in the bulk (b) of the semiconductor; at the surface, photogenerated electrons can reduce an electron acceptor A (reaction (c)) and holes can oxidise an electron donor species D (reaction (d)). For a semiconductor to be efficient, the different interfacial electron processes involving electrons and holes i.e. reactions (c) and (d) in Fig. 1.3, must compete effectively with the major deactivation processes involving recombination, i.e. reactions (a) and (b).

---

[20] A. Mills, S. Le Hunte, *Journal of Photochemistry and Photobiology A: Chemistry* **1997**, 108, 1

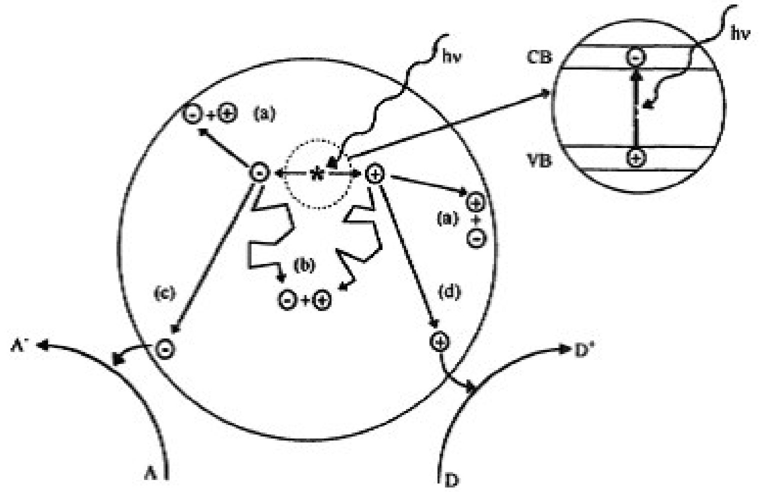

Fig. 1.3: processes occurring on a semiconductor particle upon photoexcitation

One of the most important feature for a photocatalyst is the availability, both synthetic or natural, and in this frame titanium dioxide is an ideal candidate. Moreover it is a low-cost material, chemically stable and the photogenerated holes are highly oxidizing. In addition, photogenerated electrons are reducing enough to produce superoxide from dioxygen [21]. TiO_2 story as a photocatalyst began with photoelectrochemical solar energy conversion and then shifted into the area of environmental photocatalysis, including self-cleaning surfaces, and more recently into the area of photoinduced hydrophilicity [22]. The possibility of solar photoelectrolysis was demonstrated for the first time in a system in which a n-type TiO_2 semiconductor electrode, that was connected through an electrical load to a platinum black counter electrode, was exposed to near-UV light [23]. When the surface of the titania electrode was irradiated with light consisting of a wavelengths shorter than 415 nm (TiO_2 Band Gap is and 3.0 for rutile, that corresponds, from the Plank equation to 415 nm), photocurrent flowed from the platinum counter electrode to the TiO_2 electrode through the external circuit. The direction of the current reveals that the oxidation reaction (oxygen

---

[21] A. Fujishima, T.N. Rao, D.A. Tryk, *Journal of Photochemistry and Photobiology C: Photochemistry Reviews* **2000**, 1, 1

[22] A. Fujishima, X. Zhang, *Comptes Rendus Chimie* **2005**,8, 750

[23] A. Fujishima, K. Honda, *Nature* **1972**, 238, 37

evolution) takes place at the semiconductor electrode and the reduction (hydrogen evolution) at the Pt side. This evidence shows that water can be decomposed using light without the application of an external bias. For thermodynamic considerations, if the photogenerated electron in the CB can reduce water, the potential of the band must be less than the redox potential of proton reduction; it also follows that, if the hole can oxidise water, the potential of the VB must be greater than that of oxygen formation. In Fig. 1.4 it is possible to see band positions of various semiconductors together with the relevant potentials of some redox couples.

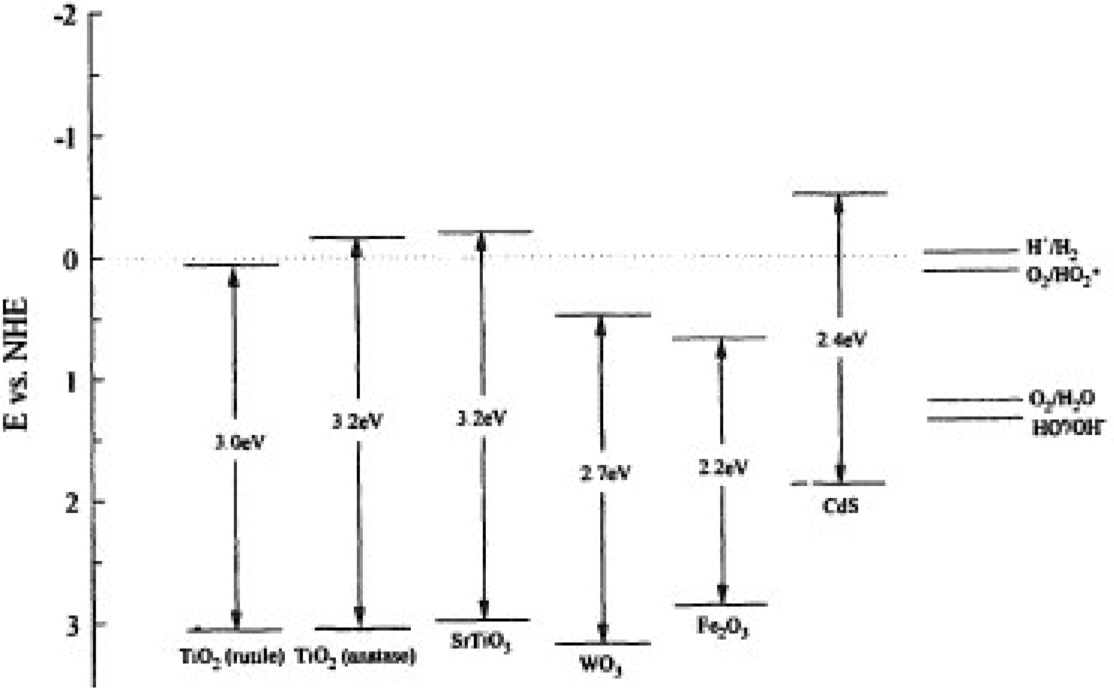

Fig. 1.4: band positions of some semiconductors together with redox potentials of two important redox couples.

Among the semiconductors that satisfy the energy levels requirement for oxygen and hydrogen production without an applied potential we can find titania, $SrTiO_3$, $CaTiO_3$ and Ta_2O_5. On the other hand, the employment of an external bias or of a difference in pH between the anode and the cathode is required in the case of other materials in order to achieve hydrogen evolution.

1.1.3 Mesoporous TiO_2

TiO_2 has commonly been utilized as a white pigment from ancient time. It is cheap, chemically stable, innocuous, biocompatible and environmental friendly. It has been found that titania is a promising material for energy generation. In 1972 Fujishima and Honda discovered photocatalytic water splitting on crystalline titania electrodes for hydrogen production [24] and subsequently the interest towards this material has grown significantly. Besides, titania has been found to be capable of decomposing contaminants in water and air and the research in this environmental clean up is one of the most active areas in heterogeneous photocatalysis [25, 26]. On the other hand, O'Regan and Gratzel discovered a new kind of solar cell based on a dye-sensitized titania electrode, called Dye Sensitized Solar Cell (DSSC) that has attracted attention due to its low cost and flexibility [27]. In all these photocatalytic applications TiO_2 with high surface areas, high crystallinity and mass diffusion within the network is necessary to achieve high efficiencies [28] and one way to have all these characteristics is to synthesise a mesoporous material.

According to the IUPAC definition, porous solids are classified into three groups based on their pore diameter, namely microporous (<2 nm), mesoporous (2-50 nm) and macroporous (>50 nm) materials. The term nanoporous is not clearly defined and loosely refers to pores in the nanometer size range.

The first synthesis of an ordered mesoporous materials was described in a patent in 1971 [29] but the key features of this new class of porous materials were not completely recognized due to a lack in the analysis method at that time. In 1992, scientists working for the Mobil Oil Corporation reported a new class of of mesoporous silicates, denoted ad M41s that opened up a new field of research [30].

---

[24] A. Fujishima, K. Honda, *Nature* **1972**, 238, 37

[25] H. Chen, C.E. Nanayakkara, V. Grassian, *Chemical Reviews* **2012**, 112, 5919

[26] U.I. Gaya, A.H. Abdullah, *Journal of Photochemistry and Photobiology C: Photochemistry Reviews* **2008**, 9,1

[27] B. O'Regan, M. Gratzel, *Nature* **1991**, 353, 737

[28] J.L. Vivero-Escoto, Y.D. Chiang, K.C.W. Wu, Y. Yamauchi, *Science and Technology Advanced Materials* **201**2, 13, 013003

[29] V. Chiol, J.E. Ritsko, C.D. Vanderpool, US Patent No. 3556725, **1971**

[30] C.T. Kresge, M.E. Leonowicz, W.J. Roth, J.C. Vartuli, J.S. Beck, *Natur*e **1992**, 359, 710

Subsequently, great attention has been devoted to synthesis and application of mesoporous materials and various mesostructures [31, 32], pore wall parameters [33, 34] and morphology [35].

The composition of mesoporous materials extends from silica to carbon, metals and oxides in which mesoporous titania is a kind of most important material as it shows great potentials in many applications [36].

The synthesis of mesoporous titania can be achieved by two main pathways, one is the soft-templating method and the other is hard-templating nanocasting approach.

1.1.3.1 Synthesis

1.1.3.1.1 Soft-templating Method

In the synthesis of mesoporous titania, organic surfactants molecules have a decisive role in generating the porosity and act as templates or structure directing agents (SDA). The soft templating method is the most successful pathway for the synthesis of ordered and disordered mesoporous matrices [37]. The SDA can be of different types. Surfactants can be used as templates, the essential feature is the coexistence of chemically bonded hydrophobic hydrocarbon tails and hydrophilic head groups; these molecule aggregate in a solvent to form self-assembled micelles [38]. There are others SDAs bearing hydrophobic-hydrophilic groups in a single molecule that are not surfactants but play the role of template and they may or may not form micelles [39]. Another type of SDA is dendrimer or

---

[31] Y. Sakamoto, M. Kaneda, O. Terasaki, D.Y. Zhao, J.M. Kim, G. Stucky, H.J. Shim, R. Ryoo, *Nature* **2000**, 408, 449

[32] C.Z. Yu, J. Fan, B.Z. Tian, G.D. Stucky, D.Y. Zhao, *Journal of Physical Chemistry B* **2003**, 107, 13368

[33] M. Widenmeyer, R. Anwader, *Chemistry of Materials*, **2002**, 14, 113827

[34] T.W. Kim, F. Kleitz, B. Paul, R. Ryoo, *Journal of the American Chemical Society* **2005**, 127, 7601

[35] H. Yang, N. Coombs, I. Sokolov, G.A. Ozin, *Nature* **1996**, 381, 589

[36] R. Zhang, A.A. Elzatahry, S.S. Al-Deyab, D. Zhao*, Nano Today* **2012**, 7, 344

[37] N. Pal, A. Bhaumik, Advances in Colloid and Interface Science **2013**, 189, 21

[38] J.S. Beck, J.C. Vartuli, W.J. Roth, M.E. Leonowicz, C.T. Kresge, K.D. Schmitt et al, *Journal of the American Chemical Society* **1992**, 114, 10834

[39] J.Y. Zheng, J.B. Pang, K.Y. Qiu, Y. Wei, *Journal of Material Chemistry* **2001**, 11, 3367

polymer, that can be single molecules having high molar weight [40]. In Fig. 1.5 is possible to see a classification of the SDA used as soft-templates

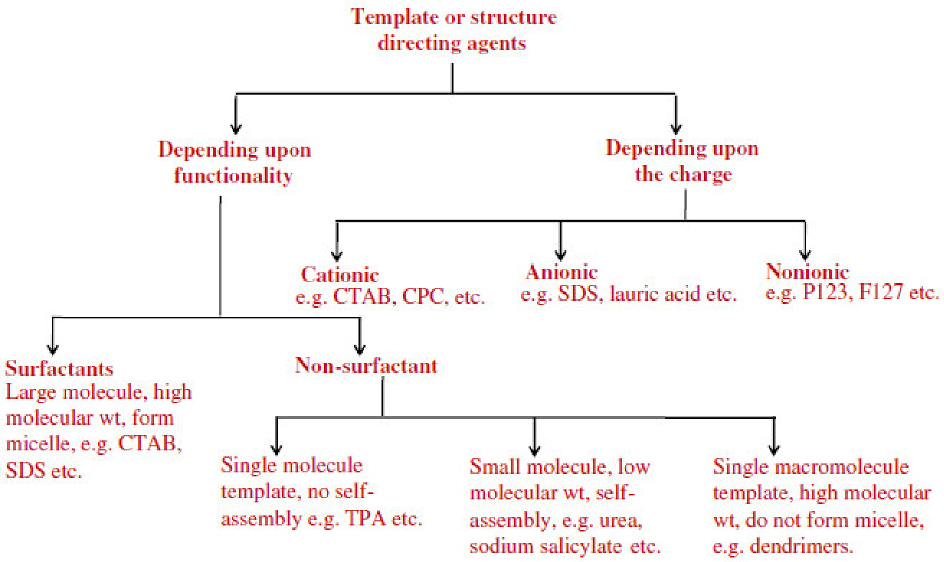

Fig. 1.5: Representation of various categories of soft templates

Surfactants have a hydrophobic and a hydrophilic part and can behave differently in polar and non-polar solvents. In aqueous media the polar moiety interacts with water. There are two ways for these molecules to stabilise in water (Fig. 1.6). The surfactant (Fig. 1.6 A) can arrange itself at the surface of water (Fig. 1.6 B) disrupting the cohesive energy at the surface and lowering the surface tension, or it can form aggregates in which the hydrophobic portions orient within a cluster and the hydrophilic portions are exposed to the solvent (Fig. 1.6 C), forming a so-called micelle. At low concentrations surfactants favour the arrangement on the surface but, as the surface becomes crowded, the molecules will arrange into micelles; at a certain concentration the surface becomes completely loaded and any further addition must arrange as micelles; this concentration in called the Critical Micelle Concentration (CMC) and different SDAs have different CMC. Beyond the CMC value, micelles self-assembly to form 3D spherical or 2D rod like array with further increasing concentration and this self-assembly helps in pore generation. Actually,

---

[40] G. Larsen, E. Lotero, M. Marquez, *Chemistry of Materials* **2000**, 12, 1513

the SDA molecules are the placeholders, what becomes the void space to produce porous materials.

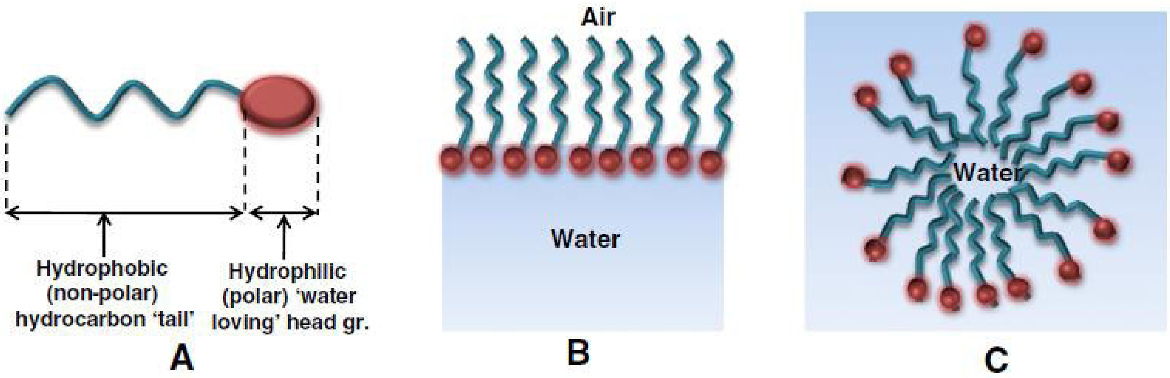

Fig. 1.6: surfactant molecule and its behaviour in aqueous media

Basing on the dissociation of the surfactant molecules in aqueous media, three type of amphiphilic surfactants can be recognised:

- Cationic surfactants that dissociate into an amphiphilic cation and anion, most often halide type. Common examples are cetyltrimethylammonium bromide (CTAB), N-Dodecyl pyridinium chloride etc.
- Anionic surfactants dissociate in water into an amphiphilic anion and a cation, which is in general an alkaline metal or a quaternary ammonium ion. They include alkylbenzene sulfonates (detergents), lauryl sulphate (foaming agent) etc.
- Nonionic surfactants do not ionize in water because their hydrophilic components are not-dissociable like alcohol, ether, ester, amide etc. A large variety of this type of surfactants is made hydrophilic by the presence of polyethylene glycol chain obtained by the polycondensation of ethylene oxide. Common examples are Pluronic P123, F127 etc.

In the soft templating method there are three steps to form a mesoporous material. First, the surfactant self-assembly, second is the organization of inorganic precursor over the surfactant assembly and formation of a stable organic-inorganic hybrid, and third is the successful removal of the organic template. Detailed studies on the formation of the composite materials revealed that two different mechanism are involved in this route. One is the Cooperative Self-Assembly (CSA) and the other is True Liquid Crystal Template (TLCT) mechanism [41]. In the CSA a simultaneous aggregation of self-assembled SDA along with the already added inorganic species occur, and a liquid-crystal phase with hexagonal, cubic, or laminar arrangement containing both the organic micelle and inorganic precursor can be developed (Fig. 1.7 a). On the other hand, the TLCT (Fig. 1.7 b) is 'true' since it covers all the possibility beyond mesophase formation [38]. The concentration of the surfactant is so high that, under the prevailing conditions, a lyotropic liquid-crystalline phase is formed without requiring the presence of the precursor inorganic material.

The final synthetic step, as already said, regarding the template removal and calcination in aerial atmosphere is the most familiar method to eliminate the organic part completely. Obviously, different temperatures are required for different templates; further, high temperature treatment increases the degree of crystallinity in the mesoporous material.

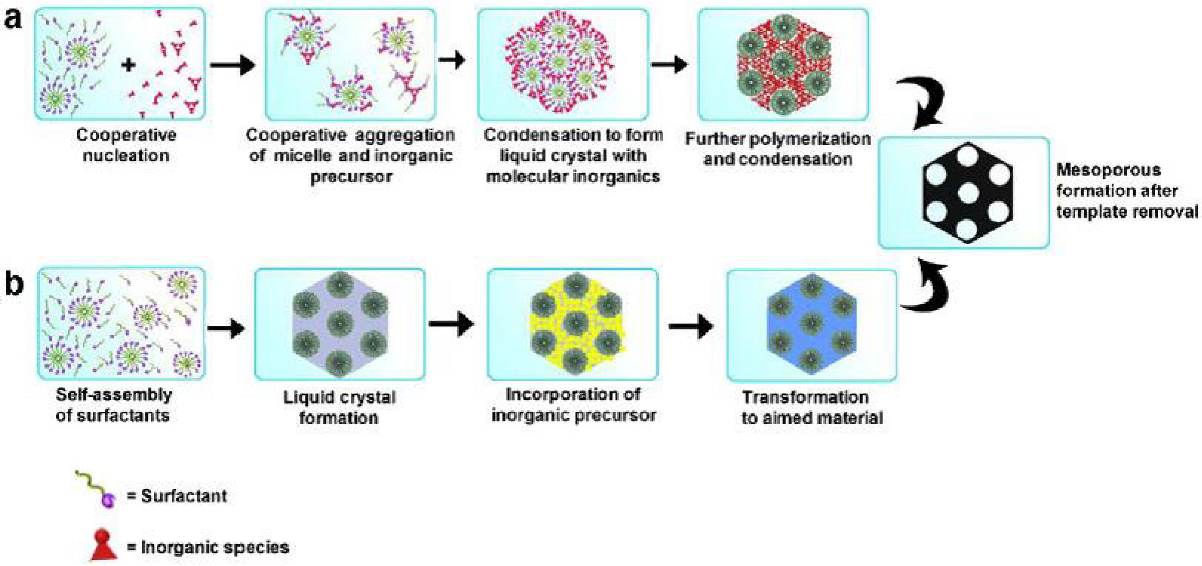

Fig. 1.7: formation of mesoporous structures (a) CSA (b) TLCT

---

[41] J.Y. Ying, C.P. Mehnert, M.S. Wong, *Angewandte Chemie International Edition* **1999**, 38, 56

Another soft-templating method that is often used for the synthesis of mesoporous titania, is the Evaporation Induced Self-Assembly (EISA) and, as it is considered a very promising method, it will be discussed separately in the next section.

1.1.3.1.2 Evaporation Induced Self-Assembly (EISA)

A definition of self-assembly is the spontaneous organization of materials into well-defined supramolecolar systems through non-covalent interactions [42].

Basing on this concept and on the discovery of silica- surfactant co-assembly in aqueous solutions, the groups of Brinker and Ozin were the first to apply the EISA process [43, 44] to the synthesis of mesostructured silica thin films. This sol-gel method implies the dispersion of a surfactant and of the chosen precursors, in an alcoholic acidic media at temperatures lower than 100°C. The surfactant is added in a concentration that is lower than its critical micelle concentration (CMC), then, by the slow evaporation of the solvent under controlled temperature and humidity, it starts assembling into micelles and, at higher concentrations, cylindrical micelles are formed; meanwhile also the synthetic precursors start to hydrolyse and condense around these micelles [45] and the cooperative nucleation and aggregation leads to the formation of an organic-inorganic hybrid structure. The final removal of the template is done usually by calcination and this step gives the final porosity and the complete condensation of the inorganic network. The whole process is summarised in Fig. 1.8.

---

[42] C.J. Brinker, Y. Lu, A. Sellinger, H. Fan, *Advanced Materials* **1999**, 11, 579

[43] H. Yang, N. Coombs, I. Sokolov, G.A. Ozin, *Natur*, **1996**, 381, 589

[44] Y. Lu, H. Fan, A. Stump, T.L. Ward, T. Rieker, C.J. Brinker, *Nature* **1999**, 398, 223

[45] L. Mahoney, R.T. Koodali, *Materials* **2014**, 7, 2697

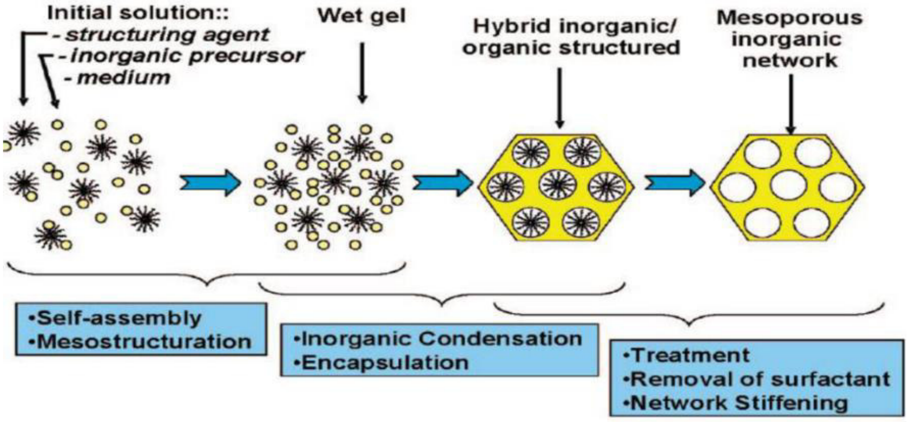

Fig. 1.8: the steps of an EISA process

The EISA process is usually applied for the preparation of ordered mesoporous thin films [46, 47] but it has also been used for the synthesis of powders such as TiO_2 [1, 2].

The templates can be divided in non-ionic or cationic surfactants. The first ones can be classified as diblock (ABAB repeating units) or triblock (ABC) co-polymers while the second class includes alkyltrimethyl quaternary ammonium and more complex structures as gemini, bolaform, tri-head group and tetra-head group rigid bolaform [48].

The majority of mesoporous titania is synthesised using a non-ionic surfactant employing a pluronic co-polymer that have the formula $[PEO]_n[PPO]_m[PEO]_n$, where PEO is poly(ethylene oxide) and PPO is poly(propylene oxide).

The synthesis of mesoporous titania is much more challenging than that of silica and this is due to the higher electrophilicity of Ti^{4+} ion compared to Si^{4+} that leads to uncontrolled hydrolysis and condensation of the former and to the formation of a poorly structured and dense inorganic network. Therefore several factors have to be taken into account during TiO_2 synthesis: the moisture level has to be strictly controlled to avoid fast hydration kinetics of the precursors, the pH of the solution has to be low for the same reason and an optimization of the removal of the template is required for avoiding shrinkage and even

---

[46] E.L. Crepaldi, G.J.A.A. Soller-Illa, D. Grosso, F. Cagnol, F. Ribot, C. Sanchez, *Journal of the American Chemical Society* **2003**, 125, 9770

[47] S.Y. Choi, M. Mamak, N. Coombs, N. Chopre, G.A. Ozin, *Material Science and Engineering B* **1997**, 47, 33

[48] Y. Wan, D. Zhao, *Chemical Reviews* **2007**, 107, 2821

collapse of the mesostructure [49]. In Fig. 1.9 it is possible to see a typical synthetic procedure to obtain mesoporous titania [50].

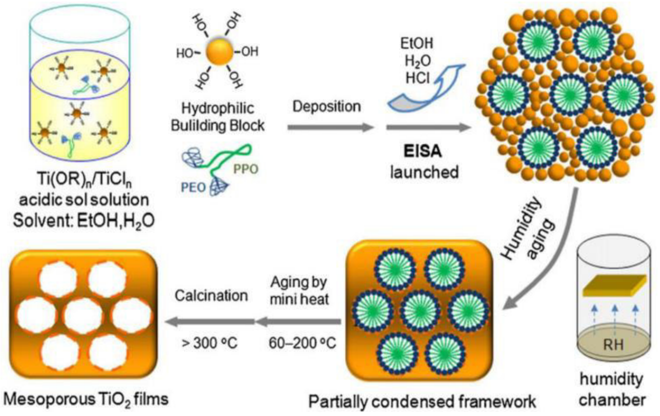

Fig. 1.9: Representation of the formation of a titania thin film

In order to control all the above mentioned issues related to the synthesis of mesoporous titania, several strategies can be applied: for lowering the hydration kinetics of titanium precursors, usually alcoxides, the addition of controlling agent acetylacetone is often used. Acetylacetone (acacH) acts as a coordinating ligand that chelates the precursors leading to metal complexes with lower hydration kinetics [51, 52]. Another possibility is to keep a low pH level during the synthesis by adding HCl, but recently another alternative was represented by the use of titanium chloride, together with a titanium alcoxide in a so called acid-base pairs approach [53], with the former being the pH adjustor and hydrolysis-condensation controller. The use of titanium chloride together with an alcoxide has also been applied for fine tuning the crystal composition of mesoporous titania powders and to obtain anatase/rutile mixed phases that resemble Degussa P25, a very photoactive commercial titania with a 20% rutile and 80% anatase composition [54, 55].

---

[49] P.D. Yang, D.Y. Zhao, D.I. Margolese, B.F. Chmelka, G.D. Stucky, *Nature* **1998**, 396, 152

[50] J.H. Pan, X.S. Zhao, W.I. Lee, *Chemical Engineering Journal* **2011**, 170, 363

[51] A. Yamamoto, S. Kambara, *Journal of the American Chemical Society* **1957**, 79, 4344

[52] J. Zhang, Y. Deng, D. Gu, S. Wang, L. Sha, R. Che, Z.S. Wang, B. Tu, S. Xie, D. Zhao, *Advanced Energy Materials* **2011**, 1, 241

[53] B. Tian, X. Liu, B. Tu, C . Yu, J. Fan, L. Wang, S. Xie, G.D. Stucky, D. Zhao, *Nature Materials* **2003**, 2, 159

[54] E. Masolo, M. Meloni, S. Garroni, G. Mulas, S. Enzo, M.D. Baro, E. Rossinyol, A. Rzeszutek, I. Herrmann-Geppert, M. Pilo, *Nanomaterials* **2014**, 4, 583

[55] E. Masolo, N. Senes, E. Pellicer, M.D. Baro, S. Enzo, M.I. Pilo, G. Mulas, S. Garroni, *International Journal of Hydrogen Energy* **2015**, 40, 14483

Another key step in the preparation of mesoporous materials is, as already said, the template removal by thermal treatment methods. Non-ionic surfactants are usually removed in the range of 300-350°C because excessive sintering may cause pore wall collapse [45, 49, 56.] Ozin and co-workers used P123 as a surfactant and calcined the obtained titania at 350 or 400°C obtaining reasonable hexagonal pore ordering [47].

1.1.3.1.3 Hard-templating Method

The Hard-templating approach is usually used to prepare mesoporous materials in a confined space, in which the growth of the inorganic matrix is restricted to the surface, cages, channels, or substrate of a 'hard template'. If a highly ordered mesoporous material is used as a template, an ordered mesoporous replica can be obtained by a controllable nanocasting process.

Despite the great success of the soft templating method, the hard templating method offers the possibility to avoid the issues connected to the former path, like the fast hydration kinetics of titanium precursors, lack of complete condensation, weak connection with surfactants or phase transitions accompanied by thermal breakdown of the structural integrity. In this context Ryoo and co-workers employed a siliceous matrix, KIT-6, as a hard template for the synthesis of ordered mesoporous materials via three steps [57]: (i) precursor infiltration inside mesochannels of the silica template; (ii) conversion of the precursors in the nanochannels; (iii) removal of the mesoporous silica template (usually by chemical reaction methods), which is well-known as nanocasting because the entire manufacturing procedure is similar to the traditional casting method but on the nanoscale. The demonstration of this strategy led to the concept of hard templating for preparing mesoporous materials. In this nanocasting approach (Fig. 1.10) the regular arrangements arises from the preformed mesoporous template. It should be mentioned that the small mesotunnels inside the template's pore walls are necessary for nanocasting. Moreover, the resultant replica can be used as a new template for other materials.

---

[56] W. Zhou, F. Sun, K. Pan, G. Tian, B. Jiang, Z. Ren, C. Tian, H. Fu, *Advanced Functional Materials* **2011**, 21, 1922

[57] R. Ryoo, S.H. Joo, S. Jun, *Journal of Physical Chemistry B* **1999**, 103, 7743

Fig. 1.10: representation of the hard templating method

However nanocasting has some limitations; for example, there are far fewer hard templates that can be used for nanocasting than soft templates. The procedure is also very complex and time-consuming because the hard templates are produced by the soft templating process (Fig. 1.11), and nanocast meoporous materials tend to be expensive and difficult to industrialize. Moreover, mesopores sizes obtained through this process are relatively small and not easy tunable.

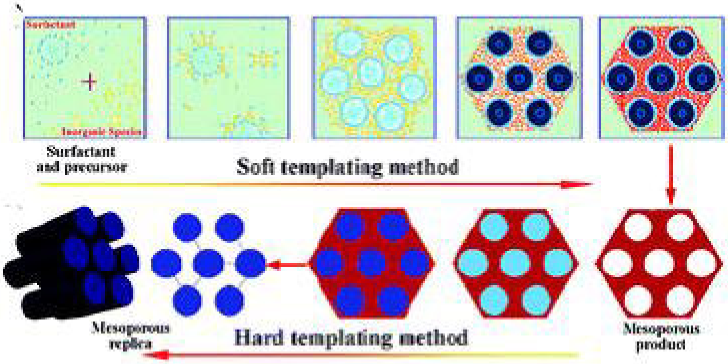

Fig 1.11: from soft to hard templating

1.1.3.2 Chromophores sensitization of mesoporous titanium dioxide

As already said in the previous paragraphs, titania is a widely studied photocatalyst that, due to its bandgap of 3-3.2 eV, absorbs part of the UV component of the solar radiation corresponding to only 4% of the total available spectrum. Various strategies can be used to improve the photocatalytic performances of this semiconductor, and one possibility is to extend the absorption in the visible region of the solar spectrum; among these strategies, non-metal doping, metal doping or co-doping, and dye sensitisation are the most popular [58].

In particular, dye-sensitisation is one of the most effective ways to extend titania photoresponse in the visible region and this type of functionalization is exploited in the well-known Dye Sensitised Solar Cells (DSSCs). DSSCs are a third generation Solar Cells that differ from the classical silicon-based photovoltaics because of much lower costs and easier fabrication. Moreover, they separate the function of light absorption (dye) from charge carrier transport (semiconductor and electrolyte). The first DSSC was presented by O'Reagan and Gratzel in 1991 [59], that used a trimeric Ru complex ($RuL_2(\mu\text{-}CN)Ru(CN)L'_2)_2$) with L= 2,2'-bipyridine-4,4'-dicarboxylic acid and L'=2,2'-bipirydine) as a dye. The heart of the system is a mesoporous titania layer composed of nanometer-sized particles sintered together on a conductive layer (usually conductive glass like ITO, indium-tin oxide) to allow to electronic conduction to take place. A monolayer of a chosen dye is attached to the surface of the semiconductor film. Photoexcitation of the dye results in the injection of an electron into the CB of titania, then the dye is regenerated by an electrodonating electrolyte, usually an organic solvent with a redox couple iodide/triiodide; the iodide is regenerated, in turn, by the reduction of the triiodide at a countereletrode, and the circuit is completed via electron migration through an external load (see Fig. 1.12 and 1.13 for the schematic representation and the mechanism of a DSSC).

After photoexcitation the dye molecule is in its oxidised state, then a possible drawback can be the recombination of the photogenerated electron with the positively charged dye, that can lead to lower performances of the cell.

---

[58] M. Pealez, N.T. Nolan, S.C. Pillai, M.K. Seery, P. Falaras, A.G. Kontos, P.S.M. Dunlop, J.W.J. Hamilton, J.A. Byrne, K. O'Shea, M.H. Entezari, D.D. Dionysiou, *Applied Catalysis B: Environmental* **2012**, 125, 331

[59] B. O'Regan, M. Gratzel, *Nature* **1991**, 353, 737

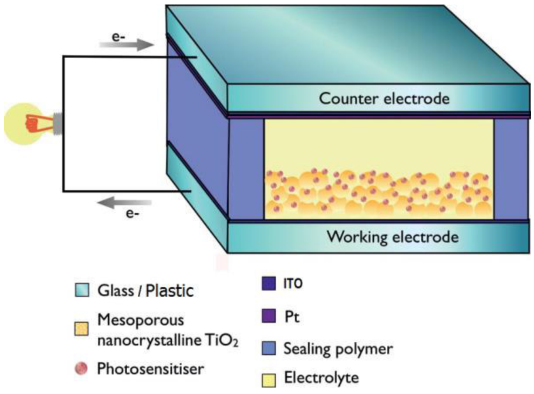

Fig. 1.12: schematic representation of a DSSC

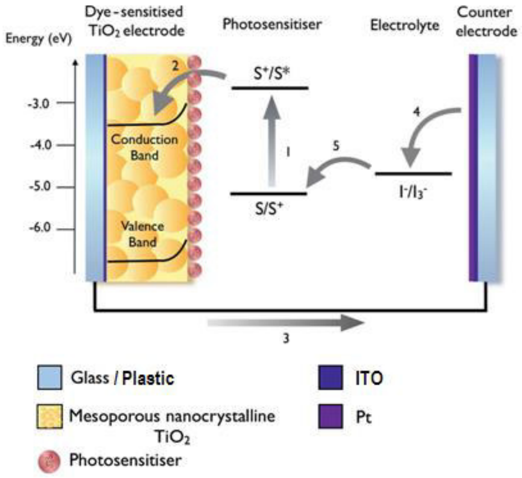

Fig. 1.13: working mechanism of a DSSC

Dyes efficiencies depends on some important features [60]: the HOMO value of the dye should be sufficiently positive in respect to the redox potential of the electrolyte to favour dye regeneration; the LUMO value of the dye should be sufficiently negative to efficiently inject electrons in the CB of the semiconductor (see Fig. 1.13).

In the lasts 15-20 years a lot of effort has been devoted to the synthesis and investigation of materials for DSSCs. Efforts in the synthesis of sensitizers can be grouped into two main areas:

- functional Ru(II)-polypyridyl complexes
- metal-free organic dyes with a donor-acceptor (D-A) structure.

---

[60] 60 L. Schmidt-Mende, U. Bach, R. Humphry-Baker, T. Horiuchi, H. Miura, S. Ito, S. Uchida, M. Gratzel, *Advanced Materials*, **2005**, 17, 813

In the following part a brief description of the development of new dyes of both categories will be given.

Since the work by Gratzel [59] ruthenium complexes have been studied for DSSC applications due to their favourable photoelectrochemical properties and high stability in the oxidised state. The high efficiencies of ruthenium(II)-polypyridyl DSSCs can be attributed to their wide absorption that ranges from the visible to the near-infrared part of the solar spectrum due to metal-to-ligand charge transfers (MLCT). The paradigm of heterogeneous charge transfer is represented by **N3** **[61]** dye $RuL_2((NCS)_2$, where L= 4,4'-dicarboxy-2,2'-bipyridine, that showed the best performances both in term of conversion yield (efficiencies around 11%) and long term stability, and also by its analogues **N719** [62] and the so-called **black dye** [63] (Fig. 1.14). The role of the carboxylate group is to allow immobilization of the sensitiser on titania film via the formation of ester linkages whilst the –NCS groups enhance the visible light absorption [63]. In ruthenium-complexes ligands can be classified as 'anchoring' or 'auxiliary': the former class (usually carboxylate groups) is responsible for the dye adsorption on titania layer, while the latter involves compounds not directly bound to the semiconductor. The chemical structure of auxiliary ligands can be finely tuned to improve the performances of the dyes.

---

[61] M.K. Nazeeruddin, A. Kay, I. Rodicio, R. Humphry-Baker, E. Muller, P. Liska, N. Vlachopoulos, M. Gratzel, *Journal of the American Chemical Society* **1993**, 115, 6382

[62] M.K. Nazeeruddin, S.M. Zakeeruddin, R. Humphry-Baker, M. Jirousek, P. Liska, N. Vlachopoulos, V. Shklover, C.H. Fischer, M. Gratzel, *Inorganic Chemistry* **1999**, 38, 6298

[63] M.K. Nazeeruddin, P. Pechy, T. Renouard, S.M. Zakeeruddin, R. Humphry-Baker, P. Comte, P. Liska, C. Le, E. Costa, V. Shklover, L. Spiccia, G.B. Deacon, C.A. Bignozzi, M. Gratzel, *Journal of the American Chemical Society* **2001**, 123, 1613

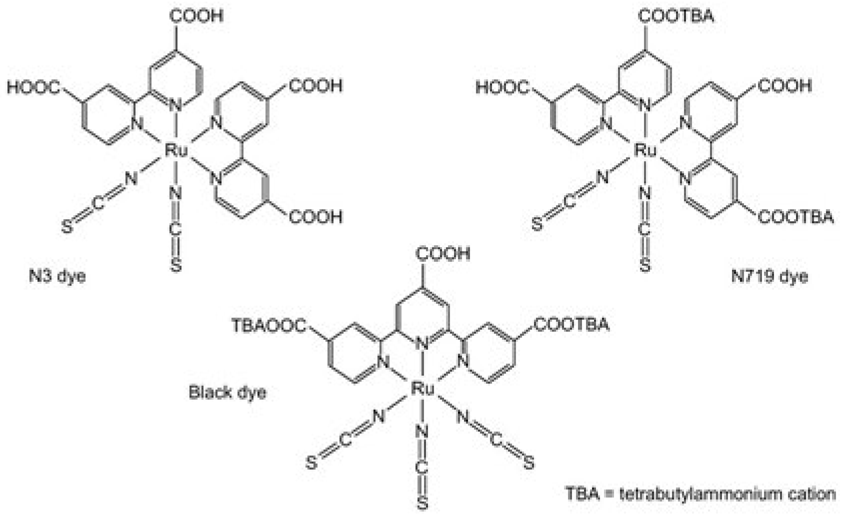

Fig. 1.14: N3, N719 and black dye

The carboxylic anchoring group is usually labile and water-induced desorption may occur. To overcome this problem Nazeeruddin et al. [63] synthesised a series of ruthenium complexes with alkyl-substituted bipiridyne, conferring hydrophobic properties to the complexes (Fig. 1.15). These complexes showed excellent stability towards desorption and also a broad UV-Vis spectra with adsorption maxima at around 530 nm.

As already said, **N3** is a paradigm in the area of titania sensitizers, and the vast majority of dyes are based on its design. In spite of this, **N3** suffers from a lack of adsorption in the red region of the visible spectrum and also from a low molar extinction coefficient.

A series of high molar extinction sensitisers has been developed (Fig. 1.16) [64], all featuring alkyloxy groups with the purpose of extending the π-conjugation with substituted methoxy group. The adsorption spectra of these complexes are dominated by metal-to-ligand charge transfers (MLCT) in the visible region and the molar extinction coefficients were higher than **N3**, being close to 35000 and 19000 $M^{-1}cm^{-1}$.

---

[64] P. Wang, C. Klein, R. Humphry-Baker, S.M. Zakeeruddin, M. Gratzel, *Applied Physical Letters* **2005**, 86, 123508

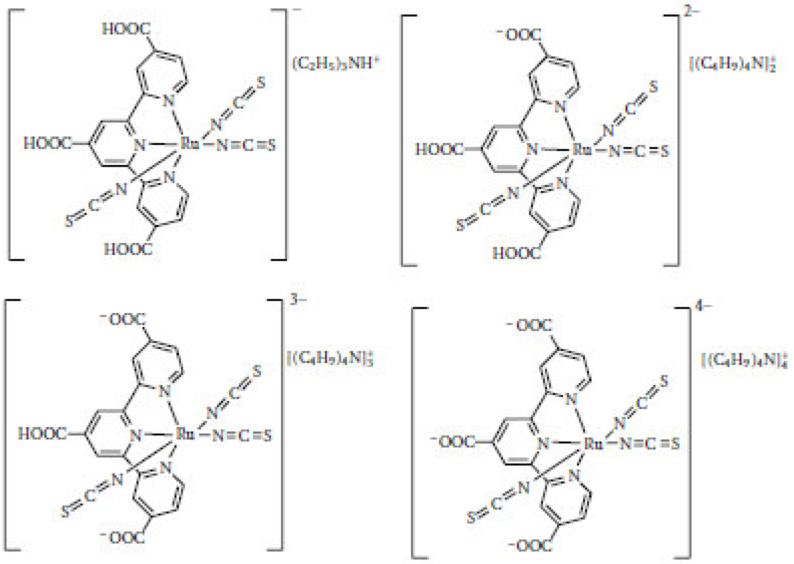

Fig. 1.15: Ru sensitisers synthesised by Nazeeruddin et al. [63]

In recent years an intermediate between hydrophobic and high molar extinction sensitizers appears. It is based on heteroleptic sensitisers with a ligand bearing a thiophene moiety to extend the delocalization of the complex and functionalised with an alkyl chain to shield titania surface from the redox mediator (Fig. 1.17) [65]. These sensitisers showed excellent performances as their molar extinction coefficients are high at around 18000 $M^{-1}cm^{-1}$.

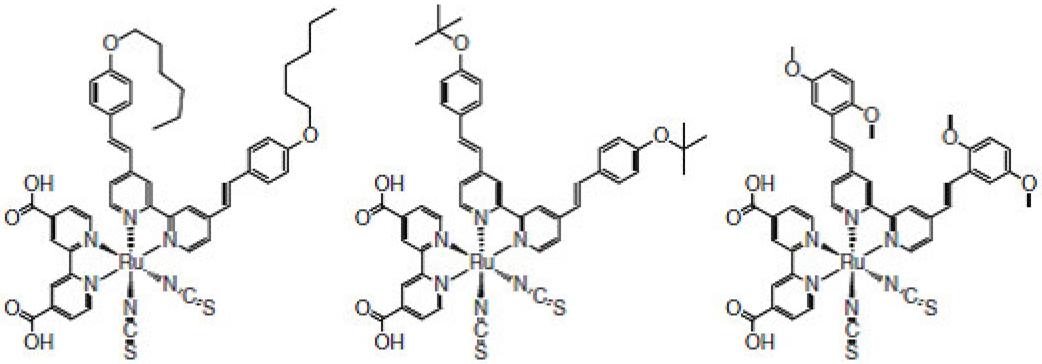

Fig. 1.16: complexes synthesised by Wang et al. [64]

---

[65] Y. Cao, Y. Bai, Q. Yu, Y. Cheng, S. Liu, D. Shi, F. Gao, P. Wang, *Journal of Phisical Chemistry* C **2009**, 113, 6290

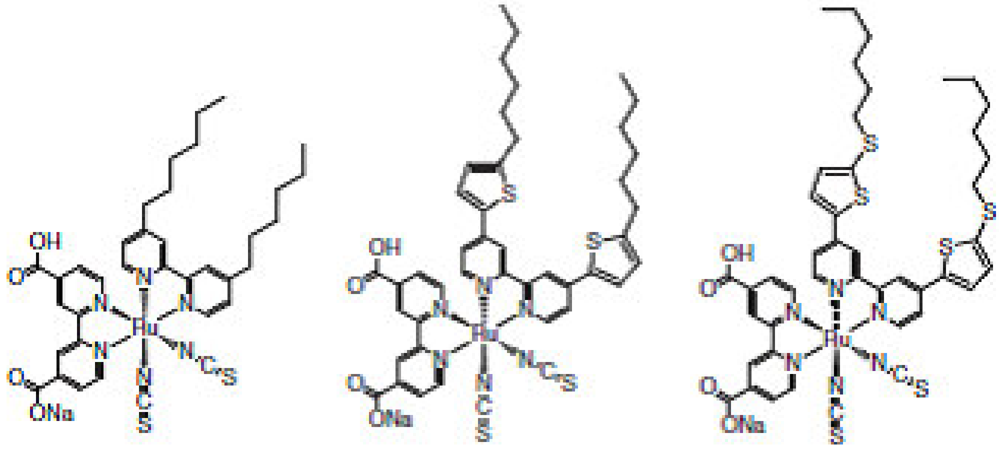

Fig. 1.17: Thiophene substituted complexes [65].

The thiocyanate ligands are considered as the most fragile part of the dye because they are monodentate and also because they can coordinate with the sulphur or with the nitrogen atom. Efforts have been made to replace those ligands and one of the most promising alternative was obtained with a cyclometallated 2,4-difluorophenylpyridine, yielding the complex **YE05** (Fig. 1.18) [66]. Its spectral response was significantly red-shifted when compared to **N719**, because the cyclometallated ligand is a stronger donor than the thiocyanates and this resulted in a stronger destabilization of the HOMO than the LUMO. Moreover the Ru-C σ bond can reduce the local symmetry of the metal site to generate a relatively broad absorption envelope and destabilise metal-centered (MC) excited states that provide access to non-radiative pathways [67]. In addition, the replacement of –NCS offers the opportunity to independently tune both the metal-based HOMO and the ligand π*-based LUMO [68].

---

[66] T. Bessho, E. Yoneda, J-H. Yum, M. Guglielmi, I. Tavernelli, H. Imai, U. Rothlisberger, M.K. Nazeeruddin, M. Gratzel, *Journal of the American Chemical Society* **2009**, 131, 5930

[67] P.G. Bomben, K.C.D. Robson, P.A. Sedach, C.P.Berlinguette, *Inorganic Chemistry* **2009**, 48, 9631

[68] P.G. Bomben, B.D. Kovisto, C.P.Berlinguette, *Inorganic Chemistry* **2010**, 49, 4960

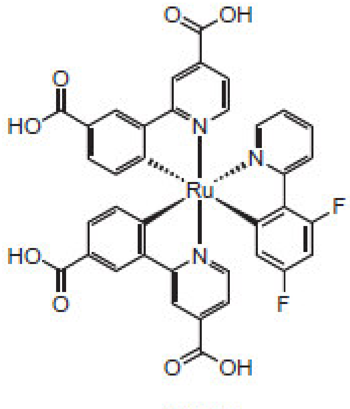

YE05

Fig. 1.18: cyclometallated dye **YE05**

Ruthenium-based sensitizers are, of course, expensive and require careful synthesis and tricky purification steps. As a matter of facts a new class of metal-free organic dyes has emerged as an alternative to Ru complexes [69].

Organic dyes offer the advantage of lower costs and the possibility to extend the electronic properties of the materials. Moreover, their high molar extinction coefficients (ε) (higher than Ru complexes) often imply a HOMO distributed over a significant portion of their structure and spatially separated from the LUMO.

For the as-mentioned reasons, an approximate trend can be deduced, with respect to organic dyes, for their design: in principle the general scheme for a sensitizer consists of a donor-acceptor substituted π-conjugated "bridge" to which the anchoring group to the TiO_2 is attached at the side of the acceptor (Fig. 1.19); this arrangement facilitates a light-driven π-π* transition.

---

[69] A. Mishra, M.K.R. Fischer, P. Bauerle, *Angewandte Chemie International Edition* **2009**, 48, 2474

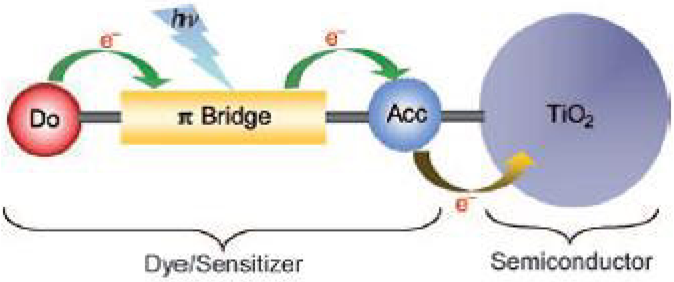

Fig. 1.19: general scheme of an organic dye

Analysis of data concerning the best type of donors (D), π-bridge, and acceptor (A) reveals that among the best donors electron-rich arylamines (triphenylamine and indoline) play an important role because of their non-planar structure that suppress dye aggregation. The best moieties for the conjugated bridge often contain thiophene units because of their excellent charge-transport properties. Finally, the acceptor fragment is almost the same for every dye and it is usually the cyanoacrylic acid group [69, 70] (Fig. 1.20).

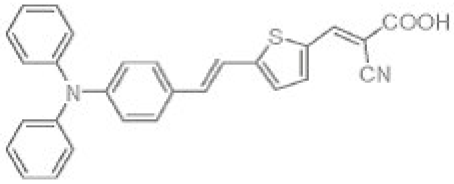

Fig. 1.20: representative structure of an organic dye bearing triphenylamine as donor, thiophene as spacer and cyanoacrylic acid as acceptor [70]

Cyanoacrylic acid can bind titania and offers the advantage of both wide adsorption spectra in the visible region and good electron injection efficiency. However, dyes with –COOH anchor units will dissociate on TiO_2 surface under long irradiation times [71]. Consequently, different anchoring groups have been tested as valid alternatives to cyanoacrylic acid.

---

[70] D.P. Hagberg, J.H. Yum, H.J. Lee, F. De Angelis, T. Marinado, K.M. Karlsson, R. Humphry-Baker, L. Sun, A. Hagfeldt, M. Gratzel, M.K. Nazeeruddin, *Journal of the American Chemical Society* **2008**, 130, 6529

[71] H. He, A. Gurung, L. Si, *Chemical Communications,* **2012**, 48, 5910

Tian et al. [72] report the synthesis of a novel electron-acceptor 2-(1,1-dicyanomethylene)rhodanine (DCRD) that has the advantages of the double electron-acceptor function of both rhodanine and dicyanomethylene. Furthermore, O and N atoms can chelate titanium ions and this coordination allows good electron coupling between the excited-state of the dye and the CB of titania. Sensitizers coded as RD-I and RD-II, that differs for the presence of a thiophene as a bridging unit, were synthesised and compared to the analogues CA-I and CA-II bearing cyanoacrylic moieties (Fig. 1.21).

Both RD-I and RD-II showed broadened absorption spectra and comparable electron injection efficiency than the cyanoacrylic counterparts and the overall efficiencies are even higher than CA-I and CA-II respectively. In particular, the presence of a thiophene bridge leads to improved performances (conversion efficiency of 7.11%). The dyes were also stable towards solar irradiation and can represent a valid alternative as a new anchoring group for organic dyes.

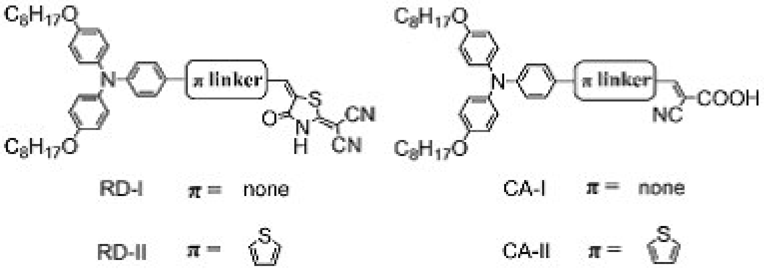

Fig. 1.21: organic dyes with DCRD anchoring unit [72]

Other groups investigated on the properties of alternative acceptor units in porphyrine- or phtalocyanine-based dyes (not organic sensitizers). Si et al. [71] reported for the first time the use of 8-hydroxyquinoline modified porphyrin (TPPZn-OQ) dye and compared it to a benzoic acid modified porphyrin (TPPZn-COOH). In Fig. 1.22 it is possible to see the structure of these dyes. The N and O atoms of hydroxyquinoline can chelate to metal ions and form stable complexes.

---

[72] J. Mao, N. He, Z. Ning, Q. Zhang, F. Guo, L. Chen, W. Wu, J. Hua, H. Tian, *Angewandte Chemie International Edition* **2012**, 51, 9873

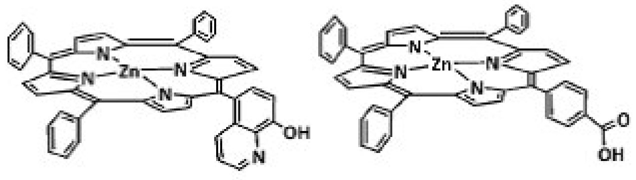

TPPZn-OQ TPPZn-COOH

Fig. 1.22: modified porphirin dyes [71]

The authors found out that the carboxylated porphyrin dissociated from titania after 3 h of irradiation, while TPPZn-OQ showed no dissociation after 3 weeks leading to the conclusion that OQ is a promising candidate as an alternative to benzoic acid for porphyrin dyes. Phosphinic acid was also tested as acceptor unit in a phtalocyanine based dye **TT-30** and **TT-32** and the performances were compared to a carboxylated analogues **TT-1** (Fig. 1.23) [73].The results showed that the adsorption on titania was higher for the carboxylated derivative. However, phosphinic acid was shown to have stronger binding properties that improved the durability of the DSSCs.

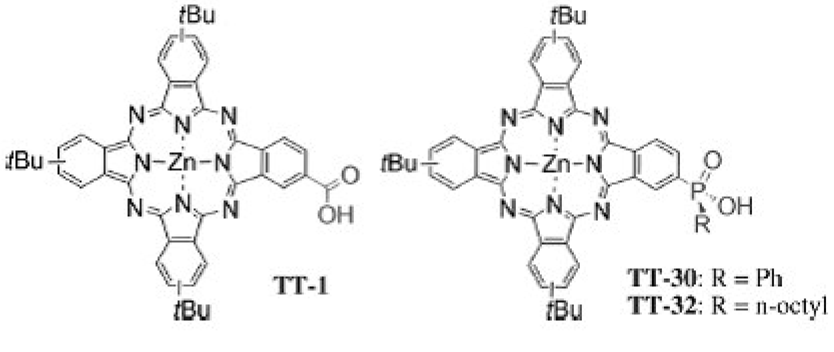

TT-1

TT-30: R = Ph
TT-32: R = n-octyl

Fig. 1.23: synthesised molecules with phosphinic acid or carboxylic acid as anchoring groups [73].

---

[73] I. Lopez-Duarte, M. Wang, R. Humphry-Baker, M. Ince, M.V. Martinez-Diaz, M.K. Nazeeruddin, T. Torres, M. Gratzel, *Angewandte Chemie International Edition* **2012**, 51, 1895

Harima et al.[74] reported the synthesis of an organic D-π-A dye bearing a pyridine ring as electron acceptor and anchoring unit. They demonstrated that the newly developed dyes **NI3-6** (that differ for the presence of alkyl chains and/or thiophene unit, Fig. 1.24) can absorb on TiO_2 surface by strong coordination bonding between the lone pair of electrons on the nitrogen atom of the pyridine and the Lewis acid sites of titania to give electron injection efficiencies comparable to or higher than those for **NI1** and **NI2** where the pyridine ring is replaced with carboxyphenyl group (Fig. 1.24).

The thiophene presence in **NI5** and **NI6** leads to higher photovoltaic performances attributed to both the red-shift of adsorption band and the good balance between the LUMO level of the dyes and the energy level of titania CB.

In an attempt to combine the favourable attributes of organic (D-π-A structure and high ε values) and inorganic (MLCT processes and broader absorption profiles) chromophores, Berlinguette et al.[75] set out a series of hybridised systems (Fig. 1.25).

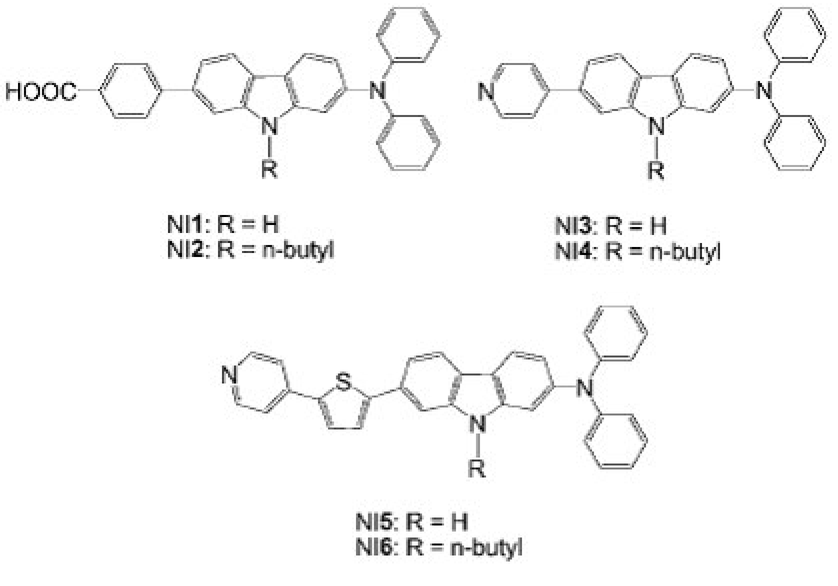

NI1: R = H
NI2: R = n-butyl

NI3: R = H
NI4: R = n-butyl

NI5: R = H
NI6: R = n-butyl

Fig. 1.24: synthesised compounds with and without pyridine moiety[74]

---

[74] Y. Ooyama, S. Inoue, T. Nagano, K. Kushimoto, J. Oshita, I. Imae, K. Komaguchi, Y. Harima, *Angewandte Chemie International Edition* **2011**, 50, 7429

[75] K.C.D. Robson, B.D. Koivisto, T.J. Gordon, T. Baumgartner, C.P. Berlinguette, *Inorganic Chemistry* **2010**, 49, 5335

The authors chose triphenylamine (TPA) as donor motif as it is a common fragment in organic dyes [69]. TPA was functionalized with a ligand (2,2’:6’,2’’-terpyridine (tpy)) capable of coordinating metal ions, obtaining organic ligands **L1-L3**. They also incorporated acetylene and 2,5-thiophene linkers to circumvent steric repulsion between aromatic rings of TPA and tpy and evaluated the role of the spacer unit on the photophysical properties of the molecules. The coordination to Ru(II) leads to **1-4** hybrid dyes. All complexes showed high ε values (from 29000 to 44000 $M^{-1}cm^{-1}$) and this highlights the positive effect of the D-A arrangement of the TPA-tpy motif on the absorption profiles of Ru(II) coordination complexes; in particular, higher molar extinction coefficients are due to the presence of acetylene or thiophene in **2**, **3** and **4** in respect to **1**. Moreover, in **3** and **4** the presence of thiophene spacer has a stronger influence on the optical properties of ligands and complexes (bathochromic shift of adsorption maxima and higher ε values) due to its polarizability, its low resonance level, and its aptitude to promote a planar arrangement between TPA and tpy.

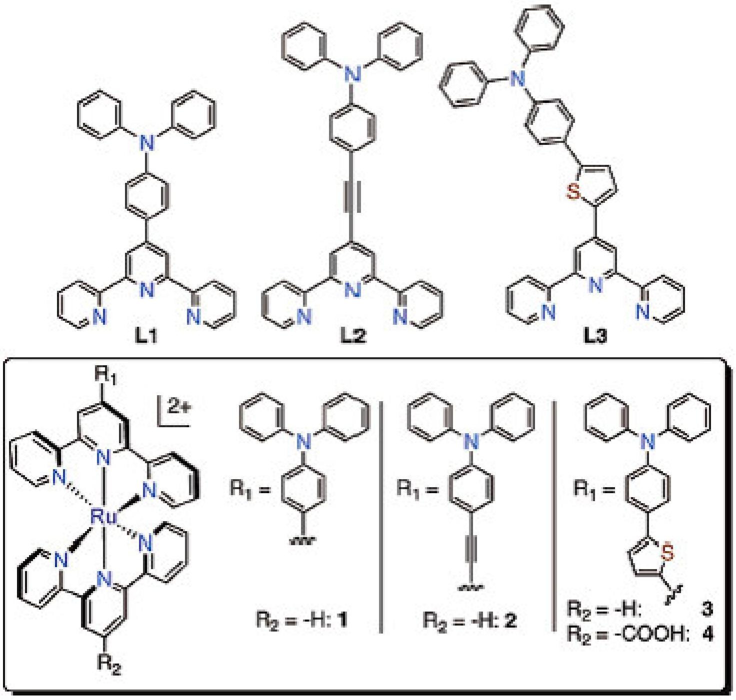

Fig. 1.25: hybrid compounds synthesised by Berlinguette et al. [75]

Another attempt to combine organic and inorganic chromophores characteristics in a cyclometallated hybrid system was done always by Berlinguette and collaborators [76], being cyclometallation an appealing way to increase complex stability. In this work they reported the synthesis of heteroleptic cyclometallated Ru(II) complexes containing an electron rich TPA-substituted tridentate ligand opposite to a tridentate chelating one with, in certain cases, electron-deficient substituents capable of binding to semiconductor surfaces (Fig. 1.26).

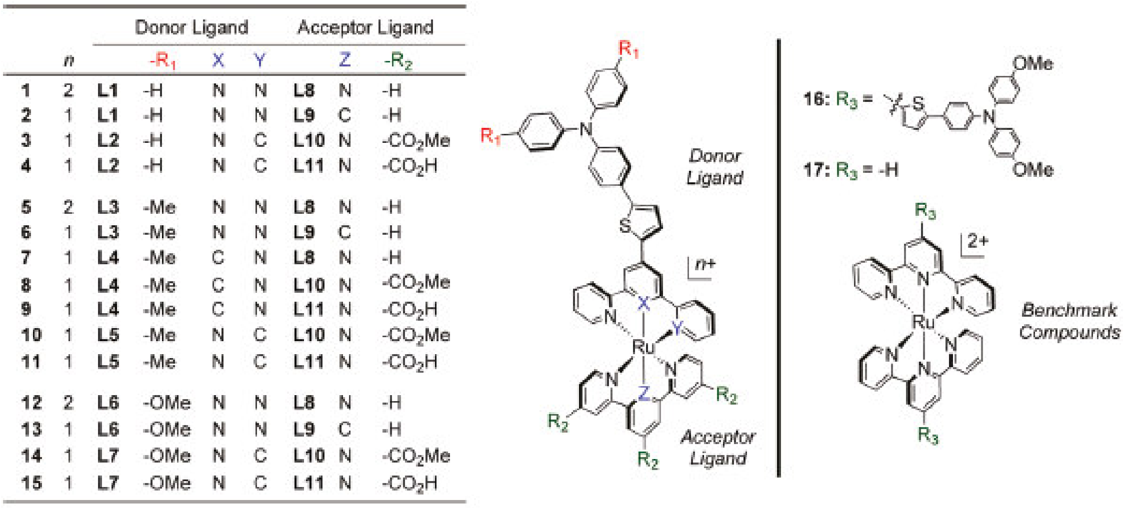

		Donor Ligand				Acceptor Ligand		
	n		$-R_1$	X	Y		Z	$-R_2$
1	2	**L1**	-H	N	N	**L8**	N	-H
2	1	**L1**	-H	N	N	**L9**	C	-H
3	1	**L2**	-H	N	C	**L10**	N	$-CO_2Me$
4	1	**L2**	-H	N	C	**L11**	N	$-CO_2H$
5	2	**L3**	-Me	N	N	**L8**	N	-H
6	1	**L3**	-Me	N	N	**L9**	C	-H
7	1	**L4**	-Me	C	N	**L8**	N	-H
8	1	**L4**	-Me	C	N	**L10**	N	$-CO_2Me$
9	1	**L4**	-Me	C	N	**L11**	N	$-CO_2H$
10	1	**L5**	-Me	N	C	**L10**	N	$-CO_2Me$
11	1	**L5**	-Me	N	C	**L11**	N	$-CO_2H$
12	2	**L6**	-OMe	N	N	**L8**	N	-H
13	1	**L6**	-OMe	N	N	**L9**	C	-H
14	1	**L7**	-OMe	N	C	**L10**	N	$-CO_2Me$
15	1	**L7**	-OMe	N	C	**L11**	N	$-CO_2H$

Fig. 1.26: series of cyclometallated compounds synthesised by Berlinguette et al. [76]

These molecular motifs were chosen for the following reasons: (i) organic dyes bearing TPA units as donors gave efficiencies higher than 10 % [77], (ii) TPA serves as a redox unit that has been shown to suppress recombination between CB electrons and the oxidised Ru dye [78], (iii) the 2,5-thiophene bridge serves to circumvent steric repulsion between the aromatic rings and encourages a planar arrangement for enhanced conjugation [75]. A comparative performance of selected dye complexes was also evaluated (benchmark in Fig. 1.26).

---

[76] K.C.D. Robson, B.D. Koivisto, A. Yella, B. Sporinova, M.K. Nazzeruddin, T. Baumgartner, M. Gratzel, C.P. Berlinguette, *Inorganic Chemistry* **2011**, 50, 5494

[77] W. Zeng, Y. Cao, Y. Bai, Y. Wang, Y. Shi, M. Zhang, F. Wang, C. Pan, P. Wang, *Chemistry of Materials* **2010**, 22, 1915

[78] P. Bonhote, J.E. Moser, R. Humphry-Baker, N. Vlachoupoulos, S.M. Zakeeruddin, L. Walder, M. Gratzel, *Journal of the American Chemical Society* **1999**, 121, 1324

The authors demonstrated that the placement of the organometallic bond and substitution at the R1 position offer the possibility of handling the position of HOMO in the molecule in a controlled fashion. They also revealed that the absorption profiles and the photoaction spectra of these systems can be extended beyond 750 nm, and that the proper design of hybridised organometallic/organic dyes without –NCS ligands are capable of generating high efficiencies (>8 %).

A D-A-π-A novel specific configuration for cyanoacetic acid organic derivatives was reported by Tian [79] by introducing additional acceptor benzothiadiazole between an indoline or TPA donor and a thiophene linker. The additional acceptor was expected to function as an electron trap where charge separation occurs thus facilitating the electron migration direction to the anchoring unit. The compounds under study can be seen in Fig. 1.27 and their properties were compared to D-π-A **LS-1** compound.

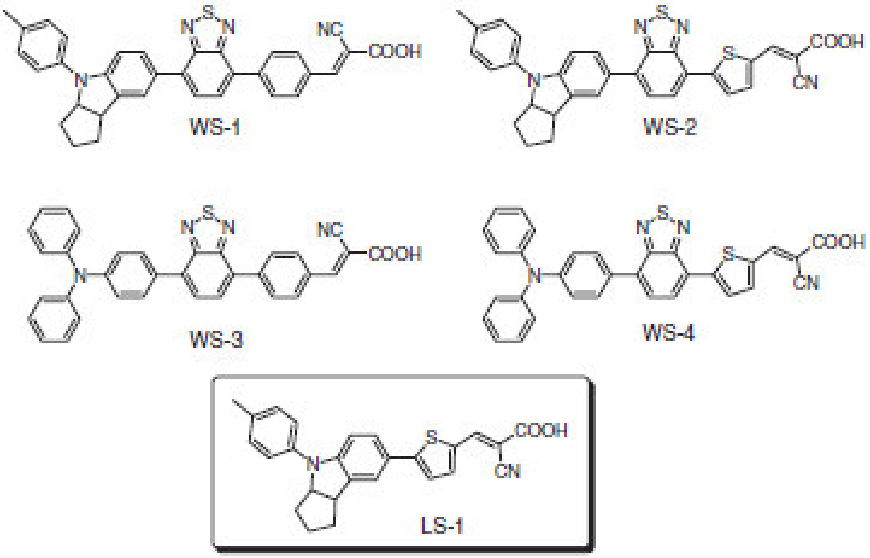

Fig. 1.27: novel D-A-π-A chromophores [79]

The authors proved that the presence of benzothiadiazole unit leads to several advantages like an enhancement in photostability of the compounds, a red-shifting absorption spectra into the NIR region and a weakening in deprotonation effect on titania film, which is beneficial to light-harvesting. The outstanding IPCE response (higher than 0.8), high

---

[79] W. Zhu, Y. Wu, S. Wang, W. Li, J. Chen, Z. Wang, H. Tian, *Advanced Functional Materials* **2011**, 21, 756

conversion efficiencies and long term stability revealed that the new D-A-π-A configuration is very interesting for molecular engineering of organic dyes.

Other works in literature can be regarded as an attempt to test this configuration, although in some cases the authors did not specify it in their articles [80, 81, 82].

Following this trend, He et al. [83] made a series of theoretical calculations to evaluate the influence of different positions of an auxiliary acceptor (benzothiadiazole) in D-A-π-A organic sensitizers on the HOMO-LUMO energy levels and the energy gaps of the sensitizers under fixed electro-donating and accepting groups (Fig. 1.28).

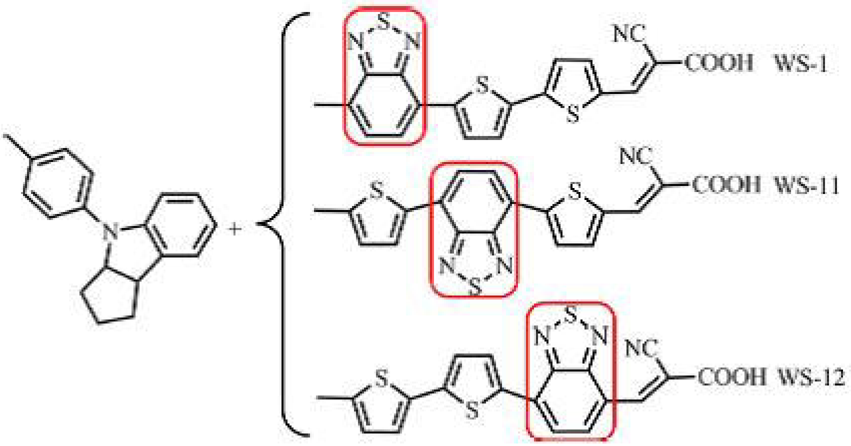

Fig. 1.28: theoretically studied D-A-π-A chromophores with various geometries [83]

By analysing electronic structures, charge transfers, lifetime of excited states and optical properties, the authors found out that WS-12, that bears the additional acceptor unit just before the anchoring cyanoacrylic acid, exhibited better theoretical performances among the three dyes leading to a high short circuit current-density and a great open-circuit potential.

Among organic dyes for DSSCs application, the class of conjugated polymers as sensitizers is gaining importance due to the advantages of sufficiently large absorption coefficient and

---

[80] M. Velusamy, K.R.J. Thomas, J.T. Lin, Y.VC. Hsu, K.C. Ho, *Organic Letters* **2005**, 7, 1899

[81] H. Tian, X. Yang, R. Chen, R. Zhang, A. Hagfeldt, L. Sun, *Journal of Physical Chemistry C* **2008**, 12, 11023

[82] H. Zu, W. Li, Y. Wu, B. Liu, S. Zhu, X. Li, H. Agren, W. Zhu, *ACS Sustainable Chemical Engineering* **2014**, 2, 1026

[83] P. Yu, F. Zhang, M. Li, R. He, *Journal of Materiasl Science* **2015**, 50, 7333

tunable energy levels. A detailed description of the use of CP will be given in the next session.

1.2 Conducting Polymers

When looking at the conductivity, materials can be divided in four categories (Fig. 1.29): insulators (conductivity lower than 10^{-7} S/cm), semiconductors (between 10^{-4} and 10 S/cm), conductors and superconductors (over 10^{3} S/cm).

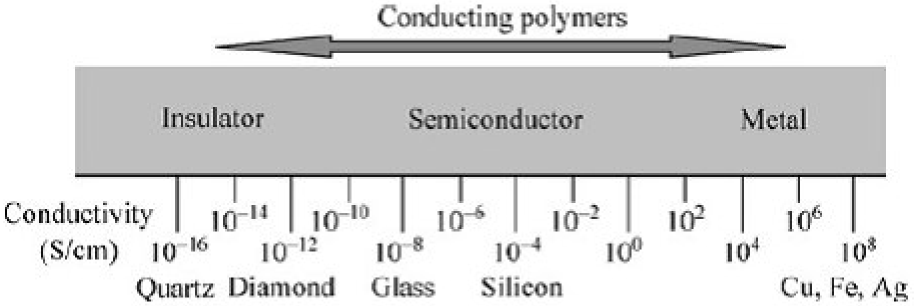

Fig. 1.29: materials classification basing on conductivity values

Since 60's organic polymers were known for their insulating properties, then, in 1977 Heeger, MacDiarmid and Shirakawa discovered that Polyacethylene (PA) showed conductivity values of 10^{3} S/cm when doped with iodine [84] at room temperature, while without doping the values were about 10^{-7} S/cm. The term 'doping' was then used to specify the phenomena of this great conductivity increase and polymers exhibiting this property were named 'conducting polymers'. In 2000 these scientists won the Nobel price for this important discovery. Since then, lot of scientific effort is done in the conducting polymers research area because of the possibility of tailoring their physical and chemical properties by doping and de-doping mechanisms.

---

[84] H. Shirakawa, E.J. Louis, A.G. MacDiarmid, C.K. Chiang, A.J. Heeger, *Journal of the Chemical Society Chemical Communications* **1977**, 578

Typical band gap values of conducting polymers lie between 1-3 eV, and this evidences the insulating or semiconducting [85] nature of the polymers; it is only through doping that polymers can have conductivities as high as those of metals.

Conducting polymers find various applications in many fields, some of them can be appreciated in Fig. 1.31.

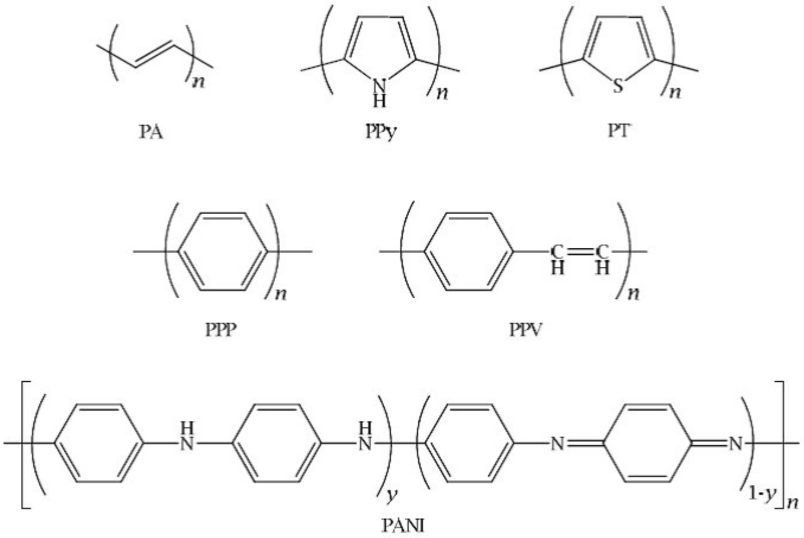

Fig. 1.30: examples of some conducting polymers

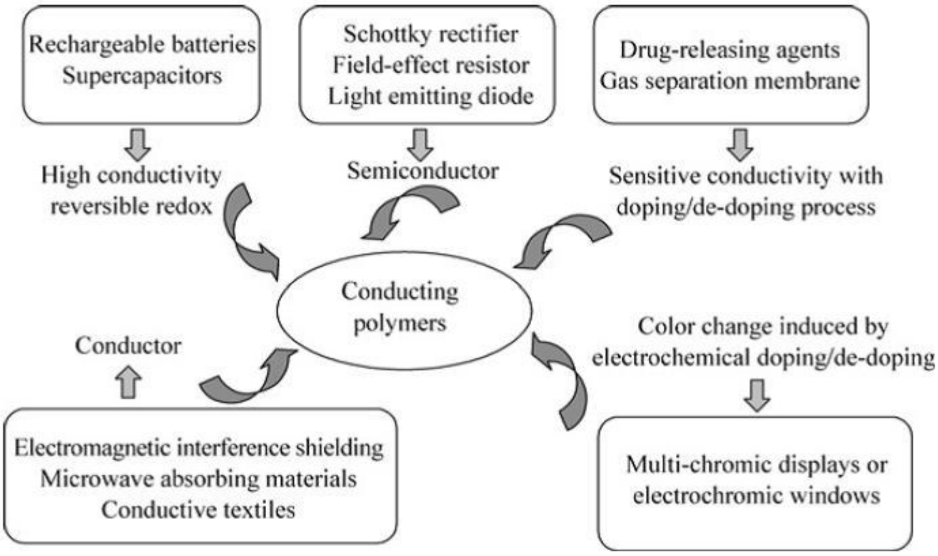

Fig. 1.31: some applications for conducting polymers

---

[85] Y. Furakawa, *Journal of Physical Chemistry*, **1996**, 100, 15644

1.2.1 Polythiophenes

Polythiophenes are a class of conducting conjugated (their π electrons are highly delocalized in the backbone) polymers with very interesting properties like high thermal stability, good solubility, especially when alkyl substituents are present, and high conductivity. They have been used in many applications: as transistors [86], LED (Light Emitting Diodes) [87], sensors [88] and in solar cells [89].

Polythiophene can undergo easier substitution in its 3 position and this allow to fine modulate the chemical structure of this polymer [90].

The structure of the polymeric backbone plays a crucial role in determining both the 3-D structure and morphology of the polymer, and this in turn can influence the physical and electronic properties. For example, In the case of polythiophenes (PT), the π overlapping along the backbone can be improved by using synthetic protocols that eliminate structural defects [91].

1.2.1.1 Polythiophenes electrochemical synthesis

Synthesis of polythiophenes can be performed through various techniques that are deeply described in various books [92, 93]. Chemical synthesis has the advantage of obtaining great polymer quantities, of controlling the stereoregularity and of achieving an easy purification that can eliminate shorter oligomeric chains leading to a long-chain polymer.

---

[86] L. Torsi, A. Tafuri, N. Cloffi, M.C. Gallazzi, A. Sassella, L. Sabbatini, P.G. Zamboni, *Sensors and actuators B: Chemical* **2003**, 93, 257

[87] A.R. Andersson, O. Thomas, W. Manno, M. Svesson, T. Theander, O. Inganas, *Journal of Materials Chemistry* **1999**, 9, 1933

[88] D.T. McQuade, A.E. Pullen, T.M. Swager, *Chemical Reviews* **2000**, 100, 2537

[89] J. Liu, T. Tanaka, K. Sivula, A.P. Alivisatos, J.M.J. Frechet, *Journal of the American Chemical Society* **2004**, 126, 6550

[90] R.J. Waltman, J. Bargon, A.F. Diaz, *Journal of Physical Chemistry* **1983**, 87, 1459.

[91] R.D. McCullough, *Advanced Materials* **1998**, 10, 93

[92] D. Fichou, Handbook of Oligo- and Polythiophenes, Wiley VCH, **1999**

[93] T.A. Skotheim, J.R. Reynolds, Handbook of Conducting Polymers, Third Edition, CRC Press, **2007**

On the other hand, polythiophene can be obtained by electrochemical synthesis [94] through an anodic oxidation process that can be seen in Fig. 1.32, where A^- is a counterion that is incorporated inside the polymer backbone for charge neutrality and *m* is a parameter that is proportional to the molecular weight.

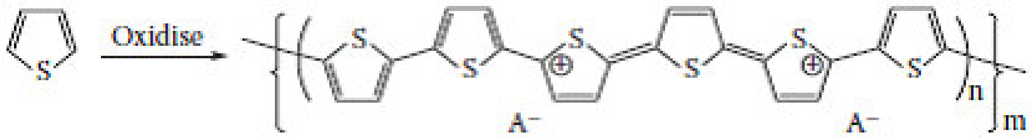

Fig. 1.32: electropolymerization reaction of thiophene

The mechanism of electropolymerisation is still not fully understood and remains subject to controversial discussion [95]; one possible path can be described as follows: the oxidising agent, an electrode, is properly polarised at an appropriate potential. At this given potential the polymerisation goes through the coupling of radical cations, following the mechanism in Fig. 1.33

---

[94] G.G. Wallace, G.M. Spinks, L.A.P. Kane-Maguire, P.R. Teasdale, Conductive Electroactive Polymers Third Edition, CRC Press, **2009**

[95] J. Heinze, B.A. Frontana-Uribe, S. Ludwigs, *Chemical Reviews* **2010**, 110, 4724

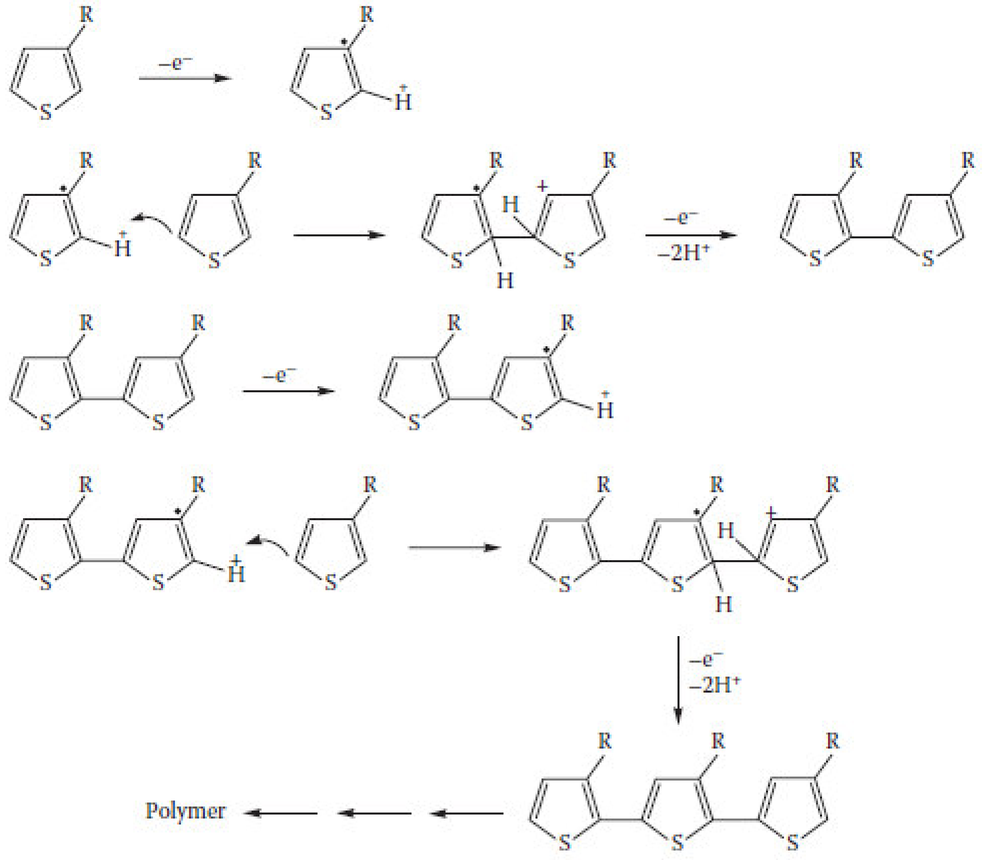

Fig. 1.33: oxidative electropolymerisation mechanism

In a first step (E) the monomer oxidation leads to the formation of a radical cation that subsequently couples with another radical (C) because of the electronic transfer that is faster than the monomer diffusion in the bulk solution; as a consequence a high concentration of these radical cations can be found near the electrode surface. At this point, after the coupling, the dicationic diidromer can loose two protons under the driving force of aromatisation, leading to a dithiophene formation (C).

This dimer can be easily oxidised to another radical cation (E) and react with another cationic monomer giving rise to a series of alternative chemical and electrochemical steps in a E(CE)n mechanism until the new polymer becomes insoluble and precipitates hopefully on the electrode surface. The reaction of the monomer with a radical cation has been demonstrated in a study where small quantities of di- or- terthiophene were added to lower the oxidation potential[96]; after the complete reaction of the added quantities the polymerisation continues at the same potentials, thus confirming that the oxidation of thiophene oligomers happens at potentials lower than the ones of the monomer. This feature is important because of the 'thiophene paradox' [97]: it is well-known that the polymer overoxidises (Fig. 1.34) at the potential at which the monomer starts to oxidise and this phenomenon led to a worsening of the polymer properties.

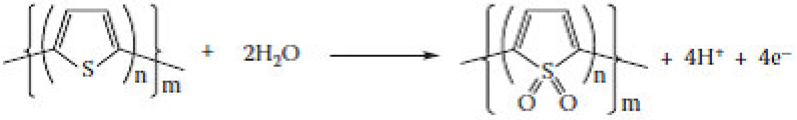

Fig. 1.34: overoxidation of polythiophene

Therefore, if using constant-current or constant-potential polymerization, the product will be a mixture of polythiophene and overoxidised polythiophenes.

The 'polythiophene Paradox' can be avoided by introducing alkyl groups on a β carbon of the thiophene; different substituted thiophenes have been synthesised, and in particular Sato [98] compared thiophene (Th 2), 3-methylthiophene (MTh 3) and 3-ethylthiophene (Eth 4) (Fig. 1.35) and concluding that potentials increase in the order MTh < Eth < Th. The harder oxidation of Eth in respect to MTh is attributable to steric effects.

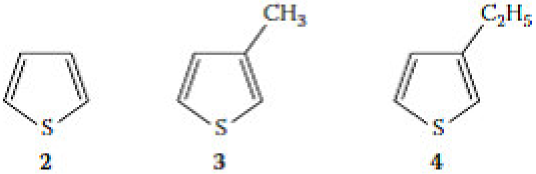

Fig. 1.35: substituted thiophenes

---

[96] Y. Wei, C.C. Chan, J. Tran, G.W. Jang, K.F. Hsueh, *Chemistry of Materials* **1991**, 3, 888

[97] B. Krische, M. Zagorska, *Synthetic Metals* **1989**, 28, 263

[98] M.A. Sato, S. Tanaka, K.J. Am, *Synthetic Metals* **1986**, 14, 279

Other research groups [99, 100] minimise the overoxidation by using bithiophenes or terthiophenes as starting monomers, that both have a lower oxidation potential when compared to thiophene.

Thiophene is more soluble in nonaqueous media, thus electropolymerisation is usually done in organic solvents, that can also offer the possibility of wider electrochemical potential window. The presence of water as low as 1% causes mislinkages and deterioration in polymer properties [101] so usually the solvent should be anhydrous and offer both a good solubility of the monomer and insolubility of the polymer. The most common solvents are acetonitrile, benzonitrile, nitrobenzene and methylene chloride. Also the nature of the counterion has an influence on themorphology [102, 103] and ion the electrochemical properties [104] of polythiophenes synthesised in MeCN; the electrolyte employed in solution is the one that gives the counterion and it has to be chemically and electrochemically inert in the chosen solvent.

The ability to incorporate different counterions in a polymeric backbone depends on the solubility of both monomer and electrolyte: for polythiophenes this possibility is limited from the need to often operate in an organic solvent; an exception regards ethylenedioxythiophene (EDOT), a monomer that is soluble and also polymerises in aqueous media.

Another variable that governs the polymerization is the nature of the electrode: polythiophenes usually grow on noble metal electrodes like Au and Pt, or on optically transparent substrates like Indium Tin Oxides glass (ITO) or on glassy carbon and steel. Platinum is, by the way, the most used material because it has a great interaction with the polymeric deposit [105].

Electropolymerization offers different advantages even if the purity levels of the polymers are not as high as those obtained through chemical polymerization; electrosynthesis require much less time, small amounts of solvents and the possibility to characterize the

---

[99] B. Krische, M. Zagorska, *Synthetic Metals* **1993**, 58, 295

[100] B. Krische, M. Zagorska, *Synthetic Metals* **1989**, 33, 257

[101] F. Beck, U. Barsch, *Makromolekulare Chemie* **1993**, 194, 2725

[102] G. Tourillon, F. Garnier, *Journal of Polymer Science: Polymer Physics* **1984**, 22, 33

[103] J.R. Reynolds, S.G. Hsu, H.J. Amott, *Journal of Polymer Science: Polymer Physics* **1989**, 27, 2081

[104] P. Marque, J. Roncali, F. Garnier, *Journal of Eletroanalytical Chemistry* **1987**, 218, 107

[105] A. Yassar, J. Roncali, F. Garnier, *Macromolecules* **1989**, 22, 804.

polymer during its formation. It is a versatile technique that also allows controlling the film thickness by monitoring the deposition current at a fixed potential.

1.2.2 Electronic Transport and Doping Mechanism

The doping of an organic polymer to achieve certain metallic properties is phenomenologically similar to the doping of a classical inorganic semiconductor in that very large increases in conductivity are observed when the material takes up very small amounts of certain chemical species [106]. However, the doping of an organic molecule is more clearly described as a redox reaction in which a neutral isolating polymer is converted to an ionic complex consisting of a cationic (or anionic) polymer and a counterion that is the reduced form of the oxidising agent.

If an oxidising agent is used, or a positive potential if talking about electropolymerisation, a *p-doping* can be obtained, while with a reducing agent or potential an *n-doping* occurs.

A good candidate with high conductivity should be oxidised or reduced at relative low potentials, and that is the reason why conducting polymer have structures consisting of π-conjugated bonds that allow low ionisation potentials or high electronic affinities. ∏ electrons can be easily removed or added for the formation of a polymer ion, without touching the strong σ-bonds that join the entire backbone.

The conducting properties of polymers can be explained if looking at the Band Theory for which in a polymer, like in a crystal, interactions between unitary cells lead to the formation of electronic bands. The highest occupied electronic levels are called *valence band* (VB) while the lowest unoccupied levels are the *conduction band* (CB). The distance between CB and VB is called *Band Gap*. Semiconductors show band gap values lower than 4 eV, while higher values are typical of insulators. The band gap values of conducting polymers lie between 1 and 3 eV. During oxidation a polymer can loose an electron from the VB or it can localise the charge on a discrete portion of the chain. The localisation causes a local distorsion due to geometric variations and this leads to an increase in the polymer energy.

---

[106] A.G. MacDiarmid, R.J. Mammone, R.B. Kaner, S.J. çPorter, R. Pething, A.J. Heeger, D.R. Rosseinsky, *Philosophical Transactions A* **1985**, 314, 3

This variation, on the other hand, lowers the ionization energy of the chain and increases the electronic affinity, allowing to more easily accommodate the charge. For the aforementioned reason the polymer tends to localize the charge.

Conducting polymers can be divided in two mail classes: polymers with a degenerate ground-state [107] like *trans*-polyacetylene and polymers with nondegenerate ground-state like polythiophene.

The oxidative doping of polythiophene is showed in Fig. 1.36, where an electron is removed from the backbone leading to a radical ion called *polaron* (1/2 spin), creating a distortion of the structure and favour the formation of two energetic states inside the band gap where the one at lower energy is individually occupied.

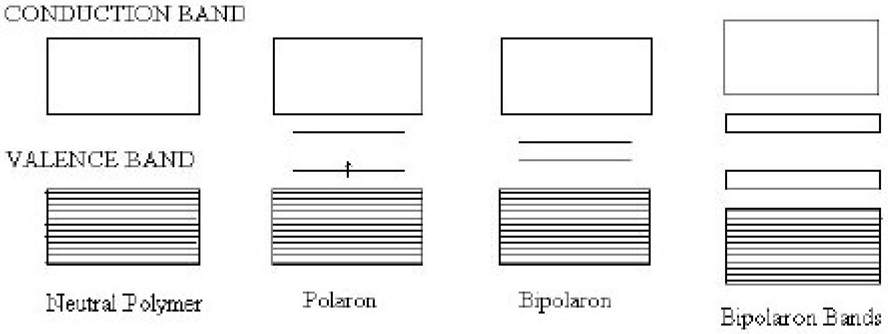

Fig. 1.36: polarons, bipolarons and bipolarons bands

In a polaron it is possible to find benzenoid domains (B) that are energetically favoured or quinoid domains (Q) (Fig. 1.37).

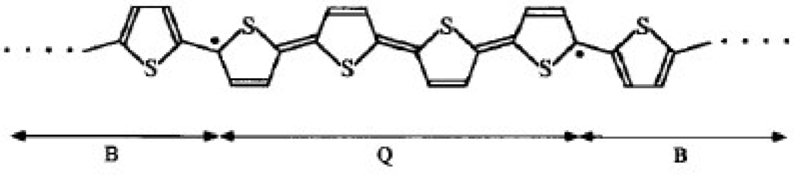

Fig. 1.37: benzenoid and quinoid-like domains

---

[107] A.J. Heeger, *Handbook of Conducting Polymers*, Cap 24, edit. Skotheim

A charged polaron is energetically stable in polythiophene at low doping levels and the charge is localised between B and Q domains on one side while on the other there is a radical. Polaron extends over 5 monomeric units in a polythiophene.

With the loss of a second electron two situation may occur: formation of another polaron or formation of a *bipolaron*. A bipolaron (Fig. 1.36) has two charges of the same sign and a strong distortion in the lattice. The electronic band structure can be seen in Fig. 1.38; because of this distortion energetic levels of the bipolaron are farther from the VB and CB edges than the polaron ones ($\Delta E^{bip} > \Delta E^{pol}$).

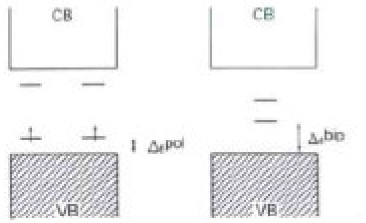

Fig. 1.38: polaron and bipolaron band structure

The bipolaron formation is thermodynamically favoured, despite the Coulombic repulsion between charges of the same sign, over the formation of two polarons because of the lowering of ionisation energy. For p-doping the bipolarons levels are empty and the spin is zero. The number of bipolarons along the chain increases with the doping level and their energetic levels form two new energetic bands (Fig. 1.38). The gap between these new bands tend to increase with the bipolarons number. At a very high doping level it is possible to speculate that the two new bands overlap the CB and VB respectively, thus allowing the polymer to reach conductivity values near to those belonging to metals.

The charge transport in a conducting polymer can take place with three different mechanisms: (a) intra-chain, (b) inter-chain and (c) inter-fibrillar (Fig. 1.39).

The intra-chain mechanism is the one already described for polarons and bipolarons, and the conductivity is influenced by the extension of the conjugation, that is by the way dependent on eventual distortions or defects in the chains.

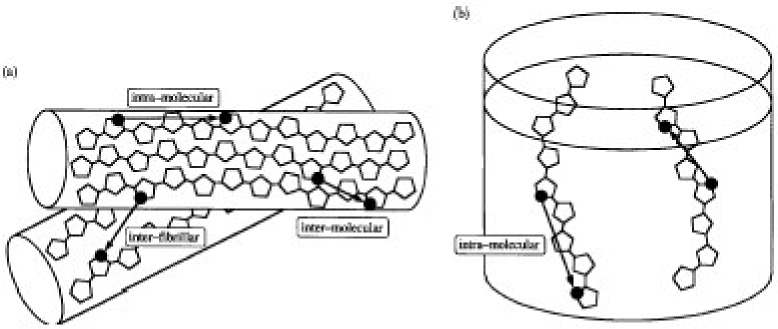

Fig. 1.39: mechanisms of charge transport in a conducting polymer

The inter-chain path is determined by the *hopping* of the carriers among different chains: the more ordered the backbone is the more important this contribution becames. The third mechanism, inter-fibrillar, takes place only at the solid state and is due to the non homogeneous fibrillar morphology of the polymers.

1.2.3 Conjugated Polymers as sensitizers for solar conversion applications

Organic solar cells have attracted increasing interest in these years for their low cost, light-weight and potential to make flexible photovoltaics devices if compared with traditional silicon-based cells. One of the main objectives is to increase the power conversion efficiencies (η) of Polymer bulk-heterojunction Solar Cells (PSCs) [108] and small molecule Dye Sensitized Solar Cells (DSSCs) [109]. In particular, the photosensitizer plays a crucial role for highly efficient DSSCs. Ruthenium complexes are among the most used molecules as sensitizers in DSSCs, but the high costs and unfriendly environmental issues still limit the large scale application of these dyes. As a consequence, great effort is devoted to replace ruthenium complexes and metal-free organic molecules are under intense study [110]. Among the metal-free dyes, it has been demonstrated that photosensitizers with a donor-π-acceptor architecture can achieve excellent performances in solar cells because the light induced intramolecular charge transfer (ICT) can easily occur from the electron donor to

---

[108] M.C. Schaber, D. Muhlbacher, M. Koppe, P. Denk, C. Waldauf, A.J. Heeger, C. Brabec, *Advanced Materials* **2006**, 18, 780

[109] A. Hagfeldt, G. Boschloo, L. Sun, L. Koo, H. Pettersson, *Chemical Reviews* **2010**, 110, 6595

[110] A. Mishra, M. Fischer, P. Bauerle, *Angewandte Chemie International Edition* **2009**, 48, 2474

the acceptor through the π-bridge [111, 112] and favour photocurrent generation [113]. In addition, triphenylamine and cyanoacetic acid moieties are found to be desirable units as electron donor and acceptor, respectively [114].

On the other hand, some conjugated polymers used as photosensitizers in DSSCs have been reported [115, 116, 117, 118, 119] due to the advantages of sufficiently large absorption coefficient and tunable energy levels. Since the discovery of photoinduced electron transfer in composites of conducting polymers and buckminsterfullerene (C_{60}) and its derivatives as acceptors [120], conjugated polymers with a D-A structure have been widely used in *Bulk Heterojunctions Solar Cells* (BHJ) and many reviews were published on this topic [121, 122, 123]. The group of Patil [124] was the first to explore D-A polymers as organic sensitizers for DSSCs applications by synthesising a diketopyrrolopyrrolo-based copolymers (Fig. 1.40). The same trend was subsequently followed by Schanze et al. [125] by using an electron-poor benzothiadiazole alternated with either a thiophene-fluorene-thiophene triad or a terthiophene segment as donors. In all these works the donor and acceptor moieties were bonded together as comonomers and were included in the main polymer chain.

The first attempt to combine the advantage of ICT in a donor-acceptor architecture and the spectral properties of conjugated polymers in a single sensitizer for DSSCs was done by Siegers in 2009 [126]. In this case, the donor and acceptor components were present as

---

[111] T. Horiuchi, H. Miura, K. Sumioka, S. Uchida, *Journal of the American Chemical Society* **2004**, 126, 12218

[112] D.P. Hagberg, J.H. Jum, H.J. Lee, D.F. Angelis, T. Marinado, K.M. Karlsson, at al., *Journal of the American Chemical Society* **2008**, 130, 6259

[113] Z.G. Chen, F.Y. li, C.H. Huang, *Current Organic Chemistry* **2007**, 11, 1241

[114] K.R.J. Thomas, Y.C. Hsu, J.T. Lin, K.M. Lee, K.C. Ho, C.H. Lai, *Chemistry of Materials* **2008**, 20, 1830

[115] S. Yahagida, G.K.R. Senadeera K. Nakamura, T. Kitamura, Y. Wada, *Journal of Photochemistry and Photobiology A: Chemistry* **2004**, 166, 75

[116] J.K. Mwaura, X. Zhao, H. Jiang, K.S. Schanze, J.R. Reynolds, *Chemistry of Materials* **2006**, 18, 6109

[117] W. Zhang, Z. Fang, M.J. Su, M. Saeys, B. Liu, *Macromolecular Rapid Communications* **2009**, 30, 1533

[118] Y.J. Liu, X. Guo, N. Xiang, B. Zhao, H. Huang, H. Li et al, *Journal of Material Chemistry* **2010**, 20, 1140

[119] Y. Tang, P. Shen, T. Ding, H. Huang, B. Zhao, S. Tan, *European Polymer Journal* **2010**, 46, 2033

[120] N.S. Saricifti, L. Smilowitz, A.J. Heeger, F. Wudl, *Science* **1992**, 258, 1474

[121] S. Guenes, H. Neugebauer, N.S. Sariciftci, *Chemical Reviews* **2007**, 107, 1324

[122] A.J. Heeger, *Advanced Materials* **2014**, 26, 10

[123] Y. Kim, S. Nam, J. Jeong, S. Lee, J. Seo, H. Han, Y. Kim, *Korean Journal of Chemical Engineering* **2014**, 31, 1095

[124] C. Kanimozhi, P. Balraju, G.D. Sharma, S. Patil, *Journal of Physical Chemistry C* **2010**, 114, 3287

[125] Z. Fang, A.A. Eshbaugh, K.S. Schanze, *Journal of the American Chemical Society* **2011**, 133, 3063

[126] C. Sieger, B. Olah, U. Wurfel, J. Hohl-Ebinger, A. Hinsch, R. Haag, *Solar Energy Materials and Solar Cells* **2009**, 93, 552

pendants and connected thanks to the presence of a polymeric chain (the hyperbranched polymer in Fig. 1.41) and not used as copolymers in the same chain (Fig. 1.40). The core of the work was the choice of a donor-acceptor pairs suitable for chemical modifications and immobilization to a dendritic or linear polymer (Fig 1.41), as well as the evaluation of the polymer as a sensitizer for nanoporous titania.

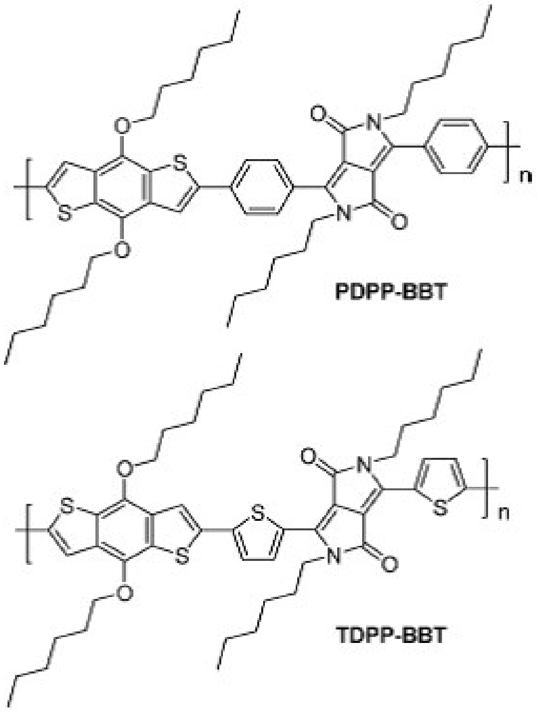

Fig. 1.40: D-A copolymers used by Patil

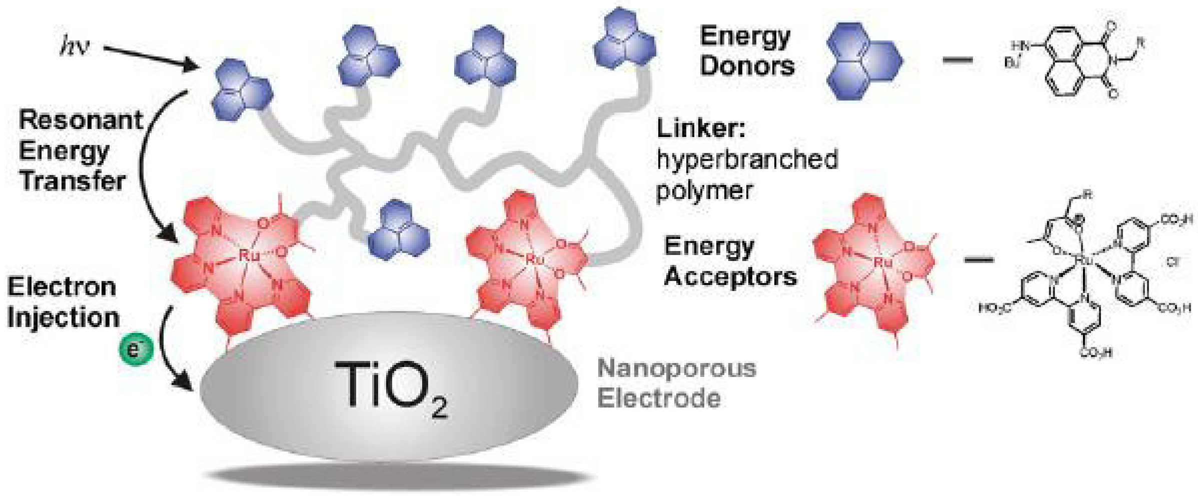

Fig. 1.41: sensitizer with a D-A structure

The authors claimed that the concept of increasing current generation of thin dye solar cells from a defined donor-acceptor dyad [127] to donor-acceptor polymers was conferred. The synthesised polymer should therefore be considered as a model that proves the general feasibility of the concept, and the optimization of these polymeric systems should be done.

In a work by Bin Liu [117] et al. the concept of combining a conjugated polymer sensitizer, containing an electron donating backbone (triphenylamine, TPA) and an electron accepting side chain (cyanoacetic acid), with conjugated thiophene units as the linkers in a D-π-A structure (Fig. 1.42) resembling organic dyes, was explored for the first time. The authors conclude that the D-π-A structure favors charge separation in the excited state, which is beneficial to electron injection to the TiO_2 layer.

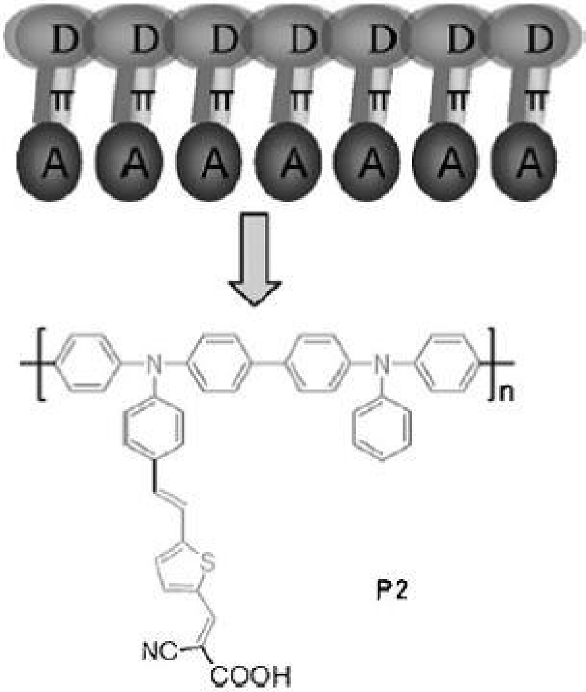

Fig. 1.42: structure of the D-π-A polymer with TPA and thiophene

Another attempt to apply a D-π-A polymer as a sensitizer in DSSCs was carried out by Tan and coworkers [119]; they synthesise three novel hyperbranched conjugated polymers (Fig

---

[127] C. Siegers, J. Hohl-Ebinger, B. Zimmerman, U. Wurfel, R. Mulhaupt, A. Hinsch, R. Haag, *Chemical Physics and Physical Chemistry* B **2007**, 8 1548

1.43) with the same core structure and different terminal units. The choice was done basing on the concept of taking advantage of the high hole-transport properties of phenylvinylenes derivatives and TPA, of increasing the photocurrent generation by D-π-A architectures and of investigating the photoelectronic properties of the hyperbranched polymers.

They found out that the architecture benefits intramolecular charge transfer and that the polymer with TPA as a donor exhibited better IPCE (incident photon to current conversion efficiencies).

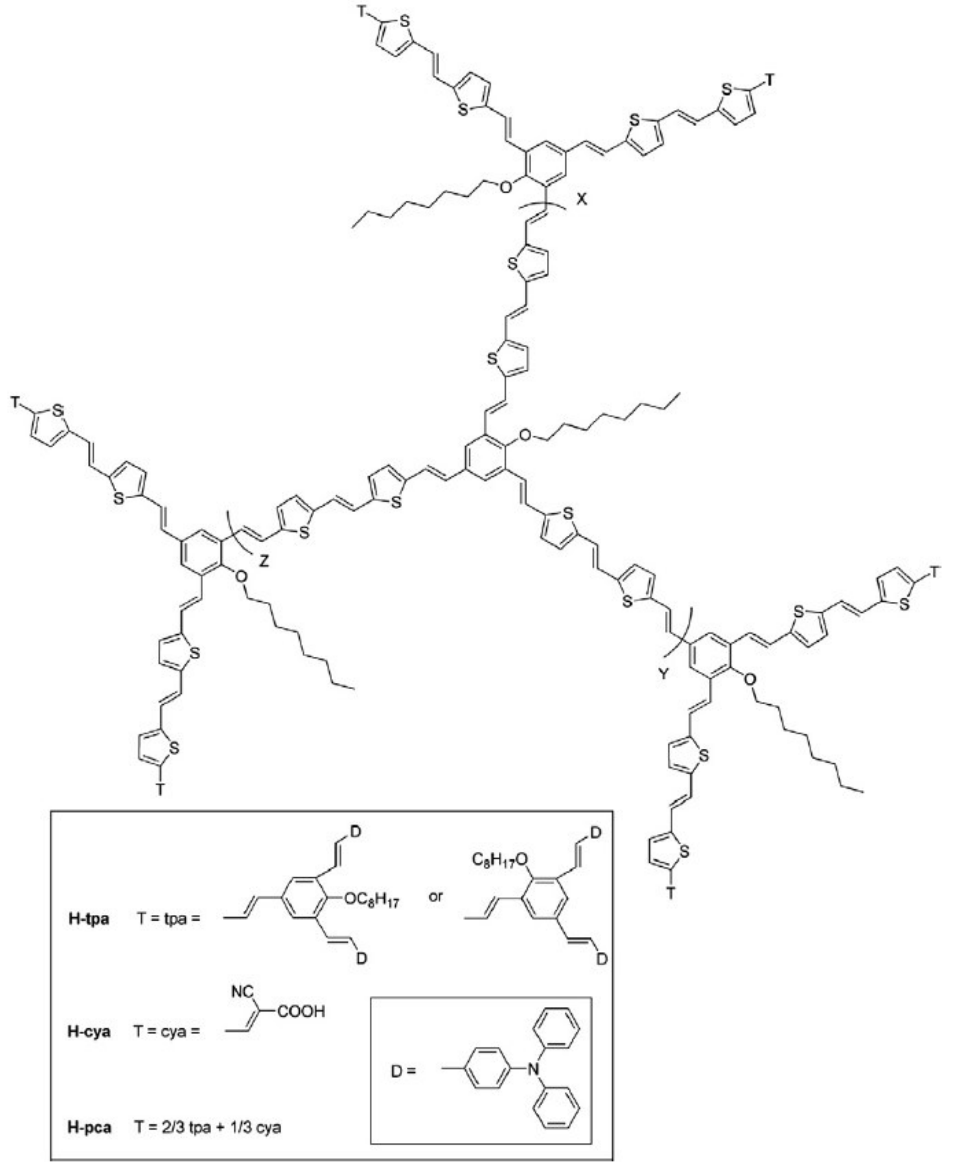

Fig. 1.43: molecular structure of the three hyperbranched polymers

As already said, dyes usually have an anchor unit to chemically bound to titania. The most used groups are carboxylic or cyanoacrylic acid, but also phosphoric acid has been used: these acids form an ester linkage with titania surface but these bonds are usually labile and readily hydrolysed by moisture, resulting in the detachment of the dyes. Alternative units have been proposed by Hanaya et al. [128], who introduced disilane as a new anchoring group that reacts with the TiO_2 surface under UV irradiation, however DSSCs based on these dyes showed low performances. More recently disilanylene polymers with D-A systems were used [129, 130] and, interestingly, the introduction of a pyridine (Py) unit into the polymer as acceptor give rise to higher performances [130] likely because the Lewis basic Py unit formed a complex with a Lewis acid site of titania surface providing a secondary bonding that facilitates the dye attachment. The adsorption on TiO_2 of a dye with a pyridine ring as electron acceptor **NI3** (Fig. 1.44) was demonstrated by means of FTIR spectra by the same research group [131] in and the optical properties were compared to **NI1** (Fig. 1.44) bearing a carboxylic group. The authors concluded that the bonding between Py and titania leads to an efficient electron injection arising from good electronic communication, rather than the formation of an ester linkage.

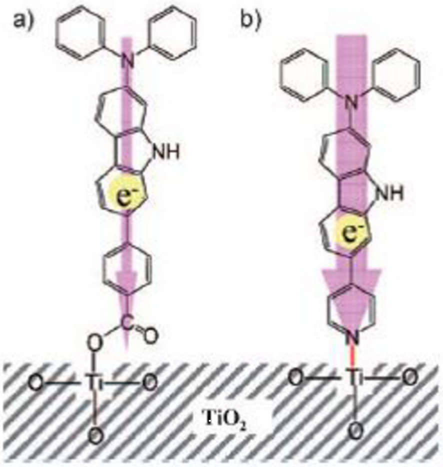

Fig. 1.44: configurations of a) **NI1** and b) **NI3** on titania surface

---

[128] K. Kakiage, M. Yamamura, E. Fujimura, T. Kyomen, M. Unno, K. Kakiage, *Chemical Letters* **2010**, 39, 260

[129] D. Tanaka, J. Ohshita, Y. Ooyama, T. Mizumo, Y. Harima, *Journal of Organometallic Chemistry* **2012**, 719, 30

[130] D. Tanaka, J. Ohshita, T. Mizumo, Y. Ooyama, , Y. Harima, *Journal of Organometallic Chemistry* **2013**, 741, 97

[131] Y. Ooyama, S. Inoue, T. Nagano, K. Kushimoto, J. Ohshita, I. Imae, K. Komaguchi, Y. Harima, *Angewandte Chemie International Edition* **2011**, 50, 7429

As a consequence another study on D-A polymers bearing pyridine or pyrazine as acceptor units, disilanobithiophene (DSBT) as the donor and with or without a thiophene spacer was carried out [132]. The electrodes for DSSCs were prepared under irradiation (photochemical conditions) or in the dark (thermal conditions). Polymers bearing pyridine or pyrazine units could attach to titania under both conditions and no evident colour difference depending on the treatments was seen. However, the UV-Vis spectra of the photochemically modified electrodes showed blue-shifted absorption bands relative to those of the thermally modified electrodes, indicating the photodegradation of the chromophores. All the polymers exhibited sensitizing effects, but for cells with pyridine or pyrazine-containing polymers no clear relationship between the performances and the attachment conditions was observed.

---

[132] J. Oshita, Y. Adachi, D. Tanaka, M. Nakashima, Y. Ooyama, *RSC Advances* **2015**, 5, 36673

Chapter 2

Experimental Part

2.1 Titania

2.1.1 Titania synthesis

2.1.1.1 Synthesis of mesoporous titania

Two different set of samples were prepared and the discussion of their characterization will be described for each set in the Results and Discussion part.

The synthesis of the first set of eight titania samples, named I-VIII were done basing on previous work by Chen et al [133].

In a 50 mL beker 1 g of Pluronic P123, and F127 in the case of sample VI, was dissolved in 20 mL of ethanol, then 1 mL of $TiCl_{4,}$, previously left in an ice bath for 1 h ($9.1*10^{-3}$ mol), and 0.78 mL of $Ti(OBu)_4$ ($2.3*10^{-3}$ mol) were added, except for samples VII and VIII (see Table x), and the solution was kept under stirring at 25°C for two hours. In some cases a certain amount of water was added (see Table 2.1). The reaction mixture was then transferred in a Petri dish and put in an oven at controlled moisture level (thanks to an hygrometer), between 40-60 %, and at 40°C for 24 h. The obtained gel was finally calcined in a muffle at 350 °C (1 °C/min) for 6 hours.

Table 2.1: synthetic parameters for the synthesis of samples I-VIII

Samples	Precursors (mL)	Added water (mL)	Surfactant
I	$TiCl_4$ 1.00 $Ti(OBu)_4$ 0.78	-	P123
II	$TiCl_4$ 1.00 $Ti(OBu)_4$ 0.78	1.1	P123
III	$TiCl_4$ 1.00 $Ti(OBu)_4$ 0.78	1.3	P123
IV	$TiCl_4$ 1.00 $Ti(OBu)_4$ 0.78	0.3	P123
V	$TiCl_4$ 1.00 $Ti(OBu)_4$ 0.78	0.5	P123
VI	$TiCl_4$ 1.00 $Ti(OBu)_4$ 0.78	-	F127
VII	$TiCl_4$ 2.00 $Ti(OBu)_4$ 0.78	0.3	P123
VIII	$TiCl_4$ 0.50 $Ti(OBu)_4$ 0.78	0.3	P123

The second set of eight samples (named 1-8), was synthesised in the following way: 1 g of surfactant (Pluronic P123) was dissolved in 20 mL of ethanol, then in some cases 1.17 mL of acetylacetone were added, subsequently 1 mL of $TiCl_4$ and 0.78 mL of $Ti(OBu)_4$ or 2.94 mL of $Ti(O^iPr)_4$ with 3 mL of HCl 37% v/v are put in the previous solution. The mixture was kept under stirring for two hours at room temperature and is then transferred in a Petri dish and put at 45°C with a moisture level of 40-60% for 24 hours. The obtained gel was finally calcined at 400°C for 12 hours using different rates, 1 °C/min^1 or 5 °C/min^1. Parameters of every synthesis are reported in Table 2.2.

Table 2.2: synthetic parameters for the synthesis of samples 1-8

Samples	**Precursors**	**Acetylacetone (mL)**	**Heating rate (°C/min)**
1	$TiCl_4/Ti(OBu)_4$	-	5
2	$TiCl_4/Ti(OBu)_4$	-	1
3	$TiCl_4/Ti(OBu)_4$	1.17	5
4	$TiCl_4/Ti(OBu)_4$	1.17	1
5	$Ti(O^iPr)_4$-HCl	-	5
6	$Ti(O^iPr)_4$-HCl	1.17	5
7	$Ti(O^iPr)_4$-HCl	-	1
8	$Ti(O^iPr)_4$-HCl	1.17	1

2.1.1.2 Preparation of titania electrodes

The preparation of the electrodes for photoelectrochemical measurements started with creating a paste with 20 mg of each titania sample, 15 mg of polyethylene glycol (PEG 20,000 g/mol) and 1.6 mL of ethanol. The paste was then sonicated until homogeneous and is then deposited onto an indium tin oxide (ITO) glass with a conductive area of 1 cm^2 by the doctor blade technique using four pieces of adhesive tape to control the thickness of the titania layer. The TiO_2/ITO deposits were then thermally treated in a muffle furnace at 400°C for one hour.

2.1.2 Characterization of titania samples

2.1.2.1 X-ray Powder Diffraction (XRPD)

Diffraction is the phenomenon associated with the interference processes that occur when electromagnetic radiation is scattered by atoms in solids, liquids and gases [134]. For the electromagnetic radiation with a wavelength comparable to interatomic distances in the substance, the resulting scattered waves are a result of the atomic arrangements; X-rays have wavelength similar to typical interatomic distances, approximately 0.1 nm, thus X-ray diffraction is an important technique for determination of atomic arrangements in materials.

X-Ray Powder Diffraction, in particular, is a technique used for phase identification of a crystalline material in the form of powder and can provide information on unit cells and phase composition of a sample. The interaction of the incident rays with the sample produces constructive interference, a diffracted ray, when conditions satisfy Bragg's Law $n\lambda=2d\sin\theta$. This law relates the wavelength of electromagnetic radiation to the diffraction angle and the lattice spacing in a crystalline sample (Fig. 2.1). The diffracted X-rays are then detected, processed and counted. By scanning the material through a range of 2θ angles, all possible diffraction directions of the lattice should be attained. Conversion of the diffraction peaks to d-spacings allows identification of the material usually by comparison with reference patterns.

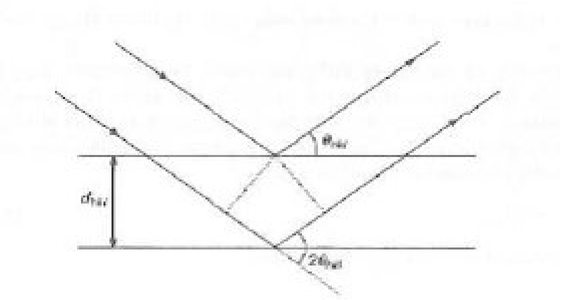

Fig. 2.1: illustration of Bragg's Law

---

[134] R. Jenkins, R. Snyder, *Introduction to X-Ray Powder Diffraction* **1996**, Wiley

The structural characterization of the titania samples was carried out by XRPD with a Rigaku DMax diffractometer equipped with a graphite monochromator on the diffracted beam. The synthesised materials are deposited on a glass substrate. The Rietveld method through Maud software [135] was used for qualitative and quantitative analysis of phase content and microstructural parameters.

2.1.2.2 N_2 Physisorption measurements

Gas adsorption measurements are widely used for determining the surface area and pore distribution of a variety of different solid materials, such as industrial adsorbents, catalysts, pigments, ceramics and building materials. *Physisorption* is a general phenomenon that occurs whenever an adsorbable gas (the adsorptive) is brought into contact with the surface of a solid (the adsorbent). The gas (usually nitrogen) can form a layer on the material and the complete coverage of the surface area will lead to the formation of a *monolayer* from which it is possible to have information about the surface area of the material; with increasing nitrogen pressure, more layers can form leading to a *multilayer*, where all the molecules of the adsorptive are in contact with the adsorbent and a phenomenon that resembles a gas condensation process takes place (Fig. 2.2); in porous materials a capillary condensation happens where the adsorbed gas condense inside the pores and from this process information on the pore distribution, morphology and size can be extrapolated using different mathematical models [136, 137].

In our measurements, N_2 sorption isotherms were collected with a Sorptomatic 1990 instrument; the superficial area was calculated with BET method while the pore distribution with BJH method [137]. 200 mg of each sample were put in a quartz tube and degassed under vacuum ($1x10^{-3}$ bar) at 250°C for 24 hours. The dead volume was evaluated through adsorption helium measurements.

---

[135] P. Scardi, L. Lutterotti, P. Maistrelli, *Powder Diffraction* **1994**, 6, 180-186

[136] S. Brunaumer, L.S. Deming, W.S. Deming, E. Teller, *Journal of the American Chemical Society* **1940**, 62, 1723

[137] IUPAC, Physical Chemistry Division, Commission on Colloid and Surface Chemistry Including Catalysis, *Pure and Applied Chemistry* **1985**, 57,4,603

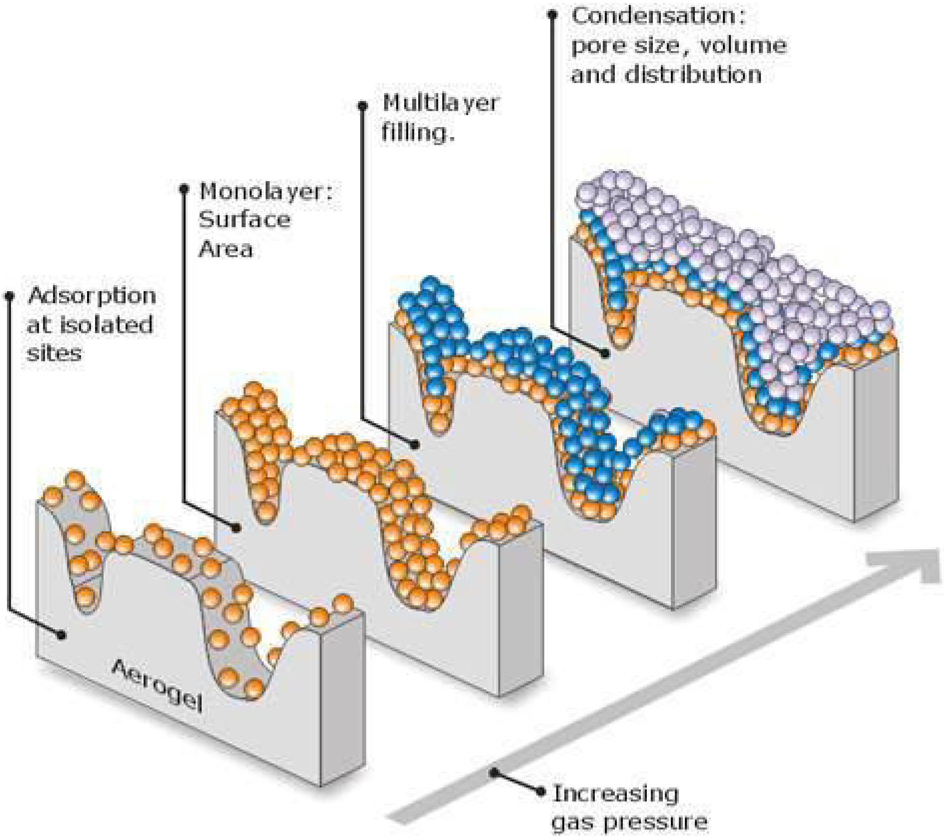

Fig. 2.2: the different phases of layers formation on an adsorbate

2.1.2.3 Transmission Electron Microscopy (TEM)

This technique is based on the interaction between a concentrated electron beam and a solid phase that has to be analyzed. An image is formed from the interaction of the electrons transmitted through the specimen; the image is magnified and focused onto an imaging device. TEMs are capable of imaging at a significantly higher resolution than light microscopes, owing to the small de Broglie wavelength of electrons. At smaller magnifications TEM image contrast is due to absorption of electrons in the material, due to the thickness and composition of the material. At higher magnifications TEM allows to observe modulations in chemical identity, crystal orientation, electronic structure and sample induced electron phase shift as well as the regular absorption based imaging.

For Transmission Electron Microscopy TEM (Jeol-JEM 2011, 200 kW, Jeol Ltd., Tokyo, Japan), samples were prepared by dispersing a few milligrams in ethanol followed by the deposition of one or two drops of the suspension on a holey carbon supported grid. All measurements were done at the Servei de Microscòpia in Universitat Autònoma de Barcelona.

2.1.2.4 Linear Sweep Voltammetry (LSV)

Linear sweep voltammetry is an electrochemical potentiodynamic technique where a current *I* that flows through a working electrode (WE) is measured at an applied potential. The potential of the WE varies with a speed that is expressed in V/s. A three-electrode compartment cell is usually used and measurements are made with a WE, a Reference electrode (RE) and a Counter electrode (CE). In this configuration, current is measured between WE and CE thus avoiding the polarisation of the RE; the potential is measured between the RE and the WE. The current is plotted against the applied voltage in a so-called *voltammogram*. In the cell an electrolyte is present to prevent the migration of the electroactive species under the electric gradient, the solution is not under stirring to eliminate the convection contribution ans as a consequence the system is under diffusive control.

Current-Voltage measurements are the main way to determine the performance characteristics of a photoanode and they allow to quickly obtain information on the photocurrent density generated by the material, on the dark current as a function of applied potential and as a consequences on the photoelectrochemical performances of a sample.

All titania samples I-VIII were deposited on ITO surface with the procedure reported in Section 2.1.1.2. For samples I-VIII all (photo)electrochemical characterizations were performed in a home-made single-compartment three electrode quartz cell under inert atmosphere in a previously degassed NaOH 1M solution using the prepared TiO_2/ITO as working electrodes, a platinum wire as auxiliary electrode and Ag/AgCl as reference electrode (E = 207.6 mV vs NHE). Linear Sweep Voltammetry (LSV) tests were recorded at a scan rate of 5 mVs^{-1}. Experiments were run starting from the open circuit potential of the system, first in the dark and then under direct illumination, and controlled by an Autolab PGSTAT 12 (EcoChemie) potentiostat/galvanostat interfaced with a PC under General Purpose Electrochemical Systems (GPES) software. Potentiostatic photoelectrolysis experiments were carried out under direct illumination for 1 h at a potential value chosen from the LSV scan. The amount of H_2, considering the reduced area (< 1.5 cm^2) of the ITO glass where the m-TiO_2 was deposited and the low photoactivity under sun illumination for non-doped titania, is theoretically obtained according to the Faraday's Law [138], considering the charge (in Coulomb) flowed during the electrolysis at 0.9 V vs Ag/AgCl and the visible H_2 evolution from the water splitting reaction. The light source was provided by an ABET TECHNOLOGIES Sun 2000 Solar Simulator with an irradiating power of 1 sun (AM 1.5).

For titania samples 1-8, photoelectrochemical characterizations were performed thanks to Helmholtz Centre Geesthacht, in a teflon lined quartz cell (PECC-1, from Zhaner, Kansas City, Missouri, USA) under inert atmosphere in a degassed 1 M NaOH solution using the prepared TiO_2/ITO electrodes as working electrodes, a Pt wire as counter electrode and Ag/AgCl as a reference electrode. Linear Sweep Voltammetry (LSV) responses were recorded at 10 mV/s. Experiments were run starting from the open circuit potential of the system, first in the dark and then under direct illumination, under the control of a Zhaner Zennium Mess Systeme PP221 potentiostat (Zahner, Kansas City, Missouri, USA). The light source was a LOT Oriel Solar Simulator (LOT- QuantumDesign, Darmstadt, Germany) with AM (air mass) 1.5 G filter, ozone free and with an output power of 1 sun. The polarization experiments were carried out with chopped light at 0 V (in order to evaluate the electrodes performances without an applied bias) *vs.* Ag/AgCl for an hour in the same electrochemical system.

---

[138] A.J. Bard, L.R. Faulkner, Electrochemical Methods – Fundamentals and Applications. 2nd ed. New York. Wiley **2001**

2.1.2.5 UV-Vis Spectroscopy

UV-Vis spectroscopy (or spectrophotometry) refers to absorption or reflectance spectroscopy in the ultraviolet-visible spectral region. This means it uses light in the visible and adjacent (800-190 nm) ranges. In this region of the electromagnetic spectrum, molecules undergo electronic transitions and by analyzing their absorption spectra it is possible to evaluate the band gap of a semiconductor.

UV-vis spectra were recorded on a water suspension of each sample (1 mg of titania in 100 mL) using a Hitachi U-2010 equipment and the band gap was evaluated from the λ_{onset} that arised from the analysis of the absorption spectra with the tangent method, and then by applying the Plank Equation.

2.2 Chromophores

2.2.1 Synthesis of chromophores

All the synthesized chromophores have a secondary name given by keeping the BT (bithiophene) tag and varying the name of the substituents on its 4 and 4' position.

2.2.1.1 Synthesis of 4-(4'-bromo-2,2'-bithiophenyl)-2-methyl-3-butyn-2-ol (Br-BT-OH)

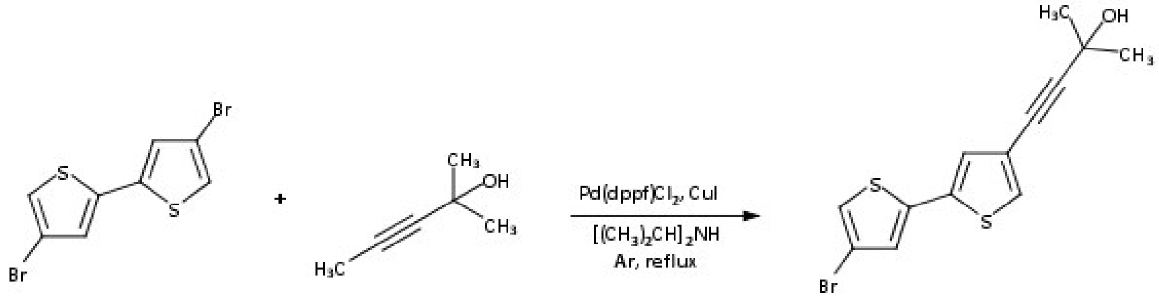

A two-neck 25 mL flask equipped with a condenser, a magnetic stirrer and an Ar inlet, was charged, under inert atmosphere, with 0.3000 g of 4,4'-dibromo-2,2'-bithiophene (Br-BT-Br, $9.26*10^{-4}$ mol), 0.0076 g of [1,1'-bis(diphenylphosphino)ferrocene]dichloropalladium ($Pd(dppf)Cl_2$, $9.26*10^{-6}$ mol), and 3% of CuI (0.0053 g, $2.78*10^{-5}$ mol) in 5 mL of diisopropylamine. Then 3-methyl-3-butyn-2-ol in a molar ratio of 1/1.5 of Br-BT-Br/alcol is added to the initial solution (0.135 mL, $1.39*10^{-3}$ mol). The mixture is left under stirring at reflux and monitored by TLC (petroleum ether/ethyl acetate 3/2). After 15' the reaction is left to cool to room temperature and added with 50 mL of CH_2Cl_2, washed with a saturated $NaHCO_3$ (50 mL) solution and then with 3*50 mL water. The organic solution was then subjected to anhydrification with $MgSO_4$, filtered and the solvent evaporated under vacuum. The residue undergoes purification through column chromatography on alumina using petroleum ether/ethyl acetate 3/2 as eluent and the desired product is obtained with 23 % yield.

^{1}H NMR (CD_2Cl_2, ppm):): δ_H = 7.34 (s, 1H); 7.18 (s, 1H); 7.11 (s, 1H); 2.04 (s, 1H, OH); 1.57 (s, 6H, CH_3).

Elemental Analysis: theoretical for $C_{13}H_{11}OBrS_2$: C, 47.69; H, 3.39;experimental: C, 48.28; H, 3.51.

UV spectrum in CH_3CN, 5x10^{-5} M: λ_{max} = 308 nm.

2.2.1.2 Synthesis of 4-4’-(2,2’-bithiophenyl)bis(2-methyl-3-butyn-2-ol) (OH-BT-OH)

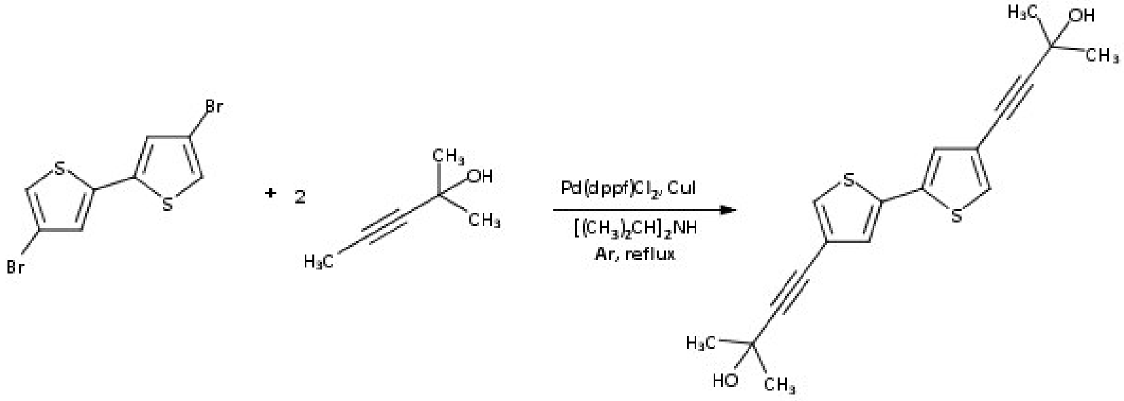

A two-neck 25 mL flask equipped with a condenser, a magnetic stirrer and an Ar inlet, was charged, under inert atmosphere, with 0.2000 g of 4,4’-dibromo-2,2’-bithiophene (Br-BT-Br, 6.17*10^{-4} mol), 0.0053 g of [1,1’-bis(diphenylphosphino)ferrocene]dichloropalladium ($Pd(dppf)Cl_2$, 6.12*10^{-6} mol), and 3% of CuI (0.0031 g, 1.57*10^{-4} mol) in 5 mL of diisopropylamine. Then 3-methyl-3-butyn-2-ol in a molar ratio of 1/2 of Br-BT-Br/alcol is added to the initial solution (0.120 mL, 1.24*10^{-3} mol). The mixture is left under stirring at reflux and monitored by TLC on alumina (petroleum ether/ethyl acetate 3/2).

The reaction is left to cool to room temperature and added with 50 mL of CH_2Cl_2, washed with a saturated $NaHCO_3$ (50 mL) solution and then with 3*50 mL water. The organic solution was then subjected to anhydrification with $MgSO_4$, filtered and the solvent evaporated under vacuum. The residue undergoes purification through column chromatography on alumina using petroleum ether/ethyl acetate 3/2 as eluent and the desired product is obtained with 75 % yield.

^1H NMR (CD_2Cl_2, ppm): δ_H = 7.32 (s, 2H); 7.16 (s, 2H); 2.04 (s, 2H, OH); 1.57 (s, 12H, CH_3).

Elemental Analysis: theoretical for $C_{18}H_{18}O_2S_2$: C, 65.40; H, 5.49; experimental: C, 65.28; H, 5.63.

UV spectrum in CH_3CN, 5x10^{-5} M: λ_{max} = 310 nm.

2.2.1.3 Synthesis of 4-bromo-(4'-ethynyl)-2,2'-bithiophene (Br-BT-Et)

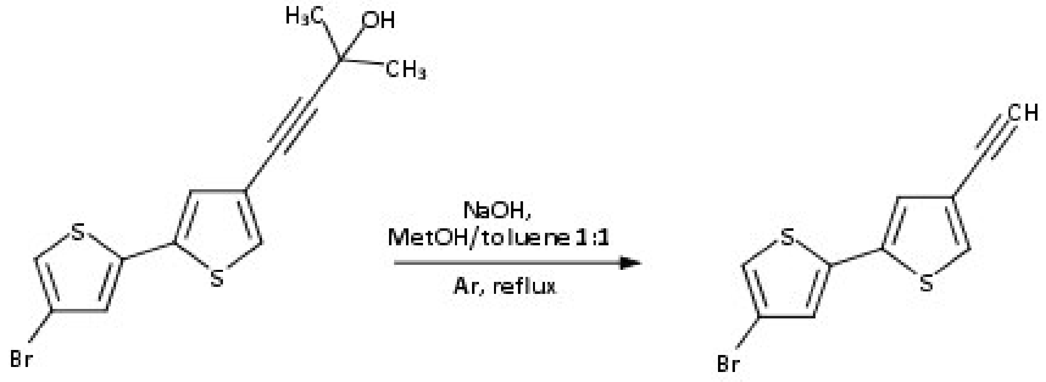

A two-neck 25 mL flask equipped with a condenser, a magnetic stirrer and an Ar inlet, was charged, under inert atmosphere, with 0.1153 g of 4-(4'-bromo-2,2'-bithiophenyl)-2-methyl-3-butyn-2-ol (Br-BT-OH, 3.52*10^{-4} mol), and 5 mL of methanol/toluene mixture 1/1 were added. Then excess of NaOH is added. The mixture is left under stirring at reflux and monitored by TLC (petroleum ether/ethyl acetate 3/2). After 24 h the reaction is left to cool to room temperature and added with 50 mL of H_2O and the organic phase is then extracted with CH_2Cl_2 (3*50 mL). The organic solution was then washed with 200 mL of a saturated NH_4Cl solution, subjected to anhydrification with $MgSO_4$, filtered and the solvent is finally evaporated under vacuum. The residue undergoes purification through column chromatography on silica using petroleum ether/ethyl acetate 3/2 as eluent and the desired product is obtained with 50 % yield.

^{1}H NMR (CD_2Cl_2, ppm): δ_H = 7.45 (s, 1H); 7.22 (s, 1H); 7.19 (s, 1H); 7.12 (s, 1H); 3.11 (s, 1H, C≡CH).

Elemental Analysis: theoretical for $C_{10}H_5BrS_2$: C, 44.58; H, 1.87; experimental: C, 43.83; H, 1.81.

UV spectrum in CH_3CN, 5x10^{-5} M: λ_{max} = 304 nm.

2.2.1.4 Synthesis of 4-(4'-ethynyl-2,2'-bithiophenyl)-N,N'-diphenylaniline (Et-BT-TPA)

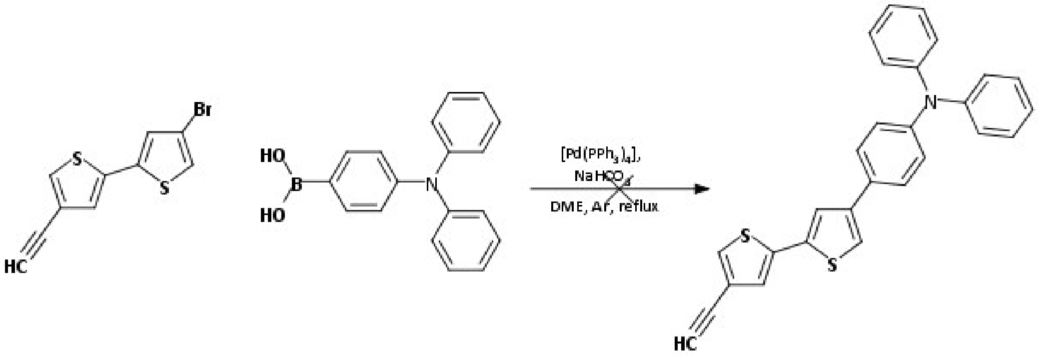

A two-neck 25 mL flask equipped with a condenser, a magnetic stirrer and an Ar inlet, was charged, under inert atmosphere, with 0.0469 g of 4-bromo-(4'-ethynyl)-2,2'-bithiophene (Br-BT-Et, $1.74*10^{-4}$ mol) and 0.0123 g of $[Pd(PPh_3)_4]$ ($1.05*10^{-5}$ mol) in 1,2-dimethoxyethane. After 10 min of stirring under Ar, 4-(N,N'-diphenylamino)phenylboronic acid is added with a molar ratio acid/substrate of 1.15/1, together with a 1 M $NaHCO_3$ solution (acid/$NaHCO_3$ ratio of 1/7.5). The mixture is left under stirring at reflux and monitored by TLC (petroleum ether/ethyl acetate 5/1). After 24h the reaction is left to cool to room temperature and filtered. 20 mL of water are added and the organic phase is then extracted with Et_2O (3*30 mL) and finally washed with water (90 mL). The organic solution was then subjected to anhydrification with $MgSO_4$, filtered and the solvent evaporated under vacuum. The residue undergoes purification through column chromatography on silica using petroleum ether/ethyl acetate 5/1 as eluent.

NMR spectra of the obtained residue show a complex mixture of different compounds and this synthetic route was not repeated.

2.2.1.5 Synthesis of 4-(4’-(4-N,N’-diphenylamino)phenyl)-2,2’-bithiophenyl)-2-methyl-3-butyn-2-ol (OH-BT-TPA)

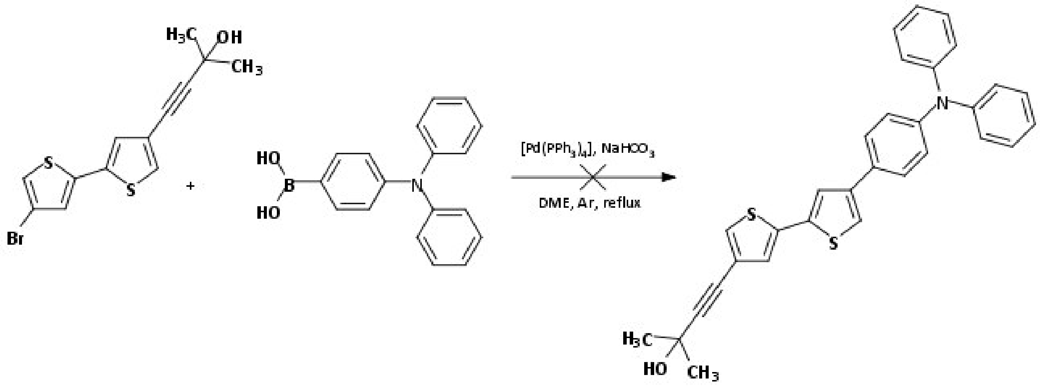

A two-neck 25 mL flask equipped with a condenser, a magnetic stirrer and an Ar inlet, was charged, under inert atmosphere, with 0.1000 g of 4-(4’-bromo-2,2’-bithiophenyl)-2-methyl-3-butyn-2-ol (Br-BT-OH, $3.06*10^{-4}$ mol) and 6% of $[Pd(PPh_3)_4]$ ($1.83*10^{-5}$ mol, 0.0212 g), in 1,2-dimethoxyethane. After 10 min of stirring under Ar, 4-(N,N’-diphenylamino)phenylboronic acid is added with a molar ratio acid/substrate of 1.15/1, together with a 1 M $NaHCO_3$ solution (acid/$NaHCO_3$ ratio of 1/7.5). The mixture is left under stirring at reflux and monitored by TLC (petroleum ether/ethyl acetate 5/1). After 48h the reaction is left to cool to room temperature and filtered. 20 mL of water are added and the organic phase is then extracted with Et_2O (3*30 mL) and finally washed with water (90 mL). The organic solution was then subjected to anhydrification with $MgSO_4$, filtered and the solvent evaporated under vacuum. The residue undergoes purification through column chromatography on silica using petroleum ether/ethyl acetate 5/1 as eluent.

NMR spectra of the obtained residue show a complex mixture of different compounds and this synthetic route was not repeated.

2.2.1.6 Synthesis of 4-(4’-bromo-2,2’-bithiophenyl)-N,N’-diphenylaniline (Br-BT-TPA)

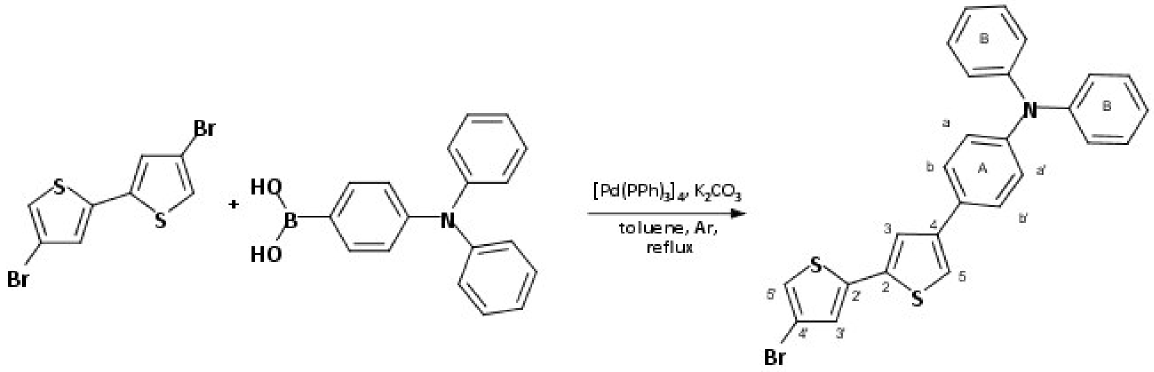

A two-neck 25 mL flask equipped with a condenser, a magnetic stirrer and an Ar inlet, was charged, under inert atmosphere, with 0.4000 g of 4,4’-dibromo-2,2’-bithiophene (Br-BT-Br, $1.23*10^{-3}$ mol) and 4-(N,N’-diphenylamino)phenylboronic acid (0.5300 g, $1.83\cdot10^{-3}$ mol, 1/1.5 bithiophene/boronic acid molar ratio) in 8 mL of toluene. After 10 min of stirring under Ar, 6% of $[Pd(PPh_3)_4]$ ($7.4*10^{-5}$ mol, 0.0862 g), together with 4.6 mL of 2M K_2CO_3 (boronic acid/ K_2CO_3 ratio of 1/7.5). The mixture is left under stirring at reflux and monitored by TLC (petroleum ether/ethyl acetate 2/1). After 4 h the reaction is left to cool to room temperature and 50 mL of CH_2Cl_2 are added; the organic phase is then extracted with Et_2O (3*30 mL). The organic solution was then washed with water (3*50 mL) and subjected to anhydrification with $MgSO_4$, filtered and the solvent evaporated under vacuum. The residue undergoes purification through column chromatography on silica using petroleum ether/ethyl acetate 2/1 as eluent. The desired product is obtained with a 50 % yield.

^{1}H NMR (CD_2Cl_2, ppm): δ_H = 7.4÷7.47 (m, br, 4H); 7.46 (s, 1H); 7.32(s, 1H); 7.29÷7.26(m, br, 4H); 7.18 (s, 1H); 7.15 (s, 1H); 7.12÷7.03 (m, br, 6H);

^{13}C NMR (CD_2Cl_2, ppm): δ_C = 129.51 (4C); 127.20 (2C); 126.26 (1C); 124.69 (4C); 123.86 (2C); 123.48 (1C); 123.28 (2C); 121.90 (1C); 119.19 (1C);

^{13}C, ^{1}H correlation:

^{13}C ppm	^{1}H ppm	
126.26	7.15	1 C-H thiophene
123.48	7.46	1 C-H thiophene
121.90	7.18	1 C-H thiophene
119.19	7.32	1 C-$H_{3\ o\ 5}$ thiophene
126.96	7.49÷7.47	2 C_A-$H_{b,b'}$ phenyl
123.86	7.12÷7.03	2 C_A-$H_{a,a'}$ phenyl
124.69	7.12÷7.03	4 C_B-H phenyl (orto)
129.51	7.29÷7.26	4 C_B-H phenyl (meta)
123.28	7.49÷7.47	2 C_B-H phenyl (para)

Elemental analysis: theorethical for $C_{26}H_{18}BrNS_2$: C, 63.93; H, 3.71; N, 2.87; experimental: C, 66.23; H, 4.23; N, 3.15.

UV-Vis spectra in CH_3CN, $5x10^{-5}$ M analyte concentration: λ_{max} = 320 nm.

2.2.1.7 Synthesis of 4-{4'-(4-N,N'-diphenylamino)phenyl]-2,2'-bithiophenyl}-2-methyl-3-butyn-2-ol (OH-BT-TPA)

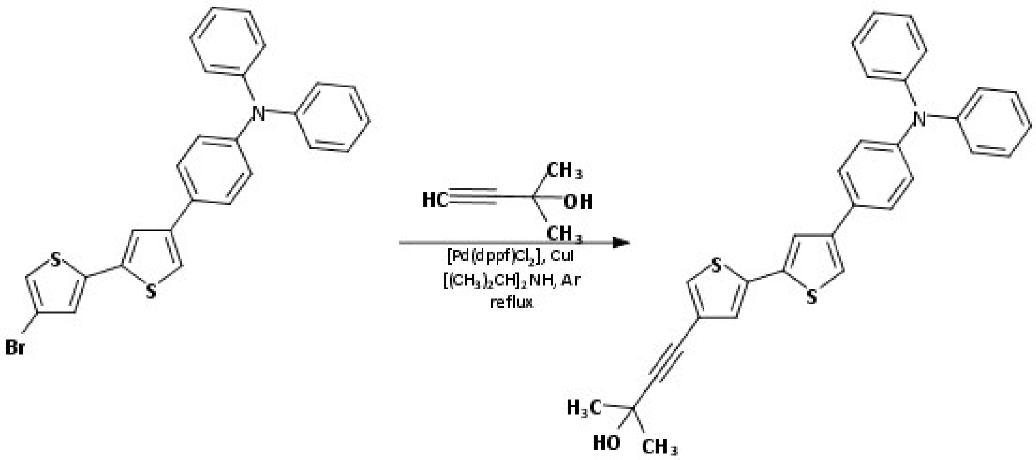

A two-neck 25 mL flask equipped with a condenser, a magnetic stirrer and an Ar inlet, was charged, under inert atmosphere, with 0.3000 g of Br-BT-TPA (6.14*10^{-4} mol), 0.0054 g of [1,1'-bis(diphenylphosphino)ferrocene]dichloropalladium (Pd(dppf)Cl_2, 6.14*10^{-6} mol), and 3% of CuI (0.0071 g, 3.68*10^{-5} mol) in 5 mL of diisopropylamine. Then 3-methyl-3-butyn-2-ol in a molar ratio of 1/1.5 of Br-BT-TPA/alcol is added to the initial solution (0.089 mL, 9.21*10^{-4} mol). The mixture is left under stirring at reflux and monitored by TLC on silica (petroleum ether : ethyl acetate 2:1).

After 8 h the reaction is left to cool to room temperature and added with 50 mL of CH_2Cl_2, washed with a saturated $NaHCO_3$ (50 mL) solution and then with 3*50 mL water. The organic solution was then subjected to anhydrification with $MgSO_4$, filtered and the solvent was evaporated under vacuum. The residue undergoes purification through column chromatography on silica using petroleum ether/ethyl acetate 2/1 as eluent and the desired product is obtained with 60 % yield.

^{1}H NMR (CD_2Cl_2, ppm): δ_H = 7.51÷7.49 (m, br, 4H); 7.46 (s, 1H); 7.34 (s, 1H); 7.32÷7.28 (m, br, 4H); 7.27 (s,1H); 7.21 (s, 1H); 7.12÷7.04 (m, br, 6H); 2.01 (s, OH); 1.60 (s, 6H, CH_3).

Elemental Analysis: theorethical per $C_{31}H_{25}NOS_2$: C, 75.73; H, 5.13; N, 2.85; experimental: C, 75.02; H, 5.69; N, 2.74.

UV-Vis spectra in CH_3CN, 5x10^{-5} M analyte concentration: λ_{max} = 320 nm.

2.2.1.8 Synthesis of 4- (4’-ethynyll-2,2’-bithiophenyl)-N,N’-diphenylaniline (ET-BT-TPA)

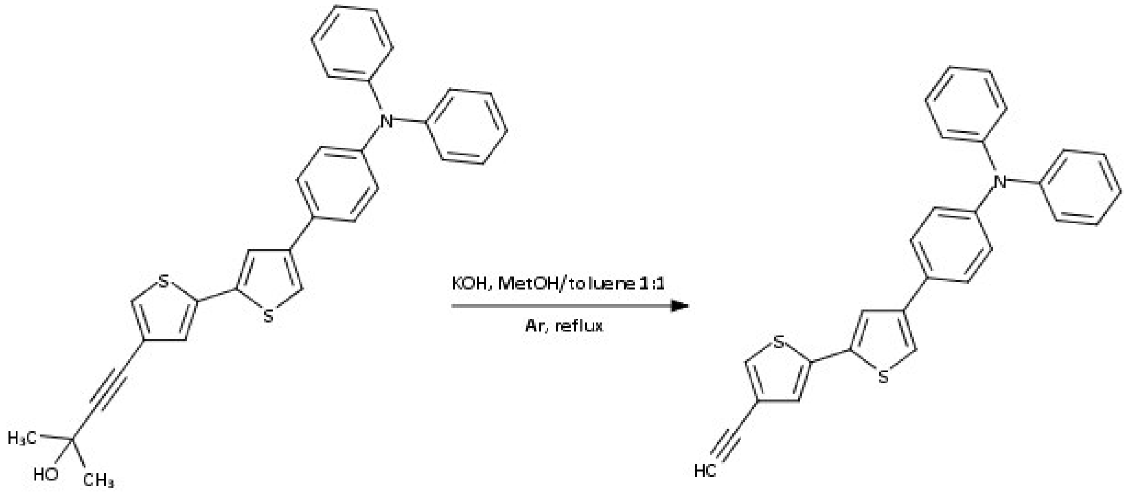

A two-neck 25 mL flask equipped with a condenser, a magnetic stirrer and an Ar inlet, was charged, under inert atmosphere, with 0.1383 g of OH-BT-TPA ($2.81*10^{-4}$ mol), and 5 mL of methanol/toluene mixture 1/1 were added. Then excess of KOH is added and the mixture is left under stirring at reflux and monitored by TLC (petroleum ether/ethyl acetate 2/1). After 24 h the reaction is left to cool to room temperature and added with 50 mL of H_2O and the organic phase is then extracted with CH_2Cl_2 (3*50 mL). The organic solution was then washed with 200 mL of a saturated NH_4Cl solution, subjected to anhydrification with $MgSO_4$, filtered and the solvent is finally evaporated under vacuum. The residue undergoes purification through column chromatography on silica using petroleum ether/ethyl acetate 2/1 as eluent and the desired product is obtained with 68 % yield.

^{1}H NMR (CD_2Cl_2, ppm): δ_H = 7.49÷7.46 (m, br, 5H); 7.43 (s, 1H); 7.31÷7.34 (m, br, 6H); 7.11÷7.02 (m, br, 6H); 3.11 (s, 1H, C≡CH).

Elemental Analysis: theoretical for $C_{28}H_{19}NS_2$: C, 77.56; H, 4.42; N,3.23 experimental: C, 77,70; H, 4.40; N, 2.79.

UV spectrum in CH_3CN, $5x10^{-5}$ M: λ_{max} = 321 nm.

2.2.1.9 Synthesis of 4’-(2,2’:6’:2”-terpyridin-4’-ethynyl)-2,2’-bithiophenyl-4-N,N’-diphenylaniline (Tpy-ET-BT-TPA)

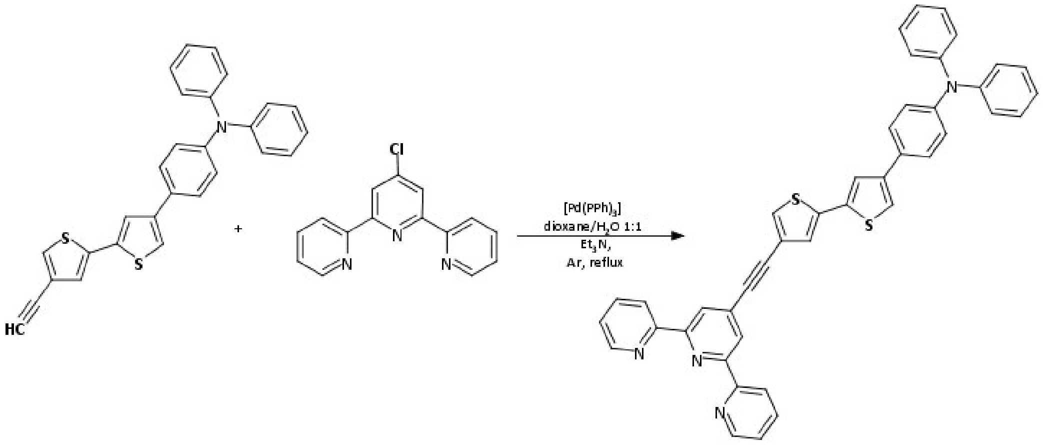

A two-neck 25 mL flask equipped with a condenser, a magnetic stirrer and an Ar inlet, was charged, under inert atmosphere, with 0.0400 g of Et-BT-TPA ($9.24*10^{-5}$ mol) and 0.0262 g of 4’-chloro-2,2’:6’,2’’-terpyridine ($9.24*10^{-5}$ mol) in 8 mL of 1,4-dioxane/H_20 3/1. After 10 min of stirring under Ar, 5% of [Pd(PPh_3)$_4$] ($4.62*10^{-6}$ mol, 0.0053 g), together with 10 % of CuI (0.0017 g, $9.20·10^{-6}$ mol) and 0.026 mL of Et_3N in a Et-BT-TPA/amine ½ molar ratio ($1.85*10^{-4}$ mol) were added. The mixture is left under stirring at reflux and monitored by TLC (petroleum ether/ethyl acetate 2/1). After 24 h the reaction is left to cool to room temperature and filtered, then it is washed with CH_2Cl_2 and the solvent is evaporated under vacuum. The desired product is obtained with a 49 % yield.

^{1}H NMR (CD_2Cl_2, ppm):): δ_H = 8.69÷8.61 (m, br, 4H); 8.50 (s, 2H); 7.90 (m, br, 2H); 7.50÷7.46 (m, br, 6H); 7.39 (m, br, 2H); 7.30÷7.26 (m, br, 6H); 7.12÷7.03 (m, br, 6H).

Elemental Analysis: theoretical for $C_{43}H_{28}N_4S_2$: C, 77.68; H, 4.24; N, 8.43; experimental: C, 76.54; H, 4.38; N, 8.12.

UV spectrum in CH_2Cl_2, $5x10^{-5}$ M: λ_{max} = 330 nm, 314 (shoulder) nm and 288 nm

2.2.1.10 Synthesis of 4,4'-diethynyl-2,2'-bithiophene (Et-BT-Et)

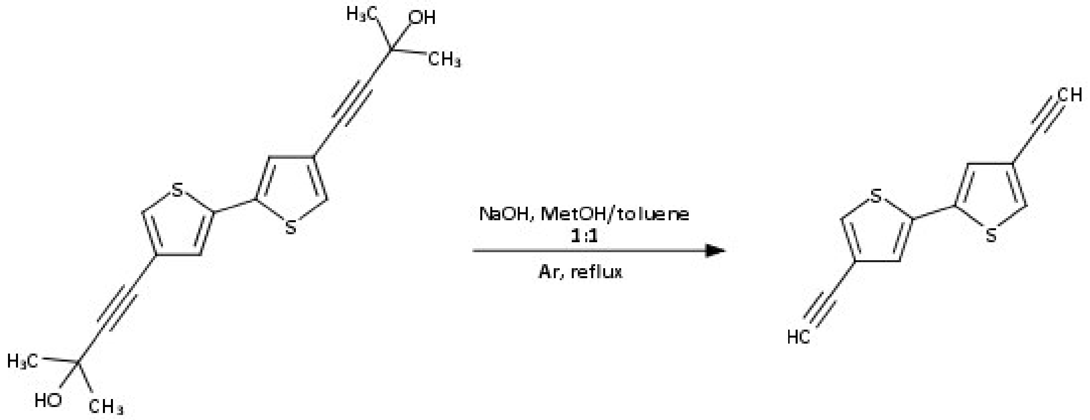

A two-neck 25 mL flask equipped with a condenser, a magnetic stirrer and an Ar inlet, was charged, under inert atmosphere, with 0.1552 g of OH-BT-OH ($4.69*10^{-4}$ mol) and NaOH (large excess) in 8 mL of a MeOH/toluene 1/1 solution.

The mixture is left under stirring at reflux and monitored by TLC (petroleum ether/ethyl acetate 5/2). After 24 h the reaction is left to cool to room temperature and 50 mL of water are added; then an extaction with CH_2Cl_2 is performed and the organic solution is then washed with 200 mL of a saturated NH_4Cl solution, subjected to anhydrification with $MgSO_4$, filtered and the solvent is finally evaporated under vacuum. The residue undergoes purification through column chromatography on silica using petroleum ether/ethyl acetate 5/2 as eluent and the desired product is obtained with 60 % yield.

^1H NMR (CD_2Cl_2, ppm):): δ_H = 7.48 (s, 2H); 7.26 (s, 2H); 3.15 (s, 1H, CΞCH)

UV spectrum in CH_2Cl_2, $5x10^{-5}$ M: λ_{max} = 310 nm

2.2.1.11 Synthesis of 4-(4’-ethynyl-2,2’-bithiophen-4-yl)ethynyl-N,N’-diphenylaniline (Et-BT-Et-TPA)

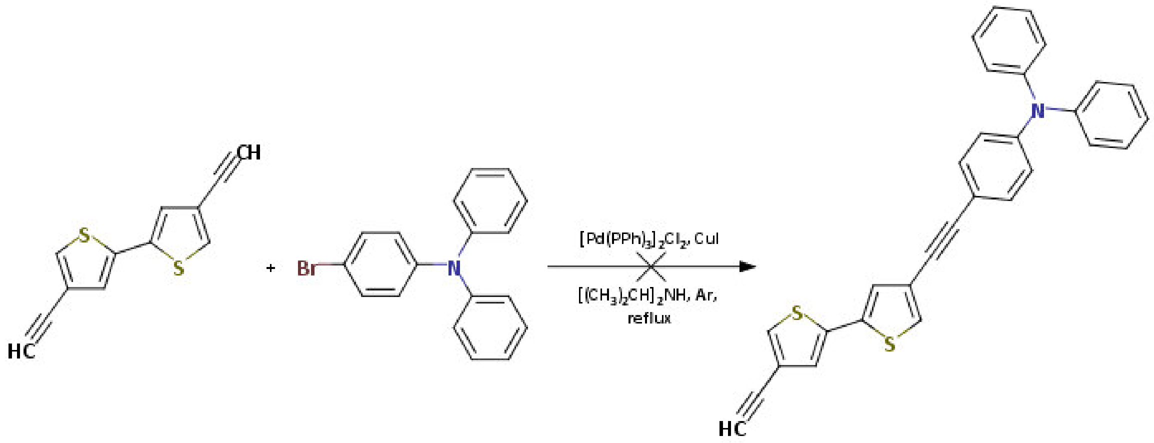

A two-neck 25 mL flask equipped with a condenser, a magnetic stirrer and an Ar inlet, was charged, under inert atmosphere, with 0.0900 g of Et-BT-Et ($4.19*10^{-4}$ mol), 1% of $Pd(PPh_3)_2Cl_2$ (0.0034 g $4.19*10^{-6}$ mol), 3% of CuI (0.0024 g, $1.25*10^{-5}$ mol) in diisopropylamine (5 mL). Then, Br-TPA was added (0.1086 g, $3.35*10^{-4}$ mol) with a Et-BT-Et/Br-TPA 1/0.8 molar ratio.

The mixture is left under stirring at reflux and monitored by TLC (petroleum ether/ethyl acetate 5/2). After 48 h the starting reagents are still present and no product is detected.

2.2.1.12 Synthesis of 4-[4-(diphenylamino)phenyl]-2-methyl-3-butyn-2-ol (OH-TPA)

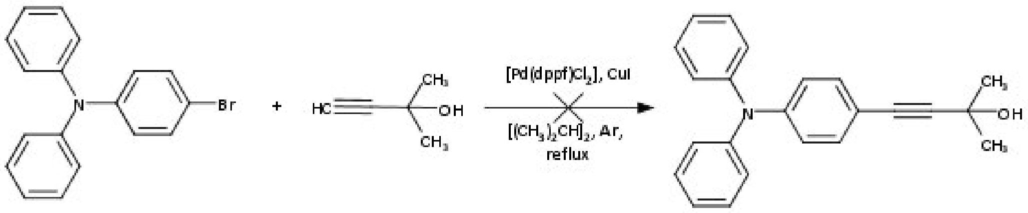

A two-neck 25 mL flask equipped with a condenser, a magnetic stirrer and an Ar inlet, was charged, under inert atmosphere, with 0.2000 g of Br-TPA ($6.17*10^{-4}$ mol), 0.0053 g of [1,1'-bis(diphenylphosphino)ferrocene]dichloropalladium (Pd(dppf)Cl_2, $6.17*10^{-6}$ mol), and 3% of CuI (0.0031 g, $1.85*10^{-5}$ mol) in 5 mL of diisopropylamine. Then 3-methyl-3-butyn-2-ol in a molar ratio of 1/2 of Br-TPA/alcol is added to the initial solution (0.120 mL, $1.23*10^{-3}$ mol). The mixture is left under stirring at reflux and monitored by TLC on silica (petroleum ether : ethyl acetate 3:2).

The reaction is left to cool to room temperature and added with 50 mL of CH_2Cl_2, washed with a saturated $NaHCO_3$ (50 mL) solution and then with 3*50 mL water. The organic solution was then subjected to anhydrification with $MgSO_4$, filtered and the solvent evaporated under vacuum. The residue undergoes purification through column chromatography on silica using petroleum ether: ethyl acetate 3:2 as eluent .

The synthesis did not lead to the desired product and no starting reagents were recovered.

2.2.1.13 Synthesis of 4-ethynyl-trimethylsilyl-N,N’-diphenylaniline (TMS-TPA)

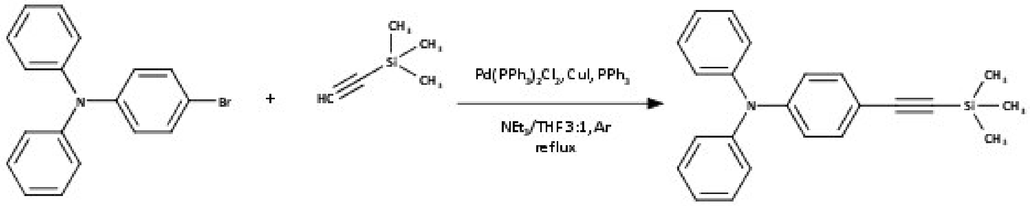

The synthetic procedure was suggested by the work of Wu [139].

A two-neck 25 mL flask equipped with a condenser, a magnetic stirrer and an Ar inlet, was charged, under inert atmosphere, with 0.2000 g of Br-TPA (6,17*10^{-4} mol), 6% of $Pd(PPh_3)_4$ (0.0260 g, 3.70*10^{-5}), 3% of CuI (0.0036 g, 1.85*10^{-5} mol) and 3 % of PPh_3 (0.0049 g, 1.85*10^{-5} mol) in 5 mL of triethylamine/THF 3/1. Then trimethylsilylacetylene in a molar ratio of 1/1.5 of Br-TPA /TMS is added to the initial solution (0.131 mL, 9.25*10^{-4} mol). The mixture is left under stirring at reflux and monitored by TLC on silica (hexane/CH_2Cl_2 3:1). After 24 h the reaction is left to cool to room temperature and added with 20 mL of water, the solution is then washed with CH_2Cl_2 (3*25 mL). The organic solution was then subjected to anhydrification with $MgSO_4$, filtered and the solvent evaporated under vacuum. The residue undergoes purification through column chromatography on silica using hexane/CH_2Cl_2 3/1 as eluent. The product was obtained with 84 % yield.

^1H NMR ($CDCl_3$, ppm):): δ_H = 7.36÷7.31 (m, br,4H); 7.26 (d, 2H); 7.01 (m, br, 6H); 6.96 (d, 2H); 1.56 (s, 9H, CH_3)

UV spectrum in CH_2Cl_2, 5x10^{-5} M: λ_{max} = 333 nm (shoulder) and 293 nm

---

[139] W. Wu, C. Cheng, W. Wu, H. Guo, S. Ji, P. Song, K. Han, J. Zhao, X. Zhang, Y. Wu, G. Du, *European Journal of Inorganic Chemistry* **2010**, 29,4683

2.2.1.14 Synthesis of 4-ethynyl-N,N'-diphenylaniline (Et-TPA)

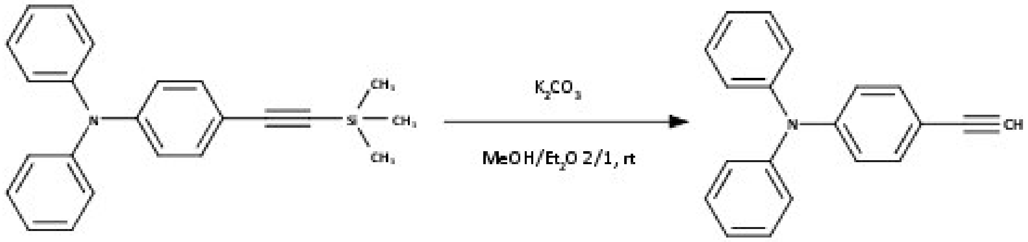

A two-neck 25 mL flask equipped with a condenser, a magnetic stirrer and an Ar inlet, was charged, under inert atmosphere, with 0.3550 g of TMS-TPA ($1.05*10^{-3}$ mol) and K_2CO_3 excess in 8 mL of MeOH/ethylether 2/1 . The mixture is left under stirring at reflux and monitored by TLC on silica (hexane/CH_2Cl_2 3:1).

After 24 h the reaction is left to cool to room temperature and added with 10 mL of water, then it was extracted with CH_2Cl_2. The organic solution was then subjected to anhydrification with $MgSO_4$, filtered and the solvent evaporated under vacuum. The product was obtained with a 55 % yield.

^{1}H NMR ($CDCl_3$, ppm):): δ_H = 7.36÷7.31 (m, br, 4H); 7.26 (d, 2H); 7.14÷7.04 (m, 6H); 6.98 (d, 2H); 3.04 (s, 1H, CΞCH)

UV spectrum in CH_2Cl_2, $5x10^{-5}$ M: λ_{max} = 335 nm (shoulder) and 306 nm.

2.2.1.15 Synthesis of 4[(4’-bromo-2,2’-bithiophen-4-yl)ethynyl]-N,N’-diphenylaniline (Br-BT-Et-TPA)

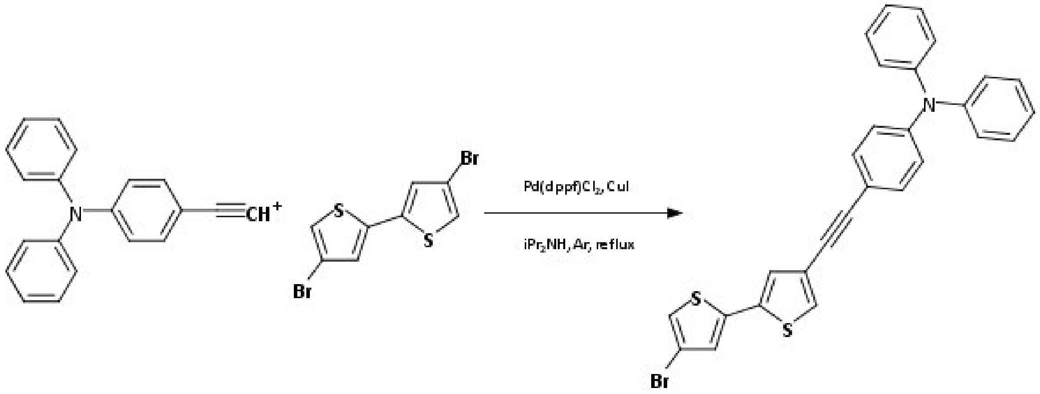

A two-neck 25 mL flask equipped with a condenser, a magnetic stirrer and an Ar inlet, was charged, under inert atmosphere, with 0.0900 g of Et-TPA ($3.35*10^{-4}$ mol), 0.0027 g of [1,1’-bis(diphenylphosphino)ferrocene]dichloropalladium (Pd(dppf)Cl_2, $3.35*10^{-6}$ mol, 1%), and 3% of CuI (0.0019 g, $1.01*10^{-5}$ mol) in 5 mL of diisopropylamine. Then Br-BT-Br was added (0.1085, $3.35*10^{-4}$) in a Et-TPA/Br_BT-Br 1/1 molar ratio. The mixture is left under stirring at reflux and monitored by TLC on silica (petroleum ether/CH_2Cl_2 2/1).

After 6 h the reaction is left to cool to room temperature and added with 50 mL of CH_2Cl_2, washed with a saturated $NaHCO_3$ (50 mL) solution and then with 3*50 mL water. The organic solution was then subjected to anhydrification with $MgSO_4$, filtered and the solvent was evaporated under vacuum. The residue undergoes purification through column chromatography on silica using petroleum ether/CH_2Cl_2 2/1as eluent and the desired product is obtained with 60 % yield.

^{1}H NMR ($CDCl_3$, ppm): δ_H = 7.38 (s,1H); 7.35 (s, 1H); 7.32 (s, 1H); 7.28 (s, 1H); 7.26 (d, 2H); 7.18÷7.11 (m, br, 4H); 7.02 (d, 2H); 2.01 (s, OH); 6.98 (d, 2H).

UV-Vis spectra in CH_2Cl_2, $5x10^{-5}$ M analyte concentration: λ_{max} = 349 nm, 303 nm.

2.2.1.16 Synthesis of 4[(4'-diphenylamminophenyl)-2,2'-bithiophen]-2-methyl-3-butyn-2-ol (OH-BT-Et-TPA)

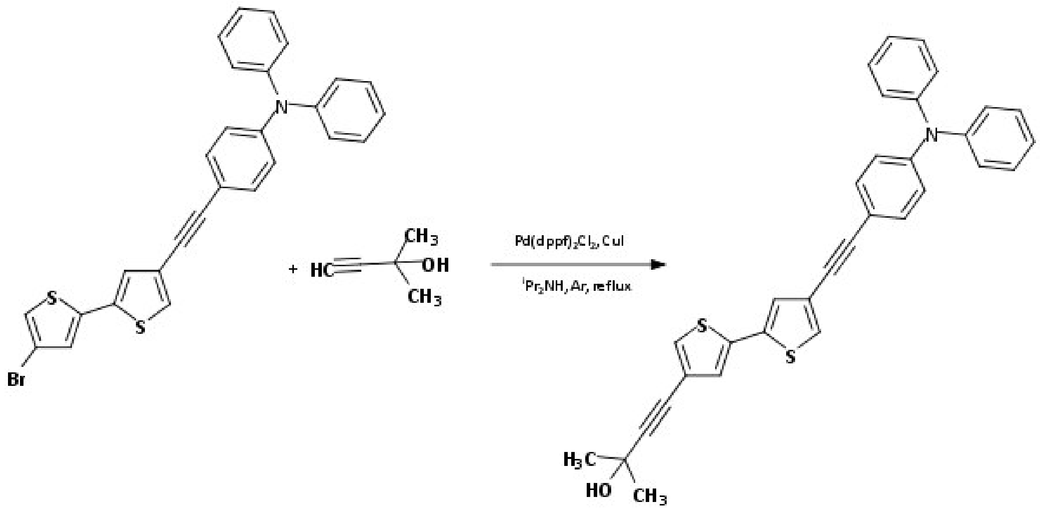

A two-neck 25 mL flask equipped with a condenser, a magnetic stirrer and an Ar inlet, was charged, under inert atmosphere, with 0.1715 g of Br-BT-Et-TPA ($3.35*10^{-4}$ mol), 0.0027 g of [1,1'-bis(diphenylphosphino)ferrocene]dichloropalladium ($Pd(dppf)Cl_2$, $3.35*10^{-6}$ mol), and 6% of CuI (0.0038 g, $2.01*10^{-5}$ mol) in 5 mL of diisopropylamine. Then 3-methyl-3-butyn-2-ol in a molar ratio of 1/1.15 of Br-BT-Et-TPA/alcol is added to the initial solution (0.032 mL, $3.85*10^{-4}$ mol). The mixture is left under stirring at reflux and monitored by TLC on silica (petroleum ether/CH_2Cl_2 3/1).

After 24 h the reaction is left to cool to room temperature and added with 50 mL of CH_2Cl_2, washed with a saturated $NaHCO_3$ (50 mL) solution and then with 3*50 mL water. The organic solution was then subjected to anhydrification with $MgSO_4$, filtered and the solvent was evaporated under vacuum. The residue undergoes purification through column chromatography on silica using petroleum ether/CH_2Cl_2 3/1 as eluent and the desired product is obtained with 60 % yield.

^1H NMR ($CDCl_3$, ppm): δ_H = 7.39÷7.35 (m, br, 4H); 7.33 (s, 1H); 7.30 (s, 1H); 7.24 (s, 1H); 7.18 (s,1H); 7.13 (d, 2H); 7.11÷7.05 (m, br, 4H); 7.01 (d, 2H); 2.18 (s, OH); 1.63 (s, 6H, CH_3).

UV-Vis spectra in CH_2Cl_2, $5x10^{-5}$ M analyte concentration: λ_{max} = 339 nm.

2.2.1.17 Synthesis of 4(4’-ethynyl-2,2’-bithiophen-4-yl)-ethynyl-N,N’-diphenylaniline (Et-BT-Et-TPA)

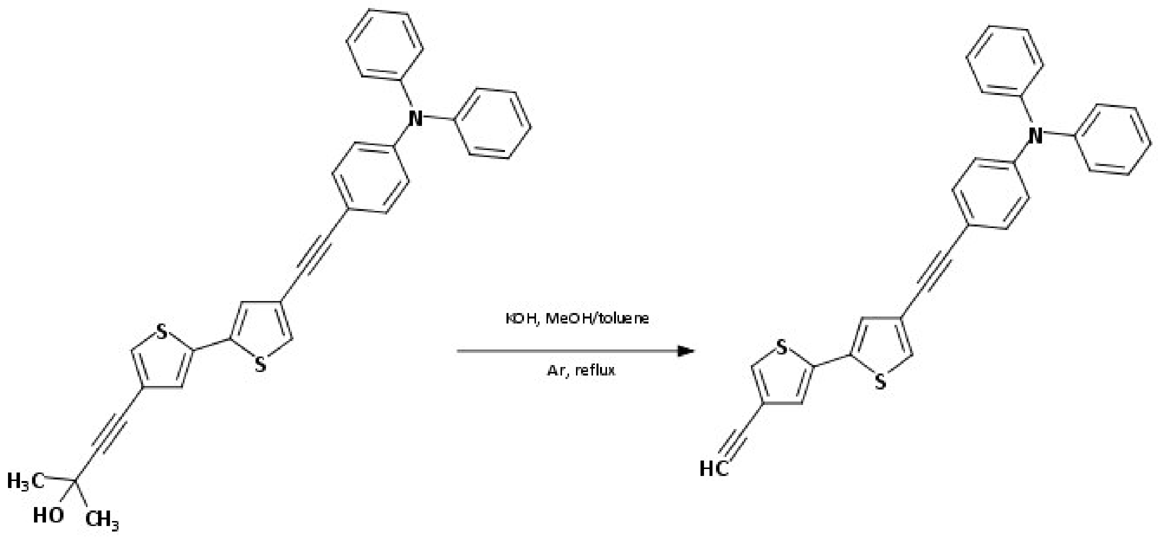

A two-neck 25 mL flask equipped with a condenser, a magnetic stirrer and an Ar inlet, was charged, under inert atmosphere, with 0.0403 g of OH-BT-Et-TPA ($7.76*10^{-5}$ mol), and 5 mL of methanol/toluene mixture 1/1 were added. Then excess of KOH is added and the mixture is left under stirring at reflux and monitored by TLC (petroleum ether/CH_2Cl_2 1/3). After 24 h the reaction is left to cool to room temperature and added with 50 mL of H_2O and the organic phase is then extracted with CH_2Cl_2 (3*50 mL). The organic solution was then washed with 200 mL of a saturated NH_4Cl solution, subjected to anhydrification with $MgSO_4$, filtered and the solvent is finally evaporated under vacuum. The residue undergoes purification through column chromatography on silica using petroleum ether/CH_2Cl_2 1/3 as eluent and the desired product is obtained with 60 % yield.

^1H NMR ($CDCl_3$, ppm): δ_H = 7.42 (s, 1H); 7.38÷7.33 (m, br, 4H); 7.30 (s, 1H); 7.26 (s, 1H); 7.24 (s, 1H); 7.19 (d, 2H); 7.14÷7.10 (m, br, 4H); 7.07 (d, 2H); 7.01 (d, 2H); 3.06 (s, 1H, $C\equiv CH$).

UV spectrum in CH_2Cl_2, $5x10^{-5}$ M: λ_{max} = 321 nm.

2.2.1.18 Synthesis of 4’-[(2,2’:6’,2’’-terpyridin-4’-ethynyl)-4-(2,2’-bithiophen-4-yl)]-N,N’(Tpy-BT-Et-TPA)

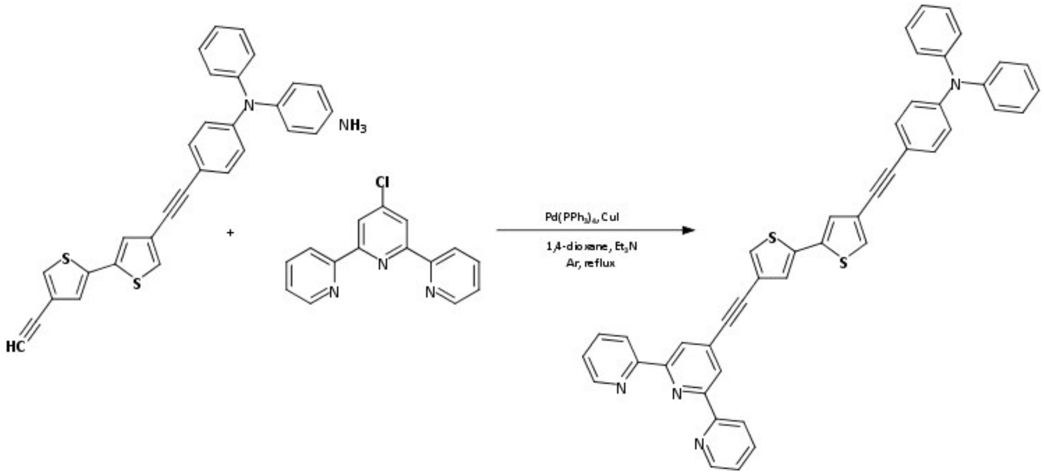

A two-neck 25 mL flask equipped with a condenser, a magnetic stirrer and an Ar inlet, was charged, under inert atmosphere, with 0.0400 g of Et-BT-Et-TPA (8.75*10^{-5} mol) and 0.0282 g of 4’-chloro-2,2’:6’,2’’-terpyridine in a Et-BT-Et-TPA/Tpy 1/1.1 molar ratio (9.62*10^{-5} mol) in 8 mL of 1,4-dioxane/H$_2$0 3/1. After 10 min of stirring under Ar, 5% of [Pd(PPh$_3$)$_4$] (4.37*10^{-6} mol, 0.0053 g), together with 10 % of CuI (0.0016 g, 8.75·10^{-6} mol) and 0.024 mL of Et$_3$N (1.75*10^{-4} mol in a Et-BT-Et-TPA/amine molar ratio) were added. The mixture is left under stirring at reflux and monitored by TLC (petroleum ether/ethyl acetate 2/1). After 24 h the reaction is left to cool to room temperature and filtered, then it is washed with CH$_2$Cl$_2$ and the solvent is evaporated under vacuum. The desired product is obtained with a 40 % yield.

^{1}H NMR (CD$_2$Cl$_2$, ppm):): δ_H = 7.73÷7.66 (m, br, 6H); 7.59÷7.54 (m, br, 4H);); 7.52÷7.45 (m, br, 6H);); 7.40÷7.35 (m, br, 2H);); 7.17÷7.06 (m, br, 6H);); 7.03÷6.99 (m, br, 2H);); 6.68÷6.54 (m, br, 2H).

UV spectrum in CH$_2$Cl$_2$, 5x10^{-5} M: λ_{max} = 345 nm, 274 nm

2.2.2 Characterization

2.2.2.1 Cyclic Voltammetry (CV)

Cyclic Voltammetry is an electrochemical technique that gives analytical (concentration), thermodynamic (redox potentials and equilibrium constants) and kinetic (reaction rates) information of a system that has to be characterised.

In CV the current (i) that flows in a working electrode (WE) at a variable potential is measured when electroactive species are present. The WE potential (V_1) can be varied with different rates that are expressed in V/s until a chosen potential (V_2) at which the electrodic process ends; then the potential scanning direction is usually inverted and taken back to V_1.

A three-electrode cell is usually used in CV (Fig. 2.3); the WE is labelled as 1, then a reference electrode (RE, 2) and a counter electrode (CE, 3) complete the measurement apparatus.

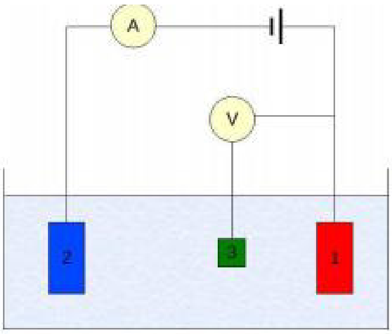

Fig. 2.3: general scheme of an electrochemical cell

With this configuration the current is measured between the WE and the CE (thus avoiding the polarization of the RE), while the potential is measured between the WE and the RE.

The resulting current is reported as a function of the applied potential to give a so called *voltammogram*.

In the cell an electrolyte is present to prevent the migration of the electroactive species under the electric gradient, the solution is not under stirring to eliminate the convection contribution and as a consequence the system is under diffusive control. The most common electrolytes are inorganic salts like $NaClO_4$ or $NaBF_4$ for polar solvents and tetraalkylammonium salts for less polar solvents.

Common solvents vary from CH_2Cl_2 to CH_3CN and they all possess a catho-anodic potential window (the range between the reduction and oxidation potential of the solvent system without analytes) between -2 V and +2 V.

Among the WE, usually Pt, Au and glassy carbon are used. When an electroactive species is present in the system, an electrodic reaction takes places as can be seen in Fig. 2.4.

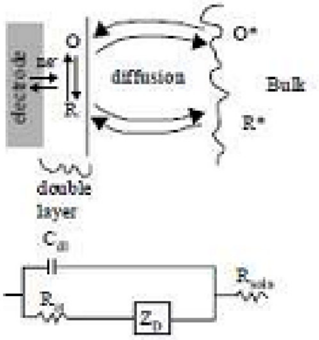

Fig. 2.4: diffusive mechanisms that take place at the electrode/solution interface.

In a reduction process, the oxidised species (Ox) takes electrons from the electrode and then diffuse far from the electrode. At the electrode/solution interface a current is generated due to the electrons transfer and in the solution the current is caused by the ions migration. This current is known as 'faradic' and depends on two factors: the electronic transfer rate and the diffusion rate of the electroactive species toward the electrode.

All electrochemical reactions are governed by the Nernst Equation:

$$\mathrm{E} = \mathrm{E}^0 + \frac{RT}{nF}\, ln \frac{Cox}{Cred}$$

Where

-E^0 is the standard potential of the electroactive species,

- R is the gas constant

- T is the absolute temperature

- F is the Faraday constant

- C are the concentrations of the oxidised or reduced species at the electrode interface.

During the experiment, the WE is used as anode or cathode, depending on the applied potential; when a potential is applied from V_1 to V_2 in Fig 2.5 a, a rapid increase of the current is recorded until it becomes constant. When changing the scanning direction the same response can be seen: the current will change the sign and will finally go to zero at the end of the experiment.

For example, if a negative potential is applied, the concentration of the electroactive species decreases and creates a concentration gradient until it becomes equal to zero; contemporary the bulk concentration of the oxidised species decreases and the gradient starts to decrease. While the gradient decreases also the species flux to the electrode slows down, and as a consequence the current will start decreasing and will give the response shown in Fig. 2.5 b.

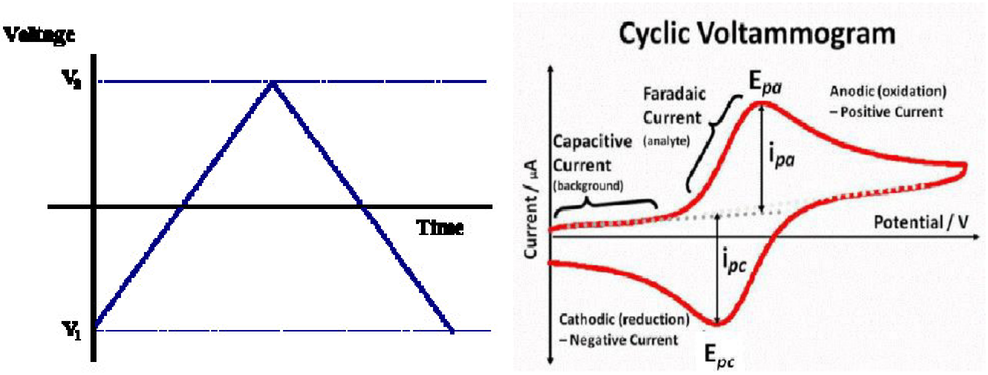

Fig. 2.5: (a) Potential agains time, (b) current-voltage response

With the inversion of the applied potential the same profile will appear if the process is reversible.

The peak current for an electroactive species in given by the formula:

$$i_p = kn^{3/2}AD^{1/2}\,\nu^{1/2}C_{bulk}$$

- n are the transferred electrons moles for each mole of transformed electroactive species
- A is the electrode area (cm^2)

- D is the diffusion coefficient of the species (cm^2/s)
- v is the scan rate (V/s)
- Cbulk is the concentration of the analyte (mol/cm^3)
- k is a costant ($2.69*10^5$)

Important information can be deduced from a voltammogram:

- The peak current i_p is directly proportional to the analyte concentration and the scan rate.
- The peak potential (E_p) is independent from the scan rate if the electron transfer rate is elevated.

The study of polymers by means of CV is useful because it gives the possibility of generating a redox partner of an electroactive compound and thus to monitor the properties by inverting the scan direction.

For electropolymerisable monomers, the radical cation can be generated and studied: if an associated peak appears the cation is stable, if no return phenomenon can be appreciated, the cation is not stable.

Other important information that can be deduced from cyclic voltammograms era related to HOMO and LUMO values of the electroactive analytes; for polymers also polarons formation can be seen in CV and the polymeric film stability can be evaluated when performing charging and discharging cycles.

For CV measurements a $CH_3CN/TEAPF_6$ 0.1 M or a $CH_2Cl_2/TEAPF_6$ 0.1 M solution was used, with an analyte concentration of $5*10^{-3}$ M.

The one compartment three-electrode cell was taken from a stove at 100 °C, was left to reach room temperature and the $CH_3CN/TEAPF_6$ 0.1 M or a $CH_2Cl_2/TEAPF_6$ 0.1 M solution was added. The electrodes are then placed in the cell after being cleaned with Al2O3, sonicated and washed with ultrapure acetone (WE=Pt, RE=Ag/AgCl, CE=graphite). The solution is then left under Ar bubbling for 10 min to eliminate oxygen. The voltammetric response of the solvent system is then recorded at 100 mV/s. The catho-anodic window varies with the solvent and usually lies between -2 V and +2 V. The solvent system voltammogram is accepted if no catho-anodic signals are recorded in the window interval.

After that, the analyte is added and the solution is left under Ar for other 15 min, then the CV is recorded under Ar flow at 100 mV/s if not differently specified.

The CV characterisation of the polymeric film is done in a $CH_3CN/TEAPF_6$ 0.1 M or a $CH_2Cl_2/TEAPF_6$ 0.1 M solution in the absence of the monomer at 100 mV/s.

All CV characterisations were made using Autolab PGSTAT 12 (EcoChemie) potentiostat/galvanostat interfaced with a PC under NOVA 1.10 software.

2.2.2.2 Chronoamperometry

Chronoamperometry is a simple potentiostatic electrochemical technique where a working electrode, in a quiescent solution of a solvent and electrolyte, is polarized with an applied potential; at time zero a potential step is applied till a proper potential value is obtained. This potential is kept constant for the entire analysis. The current associated to the faradic process varies with time and is recorded in a fixed time interval. The current response follows Cottrell Law

$$i\,(t)=nFAD_0^{1/2}C^b\pi^{-1/2}t^{-1/2}$$

where:

- n is the number of exchanged electrons
- F is the Faraday constant
- D_0 is the diffusion coefficient of the species
- A is the electrode surface area
- C_b is the bulk concentration of the analyte.

During the experiment the analyte concentration decreases near the electrode and the analyte has to diffuse from the bulk; this phenomenon will lead to a decrease in the rate of the analyte flux to the electrode and as a consequence an asymptotic behavior is seen in the response.

Chronoamperometry allows to obtain polymeric films with a quality higher than those obtained by CV because the fixed potential of the former avoids collateral electrodic processes.

Monomers have been polymerised on a Pt electrode through chronoamperometry, choosing the potential from the voltammetric responses. The deposition time was chosen case by case as to obtain films with the same thickness. After the deposition step, all films were neutralised by keeping them at 0 V bias for 60 s.

To evaluate the polymeric film thickness (d), the value of the deposition charge (Q_{dep}) is monitored during polymerisation and follows the following expression:

$$d(nm) = \alpha\, Q_{dep}\ (mC/cm^2)$$

In literature a α value of 2 is used [140]; however Semenikhin et al. [141] calculated, experimentally, a value of 2.5 nm*cm^2/mC. The current density has been calculated considering the electrode surface area of 0.0314 cm^2 and an α value of 2.5 was used.

All characterisations were made using Autolab PGSTAT 12 (EcoChemie) potentiostat/galvanostat interfaced with a PC under NOVA 1.10 software.

2.2.2.3 UV-Vis Spectrophotometry

The principles of this technique have already been briefly described in paragraph 2.1.2.5. For monomers, solution in CH_3CN or CH_2Cl_2 with an analyte concentration of $5*10^{-4}$ M were prepared and the absorbance was monitored from 800 to 250 nm. The band gap value was calculated from the λonset with tangent method (intersection between the baseline and the peak tangent) following the equation:

$$Eg = hc/\lambda_{onset}$$

where

- h is the Plank constant ($6.626*10^{-34}$ J*s)

---

[140] E. Lankinen, G. Sundholm, P. Talonen, T. Laitinen, T. Saario, *Journal of Electroanalytical Chemistry* **1998**, 447, 135

[141] O.A. Semenikhin, L. Jiang, T. Iyoda, K. Hashimoto, A. Fujishima, *Synthetic Metals* **2000**, 110, 195.

- c is the light speed ($2.988*10^8$ m/s)

considering the conversion between J and eV (1 J= $6.242*10^{18}$ eV).

For polymers, a film deposited on ITO glass was analysed. The polymer was deposited at the same conditions used for Pt electrode and the time was chosen as to obtain homogeneous films. Spectra of the polymer/ITO materials were recorded by immersion in a CH_3CN solution from 800 to 300 nm. The instrument was a T80+ UV/Vis spectrometer PG instrument Ltd with UV Win5 vs5. 0.5 software.

2.3 Instrumentation and Reagents

The instrumentation relative to the characterisation techniques that have been described in this thesis is given at the end of the corresponding paragraph.

2.3.1 Instrumentation for NMR, Elemental Analysis and Theorethical Calculations

^1H and $^{13}C\{^1H\}$ NMR spectra were recorded in CD2Cl2 or CDCl3 with a Bruker Avance III 400, at 400.0 MHz using the residual signal of the solvent as reference [142].

Elemental analysis were performed with a Perkin-Elmer 240B analyzer.

TD-DFT theorethical calculations were done with ORCA (3.0.2). The functional was B3LYP and the basis-set was def2-SVP for all atoms, also for hydrogens. All optimisations are done in vacuum.

---

[142] G.R. Fulmer, A.J.M. Miller, N.H. Sherden, H.E. Gottlieb, A. Nudelman, B.M. Stoltz, J.E. Bercaw, K.I. Goldberg, *Organometallics* **2010**, 29, 2176

2.3.2 Reagents

Commercial powders of TiO_2 (purity > 99.5 %), liquid $TiCl_4$ and $Ti(OBu)_4$ and P123 were purchased from Sigma-Aldrich and used as received.

Reagents for chromophores synthesis (TCI, Sigma-Aldrich, Riedel-deHaen, Fluka) were used without further purification. Chromatographic separations were done using alumina (Fluka for chromatograpaht basic, pH $10\underline{+}0.5$), silica gel (Merk 60, 230-400 mesh ASTM) and as eluent Aldrich or Carlo Erba solvents.

UV-Vis spectra were recorded in CH_3CN or CH_2Cl_2 from Aldrich.

$TEAPF_6$ (Fluka, electrochemical grade) was used as received and stored under vacuum.

Electrochemical tests were performed in CH_3CN or a CH_2Cl_2 (Aldrich <0.0050 % H2O) stored under nitrogen and withdrawn through a septum with a syringe.

Chapter 3

Results and Discussion

3.1 Titania Samples

As described in the experimental part, two different sets of titania samples were synthesised and their properties and characterization will be discussed separately in the following paragraphs.

3.1.1 Samples I-VIII

The mesoporous samples were synthesised with EISA method and with an acid-base precursors pairs (see Par. 1.1.3.1.2)

The preparation of the samples (experimental part) was done by adding different amounts of water (sample II, III, IV and V), or by changing the molar ratio of precursors (sample VII and VIII) or the surfactant (F127 only for sample VI) with the intent of studying the influence of each synthetic parameters on the structural and morphological properties of mesoporous titania.

3.1.1.1 X-Ray Powder Diffraction

Samples were characterized by means of XRPD and the patterns of some of the samples and relative data are reported in Fig. 3.1 (samples are reported from the lowest to the highest anatase percentage) and in Table 3.1, respectively.

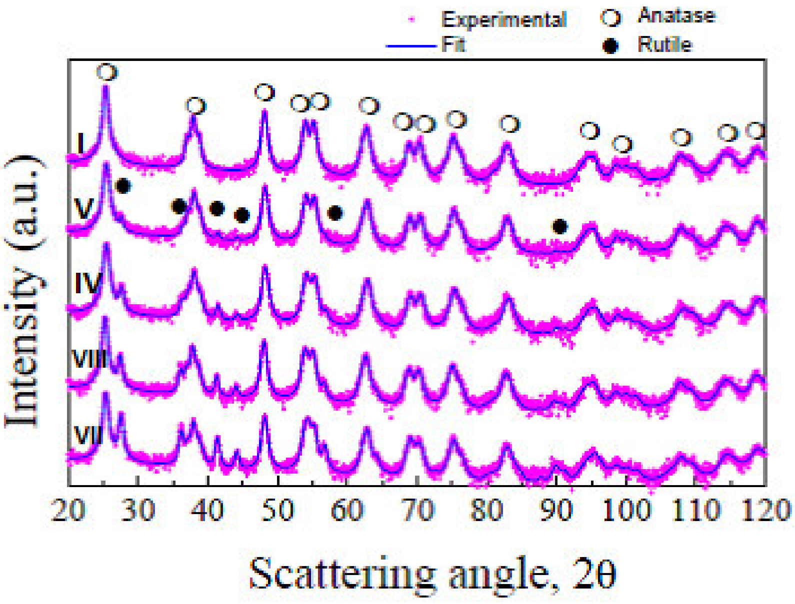

Fig. 3.1: XRPD patterns of samples I, IV, V, VII, VIII

Samples I, II, III and VI were all 100% anatase so only the pattern of sample I is reported. The evaluation of the data suggests that for these samples the synthetic conditions, in particular the change in surfactant for sample VI (F127 instead of P123) or the addition of water for samples II and III, did not have an influence on the crystalline composition.

Table 3.1: phase composition of all samples.

Samples	% Anatase	% Rutile
I, II, III, VI	100	-
IV	87	13
V	98	2
VII	74	26
VIII	92	8

For the other samples, both anatase and rutile were detected. In particular, sample VII showed the highest rutile content and this is probably due to the use of a higher $TiCl_4$ volume in its synthesis. Furthermore, the phase composition (74/26 anatase/rutile) of sample VII resembles the crystal structure composition of commercial P25, a very photoactive TiO_2 powder. On the other hand, keeping all the other parameters fixed, when lowering the acid precursor ratio, less rutile is obtained for sample VIII in respect to sample IV and VII. The crystallite size is the same for all samples, with anatase crystallite size in the range between 210-225 nm and rutile between 190-230 nm.

The thermal stability was evaluated by using Thermo Gravimetric (TG) technique: the samples were treated at 800 and 1300 °C and then analysed by means of XRPD. In Fig. 3.2 it is possible to see the diffraction pattern of sample I before and after the thermal treatments. The peaks profiles become narrower with increasing temperature because of an increasing crystalline degree due to the sintering of the powders. At 1300 °C the polycrystalline transition anatase-rutile has already taken place. All samples showed the same trend in the TG analysis.

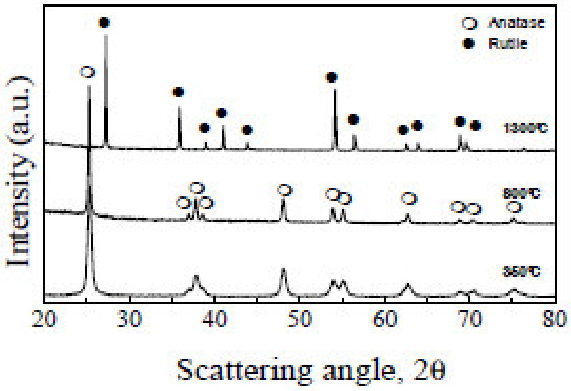

Fig. 3.2: XRPD patterns of the as-synthesised sample I and after thermal treatments at 800 and 1300°C

3.1.1.2 Transmission Electron Microscopy (TEM)

A morphological analysis of the powders was done by TEM microscopy. In Fig. 3.3 it is possible to appreciate images of sample VII before (A) and after (B) calcination; the electron diffraction images are present as insets in the figures.

In Fig. 3.3 A it is possible to highlight the presence of the surfactant/titania composite; moreover, the composite is amorphous as no electron diffraction rings can be detected in the inset.

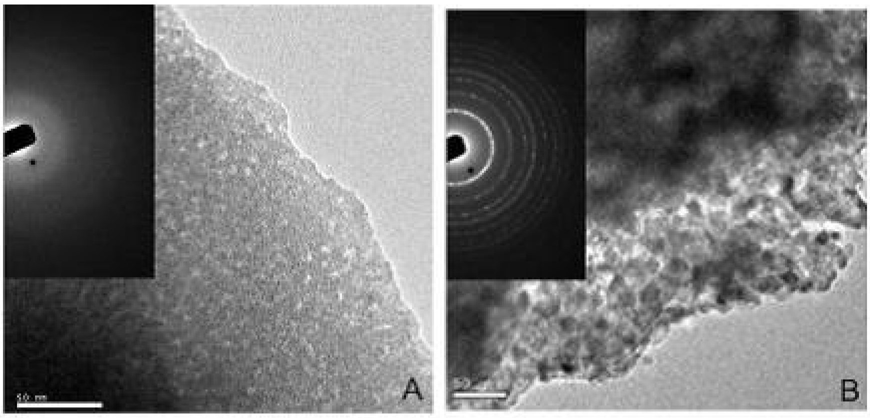

Fig. 3.3: TEM images of sample VII before (A) and after (B) calcination a 350°C. Electron diffraction images are present as insets.

After calcination (Fig. 3.3 B) no surfactant is detected and it is possible to appreciate the crystalline nature of the sample by the presence of electron diffraction rings in the inset. In addition, the morphology does not change upon calcination. The sample is a dense agglomerate of particles with sizes < 10 nm, and no long-range order in pore distribution can be found. Almost all the samples showed the same morphologies, with an exception for sample VI, where bigger particles (>10 nm and <50 nm) are distributed around bigger pores. In particular, lots of particles showed a 'donut-like' morphology where a single particle possesses a pore in the inside (Fig. 3.3 B); the difference in morphology can be attributed to the use, for sample VI, of a different surfactant (F127). Comparison between sample I and VI can be found in Fig. 3.4 and, from the electron diffraction rings, it is also quite clear the superior crystalline degree of sample VI (brighter diffraction rings).

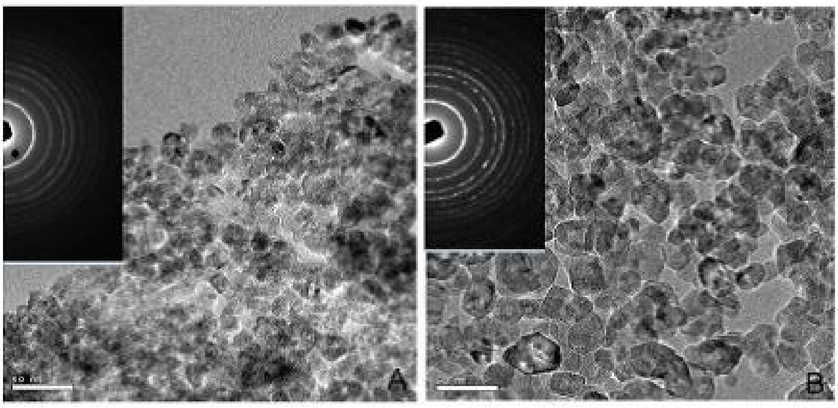

Fig. 3.4: TEM images of samples I (A) and VI (B). Electron diffraction patterns are present as insets.

It is worth mentioning the partial (it was found only in small portions of the analysed powder) order in the pore distribution for sample IV (Fig. 3.5), where regular channels of almost 5-6 nm size can be clearly seen. This evidence supports the hypothesis of a possible collapse of the mesostructure upon calcination: if some ordered regions can be found, like in sample IV, it is highly probable that the gelation step of the synthesis leads to an ordered hybrid framework (at least in some regions of the samples) and the loss of order is attributable to the subsequent calcination step.

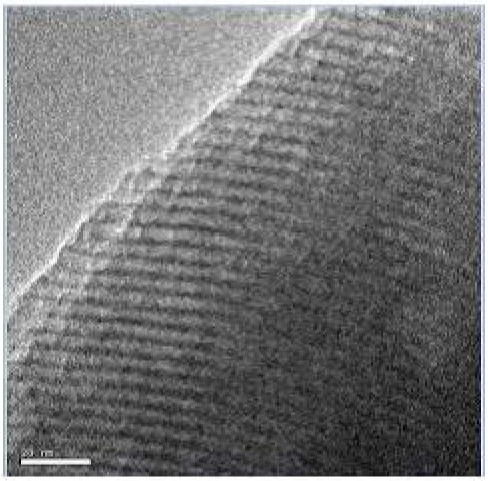

Fig. 3.5: TEM images of sample IV.

3.1.1.3 N_2 physisorption

Information on the surface areas, pore sizes and distributions were extrapolated from N_2 physisorption measurements. As an example, an adsorption/desorption isotherm of sample IV can be seen in Fig. 3.6: The adsorption branch is the one represented with white dots while the desorption part of the isotherm is represented with blue dots; the pore distribution is present as an inset.

All samples possess a typical type IV isotherm with a steep increase in the region between 0.60-0.95 p/p° and an H2-type hysteresis loop; this response confirms the mesoporous nature of the samples with an ink-bottle shaped pores [143]. The pore distribution is non perfectly unimodal and for sample IV is centred at around 7 nm. Data relative to all samples are summarised in Table 3.2.

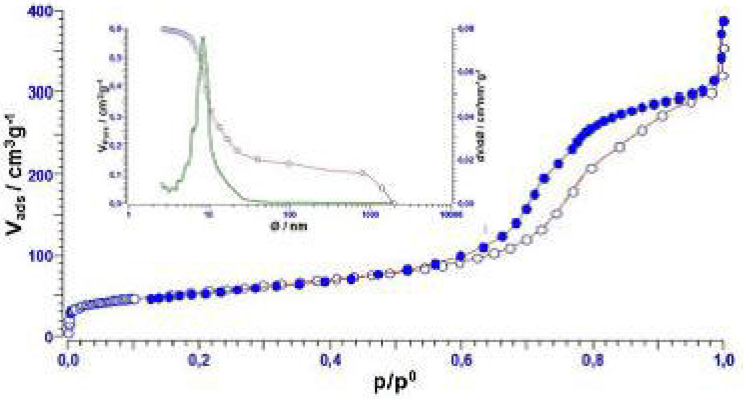

Fig. 3.6: Ad-Desorption isotherm of sample IV. The pore distribution of sample IV is present in the inset.

---

[143] D. Zhao, Y. Wan, W. Zhou, *Ordered Mesoporous Materials* **2013**, Wiley-VCH: Weinheim, Germany

Table 3.2: data extrapolated from the physisorption measurements.

Sample	Surface Areas (m^2/g)	Pore Volumes (cm^3/g)	Medium Pore Sizes (nm)
I	70	0.30	15.1
II	170	0.69	13.6
III	76	0.26	10.3
IV	196	0.45	7.1
V	150	0.64	15.1
VI	105	0.43	21.1
VII	73	0.30	13.6
VIII	92	0.26	7.8

3.1.1.4 UV-Vis Spectrophotometry

All samples were also characterised by means of UV-Vis spectrophotometry. The experimental details can be found in session 2.1.2.5. In Fig. 3.7 it is possible to see the spectrum relative to sample IV. In Fig 3.8 all absorption spectra are reported.

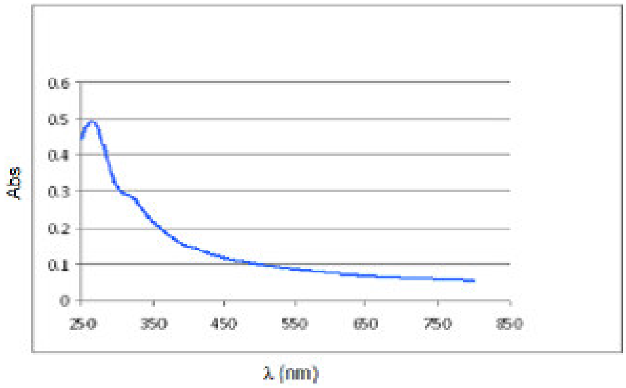

Fig. 3.7: UV-Vis absorption spectrum of sample IV.

An absorption maximum at 260 nm in present and also a shoulder at higher wavelength; this is probably caused, as already known in literature, by the presence of both anatase and rutile in sample IV [144]; also the other two-phase samples showed the same peak profile. Optical Band Gap (E_{opt}) were calculated from the onset wavelength in the spectra and relative values are summarised in table 3.3 together with the phase percentages.

Table 3.3: Band Gap values and phase composition of all samples

Samples	**Band Gap (eV)**	**% Anatase**	**% Rutile**
I	2.86	100	-
II	3.34	100	-
III	3.18	100	-
IV	3.02	87	13
V	3.10	98	2
VI	3.26	100	-
VII	3.07	74	26
VIII	3.18	92	8

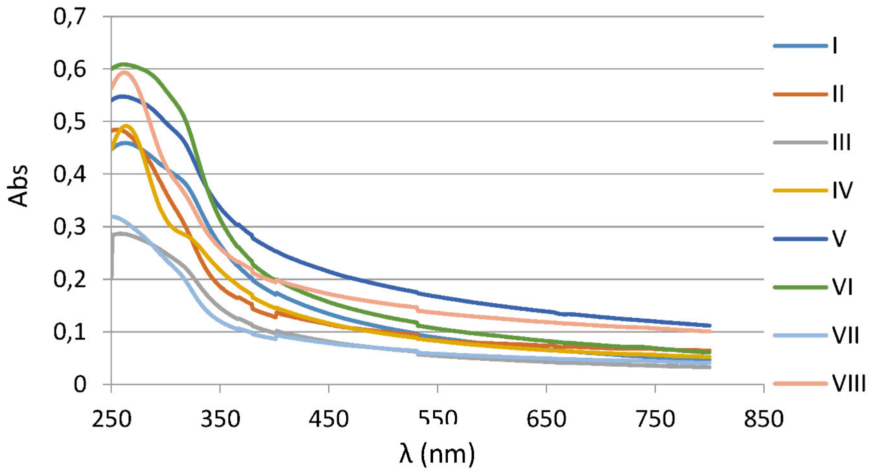

Fig. 3.8: UV-Vis spectra of all samples

---

[144] S.U.M. Khan, M. Al-Shahry, W.B. Ingler Jr, *Science* **2002**, 297, 2243

The comparison between spectroscopic and diffractometric data shows no straightforward correlation; the lowest and highest band gap value are respectively of sample I and II and both are made of pure anatase. Sample VII, with the highest rutile percentage, lies in the middle of the range. When looking at synthetic details, it seems that the variation in the precursors ratio (sample VII and VIII vs VI) or the addition of a high water volume (sample III vs IV) leads to higher Eg values. Also the use of F127 (sample VI) instead of P123 (I), keeping all the other parameters fixed, leads to an increase in the band gap of the former.

3.1.1.5 Photoelectrochemistry

Titania electrodes (see experimental part for preparation and experimental details) were tested as photoanodes in aqueous NaOH 1 M solution in the water splitting reaction.

In Fig. 3.9 a linear sweep voltammogram of sample III is represented, at potential scan rate equal to 5mV/s, chopping the light from the solar simulator at fixed intervals.

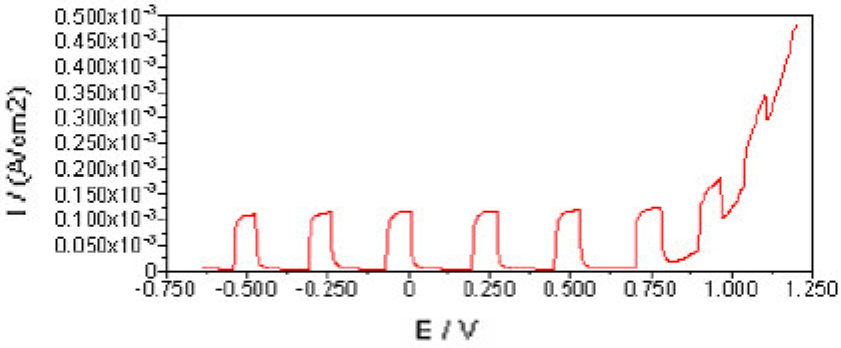

Fig. 3.9: Current density (J) curve plotted against the applied potential for electrode made with sample III and recorded under chopped light.

It is clear that titania is a photoactive material as the intensity of current decreases when the cell is not illuminated and then goes up quickly under solar illumination.

All samples were tested under illumination and the resulting curves are reported in Fig. 3.10, where also commercial P25 is present as a standard material.

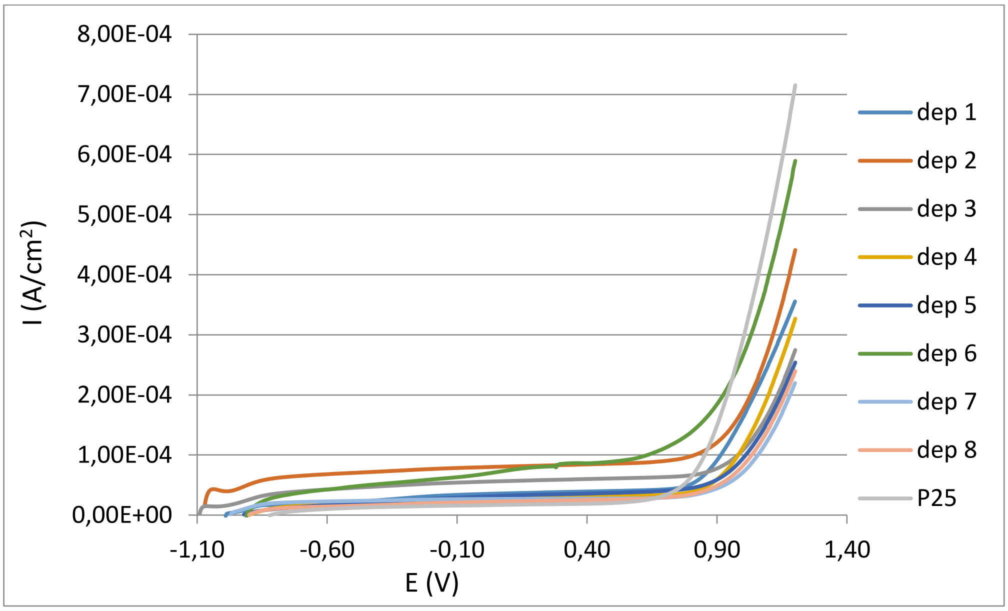

Fig 3..10: linear sweep voltammograms under light illumination of all deposited samples and P25.

The current density values of samples and of P25, at 0.9 V, are reported in Table 3.4 and also the theoretically calculated hydrogen moles at the same potential are calculated with the Faraday's law.

Table 3.4: Current density values at 0.9 V and the corresponding calculated H_2 moles.

Samples	**J (A/cm2)**	**H_2 moles (µmol/h)**
I	$6.68*10^{-5}$	10.7
II	$8.64*10^{-5}$	10.0
III	$6.42*10^{-5}$	14.8
IV	$3.67*10^{-5}$	10.9
V	$3.07*10^{-5}$	10.7
VI	$5.98*10^{-5}$	13.5
VII	$3.03*10^{-5}$	6.9
VIII	$3.39*10^{-5}$	6.4
P25	$8.47*10^{-5}$	24.0

The data confirms the high photoactivity of P25 [145]. When comparing the data of the samples, the more photoactive ones are those with a 100% anatase composition (I, II, III and VI) and especially samples III where the highest amount of water was used, and VI, where F127 was used. Low values are obtained from samples VII and VIII, where the precursors ratio was changed.

In the next chapter a comparison between P25 and sample IV, VII and VIII will be reported with the aim of evaluating the anatase/rutile phase composition on the photocatalytic performances of powders synthesised with the same procedure but varying the precursors ratio. The discussion has been recently published on International Journal of Hydrogen Energy [146].

3.1.1.6 P25, sample IV, VII and VIII

The synthesis of nanocrystalline TiO_2 powders with different anatase/rutile weight ratios (sample IV, VII and VIII) was successfully approached by evaporation-induced self assembly (EISA) method by simply varying the volume amount of $TiCl_4$ and $Ti(OBu)_4$ (acid–base pair) as metal precursors. In particular, m-TiO_2 with anatase/rutile weight ratios similar to commercial TiO_2 (P25) was obtained (sample VII). The mixture of anatase and rutile in commercial TiO_2 nanoparticles (Degussa P25) makes this material more active than other ones made of pure anatase [147]. P25 is composed of an anatase/rutile ratio of about 3:1 and its microstructure is characterized by the phase junction between these two polymorphs [147, 148]. Nevertheless, potential effects of such features are only partially explored and the relationship between the structure and the photocatalytic activity of TiO_2 is not straightforward disclosed due to the many physico-chemical parameters (microstructure, morphology, surface area, surface defects, texture, etc) involved in this process [149]. Specifically, an extended surface area with a high adsorbent surface density contributes to

---

[145] A. Bojinova, R. Kralchevska, I. Poulios, C. Dushkin, *Chemical Physics* **2007**, 106, 187

[146] E. Masolo, N. Senes, E. Pellicer, M.D. Barò, S. Enzo, M.I. Pilo, G. Mulas, S. Garroni, *International Journal of Hydrogen Energy* **2015**, 40, 14483

[147] T.Ohno, K. Sarukawa, K. Tokieda, M. Matsumura, *Journal of Catalysis* **2011**, 203, 82

[148] J. Zhang, Q. Xu, Z. Feng, M. Li, C. Li, *Angewandte Chemie International Edition* **2008**, 47, 1766

[149] Z. Hong, H. Dai, Z. Huang, M. Wei, *Physical Chemistry Chemical Physics* **2013**, 35, 307

increase the performances of the photocatalytic reaction. On the other hand, the surface of a semiconductor is typically characterized by several defects such as impurities, oxygen vacancies, step edges, etc., which can act as trap sites, thus favouring the electron-hole recombination by the SRH model (Shockley-Read-Hall Model) [150]. The electron-hole recombination at the surface represents an important limiting step and a catalyst with a large surface area and a high number of defects (poor crystallinity) can lead to low photoelectrocatalytic activities [151]. For the aforementioned reasons, in order to decrease the defects in the microstructure while keeping a significant photocatalytic activity, TiO_2 with a high crystalline framework and large surface area is highly desirable and mesoporous titania can offer these two advantages. For the abovementioned reasons mesoporous samples IV, VII and VIII were compared to P25 in an attempt to give new perspectives in the effect of the anatase to rutile relative amount in mesoporous TiO_2 (m-TiO_2) powders for the photoelectrocatalytic production of hydrogen.

The XRPD patterns of the TiO_2 samples prepared by varying the acid-base $TiCl_4$-$Ti(OBu)_4$ metal precursor volumes are reported in Fig. 3.11, together with the profile relevant to commercial P25. . Blue dots, pink, red and light green lines correspond to the experimental pattern, anatase and rutile phases contribution, and the pattern baseline, respectively. The pattern of the commercial P25 is shown for comparison.

In order to estimate the microstructural parameters of the phases contributing to the patterns with a high degree of accuracy, the full diffractograms (Fig. 3.12 A) were carefully analyzed. It can be seen that the Rietveld profiles (pink and red lines) interpolate the experimental data points (blue dots) with a high degree of accuracy. The XRPD analyses reveal that the powders consist of a mixture of anatase (A) and rutile (R) phases. As shown in detail in Fig. 3.12 B, the Bragg peaks of the A-TiO_2 phase simultaneously increase in intensity with respect to the rutile peaks, as the $TiCl_4/Ti(OBu)_4$ ratio decreases. The quantitative data gleaned from the Rietveld treatment of the XRPD patterns are summarized in Table 3.5, where the phase weight % abundance and crystallite sizes are reported for each phase in the samples. In particular, the pattern corresponding to the TiO_2

---

[150] R.N. Hall, *Physical Review* **1952**, 87, 387

[151] Z. Zhang, J.T. Yates*, Journal of Physical Chemistry C* **2010**, 114, 3098

synthesized with a 1.0/0.78 mL $TiCl_4/Ti(OBu)_4$ ratio (sample IV) shows an A:R weight % of 87:13, similar to that of commercial P25 (83:17, see Table 3.5).

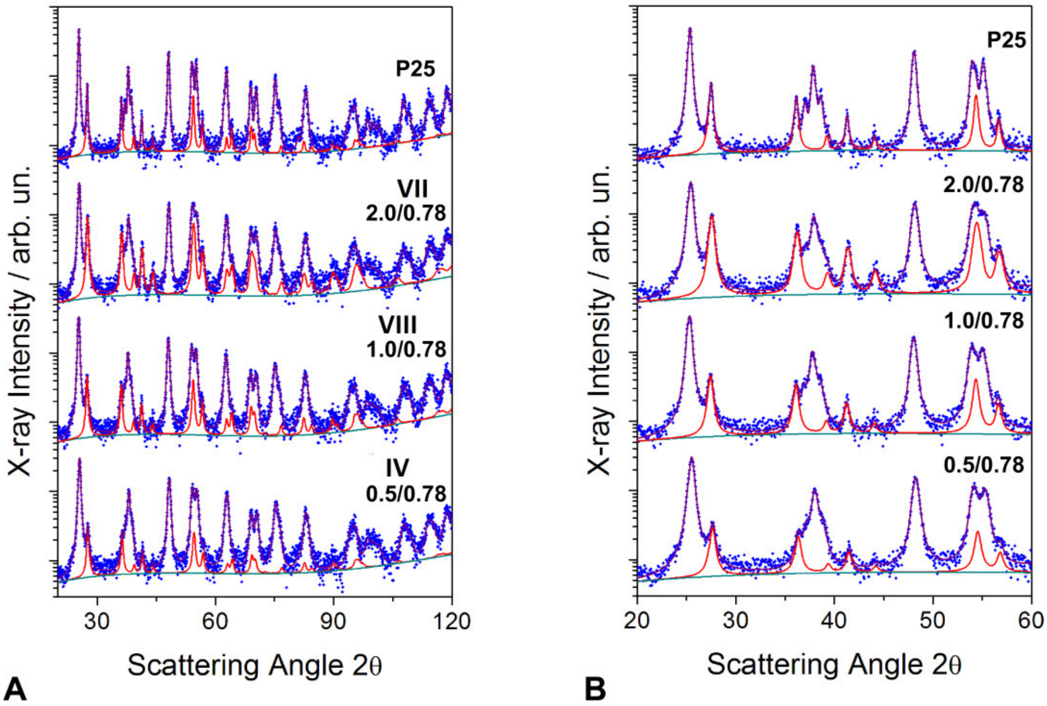

Fig. 3.12: **A.** CuKα X-ray diffraction patterns of the samples prepared with variable volume ratios (mL) of $TiCl_4$-$Ti(OBu)_4$. **B.** Zoom in the angular 2θ range 20-60°, which gives an idea of the accuracy of the Rietveld refinement.

Moreover, it is possible to appreciate a clear relationship between the amount of $TiCl_4$ used in the synthesis and the corresponding A:R ratio: keeping the $Ti(OBu)_4$ volume constant (0.78 mL), the anatase content decreases (74:26 A:R) or increases (92:8 A:R) using, respectively, higher (2.0 mL) or lower (0.5 mL) $TiCl_4$ volumes as reported in Table 3.5, and this is totally in agreement with the previous work published on this system [152].

Moreover, the shape of XRPD peaks shown in Fig. 3.12 B, together with the results arising from the Rietveld refinement, suggests that the microstructural parameters of both the anatase and rutile phases are quite similar and do not vary upon changing the $TiCl_4/Ti(OBu)_4$ volume ratios. Contrarily, the rutile shows larger crystallite size (R: 525Å)

---

[152] L. Chen, B. Yao, Y. Cao, K. Fan, *Journal of Physical Chemistry C* **2007**, 111, 11849

than the anatase counterpart (A: 350 Å) in the P25 sample (see Table 3.5). It is worth mentioning that the previously cited characteristics allow studying the influence of the anatase/rutile weight ratios on the photocatalytic activity of the as-synthesized TiO_2, excluding any eventual contribution arising from differences in the crystallite size.

Table 3.5: TiO_2 Anatase/Rutile weight % composition, corresponding crystallite sizes and specific surface area. Commercial P25 data are also reported for comparison.

$TiCl_4/Ti(OBu)_4$ (ml)	% Anatase	% Rutile	Crystallite size (Å) Anatase/Rutile	Surface Area BET (m^2/g)
P25 (commercial)	83	17	350/525	39
2.0/0.78	74	26	225/230	73
1.0/0.78	87	13	220/210	196
0.5/0.78	92	8	210/190	92

Representative TEM images of the commercial P25 and the synthesized TiO_2 samples with different anatase and rutile amounts are presented in Fig. 3.13. The commercial P25 (Fig. 3.13 A) shows homogenous particle sizes ranging from 20 to 40 nm, characterized by a rhombic- and square-like shapes, in accordance to the data reported by Martra et al. [153]. The rhombic-like shape can be associated with a truncated bipyramid particle with the longer axis oriented perpendicular to the electron beam (see inset in Fig. 3.13 A).

The size distribution of the particles is not influenced by the presence of mixed phases as it is uniform when referring to each single sample but on the other side differences in both the particle size and the pore morphology can be observed (Fig. 3.13 B, C and D). Though the samples are highly porous, no long-range ordered pore arrangement can be perceived,

---

[153] C. Deiana, M. Minella, G. Tabacchi, V. Maurino, E. Fois, G. Martra, *Physical Chemistry Chemical Physics* **2013**, 15, 307

which can be ascribed to a quick hydrolysis-condensation process during the gelation step and to a subsequent partial collapse of the pores during the calcination [154, 155].

The powders with the highest rutile content (Fig. 3.13 B) feature a worm-like structure with a particle size of 10-30 nm, whereas the anatase-rich sample (Fig. 3.13 D) is characterized by smaller and defined particles with reduced degree of interconnection. In the TiO_2 sample prepared with similar volumes of $TiCl_4/Ti(OBu)_4$ (1.0/0.78 ml), the morphology of the particles turns out to be different with respect to the previous ones (Fig. 3.13 C). The same rhombohedral shape associated to a truncated bipyramide can be observed in many particles, and are however different from those of P25 in terms of size and for the presence of well-defined holes at the center of the particles (inset in Fig. 3.13 C). These holes are attributable to the use of Pluronic 123 in the synthesis [156].

The N_2 adsorption-desorption isotherms of the titania samples and the corresponding pore size distributions are depicted in Fig. 3.14.

The P25 material (Fig. 3.14 A) shows a type II isotherm characteristic of macroporous materials [157]. A H3-type hysteresis loop is observed at high relative pressure and can be related to the typical capillary condensation and evaporation processes that take place in the presence of large pores. The sample is characterized by a BET surface area of 39 ± 2 m^2/g (see Table 3.5), and a wide pore size distribution (inset of Fig. 3.14 A) with a maximum pore width, ρ_{BJH}, of 97.5 ± 0.5 nm and cumulative pore volume of 0.47 ± 0.02 cm^3/g can be observed. All the samples prepared by the acid-base pair precursors (Fig. 3.14 B, C, D), exhibit a type IV isotherm and a H2-type hysteresis loop, characteristic of mesoporous materials (pore size between 2-50 nm) with ink-bottle shaped pores [143, 158].

---

[154] E.L. Crepaldi, G.J. Soler-Illa, D. Grosso, F. Cagnol, F. Ribot, C. Sanchez, *Journal of The American Chemical Society* **2003**, 125, 9770

[155] F. Schüt, *Chemistry of Materials* **2001**, 13, 3184

[156] Y. Wan, H. Yang, D. Zhao, *Accounts of Chemical Research* **2006**, 37, 423

[157] K.S.W. Sing, D.H. Everett, R.A.W. Haul, L. Moscou, R.A. Pierotti, J. Rouquerol, T. Siemieniewska, *Pure & Applied Chemistry* **1985**, 57, 603

[158] K.P.S. Parmar, E. Ramasamy, J.W. Leeb, J. Sung Lee, *Scripta Materialia* **2010**, 62, 223

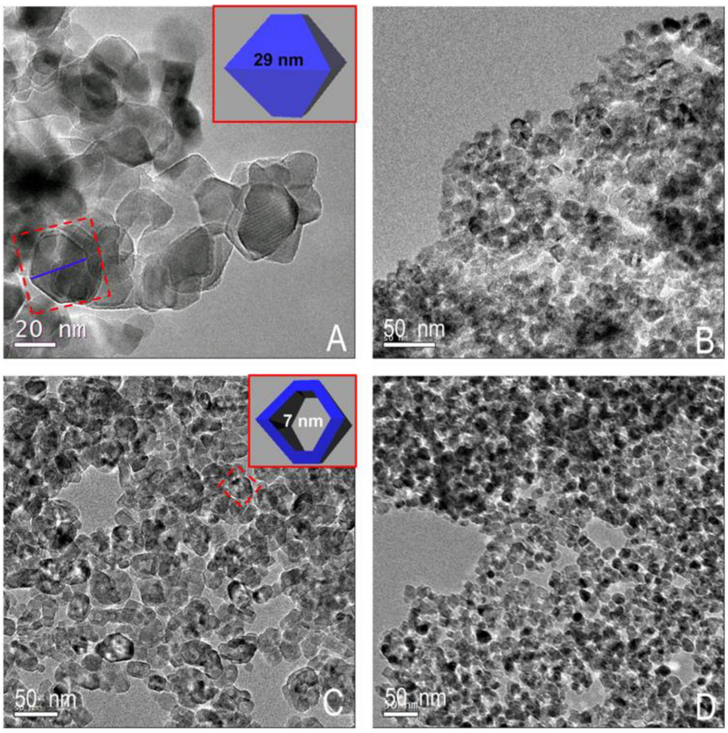

Fig. 3.13: TEM images of the commercial P25 and TiO_2 samples prepared from different relative amounts of $TiCl_4$ and $Ti(OBu)_4$ (in mL): **A.** P25. **B.** 2.0/0.78 $TiCl_4/Ti(OBu)_4$ ratio (VII). **C.** 1.0/0.78 $TiCl_4/Ti(OBu)_4$ ratio (IV). **D.** 0.5/0.78 $TiCl_4/Ti(OBu)_4$ ratio (VIII). The insets are the 3D reconstruction using Rhinoceront 3D software of the particles (red square).

Considering that no mesostructure with long-range order is observed from the TEM images, it is possible to assume that the mesoporosity, verified by N_2 physisorption measurements, is likely due to the interparticle arrangement; as well-known, there are two different types of pores, one are the interparticles pores formed from the packing of neighbouring particles and the other are the assembled pores which correspond to the position previously occupied by the surfactant P123 [159].

---

[159] W. Jing, W. Huang, W. Xing, Y Wang, W. Jin, Y. Fan, *ACS Applied Materials and Interfaces* **2009**, 1, 1607

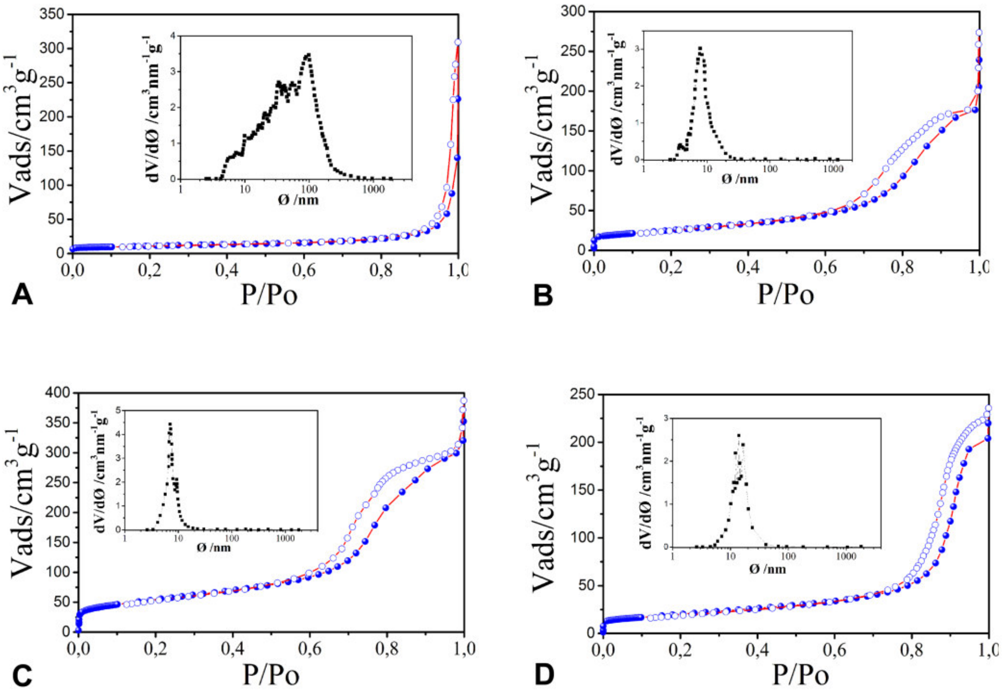

Fig. 3.14: N_2 adsorption (filled dots)-desorption (empty dots) isotherms of the commercial P25 and TiO_2 samples prepared from different amount (ml) of $TiCl_4$ and $Ti(OBu)_4$: **A.** P25 . **B.** 2.0/0.78 $TiCl_4/Ti(OBu)_4$ ratio. **C.** 1.0/0.78 $TiCl_4/Ti(OBu)_4$ ratio. **D.** 0.5/0.78 $TiCl_4/Ti(OBu)_4$ ratio. The insets are the BJH pore size distribution plots.

Pore size distributions calculated from the desorption branch of the isotherms are shown in the insets in Fig. 3.14 B, C, D. It can be noted that, with respect to P25, the profiles of the pore size distribution are located in the mesopore region in agreement with the as discussed data. Interestingly, a narrow distribution profile is achieved for the TiO_2 sample with the A:R content similar to P25 (inset in Fig. 3.14 C): the BJH analysis presents two main peaks placed at 7.1 (the most intense) and 9.3 nm. The pores with an average diameter size of 7.1 nm are those that are clearly distinguishable from the corresponding TEM analysis (Fig. 3.14 C- insert 3D particle reconstruction). This aspect implies that this particular sample is characterized not only by inter-particle porosity but probably also by intra-particle porosity, not appreciable in TEM images. The estimated cumulative pore volume is 0.63 ± 0.02 cm^3/g and its BET surface area corresponds to 196 ± 2 m^2/g, about 5 times larger than annealed P25. It can be seen that the specific surface area of the two samples composed by the A:R weight % of 74:26 and 92:8, are 73 and 92 ± 2 m^2/g, respectively, even higher than heat-treated P25, but approximately half of the m-TiO_2 87:13 (A:R weight %). Hence, the large BET surface area shown by the m-TiO_2 87:13 (A:R weight %) sample can be mainly ascribed to the presence of intraparticle pores obtained after the removal of P123.

Fig. 3.15 A shows a series of UV-VIS spectra collected in the wavelength range between 250 and 800 nm, while Fig. 3.15 B displays the J-V curves of the samples collected under solar irradiation in a 1M NaOH aqueous solution. The spectrum referred to the sample 1.0/0.78 ml $TiCl_4$/$Ti(OBu)_4$ ratio (blue curve in Fig. 3.15 A) displays a maximum absorption at 260 nm and a shoulder at around 316 nm (λ_{onset} = 410 nm), associated to the presence of both the anatase and rutile phases in the powder mixture, as also confirmed by the structural characterization [160]. The wavelength onsets and the estimated bandgap values are summarized in Table 3.6. For sample IV, the band gap (Eg) is calculated to be 3.02 eV, which is equal to the theoretical band gap of rutile (3.02 eV) [161]. However, since the band gap is strongly influenced by the particles size (d < 10 nm), its assignation to anatase or rutile phases may be questionable [162].

---

[160] Y.K. Kho, A. Iwase, W.T. Teoh, L. Madler, A. Kudo, R. Amal, *Journal of Physical Chemistry C* **2010**, 114, 2821
[161] M.V. Rao, K.Rajeshwar, V.R. Pal Verneker,J. DuBow, *Journal of Physical Chemistry* **1980**, 84, 1987
[162] Y.Wang, N. Herron, *Journal of Physical Chemistry* **1991**, 95, 525

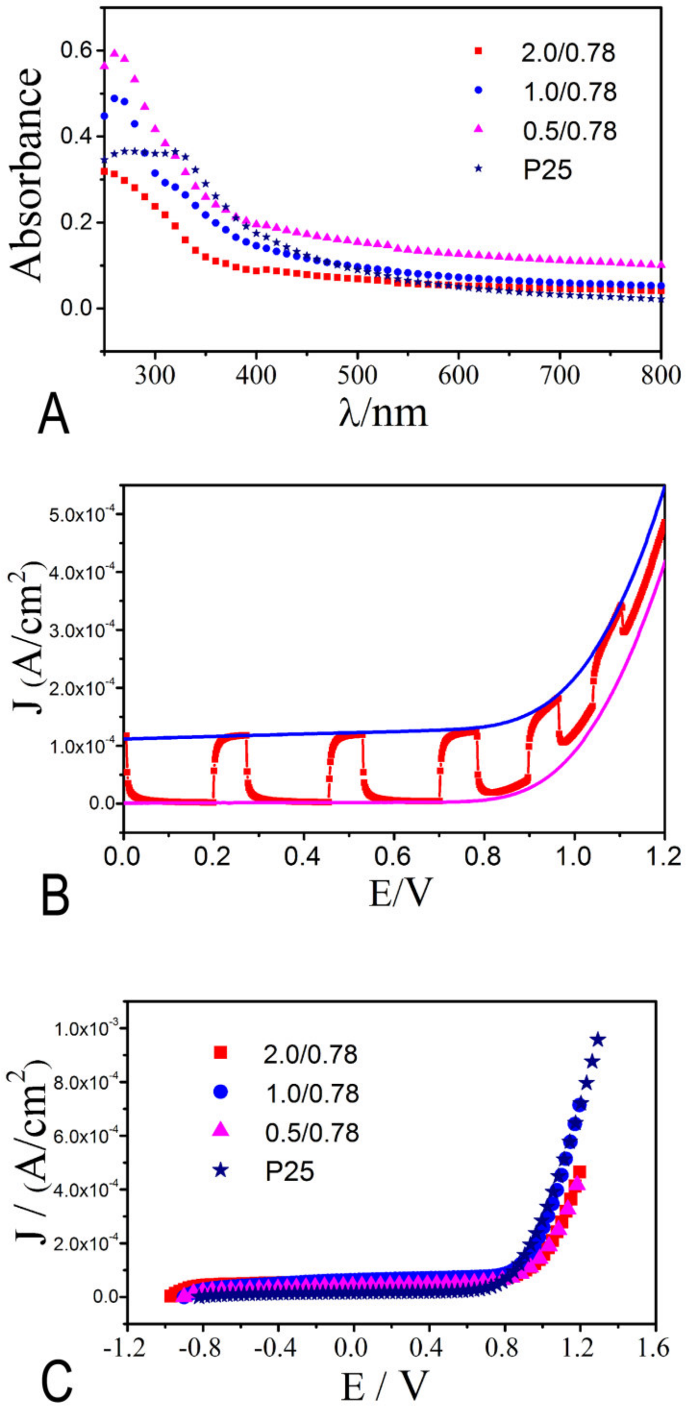

Fig. 3.15: UV-visible absorbance spectra of the mesoporous TiO_2 samples and P25 **B.** J-V curves of the m-TiO_2 recorded under solar radiation (blue line), intermittent radiation (red squares), and dark test (magenta line). **C.** J-V curves of the mesoporous TiO_2 samples and P25 under solar irradiation simulation

Table 3.6: Wavelength onset, bandgap values, photocurrent density data and H_2 evolution rate of the as-prepared m-TiO_2. Commercial P25 data are also reported for comparison.

$TiCl_4$/$Ti(OBu)_4$ (ml)	λ_{onset} (nm)	Band Gap (eV)	J (10^{-5} A/cm^2)	H_2 evolution rate (μmol/h cm^2)
P25 (commercial)	420	2.95	8.47	~10
2.0/0.78 (VII)	403	3.07	3.03	3.19
1.0/0.78 (IV)	410	3.02	3.67	4.87
0.5/0.78 (VIII)	390	3.18	3.39	3.20

For the m-TiO_2 samples characterized by the A:R weight % of 92:8 and 74:26, band gaps of 3.18 eV and 3.07 eV are calculated, which can be compared with the literature data for pure anatase (3.23 eV), and pure rutile (3.02 eV). The results indicate that the relative content of anatase and rutile, and hence the synthesizing parameters, play a very important role in the position of the band gap of the m-TiO_2 samples.

The TiO_2 samples are then tested as photoanodes in the water splitting reaction (for more details see the experimental section). The photocurrent measurements are performed in 1M NaOH aqueous solution. The potential is scanned from the open circuit potential up to 1.2 V at a scan rate of 5 mV/s while irradiating the nanocrystalline films, with a radiation power of 100 W/cm^2. A representative measure of the m-TiO_2 is reported in Fig. 3.15 B: the anodic current recorded when the film is exposed to the solar radiation (blue curve) results higher with respect to the current obtained during the dark test (magenta curve) for each potential applied. Additionally, the current acquired during the chopped test (red curve) alternatively matches with the singular light/dark signals. The difference between the current density values recorded in the presence of light and in the absence of light is used to determine the potential value at which the electrolysis has to be performed in order to verify the efficiency of the m-TiO_2 photoelectrodes as photoanodes in the production of hydrogen. Fig. 3.15 C shows the J-V curves of the films subjected to the solar irradiation. All curves are characterized by a small increase of the photocurrent density for negative potential (~ -1.0 V), whereas a significant increase of J is observed, as expected, above +0.9 V. With the aim of comparing the hydrogen evolution rate of the different titania samples, electrolysis experiments are then performed at +0.90 V and the relative data are reported in Table x. The H_2 evolution data, summarized in Table 3.6, show that commercial P25 is characterized by an elevated photocatalytic activity (~ 10 µmol/cm^2 h). For the as-prepared m-TiO_2 samples, the film with 87:13 anatase:rutile weight ratio resulted the most active. This sample showed a H_2 evolution rate value of 4.87 µmol/cm^2 h, being almost 30% more efficient than the other two systems. Considering that all the as-synthesized samples present similar crystallite sizes (see Table 3.5), the loss in photocatalytic activity of the other two samples (Fig. 3.15 B and D) cannot be attributed to the anatase (more photoactive phase) content and may then be correlated with their poorer surface area. No significant difference in terms of H_2 evolution rate is instead reported for these two samples. The m-TiO_2 with 87:13 anatase:rutile weight ratio has a much higher surface area (196 m^2/g) and a more uniform pore size, which can be associated to both a higher degree of interaction with water and also to its easier mass diffusion inside titania channels. However, this parameter alone is not sufficient to explain why the photoactivity performance of the mesoporous samples is lower when compared to the commercial P25 with a S_{BET} of 39 m^2/g. Small crystallite size accompanied by high density of microstructure defects, are considered to increase the mutual e^-/h^+ recombination rate at the surface. In fact, as determined from the Rietveld analysis, the crystallite size of both the anatase and rutile phases in P25 calcined at 400 °C are much higher (350/525 A/R) with respect to those calculated for the mesoporous samples. This implies that the crystallinity, besides the A:R ratio and the specific surface area, also plays a crucial role in the photocatalytic H_2 activity. Therefore, it emerges that although the m-TiO_2 with an A:R ratio of 87:13 (similar to commercial P25) presents a very interesting surface area and improved performances in respect to the other mesoporous samples, higher crystallinity (in particular for the rutile phase) is necessary to drastically decrease the number of lattice defects and then facilitate the interaction between the electrons and the water adsorbed at the TiO_2 surface.

3.1.2 Samples 1-8

In these synthesis (see experimental part for details) a set of parameters which, in principle, can play a key role in titania photocatalytic performances, were evaluated. In particular, the use of different titania precursors, calcination rate, and ligand addition effect on the morphology, texture and phase content of synthesized mesoporous titania samples were investigated.

The precursors are selected basing on two different approaches with EISA method (described in chapter 1): the acid-base pair, using $TiCl_4$ and $Ti(OBu)_4$, and a more classic route with $Ti(O^iPr)_4$ and HCl. For both precursors, different specimens were prepared by resorting to different calcination rates and with and without the addition of acetylacetone, that creates coordinated species with lower hydrolysis rates, and with different calcination rate. The following discussion of data has been recently published by this group in Nanomaterials [163].

A total of eight samples were synthesized by following the procedure reported in the experimental section (Table x). The intent was to tentatively relate the addition of coordinating ligands like acetylacetone, the different calcination rates and different precursors to the final morphology and crystal structure of our titania powders, keeping constant the amount of titania precursors and the pH level in all the synthesis. The calcination temperature of 400°C was chosen taking into account the temperature needed for the subsequent preparation of the titania electrodes and 12 h of calcination were necessary for the complete removal of the surfactant P123. P25 was chosen for comparison for evaluating the electrochemical performances of the powders.

3.1.2.1 X-Ray Powder Diffraction

The X-Ray Powder Diffraction (XRPD) patterns of the samples are reported in Fig. 3.16, together with the pattern of commercial P25. All the reported profiles were analysed

---

[163] E. Masolo, M. Meloni, S. Garroni, G. Mulas, S. Enzo, M.D. Barò, E. Rossinyol, A. Rzeszutek, I. Herrmann-Geppert, M. Pilo, *Nanomaterials* **2014**, 4, 583

through the Rietveld method: the microstructural parameters of each phase were assigned with a high degree of accuracy, as it can be seen from the good superimposition between the green (rutile, R), pink (brookite, B), and red (anatase, A) profiles, of the Rietveld refinement, and the Bragg peaks of the experimental patterns (blue dots). As evinced in Fig. 3.16 a, samples 1–4 show the presence of both anatase and rutile phases in good agreement with previous data reported in literature [152]. From the data extrapolated by the Rietveld analysis and reported in Table 3.7, it is worth mentioning that the addition of acetylacetone to the initial solution induces the formation of a high content anatase-based TiO_2 powders. If we take into account the calcination rate, the samples treated at 1°C/min (2 and 4) show a higher rutile content, which is the thermodynamically more stable phase. The crystallite size is almost the same for all the four samples, ranging from 18–20 nm for both phases and it was not influenced by the addition of coordinating ligands or by the calcination rates.

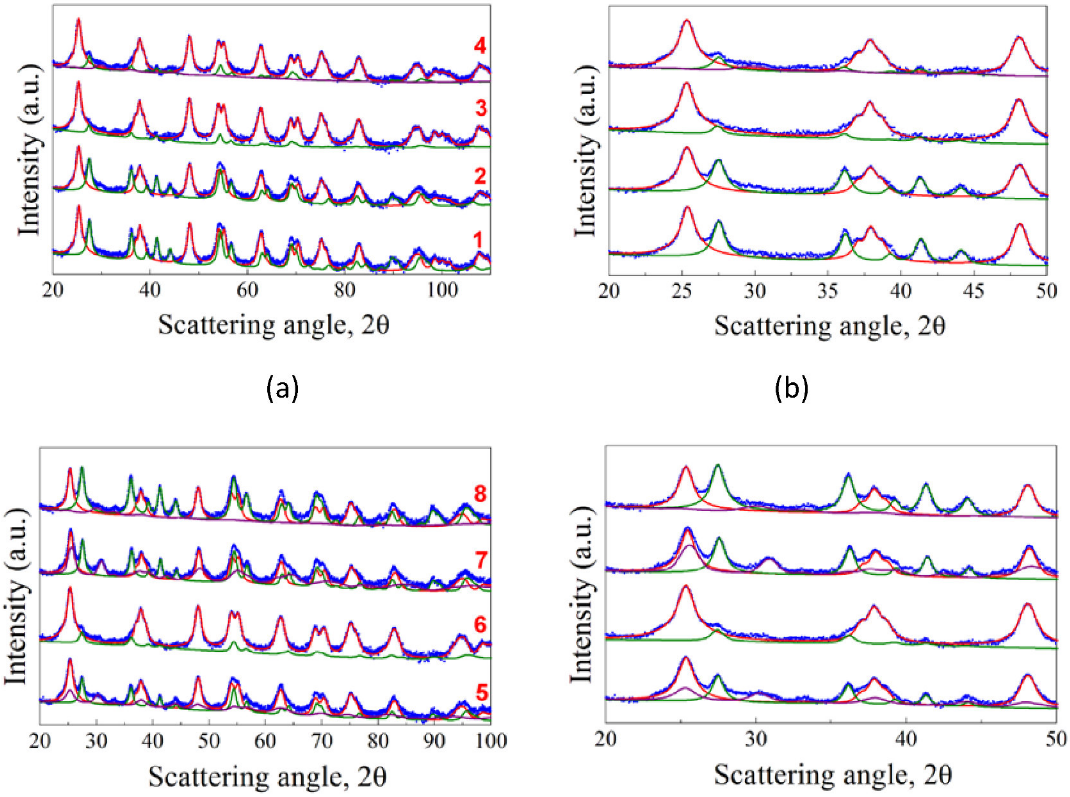

(a) (b)

(c) (d)

Fig. 3.16: (**a**) XRPD patterns of samples 1–4; (**b**) details at low angles for samples 1–4; (**c**) XRPD patterns of samples 5–8; (**d**) details at low angles for samples 5–8

Table 3.7: Relative phase composition and crystallite diameters determined by Rietveld method for samples 1–8 and P25.

Samples	% anatase	% rutile	% brookite	Anatase/Rutile/Brookite average crystallite diameter (nm)
1	70	30	-	20.6/22.0
2	64	36	-	18.3/18.5
3	97	3	-	18.1/15.9
4	91	9	-	18.8/12.7
5	65	21	14	18.5/19.6/8.3
6	70	19	11	19.0/15.0/8.6
7	43	32	25	20.6/23.8/20.1
8	36	61	3	21.0/23.0/13.0
P25	83	17	-	35.0/52.5

The XRD patterns of the samples 5–8 are presented in Fig. 3.16 c. Differently from the previous samples, the brookite polymorph appears when using $Ti(O^iPr)_4$ as titanium precursor. The presence of brookite as a polymorph, together with anatase and rutile, through a sol-gel route has already been reported previously in literature [164, 165]. The crystallite sizes are again in the range of 18–20 nm for both anatase and rutile, while they are more variable for brookite, ranging from 8 to 20 nm (Table 3.7). As already said before, no evidence of a direct influence of acetylacetone addition and of the calcination rate variation on the crystallite content can be deduced. P25 is reported for comparison and it can be seen that the A:R ratio is 83/17 while the crystallite size is much bigger than that of our samples, being 35.0 and 52.5 nm for A and R, respectively.

---

[164] S.Musić, M. Gotić,, M. Ivanda, S. Popović, A. Turković, R. Trojko, A. Sekulić, K. Furić, *Materials Science and Engineering B* **1997**, *47*, 33

[165] C. C. Wang, J. Ying, *Chemistry of Materials* **1999**, *11*, 3113

3.1.2.2 Transmission Electron Microscopy (TEM)

Representative TEM images of samples 2 and 3 are reported in Fig. 3.17. Both samples show a highly porous structure: although they are not morphologically homogeneous, they display an appreciable order in the channels orientation in some regions of the powders, especially in sample 3 (Fig. 3.17 c).

Samples 1–4, synthesized from $TiCl_4$ and $Ti(OBu)_4$, show a similar morphology though no long range pore order can be detected. These powders possess a homogeneous particles distribution in the range of 10–30 nm.

To better understand the crystalline domains, TEM images were taken also at higher resolutions (Fig. 3.17 b,d), thus allowing to appreciate the high crystallinity degree of the particles, that possess a rectangular shape associated with a truncated bipyramid with the longer axis parallel to the electron beam [153].

Samples 5 and 6 (sample 6 is reported in Fig. 3.18), obtained by using $Ti(O^iPr)_4$ and HCl, have a porous morphology and a high crystallinity degree (Figure 3.18 b). Their porous structure, displayed in TEM image of Fig. 3.18 a, shows an agglomerate of particles where it is not possible to appreciate the same channel periodicity observable in Fig. 3.17 c.

On the contrary, samples 7 and 8, also prepared from $Ti(O^iPr)_4$ and HCl too, show a significantly different morphology of both the mesoporous framework and the crystallite shape. In Fig. 3.19 it is clearly possible to see the different nature of samples 7 and 8, that alternates mesoporous aggregates with much denser titania rods with a diameter of 0.5 µm, thus reducing the degree of communication between the particles. At higher resolutions, we can appreciate the difference in the crystals morphologies, characterized by a needle-like shape particles of 10–20 nm. This difference can be due to the presence of added water in the set of samples from 5 to 8, together with hydrochloric acid, that could have led to a faster hydrolysis-condensation process of the titanium precursors that did not have enough time to surround P123 micelles before starting to form titania particles.

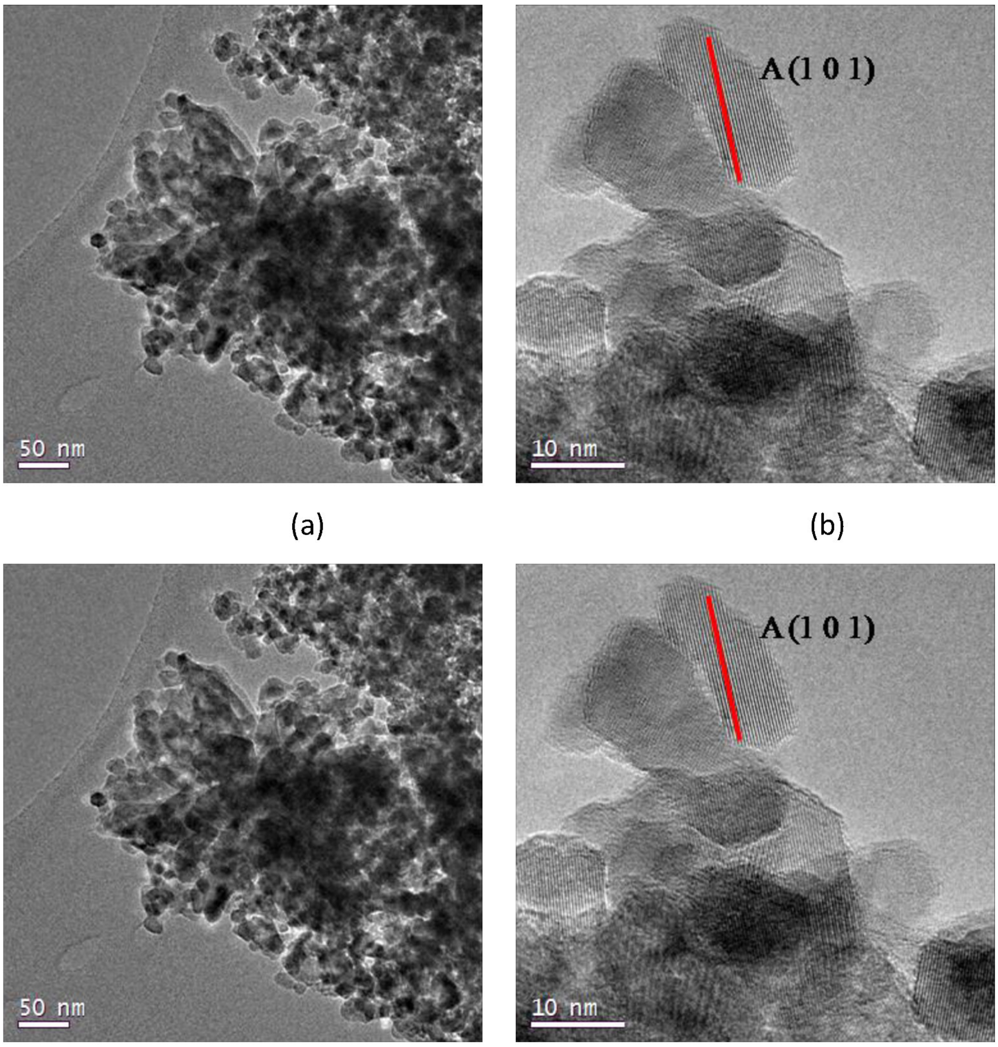

(a) (b)

(c) (d)

Fig. 3.17: (**a**) TEM images of sample 2; (**b**) detail at high resolutions for sample 2; (**c**) TEM image of sample 3; (**d**) detail at high resolution for samples 3

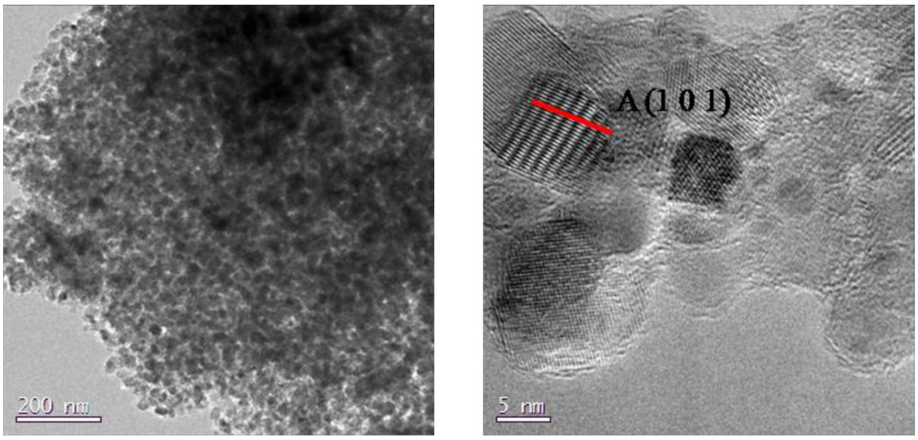

(a) (b)

Fig. 3.18**:** (**a**) TEM images of sample 6; (**b**) detail at high resolutions for sample 6

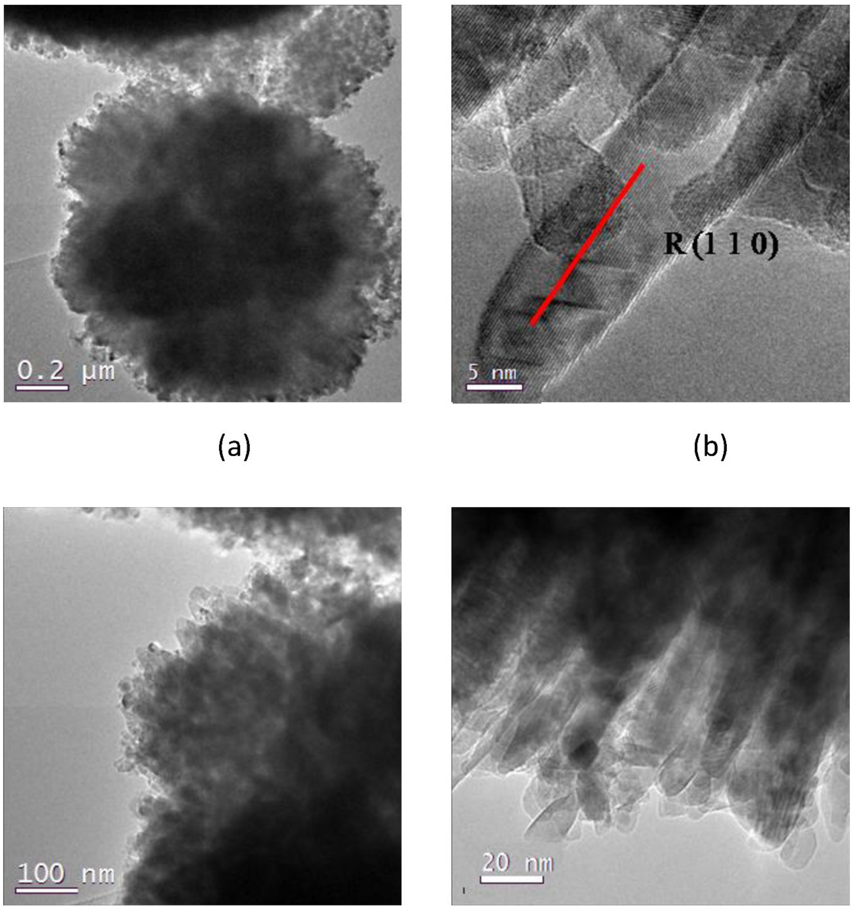

(a) (b)

(c) (d)

Fig. 3.19. (**a**) TEM images of sample 7; (**b**) detail at high resolutions for sample 7; (**c**) TEM image of sample 8; (**d**) detail at high resolution for sample 8.

P25 was analyzed by means of comparison, and in Fig. 3.20 it is possible to see that it is composed of anatase and rutile particles, analyzed by electron diffraction, with a 20–40 nm diameter and characterized by the same rhombic and square-like morphology of our samples. The samples 1–8 possess worm-like channels (not displayed here) instead of hexagonally arranged mesopores, thus suggesting a quick gelation in which the self-assembly of P123 micelles is not completed [153].

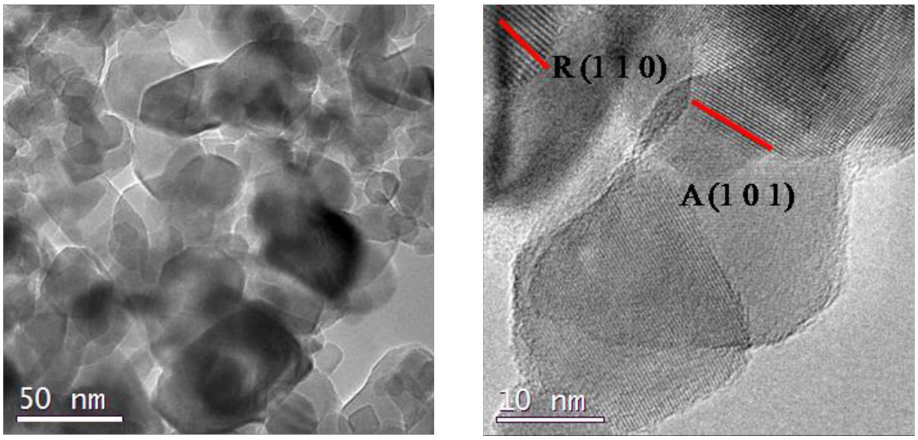

(a) (b)

Fig. 3.20: (**a**) TEM images of P25; (**b**) detail at high resolutions for P25.

3.1.2.3 N$_2$ Physisorption

N$_2$ physisorption isotherms and pore size distribution plots of all the synthesized samples are depicted in Fig. 3.21 and 3.22 respectively, with the pore size distribution in Fig. 3.23 and 3.24. BET (Brunauer, Emmett, Teller) surface areas vary from 90 to 117 m^2/g except for samples 7 and 8, where a significant reduction to 72 and 78 m^2/g, occurs (see Table 3.8). All the samples show a type IV isotherm characteristic of mesoporous materials [157] while P25 (Fig. 3.25) possess a type II isotherm with a H3-type hysteresis loop typical of macroporous materials. The specific surface area corresponds to 38 m^2/g, with a large pore size distribution ranging from 10 to 1000 nm.

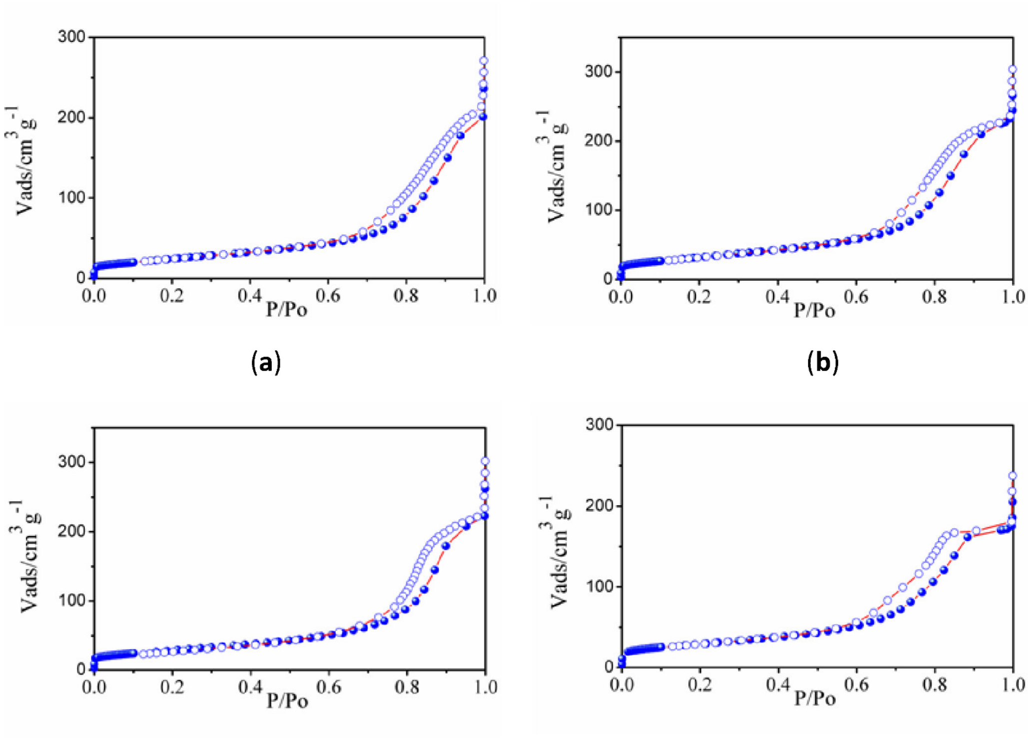

(a) (b)

(c) (d)

Fig. 3.21: N$_2$ physisorption isotherms of samples (**a**) 1 (**b**) 2 (**c**) 3 (**d**) 4 .

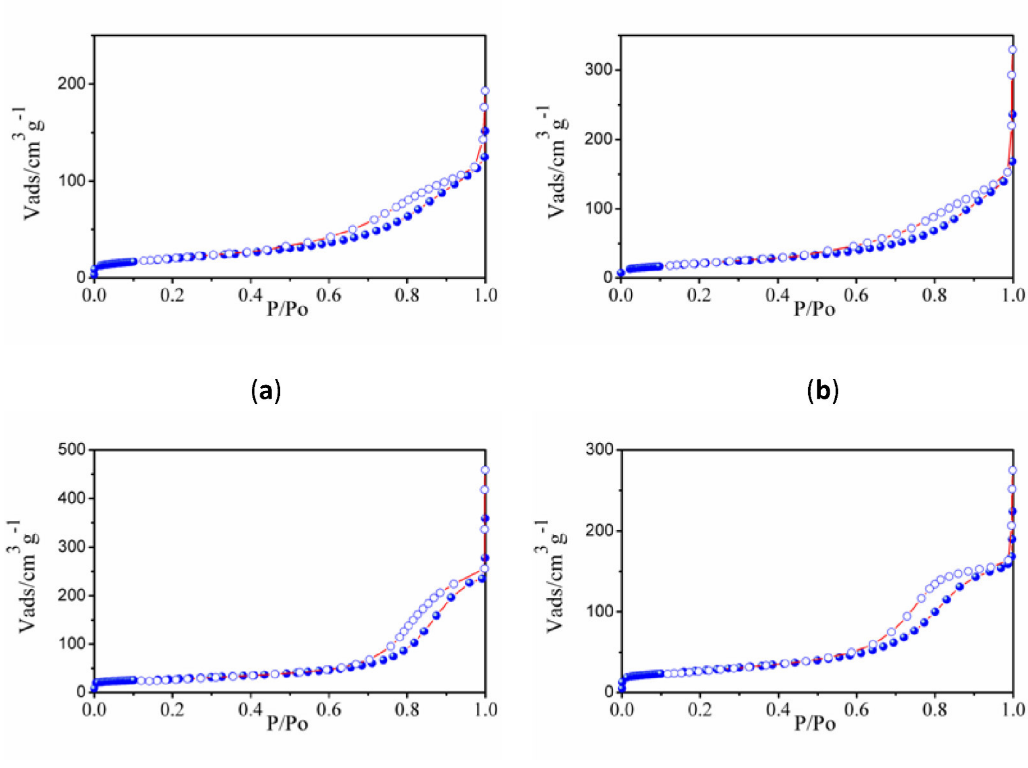

(a) (b)

(c) (d)

Fig. 3.22: N$_2$ physisorption isotherms of samples (**a**) 5 (**b**) 6 (**c**) 7 (**d**) 8

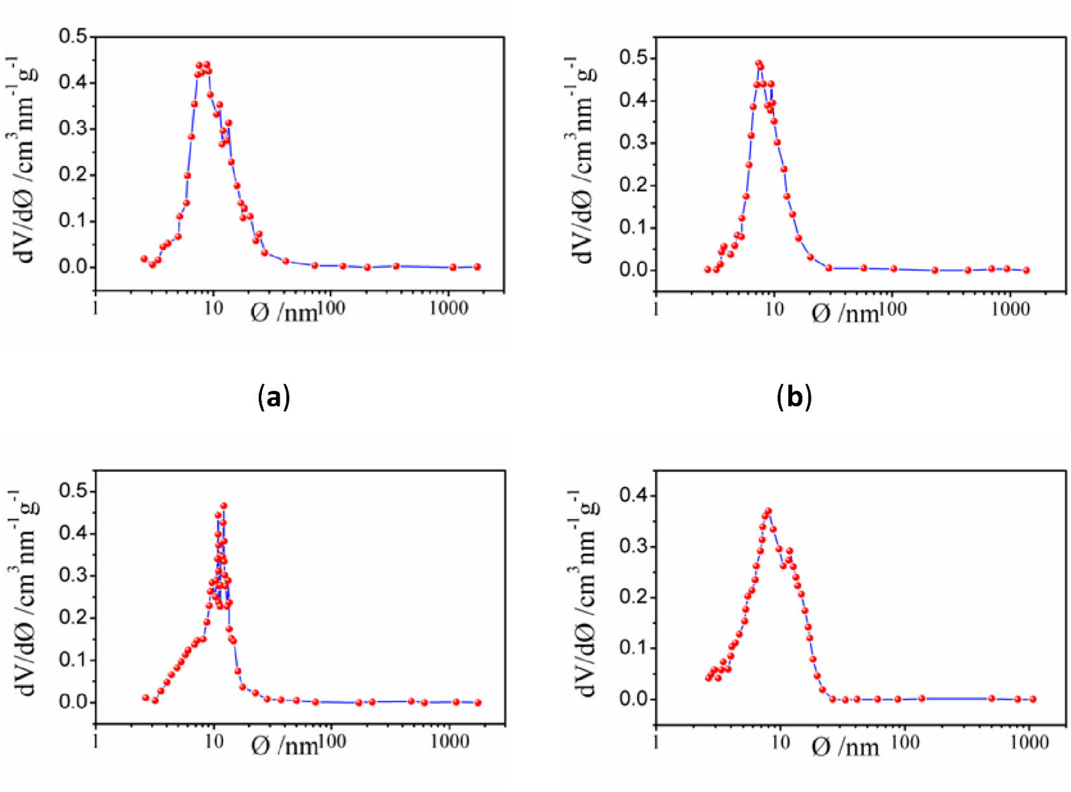

(**a**) (**b**)

(**c**) (**d**)

Fig. 3.23: pore size distribution plots for samples (**a**) 1 (**b**) 2 (**c**) 3 (**d**) 4.

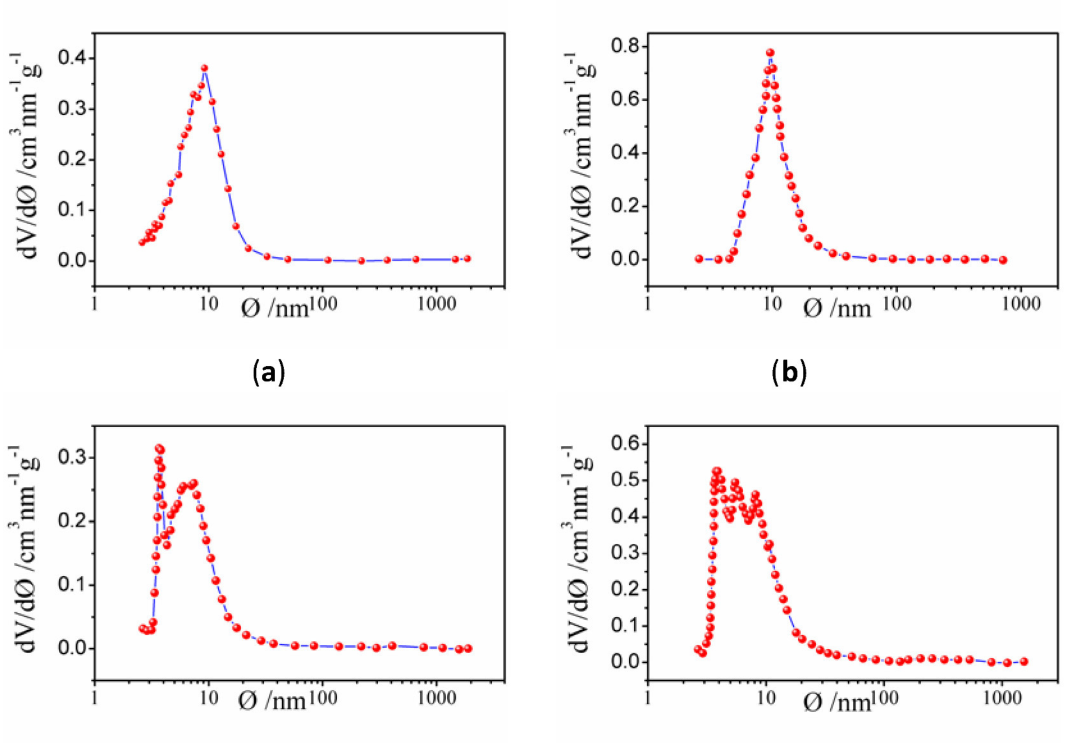

(**a**) (**b**)

(**c**) (**d**)

Fig 3.24: pore size distribution plots for samples (**a**) 5 (**b**) 6 (**c**) 7 (**d**) 8.

The hysteresis loops of samples 1–4 are a H2-type, while those belonging to samples 5–8 are in the middle between a H2- and a H4-type, often associated with narrow slit-shaped pores, thus suggesting a different pore structure between the two sets of samples, in accordance with TEM analysis.

All the pore size distribution plots (Fig. 3.23 and 3.24) present large peaks centered between 7 and 9 nm, thus in good agreement with the expected mesopore sizes when an amphiphilic triblock copolymer like Pluronic P123 is used (in the range of several nanometers to 10 nm) [156]. However, some exceptions can be underlined: a shift toward smaller diameters can be appreciated for samples 7 and 8 (around 3 nm) and this is probably due, as already said, to both a quick hydrolysis-condensation process during gelation and to a subsequent collapse of the partially formed mesostructure during calcination [154, 155].

The large distribution of the pore sizes has probably two different causes: the first one, as already mentioned, is the incomplete formation of the mesostructure that leads to a disordered mesoporous morphology, and the second one is the presence of both inter-particle pores and assembled pores [159]. As a matter of fact, in the synthesized powders it is possible to find two different types of pores, namely the interparticle pores formed from the packing of neighboring particles and the assembled pores that represent the position previously occupied by the surfactant P123.

A really ordered mesostructure is obtained only when interparticle and assembled pores are of the same size, but in our powders this aim is not achieved because of the previously illustrated issues. However it is worth mentioning the distribution of sample 3: in this case the peaks are more defined and narrow and are centered at around 12 nm, which is a higher value with respect to other samples. In this sample interparticles and assembled pores are closer in size, leading to a higher degree of communication between particles and to a more ordered structure.

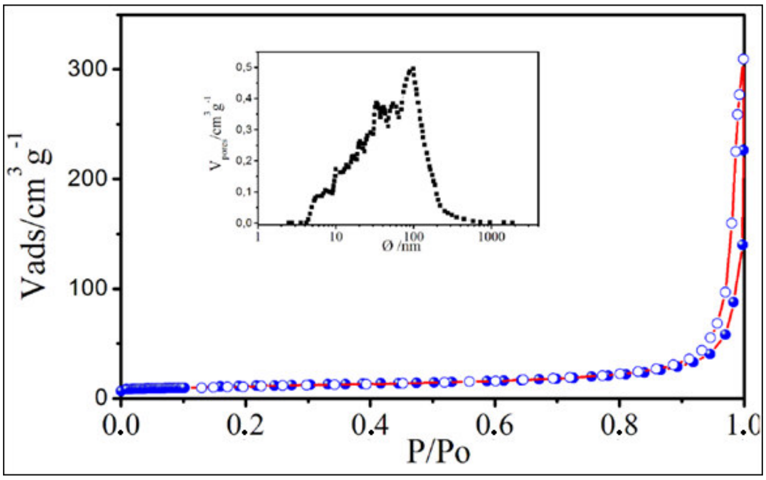

Fig. 3.25: N_2 physisorption isotherms of P25. The pore size distribution is depicted in the insert figure

Table 3.8: BET (Brunauer, Emmett, Teller) surface area, pore volume and size for samples 1–8 and P25.

Samples	**BET surface area (m^2/g)**	**Pore volume (cm^3/g)**	**Pore size (nm)**
1	90	0.43	8.8
2	117	0.49	7.4
3	103	0.48	12.2
4	103	0.37	8.0
5	96	0.42	9.4
6	96	0.73	9.7
7	72	0.30	3.7
8	78	0.52	3.8
P25	39	0.47	98.0

3.1.2.4 UV-Vis Spectrophotometry

UV-Vis absorption spectra were recorded on the electrodes and the response can be seen in Fig. 3.26. In all the spectra a strong sharp increase in absorption appears at about 360 nm and ends with a peak at about 300 nm, corresponding to the titania semiconductor. The band gap values (Table 3.10) were calculated from the onset of the wavelength (λ_{onset}) identified by the tangent method. The band gap varies from 3.18 to 3.55 eV. These values are higher than those reported in literature for bulk titania (3.02 eV for rutile and 3.20 eV for anatase) [166] and this is attributed to the small size of our titania nanocrystallites (quantum-size effect) [162]. The broad absorption bands in the visible region (550–400 nm) are attributable to interference colors resulting from the thickness of the films [167].

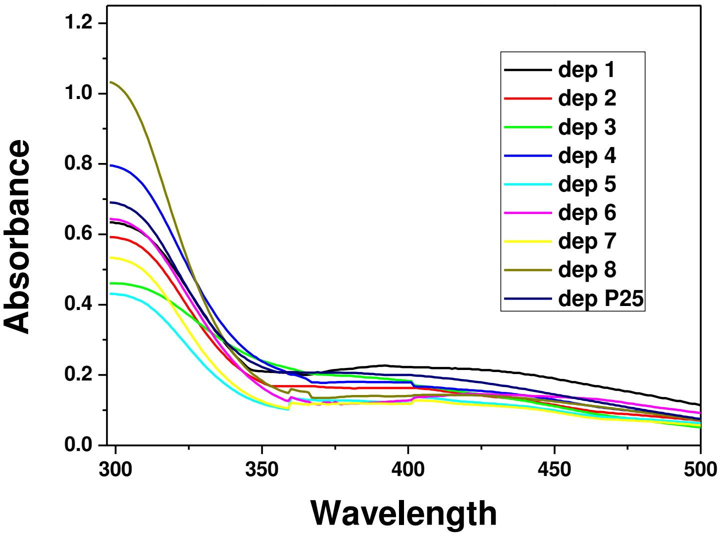

Fig. 3.26: UV-Vis spectra (electronic spectra in the ultraviolet and visible region) of samples 1–8 and P25.

---

[166] M.R. Hoffman, S.T. Martin, W. Choi, D.W. Bahnemann, *Chemical Reviews* **1995**, 95, 69

[167] K.L. Frindell, M.H. Bartl, A. Popitsch, G.D. Stucky, *Angewandte Chemie* **2002**, 114, 1002

Table 3.10**:** λ_{onset} and band gap from UV-Vis (UltraViolet-Visible) spectra of samples 1–8 and P25.

Samples	**λ_{onset} (nm)**	**Band gap (eV)**
1	362	3.41
2	363	3.42
3	388	3.18
4	359	3.44
5	351	3.53
6	361	3.43
7	354	3.47
8	349	3.55
P25	361	3.44

3.1.2.5 Photoelectrochemistry

The films were then tested as photoelectrodes for the water splitting reaction. Linear Sweep Voltammetry was used to record (photo)current density-applied voltage responses in a 1 M NaOH solution at a scan rate of 5 mV/s. The ending potential of the measurements, both in the dark and under 1 sun illumination power (AM1.5G), was chosen from previous scans in the dark to avoid electrochemical oxidation of water due to a raising concentration of holes in titania valence band.

The curves registered under illumination are presented in Fig. 3.27 a, the curves registered under chopped light for sample 3, 7, and for P25, are reported in Fig. 3.27 b and the photocurrent densities at 0 V bias vs Ag/AgCl are in Table 3.11. P25, one of the most photoactive titania powders so far, gives a current of 105 µA/cm^2. Almost all the samples give responses from 30 to 55 µA/cm^2 but two exceptions can be appreciated. Sample 7, synthesized from $Ti(O^iPr)_4$ and HCl without the addition of acetylacetone, is the one that gives far the worst result in photoactivity, while sample 3 ($TiCl_4$, $Ti(OBu)_4$ and acetylacetone) demonstrates to be even better than P25 with a photocurrent value of 134 µA/cm^2. By analyzing the differences between these two samples, 3 and 7, we saw that sample 3 is the one with the highest amount of anatase (Table 3.11), which is known to be the most photoactive titania polymorph, while sample 7 is not the one with the lowest anatase content, but it reveals the highest amount of brookite which probably reasons the low photoactivity of the sample itself. Although the role of brookite in titania photoactivity has never been deeply studied, some authors found that, together with anatase, brookite leads to high photocatalytic performances in *n*-pentane oxidation [168], but in our case the contemporary presence of rutile may play an important role by establishing interactions with the two other phases that are not fully clarified yet. Focusing on the surface area (Table 3.11), sample 3 has a high area but not the highest one, which was of sample 2. The pore volume (Table 3.11) is not negligible with 0.48 cm^3/g but is quite low in respect to sample 6, 0.73 cm^3/g or even to sample 7 (0.52 cm^3/g). The main difference lays in the much narrower pore size distribution (inset Fig. 3.23 c) and the bigger pore diameters (12 nm). All these considerations lead to the conclusion that not only a high content of brookite may worsen the photocatalytic activity, but also that neither the pore volume nor the surface area play a key role in the electrodes performances; the most important parameter seems to be the homogeneous intra- and inter-particles pore distribution, which probably leads to an optimized mass transfer and, as a consequence, to a better photoactivity.

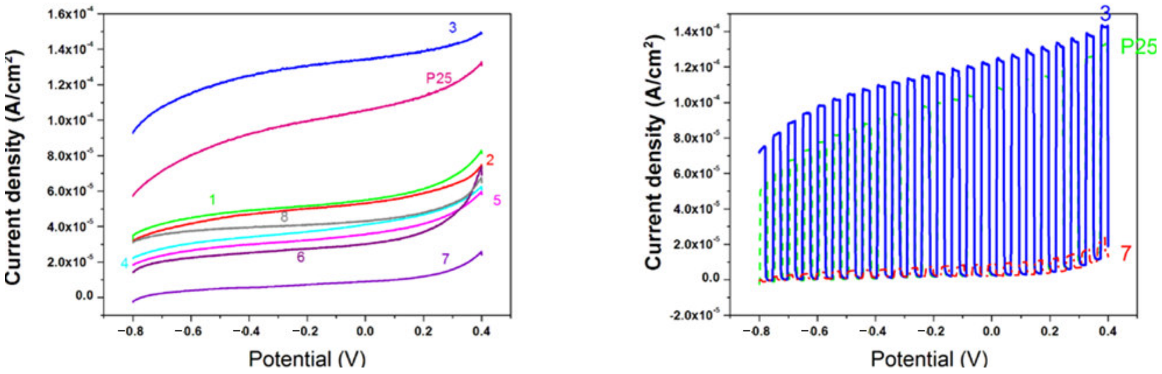

Fig. 3.27: (**a**) J-V curves under illumination for samples 1–8 and P25. WE = TiO_2/ITO, RE = Ag/AgCl, CE = Pt, NaOH 1M, 5 mV/s; (**b**) J-V curves under chopped light for samples 3, 7, and P25. WE = TiO_2/ITO, RE = Ag/AgCl, CE = Pt, NaOH 1M, 5 mV/s.

---

[168] J.C. Yu, L.Z. Zhang, J.G. Yu, *Chemistry of Materials* **2002**, 14, 4647

Table 3.11: current densities at 0 V *vs.* Ag/AgCl for samples 1–8 and P25.

Samples	**J (μA/cm^2)**
1	55
2	53
3	134
4	41
5	36
6	30
7	9
8	43
P25	105

The electrodes were then tested by exposing them, in the electrochemical cell, to a chopped light under 0 V bias for an hour while monitoring the photocurrent profile. All the electrodes lost no more than 5% of their initial current, showing good mechanical resistance between the powders and the conductive substrate (ITO) and good chemical stability, all precious characteristics for a future application.

3.2 Chromophores

The result and discussion part on the chromophores will be first divided in paragraphs on the base of the presence of one or two ethynyl moieties on a bithiophene backbone. In each paragraph presentation of the electrochemical characterisation of monomers and polymers and a final discussion on the data will be given. Finally, comparisons between analogues compounds bearing one or two ethynyl groups will be given.

3.2.1. Chromophores bearing one ethynyl group on the bithiophene backbone

3.2.1.1 Characterisation

3.2.1.1.1 Monomers

The compounds synthesised following the procedures reported in the experimental part, have been characterised through cyclic voltammetry on a Pt working electrode (2 mm diameter), with an Ag/AgCl working electrode and graphite as counterelectrode, with a 100 mV/s scan rate. The responses were recorded with a 5*10-3 M analyte concentration in $CH_3CN/TEAPF_6$ (tetraethylammonium hexafluorophosphate) 0.1 M or in $CH_2Cl_2/TEAPF_6$ 0.1 M when specified.

3.2.1.1.1.1 4,4’-dibromo-2,2’-bithiophene (Br-BT-Br)

Characterisation in CH_3CN

In Fig 3.28 it is possible to see an anodic peak at +1.74 V that can be assigned to bithiophene oxidation; the process is reversible as demonstrated by the peak at +1.34 V. Subsequent scans around the anodic peak show the increase in current values (Fig. 3.29) and the contemporary growth of a red polymeric film on the working electrode.

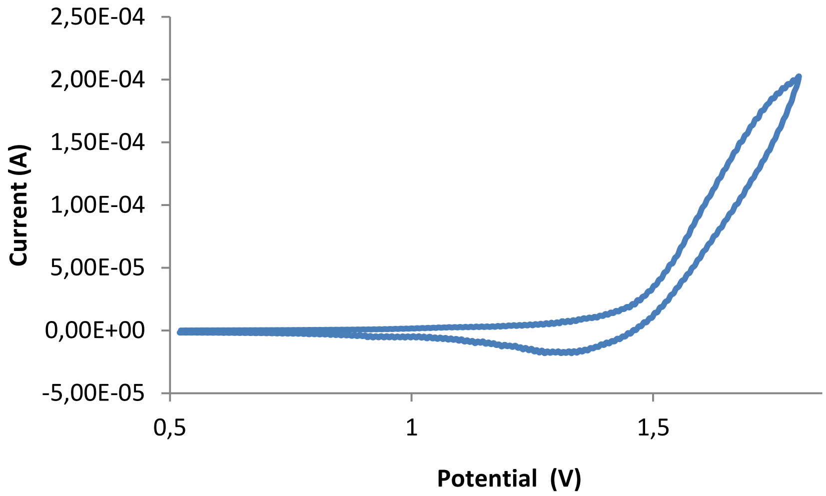

Fig. 3.28: cyclic voltammetric response of a 5*10^{-3} M solution of Br-BT-Br in CH_3CN/$TEAPF_6$ 0.1 M; WE: Pt, RE, Ag/AgCl, CE: graphite bar; v = 100 mV/s.

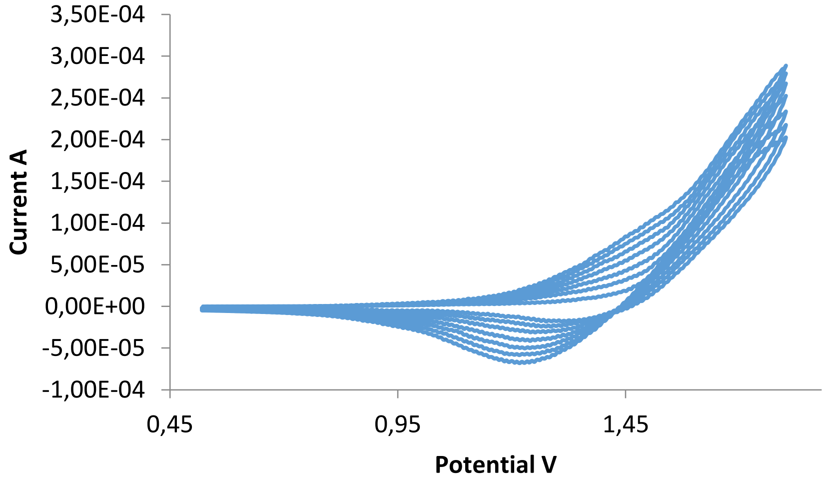

Fig. 3.29: cyclic voltammetric response of a 5*10^{-3} M solution of Br-BT-Br in CH_3CN/$TEAPF_6$ 0.1 M; WE: Pt, RE, Ag/AgCl, CE: graphite bar; v = 100 mV/s.

Characterisation in CH_2Cl_2

The same voltammetric profile was obtained for the characterisation of Br-BT-Br in CH_2Cl_2, where the anodic peak was at +1.76 V and the associated peak was at +1.07.

A red polymeric film formed after various cycles around the oxidation peak.

3.2.1.1.1.2 4-(4'-bromo-2,2'-bithiophenyl)-2-methyl-3-butyn-2-ol (Br-BT-OH)

Characterisation in CH_3CN

In the response in Fig. 3.30 an anodic peak can be seen at +1.51 V with a not perfectly defined associated peak at +1.21 V.

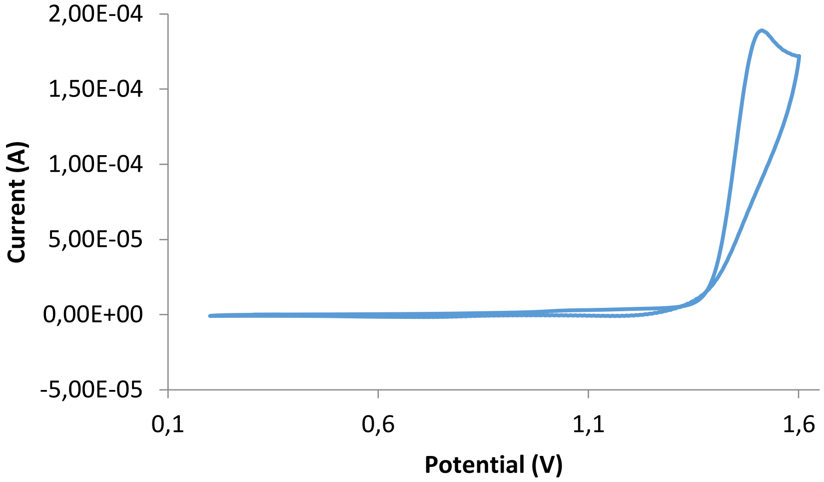

Fig. 3.30 : cyclic voltammetric response of a $5*10^{-3}$ M solution of Br-BT-OH in $CH_3CN/TEAPF_6$ 0.1 M; WE: Pt, RE, Ag/AgCl, CE: graphite bar; v = 100 mV/s.

When cycling around the anodic peak between +0.2 and +1.6 V it is possible to see a current increase (Fig. 3.31) and the formation of a red polymeric film.

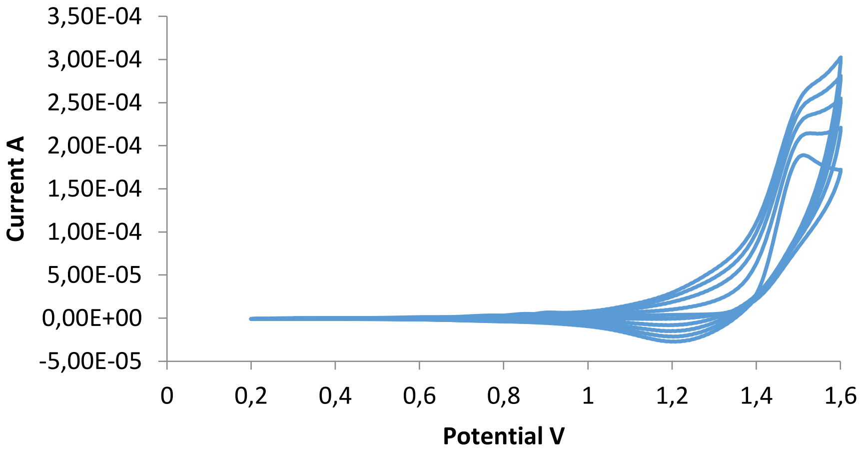

Fig. 3.31: cyclic voltammetric response of a $5*10^{-3}$ M solution of Br-BT-OH in $CH_3CN/TEAPF_6$ 0.1 M; WE: Pt, RE, Ag/AgCl, CE: graphite bar; v = 100 mV/s.

3.2.1.1.1.3 4-4'-(2,2'-bithiophenyl)bis(2-methyl-3-butyn-2-ol) (OH-BT-OH)

Characterisation in CH_3CN

In the response in Fig. 3.32 an anodic peak at +1.43 V can be seen and can be attributed to bithiophene oxidation.. Subsequent scans allow to observe the constant increase of anodic currents (Fig. 3.33) and the contemporary formation of a red polymeric film on the electrode.

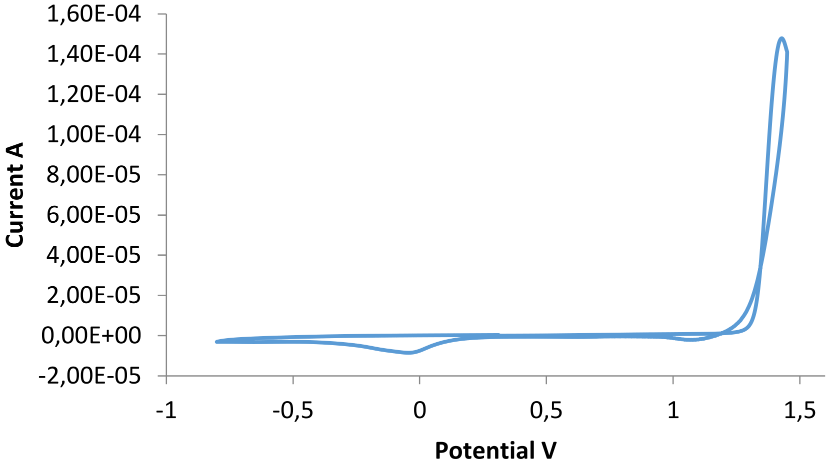

Fig 3.32: cyclic voltammetric response of a $5*10^{-3}$ M solution of OH-BT-OH in $CH_3CN/TEAPF_6$ 0.1 M; WE: Pt, RE, Ag/AgCl, CE: graphite bar; v = 100 mV/s.

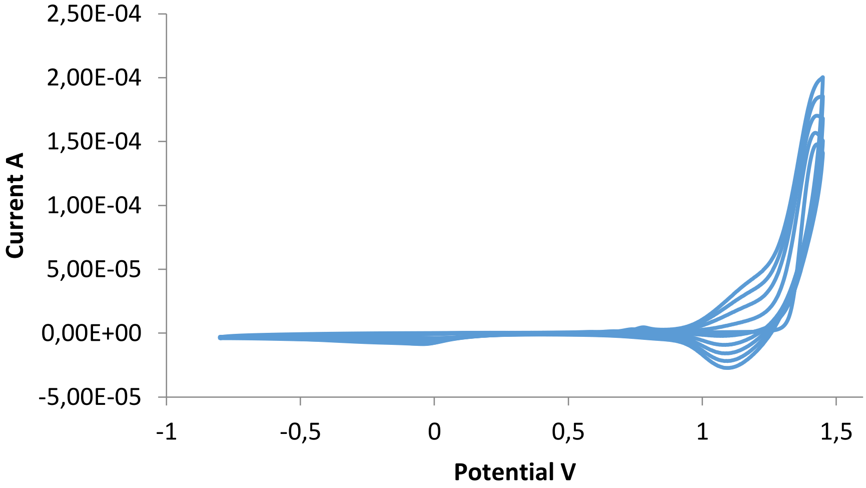

Fig. 3.33: cyclic voltammetric response of a $5*10^{-3}$ M solution of OH-BT-OH in $CH_3CN/TEAPF_6$ 0.1 M; WE: Pt, RE, Ag/AgCl, CE: graphite bar; v = 100 mV/s

3.2.1.1.1.4 4-bromo-(4’-ethynyl)-2,2’-bithiophene (Br-BT-Et)

Characterisation in CH_3CN

In Fig. 3.34 an anodic process at +1.56 V is visible.

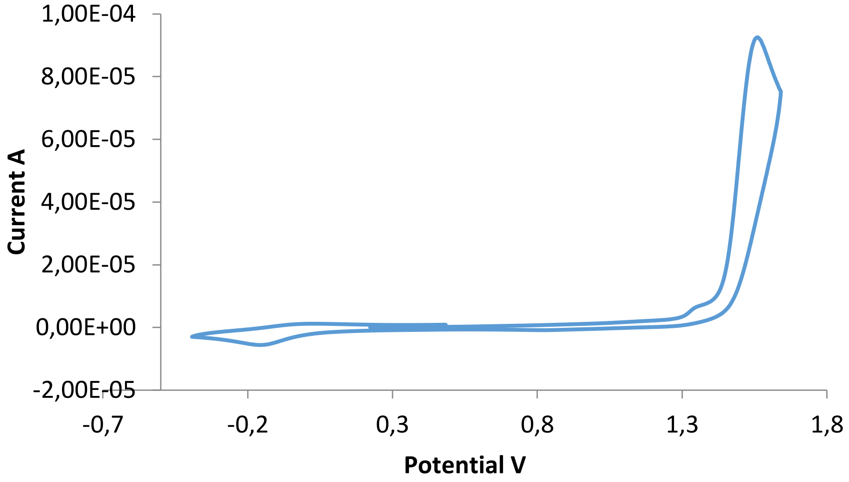

Fig. 3.34: cyclic voltammetric response of a $5*10^{-3}$ M solution of Br-BT-Et in $CH_3CN/TEAPF_6$ 0.1 M; WE: Pt, RE, Ag/AgCl, CE: graphite bar; v = 100 mV/s.

When cycling around the anodic potential, the peak shifts towards more anodic potentials and, after the third scan, the system becomes instable.

3.2.1.1.1.5 4-(4’-bromo-2,2’-bithiophenyl)-N,N’-diphenylaniline (Br-BT-TPA)

Characterisation in CH_3CN

In Fig. 3.35 four anodic peaks can be seen. The first three are centred at +0.88 V, +1.00 V and +1.06 V respectively with an associated peak at +0.77 V. From the comparison between the voltammogram of Br-BT-Br and from literature data [169], these peaks can be attributed to the oxidation of the TPA moiety. In particular, the sharp profile of the second peak (1.00 V) can be related to an adsorption process on the electrode surface. For subsequent scans

---

[169] C.H. Yang, H.L. Chen, C.P. Chen, S.H. Lian, H.A. Hsiao, Y.Y. Chuang, H.S. Hsu, T.L. Wang, Y.T. Shieh, L.Y. Lin, Y.C. Tsai, *Journal of Electroanalytical Chemistry* **2009**, 631, 43

(Fig. 3.36), the second peak seems to disappear and only two large peaks, centered at +0.88 V and +1.04 V, with an associated peak at +0.77 V, can be seen. Finally, the more anodic peak at +1.62 V, with an associated one at +1.27 V, is attributed to the oxidation of the bithiophene fragment.

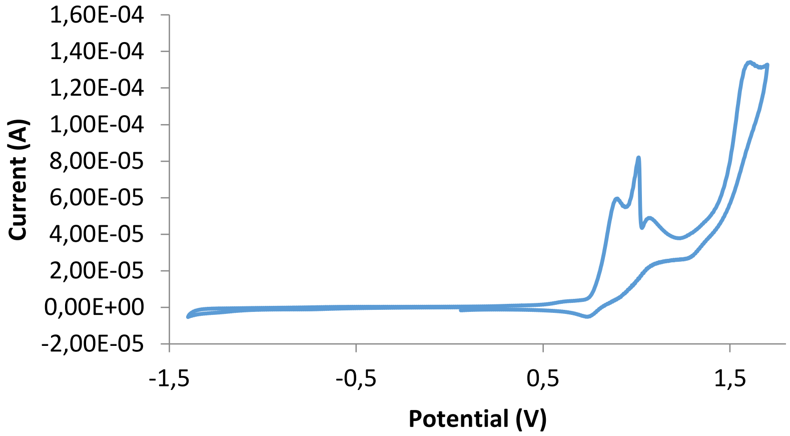

Fig. 3.35: cyclic voltammetric response of a $5*10^{-3}$ M solution of Br-BT-TPA in CH_3CN/$TEAPF_6$ 0.1 M; WE: Pt, RE, Ag/AgCl, CE: graphite bar; v = 100 mV/s.

When cycling between +0.1 V and +1.15 V, a slight increase of the current can be appreciated but no polymeric film can be seen on the electrode surface. We suppose that the presence of TPA substituent leads to the formation of oligomeric species that are probably soluble in the solvent system.

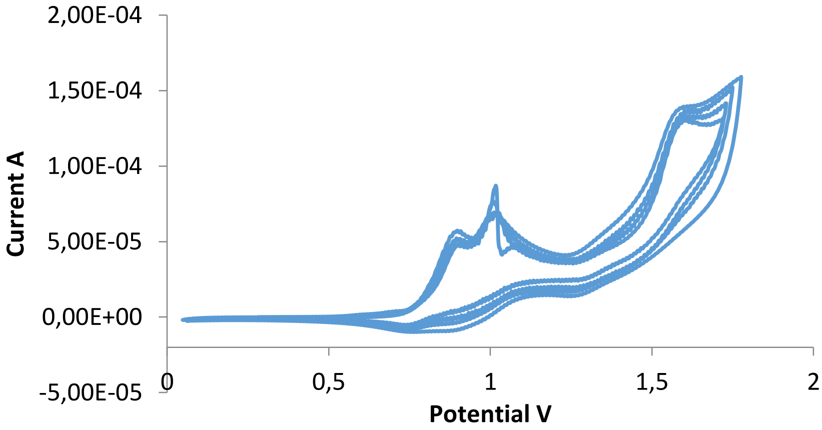

Fig. 3.36: cyclic voltammetric response of a $5*10^{-3}$ M solution of Br-BT-TPA in CH_3CN/$TEAPF_6$ 0.1 M; WE: Pt, RE, Ag/AgCl, CE: graphite bar; v = 100 mV/s.

3.2.1.1.1.6 4-(4'-(4-N,N'-biphenylamino)phenyl-2,2'-bithiophenyl)-2-methyl-3-butyn-2-ol (OH-BT-TPA)

Characterisation in CH_3CN

Three anodic peaks relative to the TPA fragment, at +0.88 V, +0.95 V and +1.04 V, with two associated peaks at +0.91 V and -0.20 V, can be seen in Fig. 3.37. The coupling of two radical cations, with a delocalised structure, that are formed during this potential interval, determines the formation of polymeric species in subsequent scans, together with the elimination of H^+ ions, whose reduction is responsible for the peak at -0.20 V. This hypothesis is confirmed by the following scans between -0.55 V and +1.15 V that highlight an increase in the peaks current values. However, the absence of a deposit on the electrode suggests a scarce adherence of the polymer or its solubility in the solvent.

Finally, the peak at +1.34 V, with an associated peak at +1.24 V, is due to the bithiophene oxidation, as confirmed by the current increase and by the formation of a film for subsequent scans between -0.1 V and +1.5 V (Fig. 3.38).

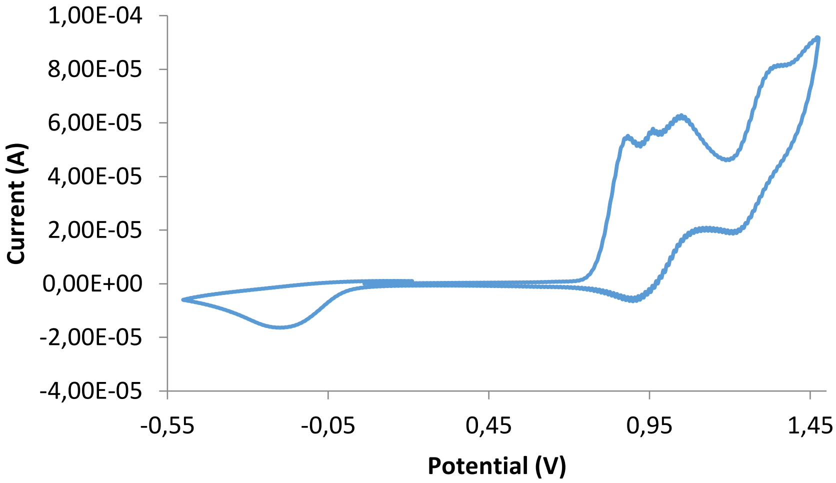

Fig. 3.37: cyclic voltammetric response of a $5*10^{-3}$ M solution of OH-BT-TPA in $CH_3CN/TEAPF_6$ 0.1 M; WE: Pt, RE, Ag/AgCl, CE: graphite bar; v = 100 mV/s.

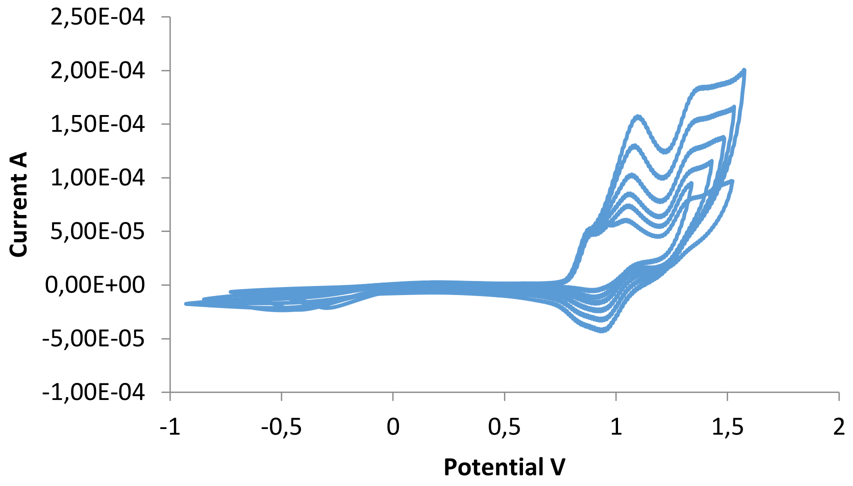

Fig. 3.38: cyclic voltammetric response of a 5*10^{-3} M solution of OH-BT-TPA in CH_3CN/$TEAPF_6$ 0.1 M; WE: Pt, RE, Ag/AgCl, CE: graphite bar; v = 100 mV/s.

3.2.1.1.1.7 4-(4’-ethynyl-2,2’-bithiophenyl)-N,N’-diphenylaniline (Et-BT-TPA)

Characterisation in CH_3CN

The response in Fig. 3.39 shows three anodic peaks at +0.87 V, +0.97 V and +1.04 V attributed to the TPA oxidation and with three associated peaks at +0.90 V, +0.73 V and -0.5 V. For different subsequent scans the three peaks tend to form only two peaks centered to +0.88 V and +1.05 V. The more anodic peak at +1.30 V is related to bithiophene oxidation and shows an associated peak at +1.24 V.

As for the alcoholic derivative OH-BT-TPA, for different scans an increase in the current is observed and the film formation occurs when scans arrive at the potentials relative to bithiophene oxidation (Fig. 3.40). For scans that stop before +1.30 V, no film can be observed but only an increase in current values.

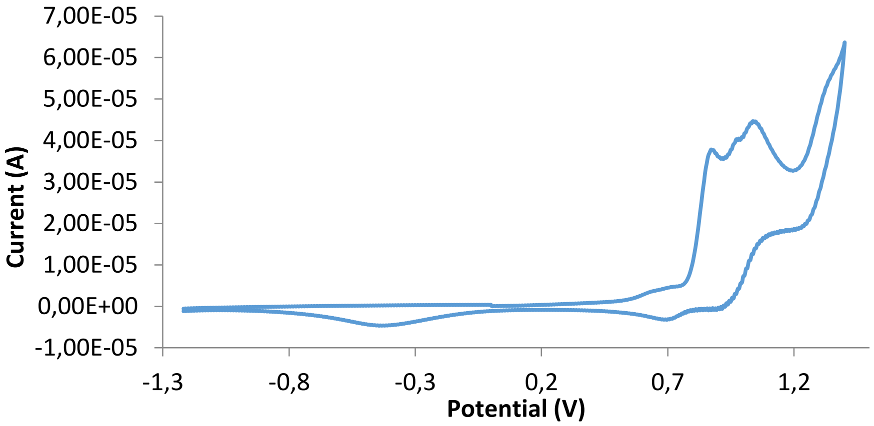

Fig. 3.39: cyclic voltammetric response of a 5*10^{-3} M solution of Et-BT-TPA in CH_3CN/$TEAPF_6$ 0.1 M; WE: Pt, RE, Ag/AgCl, CE: graphite bar; v = 100 mV/s.

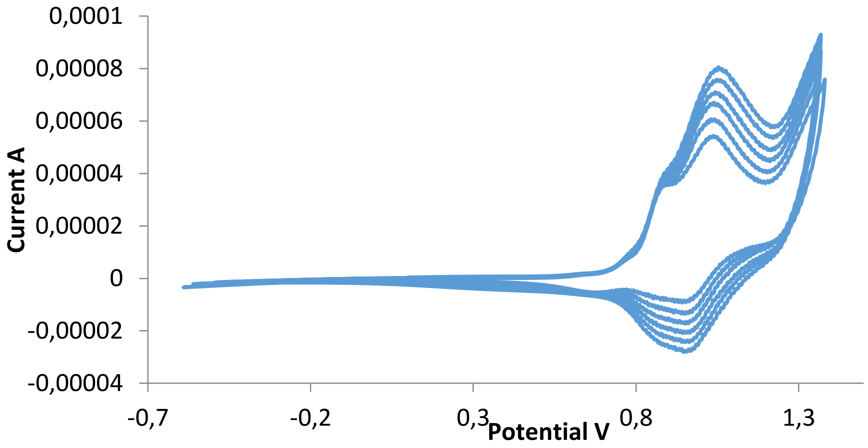

Fig. 3.40: cyclic voltammetric response of a 5*10^{-3} M solution of Et-BT-TPA in CH_3CN/$TEAPF_6$ 0.1 M; WE: Pt, RE, Ag/AgCl, CE: graphite bar; v = 100 mV/s.

Characterisation in CH_2Cl_2

To make a comparison with the terpyridine derivative Tpy-Et-BT-TPA, that is totally insoluble in CH_3CN, the ethynyl derivative has been characterised in CH_2Cl_2 (Fig. 3.41). In this solvent two not well-defined peaks at +1.0 V and +1.3 V, relative to TPA, with two associated peaks at +0.8 V and 0.0 V. The bithiophene oxidation is at +1.6 V with an associated peak at +1.23 V. After the second scan, the two peaks of TPA tend to combine in one peak, centered at +1.20 V, with an associated peak at +0.88 V (Fig. 3.42).

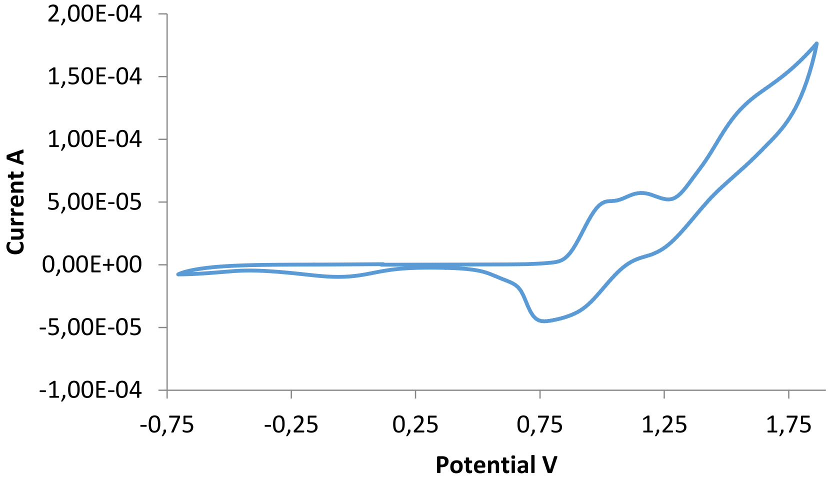

Fig. 3.41: cyclic voltammetric response of a 5*10^{-3} M solution of Et-BT-TPA in CH_2Cl_2/$TEAPF_6$ 0.1 M; WE: Pt, RE, Ag/AgCl, CE: graphite bar; v = 100 mV/s.

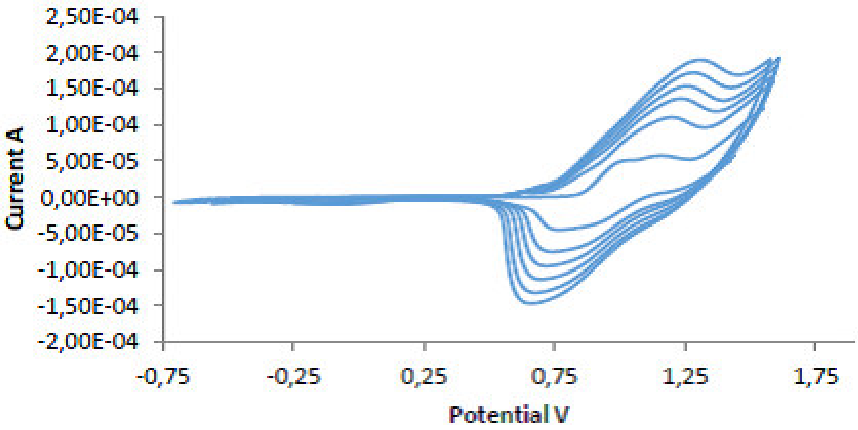

Fig. 3.42: cyclic voltammetric response of a 5*10^{-3} M solution of Et-BT-TPA in CH_2Cl_2/$TEAPF_6$ 0.1 M; WE: Pt, RE, Ag/AgCl, CE: graphite bar; v = 100 mV/s.

3.2.1.1.1.8 4’-(2,2’:6’,2’’-terpyridin-4’-ethynyl)-2,2’-bithiophenyl-4-N,N’-diphenylaniline (Tpy-Et-BT-TPA)

Characterisation in CH_2Cl_2

In Fig. 3.43 a very broad and ill-defined response at +0.88 V, with an associated peak at +0.8, and a peak at +0.99 V with an associated peak at +0.97 V, are both attributed to TPA oxidation. The more anodic peak at +1.32 V, associated peak at +1.27 V, is due to the bithiophene oxidation.

For subsequent scans (Fig. 3.44) an enlargement of the two less anodic peaks, with an increase in the current values is seen but with no deposition of a film on the electrode. A dark yellow film is formed when cycling around the peak of bithiophene oxidation.

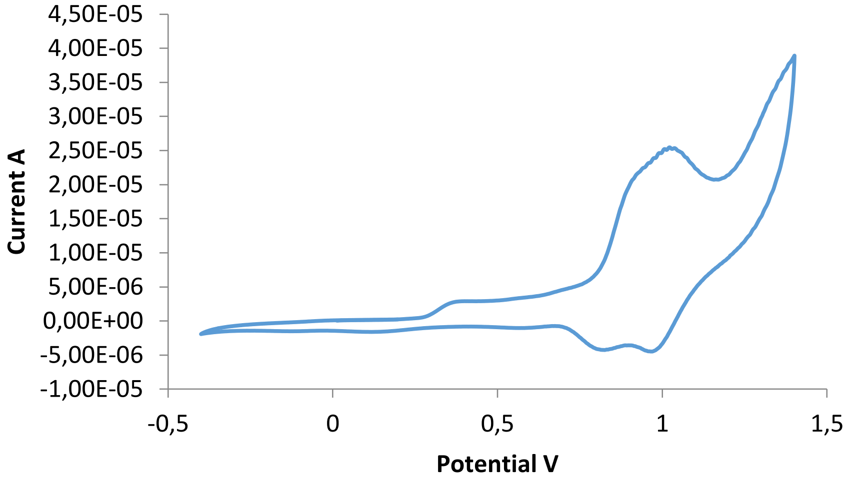

Fig. 3.43: cyclic voltammetric response of a $5*10^{-3}$ M solution of Tpy-Et-BT-TPA in $CH_2Cl_2/TEAPF_6$ 0.1 M; WE: Pt, RE, Ag/AgCl, CE: graphite bar; v = 100 mV/s.

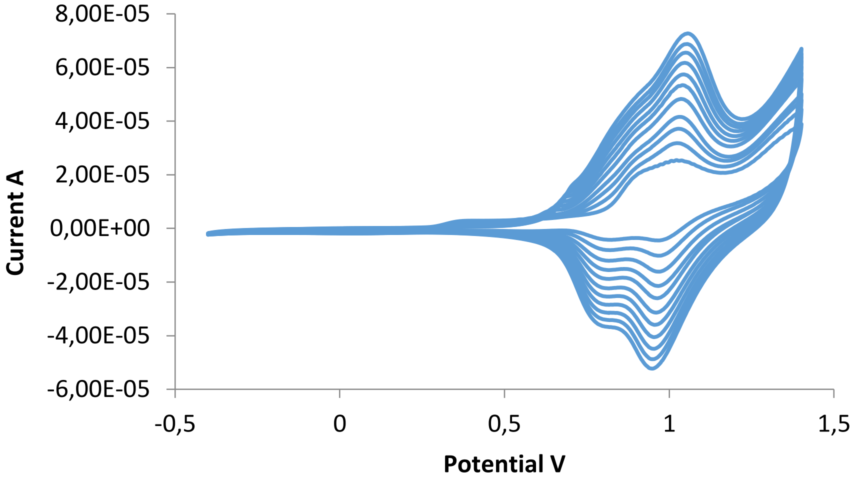

Fig. 3.44: cyclic voltammetric response of a 5*10^{-3} M solution of Tpy-Et-BT-TPA in CH_2Cl_2/$TEAPF_6$ 0.1 M; WE: Pt, RE, Ag/AgCl, CE: graphite bar; v = 100 mV/s.

3.2.1.1.2 Polymers

Monomers have been polymerised in a CH_3CN/TEAPF6 0.1 M or a CH_2Cl_2/$TEAPF_6$ 0.1 M on a Pt electrode through chronoamperometry, choosing the potential from the previously described voltammetric responses. The deposition time was chosen case by case as to obtain film with the same thickness. After the deposition step, all films were neutralised by keeping them at 0 V bias for 60 s.

The obtained polymers were characterised by means of cyclic voltammetry in CH_3CN/$TEAPF_6$ 0.1 M, with an Ag/AgCl reference electrode and a graphite counter electrode at 100 mV/s scan rate (see experimental).

3.2.1.1.2.1 poly- 4,4’-dibromo-2,2’-bithiophene, poly(Br-BT-Br)

Characterisation of the film obtained from a CH_3CN/$TEAPF_6$ 0.1 M solution

The characterisation was performed on a film deposited at +1.70 V for 60 s with a charge density corresponding to 490 nm in thickness.

In Fig. 3.45 an anodic process can be seen at around +1.66 V with an associated peak at +1.22 V, relative to p-doping and de-doping of the polymer, respectively.

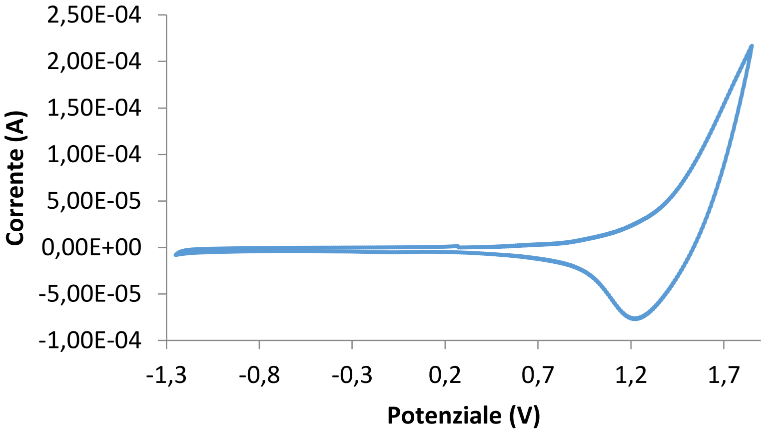

Fig. 3.45: cyclic voltammetric response of poly(Br-BT-Br) in CH_3CN 2/$TEAPF_6$ 0.1 M; WE: Pt, RE, Ag/AgCl, CE: graphite bar; v = 100 mV/s.

The UV-Vis spectra of the neutral film on ITO (120 nm in thickness) showed a large adsorption band centred at 500 nm.

3.2.1.1.2.2 poly- 4-(4'-bromo-2,2'-bithiophenyl)-2-methyl-3-butyn-2-ol, poly(Br-BT-OH)

Characterisation of the film obtained from a $CH_3CN/TEAPF_6$ 0.1 M solution

The characterisation was performed on a 420 nm film obtained with an applied potential of +1.47 V for 90 s, and then neutralized at 0 V for 60 s. In the anodic side (Fig. 3.46) a doping process can be seen at +1.25 V and the relative de-doping occurs at +1.20 V.

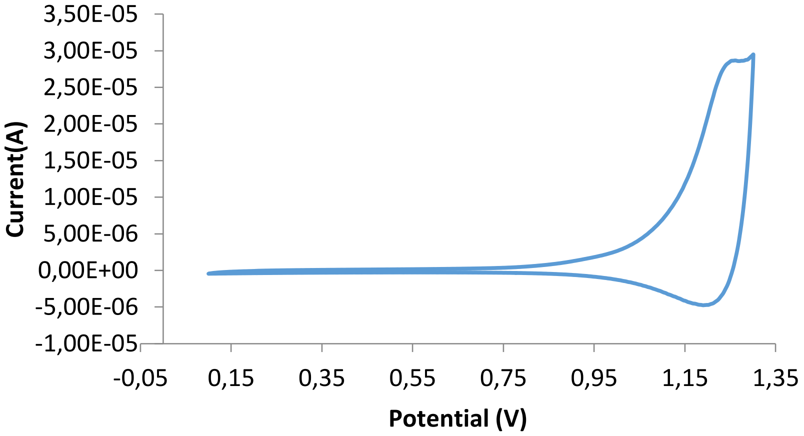

Fig. 3.46: cyclic voltammetric response of poly(Br-BT-OH) in CH_3CN /$TEAPF_6$ 0.1 M; WE: Pt, RE, Ag/AgCl, CE: graphite bar; v = 100 mV/s.

The deposition on ITO was done at 1.5 V in chronoamperometry for 60 s and then the film was neutralised at 0 V for 60 s (film of 130 nm in thickness). The absorption maxima was at 510 nm.

3.2.1.1.2.3 poly-4-4'-(2,2'-bithiophenyl)bis(2-methyl-3-butyn-2-ol), poly(OH-BT-OH)

Characterisation of the film obtained from a $CH_3CN/TEAPF_6$ 0.1 M solution

The characterisation was performed on a 420 nm film obtained with an applied potential of +1.48 V for 90 s and then neutralized at 0 V for 60 s In the anodic side a doping process can be seen at +1.26 V and the relative de-doping occurs at +1.18 V. The presence of a small peak at +1 V can be related to the presence of oligomeric species (Fig. 3.47).

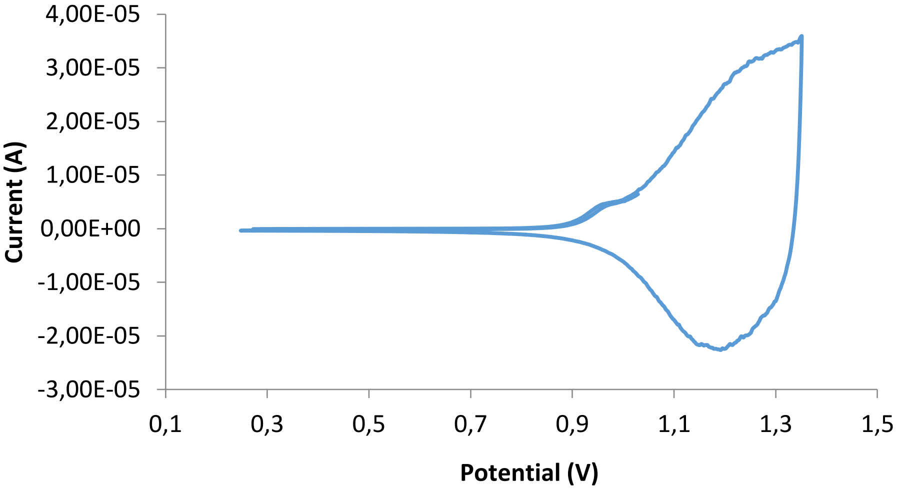

Fig. 3.47: cyclic voltammetric response of poly(OH-Bt-OH) in CH_3CN /$TEAPF_6$ 0.1 M; WE: Pt, RE, Ag/AgCl, CE: graphite bar; v = 100 mV/s. poly(OH-BT-OH)

3.2.1.1.2.4 poly-4-(4'-bromo-2,2'-bithiophenyl)-N,N'-diphenylaniline, poly(Br-BT-TPA)

Characterisation of the film obtained from a $CH_3CN/TEAPF_6$ 0.1 M solution

The deposition of this film was difficult because of the solubility of the oligomers in the solvent used for the polymerisation. Only a few trials lead to the formation of the film, in

Fig. 3.48 it is possible to see the voltammogram of a film obtained at a fixed potential of +1.52 V for 60 sand then neutralized at 0 V for 60 s, with a thickness of 394 nm. The polymer showed a p-doping peak at +1.17 V with a de-doping at +1.02 V.

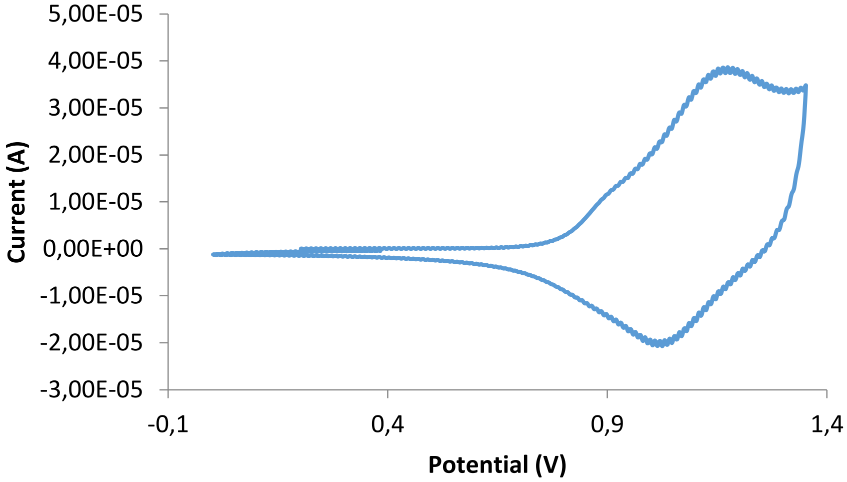

Fig. 3.48: cyclic voltammetric response of poly(Br-BT-TPA) in $CH_3CN/TEAPF_6$ 0.1 M; WE: Pt, RE, Ag/AgCl, CE: graphite bar; v = 100 mV/s.

Due to the as mention difficulties no UV-Vis spectra was recorded because no homogeneous film was obtained on ITO surface.

3.2.1.1.2.5 poly-4-(4’-((4-N,N’-diphenylamino)phenyl)-2,2’-bithiophenyl)-2-methyl-3-butyn-2-ol, poly(OH-BT-TPA)

Characterisation of the film obtained from a $CH_3CN/TEAPF_6$ 0.1 M solution

The characterisation was performed on a 420 nm thick deposit, obtained at 1.30 V for 60 s and then neutralized at 0 V for 60 s. An anodic p-doping peak can be observed in Fig. 3.49 at +1.16 V with an associated peak at +1.02 V

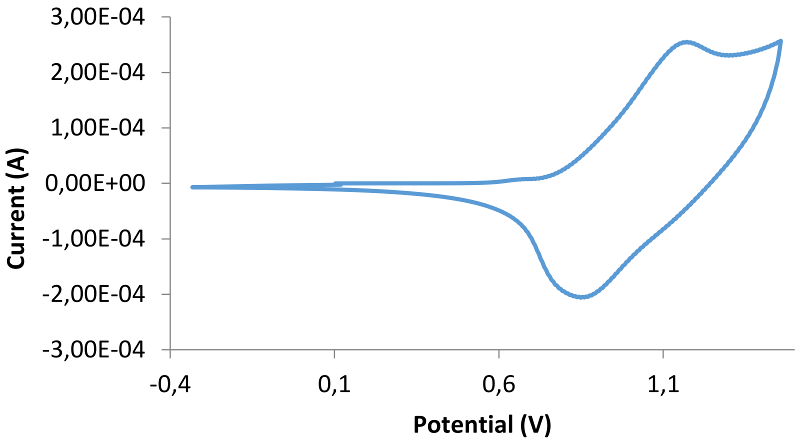

Fig. 3.49: cyclic voltammetric response of poly(OH-BT-TPA) in $CH_3CN/TEAPF_6$ 0.1 M; WE: Pt, RE, Ag/AgCl, CE: graphite bar; v = 100 mV/s.

The film on ITO was obtained at +1.5 V for 40 s and showed an absorption band at 485 nm.

3.2.1.1.2.6 poly-4-(4’-ethynyl-2,2’-bithiophenyl)-N,N’-diphenylaniline, poly(Et-BT-TPA)

Characterisation of the film obtained from a $CH_3CN/TEAPF_6$ 0.1 M solution

The characterisation was done on a film with a 438 nm thickness, obtained keeping the potential at +1.30 V for 120 s and then neutralising at 0 V for 60 s.

A doping peak at +1.12 V with an associated de-doping at +0.92 V can be seen in Fig. 3.50.

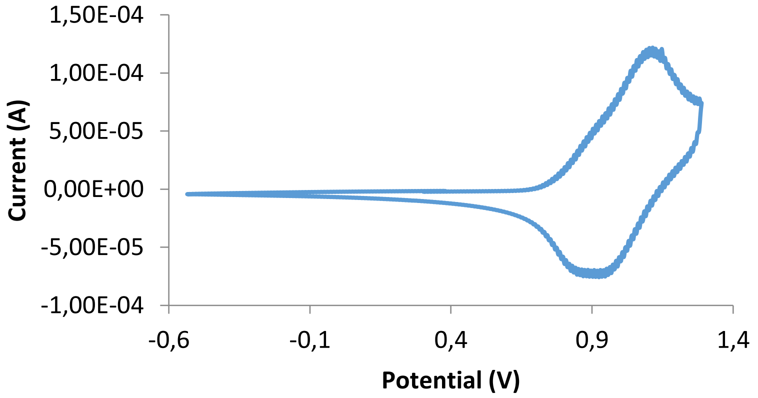

Fig. 3.50: cyclic voltammetric response of poly(Et-BT-TPA) in $CH_3CN/TEAPF_6$ 0.1 M; WE: Pt, RE, Ag/AgCl, CE: graphite bar; v = 100 mV/s. obtained from a $CH_3CN/TEAPF_6$ 0.1 M solution

The UV spectra showed a broad absorption at 330 nm on a film obtained at +1.50 V for 60 s

Characterisation of the film obtained from a $CH_2Cl_2/TEAPF_6$ 0.1 M solution

The characterisation was done on a film with a 440 nm thickness, obtained keeping the potential at +1.45 V for 60 s and at 0 V for 60 s.

A doping peak at +1.11 V with an associated de-doping at +0.85 V can be seen in Fig. 3.51

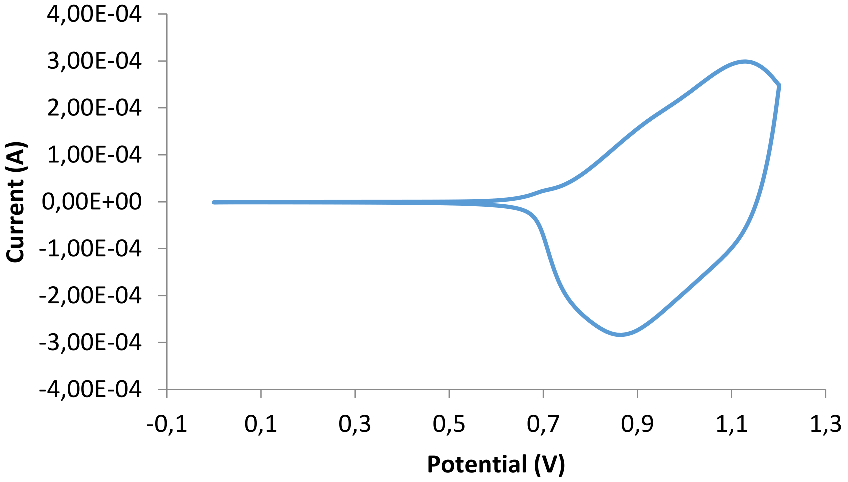

Fig. 3.51: cyclic voltammetric response of poly(Et-BT-TPA) in $CH_3CN/TEAPF_6$ 0.1 M; WE: Pt, RE, Ag/AgCl, CE: graphite bar; v = 100 mV/s obtained from a $CH_2Cl_2/TEAPF_6$ 0.1 M solution

The UV-Vis characterisation was performed on a film obtained in chronoamperometry at a fixed potential of +1.35 V for 90 s. The spectra showed a not well defined peak at 360 nm. The two films of the ethynyl derivative were characterised in $CH_3CN/TEAPF_6$ 0.1 M. The doping process can be seen at the same potential for both films, the morphology is a bit different (Fig. 3.52) while the less positive de-doping potential suggests that in the polymer obtained in CH_2Cl_2 the de-doping process is slower.

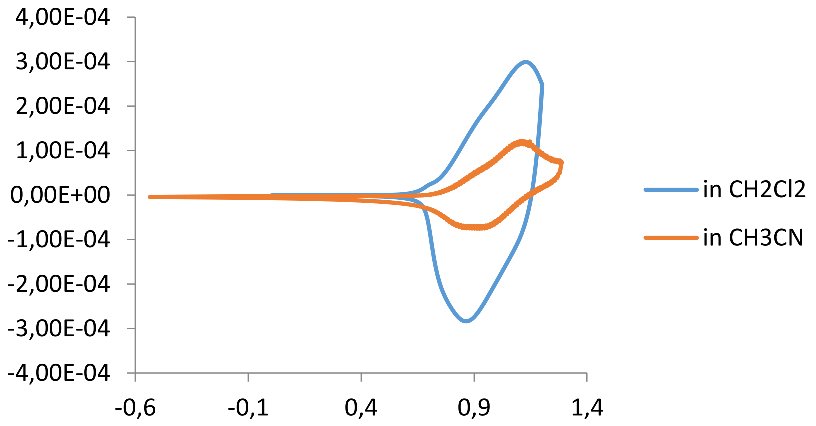

Fig. 3.52: cyclic voltammetric response of poly(Et-BT-TPA) in $CH_3CN/TEAPF_6$ 0.1 M; WE: Pt, RE, Ag/AgCl, CE: graphite bar; v = 100 mV/s obtained from a $CH_2Cl_2/TEAPF_6$ 0.1 M solution (blue) and from a $CH_3CN/TEAPF_6$ 0.1 M solution (orange)

3.2.1.1.2.7 poly-4-(4'-ethynyl-2,2'-bithiophenyl)-N,N'-diphenylaniline, poly(Tpy-Et-BT-TPA)

Characterisation of the film obtained from a $CH_3CN/TEAPF_6$ 0.1 M solution

The characterisation was done on a film with a 438 nm thickness, obtained keeping the potential at +1.35 V for 120 s and then neutralising at 0 V for 60 s.

A doping peak at +1.04 V with an associated de-doping at +0.92 V can be seen in the following figure.

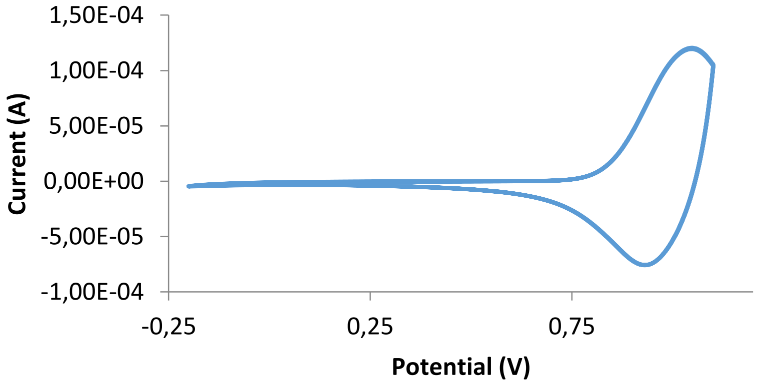

Fig. 3.52: cyclic voltammetric response of poly(Et-BT-TPA) in $CH_3CN/TEAPF_6$ 0.1 M; WE: Pt, RE, Ag/AgCl, CE: graphite bar; v = 100 mV/s obtained from a $CH_2Cl_2/TEAPF_6$ 0.1 M solution

3.2.1.2 Discussion on monomers and polymers bearing one ethynyl group on the bithiophene backbone

In this part, the discussion will cover the synthetic procedures, electrochemical and UV-Vis characterisation of the series of molecules that, step by step, led to the desired compound Tpy-Et-BT-TPA in Fig. 3.53.

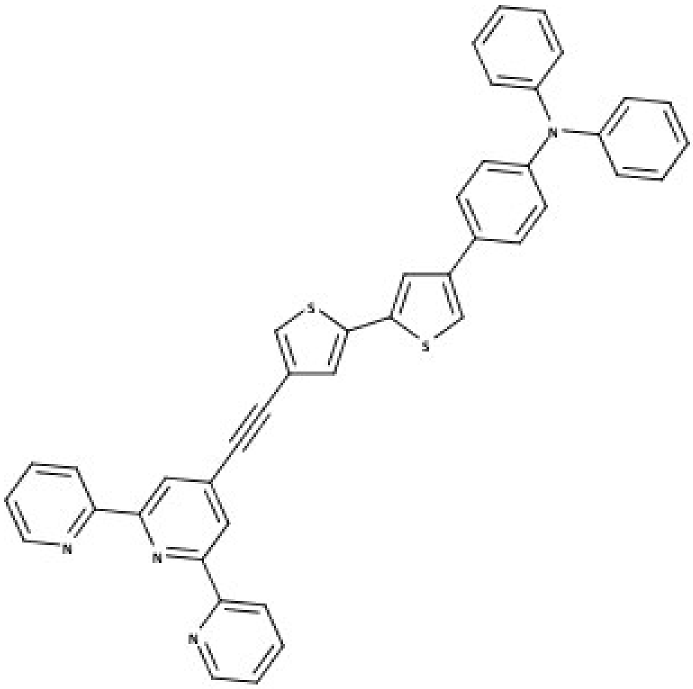

Fig 3.53: Tpy-Et-BT-TPA

The idea of synthesising a D-π-A molecule comes from the intense research in the field of chromophores for titania sensitisation for DSSCs applications, as described in the State of the Art of this thesis. Two classes of sensitizers can be found in literature: Ru-based polypyridine complexes and metal-free organic dyes. Recently, in the attempt to combine the favourable features of organic (D-π-A structure and high ε values) and inorganic (MLCT processes and broader absorption profiles) chromophores, some interesting research papers were published [65, 66] where so-called hybridised systems were synthesised and studied in DSSCs applications. In these systems an organic dyes with a D-π-A structure coordinate to Ru, whose coordination sphere is completed by using bipy- or terpyridine carboxylated ligands.

Analysis of data concerning the best type of donors (D), π-bridge, and acceptor (A) reveals that, among the best donors, electron-rich arylamines (triphenylamine, TPA) play an important role because of its non-planar structure that suppress dye aggregation. The best moieties for the conjugated bridge often contain thiophene units because of their excellent charge-transport properties, while the acceptor fragment is usually a cyanoacrylic acid group. Starting from these considerations, the idea of this thesis was to synthesise and study the electrochemical and optical properties of the organic dye in Fig. 3.53, bearing a TPA donor fragment as redox unit that suppresses recombination between conducting band (CB) electrons and oxidised dyes, and has a high molar extinction coefficients. As spacer, the bithiophene was chosed because it increases the conjugation of the system, lowers the steric hindrance between aromatic rings and increases the planarity of the dye. Moreover an ethynyl group was added as a spacer to further improve planarity and charge transport, as it also has electron-withdrawing properties, giving rise to the novel dye with a D-A-π-A structure that has recently been studied as a promising architecture for organic dyes [69-73]. Terpyridine was chosen as acceptor for two important reasons: i) it has been demonstrated that the nitrogen of a pyridine ring can form coordination bonding between the lone pair of electrons on the nitrogen atom of the pyridine and the Lewis acid sites of titania to give electron injection efficiencies comparable to or higher than similar dyes where the pyridine ring is replaced with carboxyphenyl group [64], and ii) terpyridine can also bind to Ru centre to give hybrid organic/inorganic dyes.

Thiophene units that act as spacers in organic dyes are usually functionalised in the α position. The decision of functionalising the bithiophene moiety in its 4,4’ position was taken because of the possibility of electropolymerising all the chromophores (through the free α position of the bithiophene) obtained during the synthetic steps. The resulting electropolymers allow to study both the influence on polymer electrochemical and optical properties of donor and acceptor substituents and also to evaluate the polymer properties as a possible dye for DSSCs. As a matter of fact, polymers with D-π-A structure have been recently investigated as sensitisers in Gratzel cells [107-117].

For the synthesis of the molecule in Fig. 3.53, two different approaches were followed. The first path involved a first Sonogashira-Hagihara [170] coupling reaction adapted from the work of Shin et al. [171], This reaction involves halogenated arylic compounds (with a reactivity order Cl<<Br<I<OTf) and terminal alkynes in the presence of a Pd(II) or Pd(0) catalyst and a Cu(I) co-catalyst. In this case the formation of a C-C bond is determined by the reaction between 4,4'-dibromo-2,2'-bithiophene and the acetylenic group of 2-methylbut-3-ynyl-2-ol, following the scheme in Fig. 3.54.

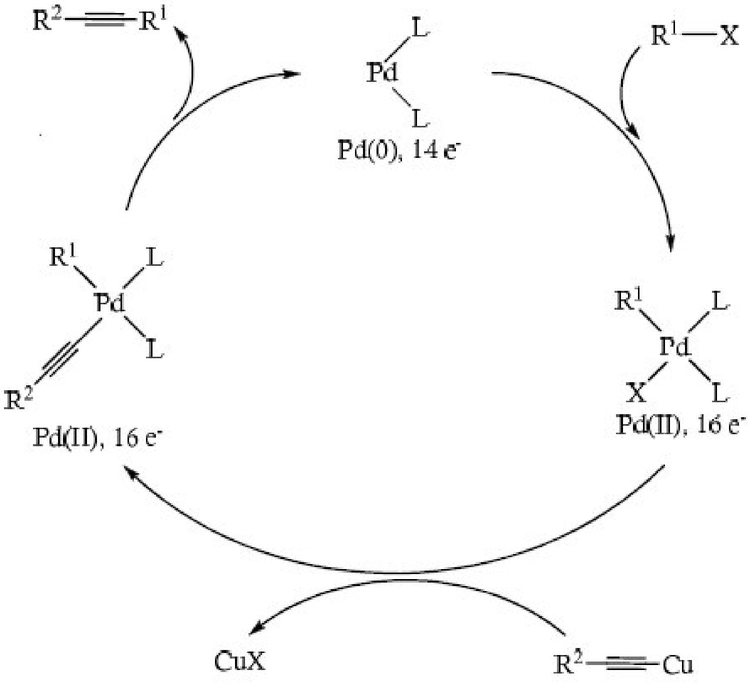

Fig. 3.54: catalytic mechanism of Sonogashira coupling reaction

At the first trial, the synthesis was conducted with a Br-BT-Br/alkyne ratio of 1/2 at 85°C and in these conditions the disubstituted OH-BT-OH product was obtained. The following step was to try to bound the TPA moiety to one of the ethynylc groups previously

---

[170] I.P. Beletskaya, G.V. Tsvetkov, *Russian Chemical Bulletin International Edition* **2004**, 53, 189
[171] S.C. Shin, D.H. Kim, B.S. Kang, *Dalton Trans*, **1998**, 1893

introduced in bithiophene but this approach led to a not distinguishable mixture of compounds. A second trial was done by synthesising Br-BT-OH, that bears only one ethynyl on the bithiophene. The desired product Br-BT-OH was obtained, although no complete conversion of the starting dibrominated thiophene was reached. The non complete conversion suggested that the reaction was of a 'consecutive' type: at the beginning of the reaction (first 15 minutes) the monosubstituted compound forms and immediately after the disubstituted start to appear, while the dibrominated substrate continues to react to give the monosubstituted product. For the as mentioned reasons, the most convenient strategy was to stop the reaction after 15 minutes and recover the starting dibromobithiophene; the yield is therefore not so high (23%), anyway Br-BT-OH is a new compound yet not reported in literature.

The alcoholic group was removed from Br-BT-OH in MeOH/toluene solution in a basic environment (NaOH excess) to give the terminal alkyne compound Br-Bt-Et.

At this point the idea was to add the TPA moiety through the reaction of Br-BT-Et and the TPA boronic acid in a classical Suzuki reaction [172] (see Fig. 3.55).

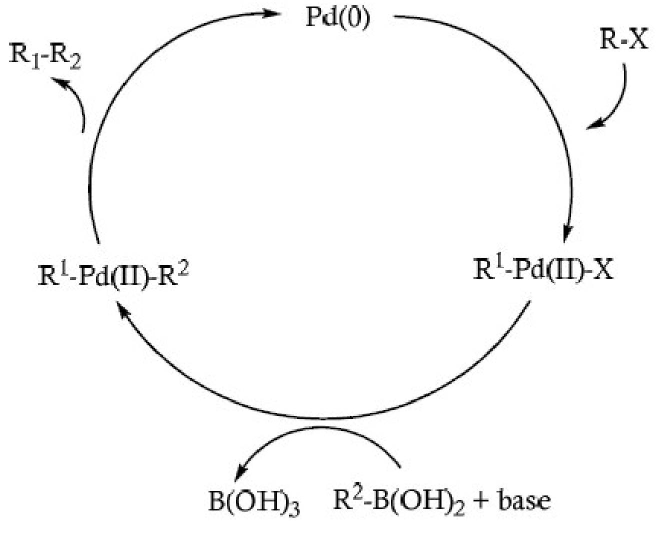

Fig. 3.55 : catalytic mechanism of Suzuki coupling reaction

---

[172] A. Suzuki, N. Miyaura, *Chemical Communications*, **1979**, 866.

The reaction between Br-Bt-Et and 4-N,N’-(diphenylamino)phenylboronic acid in DME did not lead to the desired product. Another synthetic way was then explored and the Suzuki coupling was employed between the Br-BT-OH and the TPA boronic acid but no clear results were obtained. At this point the approach was completely changed.

With the suspect that the failure in the previous synthetic strategy was due to a low stability of Br-BT-OH and Br-BT-Et, a new path was figured out: the Suzuki coupling was done as a first step between Br-BT-Br and 4-N,N’-(diphenylamino)phenylboronic acid following a procedure reported in literature [173] and the derivative Br-BT-TPA was obtained.

Br-BT-TPA was then used in the subsequent Sonogashira reaction to give OH-BT-TPA with 60% yield. The deprotection with KOH in MeOH/toluene gave the product Et-BT-TPA with a 67% yield.

The final chromophore (Fig. 3.53) Tpy-Et-BT-TPA was synthesised following a procedure established in this research group for thiophene derivatives functionalised with terpyridine [174]. This Sonogashira coupling involves a chlorinated terpyridine, even if Cl-derivatives are not very active towards this coupling. The success of the reaction in this case suggested that the presence of two highly delocalised systems (TPA-functionalised bithiophene and terpyridine) favoured the addition of Cl-terpyridine on the terminal alkyne.

All the synthesised molecules were characterised by means of CV and UV-Vis spectrophotometry, and also the corresponding polymers underwent the same characterisation (for details see chapter 2).

For monomers, elemental analysis and ^{1}H NMR were carried out (for Br-BT-TPA also ^{13}C NMR).

All the synthesised compounds were characterised with UV-Vis spectrophotometry, from which Energy Gap (E_g) values and extinction coefficient (**ε**) were calculated (see experimental). Data relative to λ_{max}, λ_{onset} and the corresponding Energy Gap values are reported in Table 3.12 and the spectra are reported in Fig. 3.56. The values for the terpyridine derivative are relative to a CH_2Cl_2, $5*10^{-5}$ M because of solubility problems of

---

[173] T. Duan, K. Fan, C. Zhong, W. Gao, X. Chen,T. Peng, J. Qin, *Journal of Photochemistry and Photobiologt A: chemistry* **2014**, 278, 39.

[174] P. Manca, M.I. Pilo, G. Casu, S. Gladiali, G. Sanna, R. Scanu, N. Spano, A. Zucca, C. Zanardi, D. Bagnis, L. Valentini, *Journal of Polymer Science A: Polymer Chemistry*, **2011**, 49, 3513

this compound in CH_3CN but it was verified that the differences in the λ_{max} and λ_{onset} between the data in the two different solvents differ only for 1-2 nm. Data relative to Br-BT-Et and Br-BT-OH showed exactly the same results (both in UV-Vis and electrochemical characterisation) and only the values of the latter are reported.

Table 3.12: Optical data for chromophores bearing one ethynyl group and their synthetic precursors in CH_3CN

Monomer	**λ_{max} (nm)**	**λ_{onset} (nm)**	**Eg,opt (eV)**	**ε (M^{-1} cm^{-1})**
Br-BT-Br	304	355	3.49	12600
Br-BT-OH	308	354	3.50	11200
OH-BT-OH	310	353	3.51	12800
Br-BT-TPA	320	368	3.36	34200
OH-BT-TPA	320	365	3.40	33100
ET-BT-TPA	321	370	3.35	29900
Tpy-ET-BT-TPA [a]	330	374	3.31	19500

[a] UV in CH_2Cl_2, $5*10^{-5}$ M

From the data it is clear how the insertion of the TPA fragment on the bithiophene (Br-BT-TPA, OH-BT-TPA, Et-BT-TPA, Tpy-Et-BT-TPA):

- increases the extinction coefficient
- leads to a 11-17 nm red-shift of the absorption maxima due to intramolecular π-π* transitions of TPA
- leads to lower Energy Gap values (0.10-0.15 eV decrease).

The ε values are high for all the molecules with the TPA moiety but this value decreases with the introduction of terpyridine.

A progressive bathochromic shift can also be appreciated with the introduction of the ethynyl substituents (Br-BT-OH, OH-BT-OH vs Br-BT-Br) on bithiophene; this shift is probably due an increase in the electrons π-delocalisation, as already known in literature [65].

For Tpy-Et-BT-TPA the red-shift is even more evident due to the high conjugation of the system. The terpyridine introduction lowers the **ε** value but it still remains higher than those of the bithiophene system with no TPA (Br-BT-Br, Br-BT-OH, OH-BT-OH).

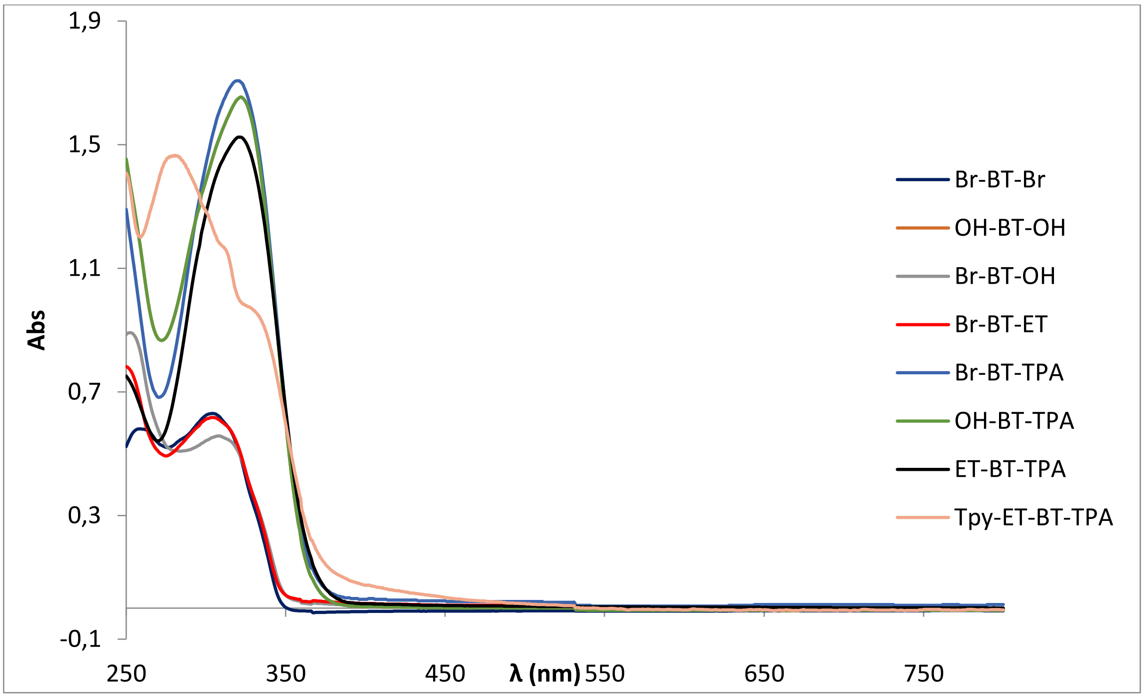

Fig 3.56: UV-Vis spectra of chromophores bearing one ethynyl group and their synthetic precursors.

The cyclic voltammetry characterisation allows to evaluate HOMO values of the molecules (Table 3.13). For this reason the E_{onset} is calculated with the tangent method. The obtained value is converted to eV with the following equation [175]:

$$\text{HOMO} = -e(E_{onset} + 4.71)(\text{eV})$$

where potentials are expressed in volts vs Ag/AgCl and 4.71 is the value of Ag/AgCl couple in vacuum vs NHE (normal hydrogen electrode).

---

[175] D. Qiu, J. Wu, Z. Xie, Y. Cheng, L. Wang, *Journal of Organometallic Chemistry* **2009**, 694, 737.

Table 3.13: voltammetric data chromophores bearing one ethynyl group and their synthetic precursors

MONOMER	**$E_{p,1}$ (V)**	**$E_{p,2}$ (V)**	**$E_{onset,1}$ (V)**	**$E_{onset,2}$ (V)**	**HOMO (eV)[c]**	**HOMO-1 (eV)[d]**
Br-BT-Br[a]	1.74		1.45		-6.16	
Br-BT-OH[a]	1.51		1.39		-6.10	
OH-BT-OH[a]	1.43		1.31		-6.02	
Br-BT-TPA[a]	0.89	1.62	0.74	1.35	-5.45	-6.06
OH-BT-TPA[a]	0.88	1.34	0.78	1.10	-5.49	-5.81
ET-BT-TPA[a]	0.87	1.30	0.78	1.08	-5.49	-5.79
ET-BT-TPA[b]	1.02	1.55	0.83	1.09	-5.54	-5.80
Tpy-ET-BT-TPA[b]	0.91	1.29	0.76	1.04	-5.47	-5.75

[a] $CH_3CN/TEAPF_6$ 0.1 M. [b] $CH_2Cl_2/TEAPF_6$ 0.1 M. [c] HOMO calcolate from the first onset potential [d] HOMO-1 value calculated from the second peak onset potential

Preliminary TD-DFT theoretical calculations give confirmation on the oxidation attribution described in section 3.2.1. In particular for Br-BT-Br, Br-Bt-Et,Br-BT-TPA, Et-BT-TPA and Terpy-Et-BT-TPA, calculations confirm the HOMO localisation on the bithiophene fragment for the first two compound (Fig. 3.57 and 3.58) and on the TPA for the other three (Fig. 3.59, 3.61 and 3.63). For derivatives with TPA the localisation of the HOMO-1 (Fig. 3.60, 3.62 and 3.64) on the bithiophene confirms the attribution of the second oxidation process.

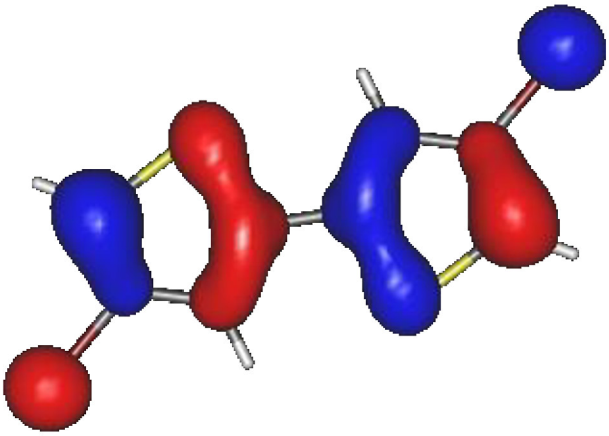

Fig. 3.57: HOMO electronic distribution for Br-BT-Br.

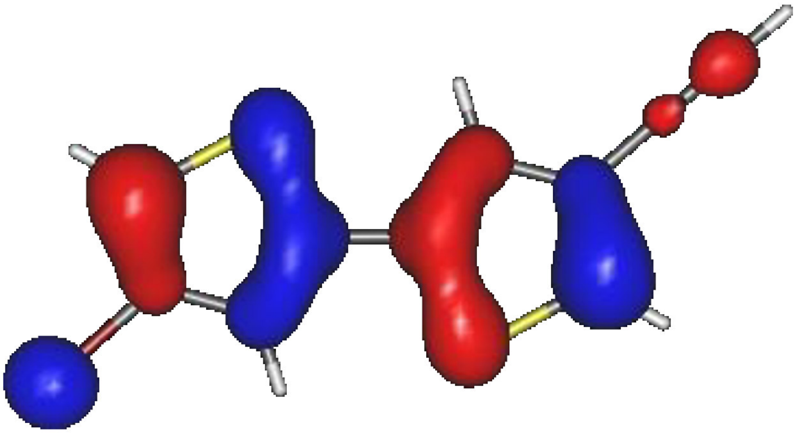

Fig. 3.58: HOMO electronic distribution for Br-BT-Et.

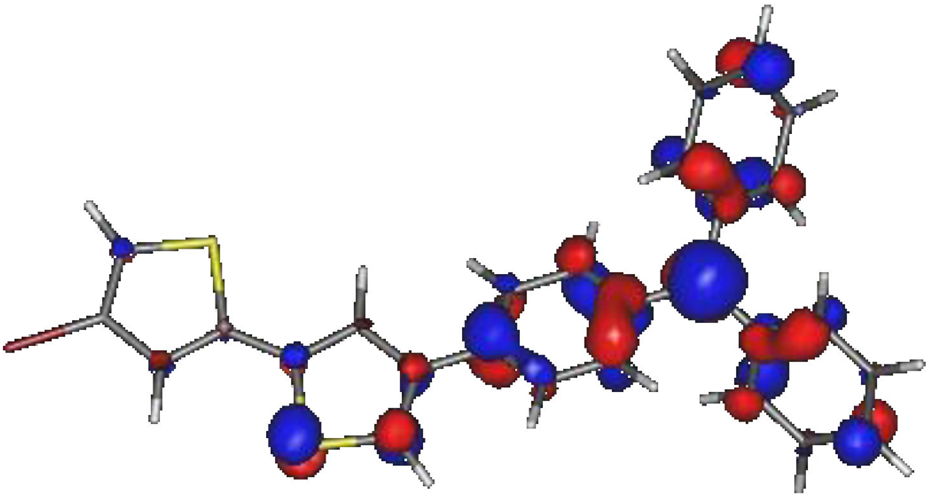

Fig. 3.59: HOMO electronic distribution for Br-BT-TPA.

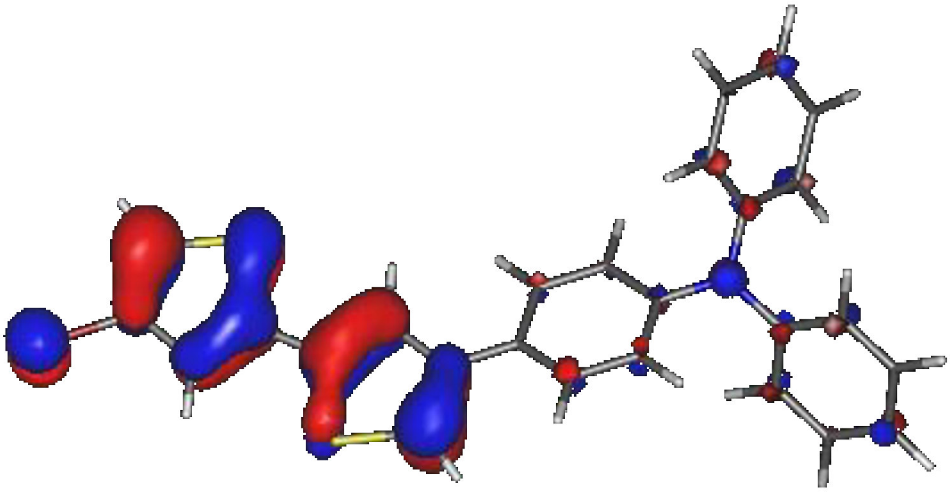

Fig. 3.60: HOMO-1 electronic distribution for Br-BT-TPA.

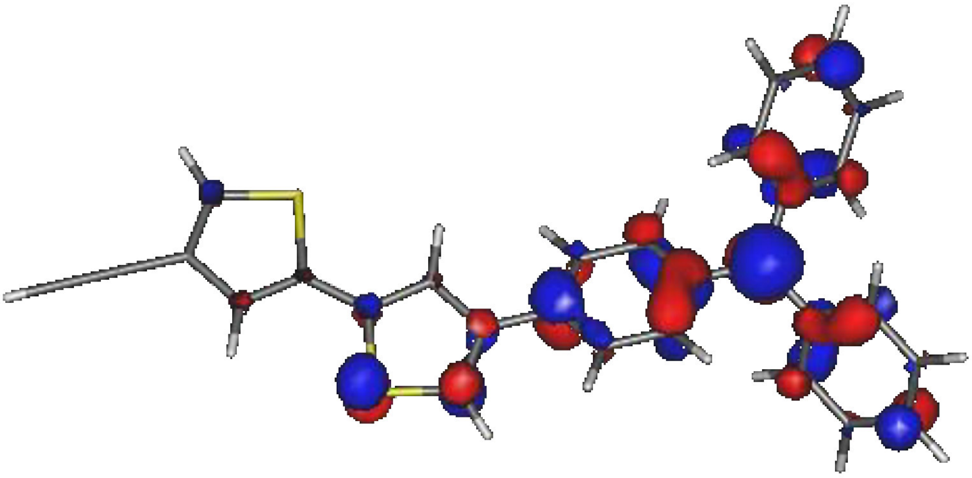

Fig. 3.61: HOMO electronic distribution for Et-BT-TPA

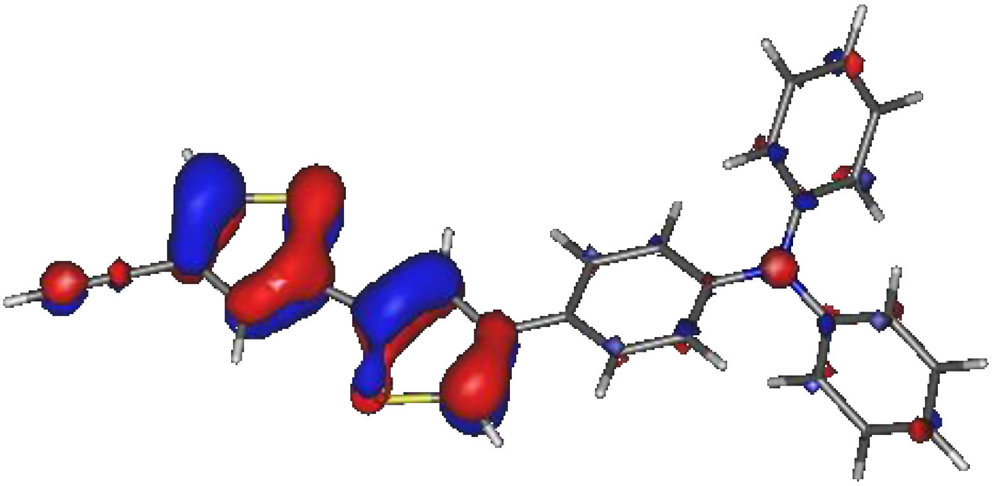

Fig. 3.62: HOMO-1 electronic distribution for Et-BT-TPA

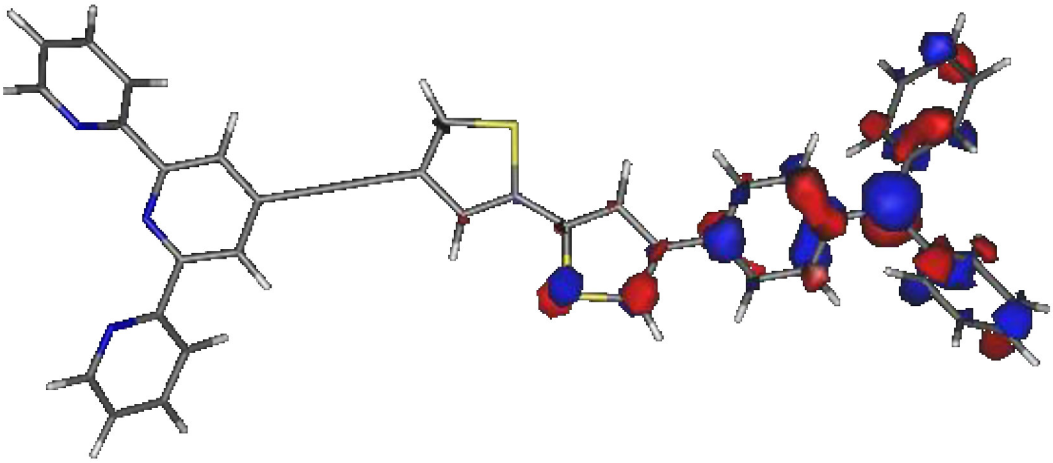

Fig. 3.63: HOMO electronic distribution for Tpy-Et-BT-TPA

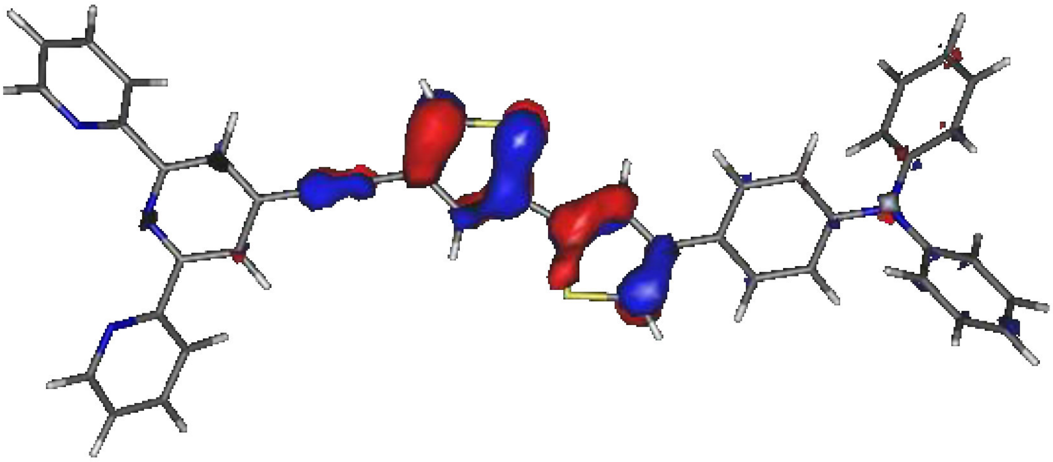

Fig. 3.64: HOMO-1 electronic distribution for Tpy-Et-BT-TPA

From voltammetric data it is possible to evidence:

- less Br atoms lead to lower oxidation potentials, probably due to the electron-withdrawing effect of bromine that attracts the electrons making the bithiophene oxidation more difficult
- the TPA addition leads to HOMO destabilisation
- the oxidation potentials tend to lower at increasing conjugation of the molecule; in particular, the introduction of ethynyl (Et-BT-TPA) in place of Br (Br-BT-TPA) does not influence the oxidation potential of TPA rings, but has a strong impact on the

bithiophene fragment oxidation, that is much lower for the ethynyl derivative (1.62 vs 1.30 V in CH_3CN).

As already said, all monomers were subjected to electropolymerization and the obtained polymeric films were characterized by means of CV and UV-Vis spectrophotometry. Voltammetric data, reported in Table 3.14 with the corresponding HOMO values suggest that:

- the substitution of a Br atom in the polymer with an alcohol- or TPA-substituent cause a clear decrease in the polymers doping values with a subsequent HOMO destabilisation
- the complete substitution of Br atoms with an alkyne moiety (Et-BT-TPA) continues to shift the doping potential to lower values and this is clearly appreciable also for the Tpy-Et-TBT-TPA.

Table 3.14: voltammetric data for polymer films deposited on a Pt electrode

POLYMERS	Ep,a (V)	E_{onset} (V)	HOMO (eV)
Poly(Br-BT-Br)	1.66	1.33	-6.04
Poly(Br-BT-OH)	1.25	1.10	-5.81
Poly(OH-BT-OH)	1.26	0.96	-5.67
Poly(Br-BT-TPA)	1.24	0.98	-5.69
Poly(OH-BT-TPA)	1.16	0.80	-5.51
Poly(ET-BT-TPA)	1.12	0.78	-5.49
Poly(Tpy-ET-BT-TPA)	1.04	0.82	-5.53

The absorption spectra were also recorded and data are reported in Table 3.15.

Table 3.15: UV-Vis data for polymer films deposited on a Pt electrode

POLYMERS	λ_{onset}	$E_{g,opt}$
Poly(Br-BT-Br)	637	1.95
Poly(Br-BT-OH)	630	1.97
Poly(OH-BT-TPA)	610	2.03
Poly(Et-BT-TPA)	542	2.28
Poly(Tpy-Et-BT-TPA)	465	2.67

The substitution on the bithiophene fragment leads to an increase in energy gap values but this does not imply a worsening of the conducting properties of the polymer. Usually energy gap values lower than 2 eV do not allow to control the electronic transitions properly. On the other side, when comparing HOMO values and band gap values it is possible to see that a HOMO destabilisation coincided with a LUMO destabilisation.

Finally, evaluation of electrochemical and optical properties of this first group of bithiophene-derivatives and of the corresponding electrogenerated polymers allowed to understand the role of donor or acceptor moieties on a bithiophene backbone. The final product Tpy-Et-BT-TPA (that showed a high molar extinction coefficient of 19500 $M^{-1}cm^{-1}$) and the corresponding polymer are organic chromophores with a D-π-A geometry suitable for light harvesting applications thanks to the absorption in the visible region of the solar spectrum. In particular, the presence of the terpyridine moiety can lead to the coordination of this molecule to a ruthenium metal center, then opening up even more promising results in energy-related applications.

3.2.2 Chromophores bearing two ethynyl groups on the bithiophene backbone

3.2.2.1 Characterisation

3.2.2.1.1 Monomers

The compounds synthesised following the procedures reported in the experimental part, have been characterised through cyclic voltammetry on a Pt working electrode (2 mm diameter), with an Ag/AgCl working electrode and graphite as counterelectrode, with a 100 mV/s scan rate. The responses were recorded with a 5*10-3 M analyte concentration in CH_2Cl_2/$TEAPF_6$ (tetraethylammonium hexafluorophosphate) 0.1 M

3.2.2.1.1.1 4-bromotriphenylamine (Br-TPA)

Characterisation in CH_2Cl_2

The voltammetric response for Br-TPA can be seen in Fig. 3.65. An anodic process at +1.06 V is attributed to the oxidation of TPA and an associated cathodic peak can be found at +0.95V.

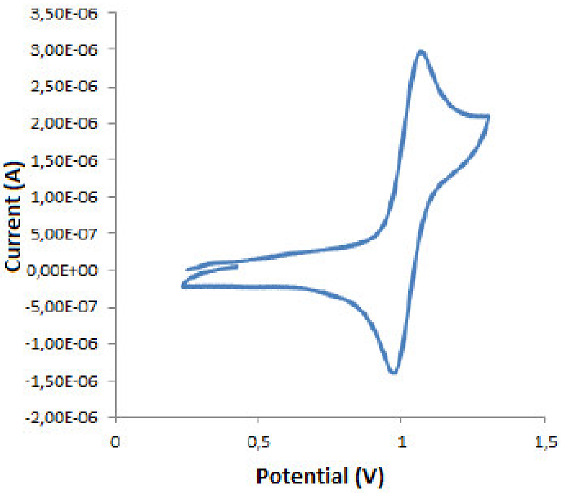

Fig 3.65: cyclic voltammetric response of a $5*10^{-3}$ M solution of Br-TPA in CH_2Cl_2/$TEAPF_6$ 0.1 M; WE: Pt, RE, Ag/AgCl, CE: graphite bar; v = 100 mV/s.

TPA is known to electropolymerise [176] but in this case no current increase for subsequent scans was appreciated, probably for the solubility, in the solvent system, of the polymeric species that form on the electrode surface.

3.2.2.1.1.2 4-ethynyl-trimethylsilyl-N,N'-diphenylaniline (TMS-TPA)

Characterisation in CH_2Cl_2

In Fig. 3.66 it is possible to see an anodic process at 1.06 V attributable to the oxidation of the triphenylamine moiety; an associated peak is present at +0.90 V.

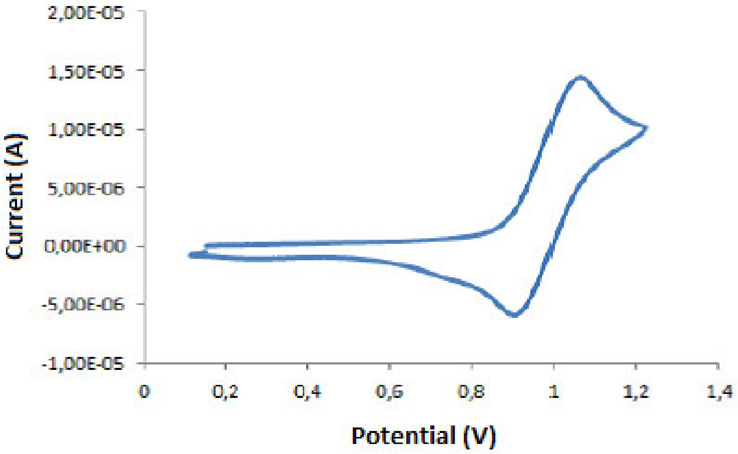

Fig. 3.66: cyclic voltammetric response of a $5*10^{-3}$ M solution of TMS-TPA in CH_2Cl_2/$TEAPF_6$ 0.1 M; WE: Pt, RE, Ag/AgCl, CE: graphite bar; v = 100 mV/s.

By changing the scan rate from 100 mV/s to 50 mV/s it is possible to distinguish two cathodic peaks associated to the anodic process, respectively at +0.92 V and +0.74 V (Fig. 3.67). The presence of two peaks can be attributed to the reduction of the two chemically different phenyl rings of TPA and this distinction can be appreciated only at lower rates. The difference between the rings is not appreciable in the anodic scan probably because of interactions between the solvent and the compound. This distinction was evident in

---

[176] E.T. Seo, R.F. Neelson, J.M. Fritssch, L.S. Marcoux, D.W. Leedy, R.N. Amadams, *Journal of the American Chemical Society* **1966**, 88, 3498

monomers bearing TPA fragment that were characterised in CH_3CN and described in the previous paragraphs.

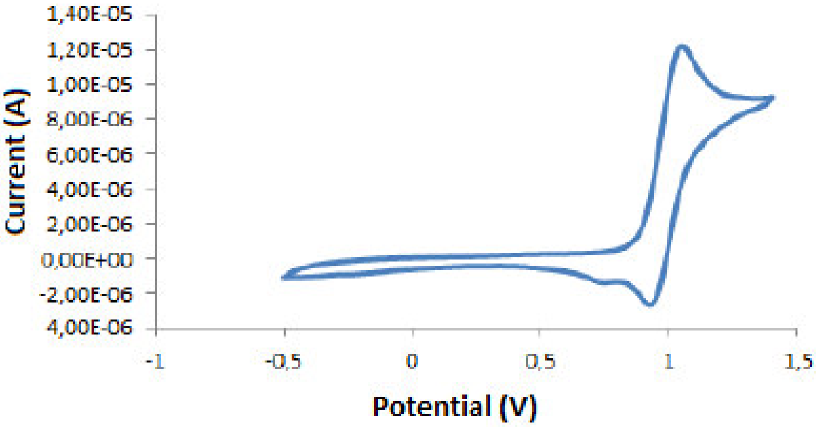

Fig. 3.67: cyclic voltammetric response of a $5*10^{-3}$ M solution of TMS-TPA in CH_2Cl_2/$TEAPF_6$ 0.1 M; WE: Pt, RE, Ag/AgCl, CE: graphite bar; v = 50 mV/s.

Different scans between -0.5 V and +1.5 V show no increase in the current, as already seen for Br-TPA.

3.2.2.1.1.3 4-ethynyl-N,N'-diphenylaniline (Et-TPA)

Characterisation in CH_2Cl_2

In Fig. 3.68 an anodic process at +1.20 V can be seen and can be attributed to the compound oxidation. Moreover, at slightly more positive potentials a second, poorly defined peak is visible. This peak can be attributed to the phenyl groups of TPA. In the inverse scan two peaks can be seen at +0.91 V and +0.72 V. Moreover a third peak in the reverse scan at +0.17 V is due to the coupling of radical cations that form during the anodic scan and leads to H^+ elimination [169].

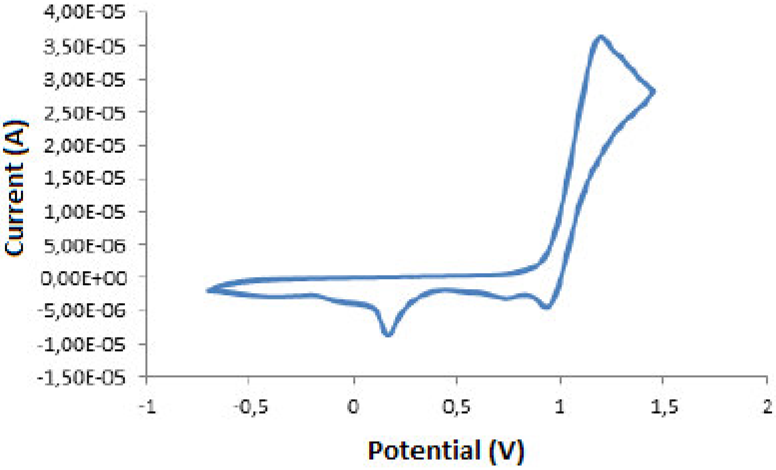

Fig. 3.68: cyclic voltammetric response of a 5*10^{-3} M solution of Et-TPA in CH_2Cl_2/$TEAPF_6$ 0.1 M; WE: Pt, RE, Ag/AgCl, CE: graphite bar; v = 100 mV/s.

Also in this case, no film forms on the working electrode for subsequent scans.

3.2.2.1.1.4 4-[(4'-bromo-2,2'-bithiophen-4-yl)ethynyl]-N,N'-diphenylaniline (Br-BT-Et-TPA)

Characterisation in CH_2Cl_2

Three not well resolved anodic processes can be distinguished in Fig. 3.69 at +1.03 V, +1.2 V and +1.54 V. The first peak is associated to TPA and the second can be due to the unsaturated substituent. The more anodic process is due to bithiophene oxidation. In the inverse cathodic scan there are two peaks at +1.0 V and +0.67 V.

As a confirmation to the previous assumption, numerous scan around this region do not lead to the deposition of a film on the electrode.

The more anodic process at +1.58 V is due to the bithiophene oxidation and has an associated peak at +1.24 V.

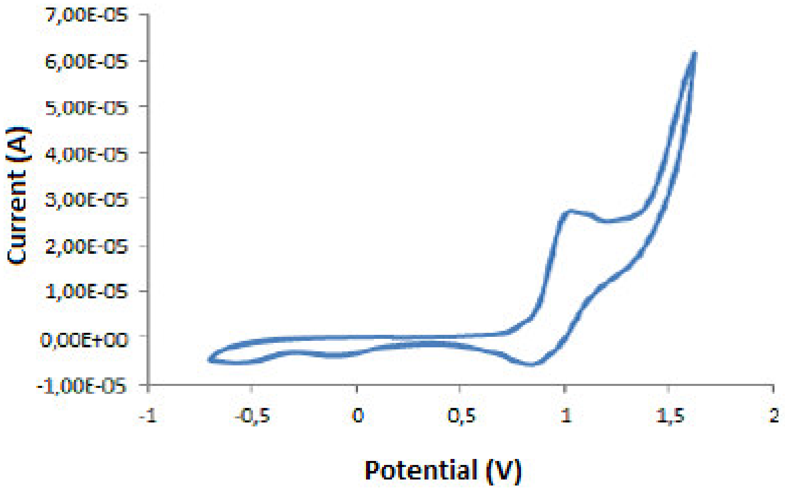

Fig. 3.69: cyclic voltammetric response of a 5*10^{-3} M solution of Br-BT-Et-TPA in CH_2Cl_2/$TEAPF_6$ 0.1 M; WE: Pt, RE, Ag/AgCl, CE: graphite bar; v = 100 mV/s.

When repeating scans around the highest oxidation potential (Fig. 3.70), a light yellow polymeric film forms on the electrode.

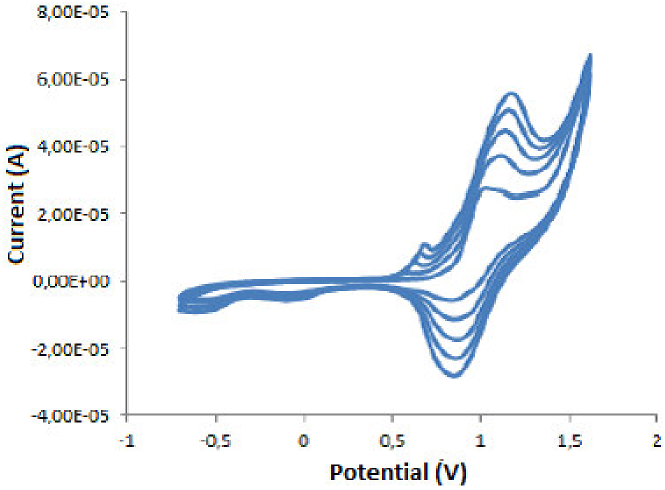

Fig. 3.70: cyclic voltammetric response of a 5*10^{-3} M solution of Br-BT-Et-TPA in CH_2Cl_2/$TEAPF_6$ 0.1 M; WE: Pt, RE, Ag/AgCl, CE: graphite bar; v = 100 mV/s.

3.2.2.1.1.5 4-[(4’-ethynyl-2,2’-bithiophen-4-il)ethinyl]-N,N’-diphenylaniline (Et-BT-Et-TPA)

Characterisation in CH_2Cl_2

The voltammogram in Fig. 3.71 shows a broad anodic process centred at +1.06 V and assigned to TPA fragment, with an associated peak at +0.88 V. At more anodic potentials the thiophene moiety oxidises at +1.55 V and an associated peak is present at +1.34 V.

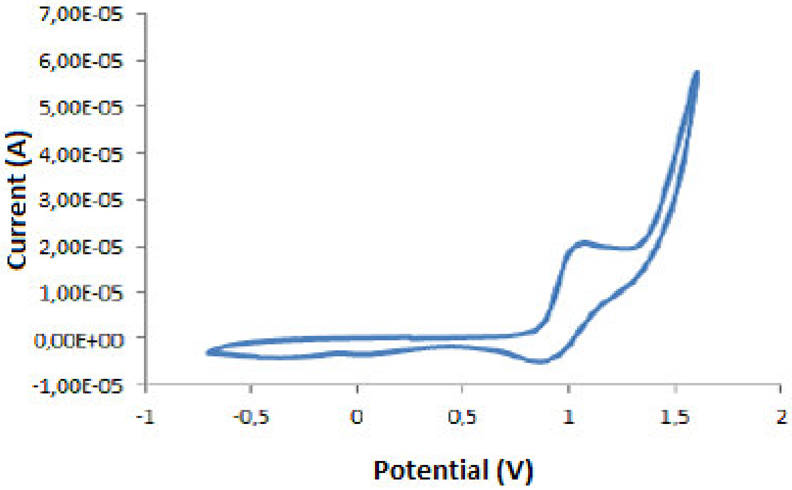

Fig. 3.71: cyclic voltammetric response of a 5*10^{-3} M solution of Et-BT-Et-TPA in CH_2Cl_2/$TEAPF_6$ 0.1 M; WE: Pt, RE, Ag/AgCl, CE: graphite bar; v = 100 mV/s.

A polymer yellow deposit forms when cycling around the oxidation potential of bithiophene (Fig. 3.72).

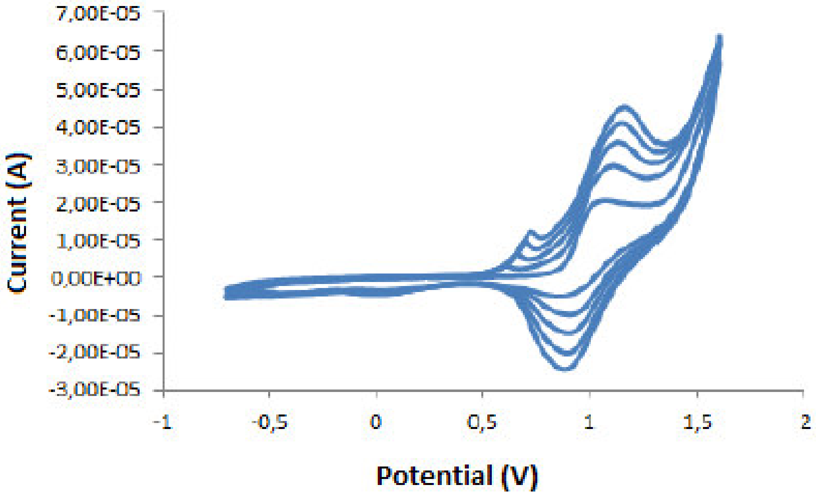

Fig. 3.72: cyclic voltammetric response of a 5*10^{-3} M solution of Et-BT-Et-TPA in CH_2Cl_2/$TEAPF_6$ 0.1 M; WE: Pt, RE, Ag/AgCl, CE: graphite bar; v = 100 mV/s.

3.2.2.1.1.6 4-[(2,2’:6’,2’’-terpyridine-4’-ethynyl)-4-(2,2’-bithiophen-4-il)ethynyl]-N,N’-diphenylaniline (Tpy-Et-BT-Et-TPA)

Characterisation in CH_2Cl_2

The terpyridine derivative shows broad oxidation processes, at 0.98 V and +1.16 V, due to the TPA fragment and probably to the unsaturated substituent bonded to the amine; in the reverse scan a peak is present at +0.88 V. At +1.45 V the oxidation of the bithiophene moiety occurs (Fig. 3.73).

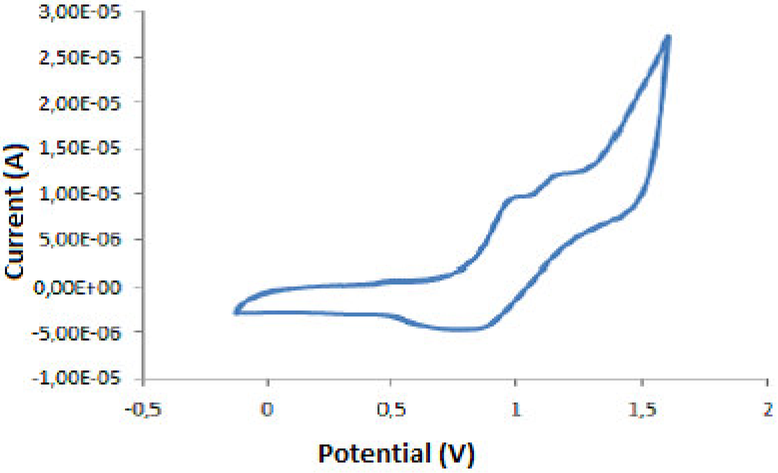

Fig. 3.73: cyclic voltammetric response of a $5*10^{-3}$ M solution of Tpy-Et-BT-Et-TPA in CH_2Cl_2/$TEAPF_6$ 0.1 M; WE: Pt, RE, Ag/AgCl, CE: graphite bar; v = 100 mV/s.

Like the other thiophene derivatives, for subsequent scans around the higher oxidation potential, a polymer green deposit forms (Fig. 3.74). This confirms that the polymer growth is attributable to the bithiophene moiety and not to the TPA portion.

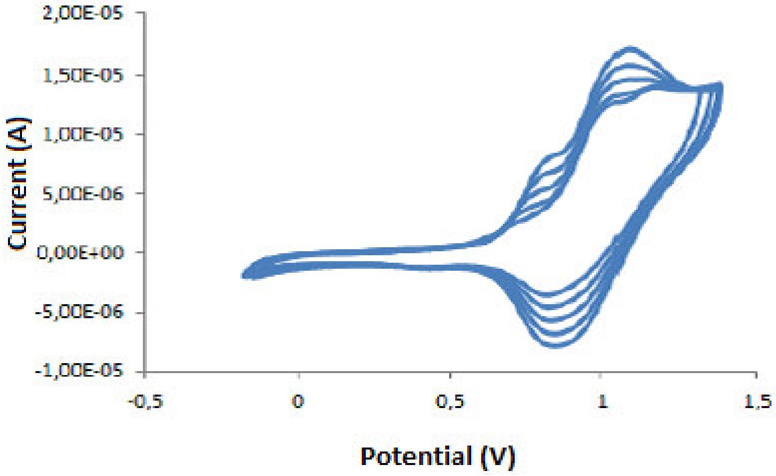

Fig. 3.74: cyclic voltammetric response of a $5*10^{-3}$ M solution of Tpy-Et-BT-Et-TPA in CH_2Cl_2/$TEAPF_6$ 0.1 M; WE: Pt, RE, Ag/AgCl, CE: graphite bar; v = 100 mV/s.

3.2.2.1.2 Polymers

Monomers have been polymerised in a CH_2Cl_2/$TEAPF_6$ 0.1 M on a Pt electrode through chronoamperometry, choosing the potential from the previously described voltammetric responses. The deposition time was chosen case by case as to obtain films with similar thicknesses. After the deposition step, all films were neutralised by keeping them at 0 V bias for 60 s.

The obtained polymers were characterised by means of cyclic voltammetry in CH_2Cl_2/$TEAPF_6$ 0.1 M, with an Ag/AgCl reference electrode and a graphite counter electrode at 100 mV/s scan rate (see experimental).

3.2.2.1.2.1 poly-4-ethynyl-N,N'-diphenylaniline, poly(Et-TPA)

Characterisation of the film obtained from a CH_2Cl_2/$TEAPF_6$ 0.1 M solution

The voltammetric characterisations of the monomers consisting of only TPA showed a scarce tendency to polymerise in potentiodynamic conditions. However, as chronoamperometry usually allows to obtain better polymeric films, we tried to obtain homogeneous deposits in chronoamperometry at fixed potential. In only one case, for poly(Ety-TPA) it was possible to obtain a film with a 340 nm thickness by applying +1.50 V for 300 s and then neutralising at 0 V for 60 s.

The response can be seen in Fig. 3.75, where an anodic process that cannot be associated to a doping mechanism can be seen. The morphology seems the one typical of a stripping process due to adsorption-desorption process on the electrode surface at varying the potential scan direction. The absence of doping or de-doping is confirmed by the difference between the anodic and cathodic peak values that are almost the same (1.03 V and 1.00 V respectively). This suggests that the poly(Et-TPA) film does not conduct any charge along the backbone leading to a non-conducting polymer.

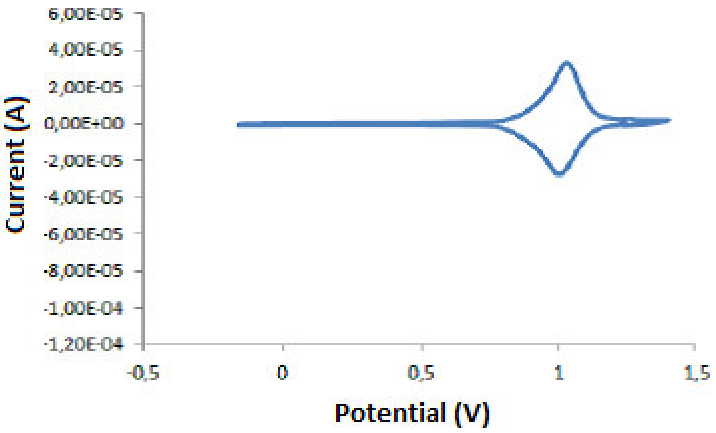

Fig. 3.75: cyclic voltammetric response of poly(Et-TPA) in CH_2Cl_2/$TEAPF_6$ 0.1 M; WE: Pt, RE, Ag/AgCl, CE: graphite bar; v = 100 mV/s

3.2.2.1.2.2 poly-4-[(4’-bromo-2,2’-bithiophen-4-yl)ethynyl]-N,N’-diphenylaniline, poly(Br-BT-Et-TPA)

Characterisation of the film obtained from a CH_2Cl_2/$TEAPF_6$ 0.1 M solution

The characterisation was done on a 320 nm thick film obtained by applying +1.60 V for 300s In Fig. 3.76 a doping process centred at +1.13 V is visible and an associated de-doping can be appreciated at +0.68 V. A pre-peak at +0.67 V can be attributed to the presence of oligomeric chains in the film.

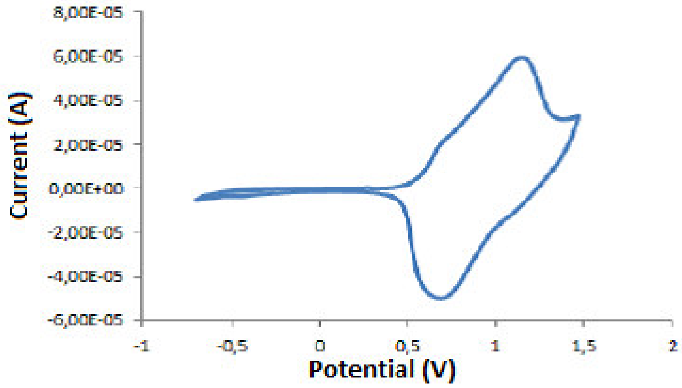

Fig. 3.76: cyclic voltammetric response of poly(Br-BT-Et-TPA)in $CH_2Cl_2/TEAPF_6$ 0.1 M; WE: Pt, RE, Ag/AgCl, CE: graphite bar; v = 100 mV/s p

At UV-Vis spectra a band at 301 nm is present.

3.2.2.1.2.3 poly-4-[(4'-ethinyl-2,2'-bithiophen-4-yl)ethinyl]-N,N'-biphenylaniline, poly(Et-BT-Et-TPA)

Characterisation of the film obtained from a $CH_2Cl_2/TEAPF_6$ 0.1 M solution

The characterisation was done on a film with a 360 nm thickness, obtained with an applied potential of +1.45 V for 300 s. The p-doping occurs at +1.08 V and the associated de-doping peak is at +1.00 V. Also in this case the presence of oligomeric chains can be deduced from the presence of a small peak at +0.82 V (Fig. 3.77).

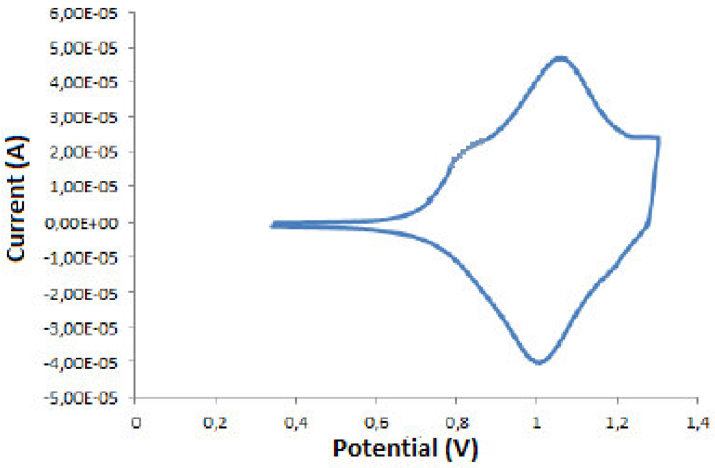

Fig. 3.77: cyclic voltammetric response of poly(Et-BT-Et-TPA)

in $CH_2Cl_2/TEAPF_6$ 0.1 M; WE: Pt, RE, Ag/AgCl, CE: graphite bar; v = 100 mV/s

The UV-Vis spectra showed an absorption at 307 nm.

3.2.2.1.2.4 poly-4-[(2,2':6':2''-terpyridine-4'-ethynyl)-4-(2,2'-bithiophen-4-yl)]-ethynyl-N,N'-diphenylaniline, poly(Tpy-Et-BT-Et-TPA)

Characterisation of the film obtained from a CH_2Cl_2/$TEAPF_6$ 0.1 M solution

The characterisation was performed on a film with a 300 nm thickness, obtained at +1.45 V for 300s. In Fig. 3.78 an anodic p-doping peak can be seen with an associated peak at +0.98 V (de-doping).

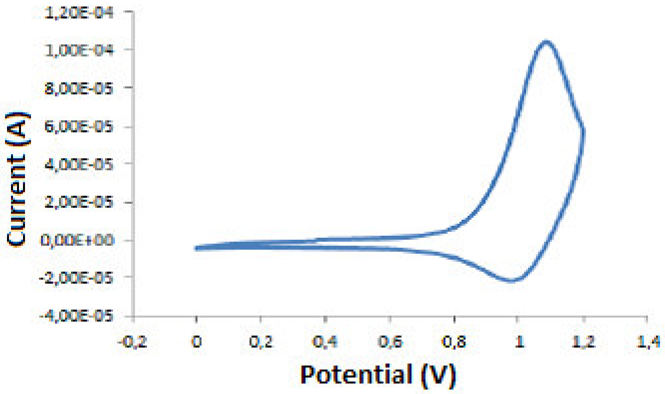

Fig. 3.78: cyclic voltammetric response of poly(Et-BT-Et-TPA) in CH_2Cl_2/$TEAPF_6$ 0.1 M; WE: Pt, RE, Ag/AgCl, CE: graphite bar; v = 100 mV/s

The UV-Vis spectra showed an absorption at 304 nm.

3.2.2.2 Discussion on monomers and polymers bearing two ethynyl group on the bithiophene backbone

Starting from all the aforementioned reason that led to the synthesis of the D-π-A chromophore of Fig. 3.53 discussed in paragraph 3.2.1.2, the decision of synthesising another novel organic dye that bears two ethynylic groups, one between the TPA donor and the bithiophene and the other one between the bithiophene and terpyridine, was due to the idea of further extending the coniugation of the system. Moreover the presence of two ethynylic groups should lighten the steric hindrance between TPA and terpyridine. The idea was also to evaluate how the introduction of another electronwithdrawing group, like ethynyl, could have an influence on the electrochemical and optical properties of monomers and corresponding polymers.

The new organic chromophore (Fig. 3.79), its precursors and polymers are completely discussed in the following.

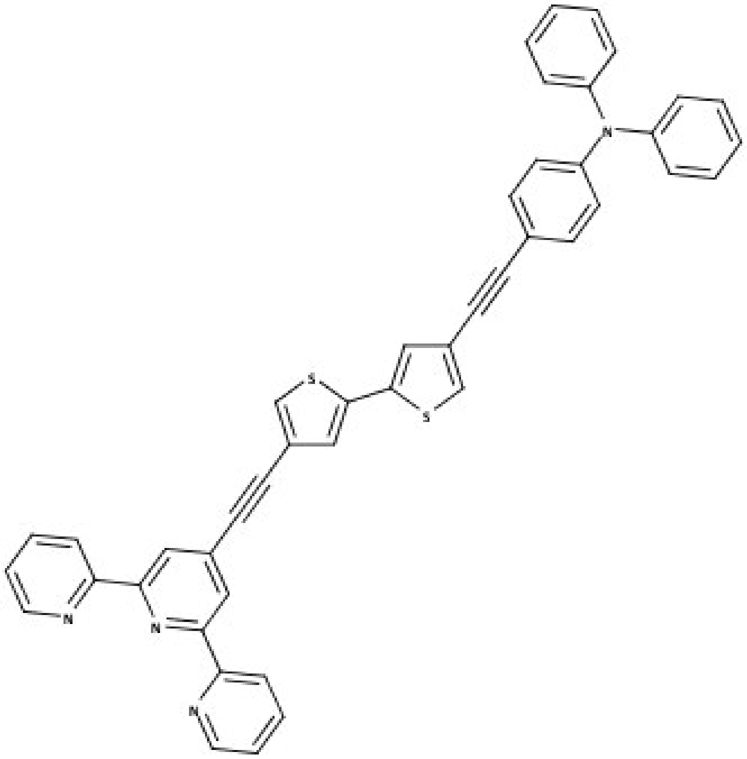

Fig 3.79: Tpy-Et-BT-Et-TPA

The synthetic path started with the idea of a one step insertion, by means of a Sonogashira coupling, of two ethynyl groups on the 4,4' positions of Br-BT-Br starting reagent and a subsequent functionalization with TPA and terpyridine respectively. This approach gave some problems probably because of the instability of Et-BT-Et derivative. A second approach [139] was followed based on the synthesis of 4-ethynyl-TPA and then on the introduction of the latter on the Br-BT-Br molecule. The obtained derivative Br-BT-Et-TPA was then used for the Sonogashira reaction with 2-methylbut-3-ynyl-2-ol, introducing the second acetylene moiety on the bithiophene fragment, thus leading to OH-BT-Et-TPA. The product was deprotected with KOH for the obtainment of Et-BT-Et-TPA. A final Sonogashira coupling with Cl-terpyridine led to the desired molecule Tpy-Et-BT-Et-TPA.

The commercial precursors and all the synthesised species, together with the corresponding polymers, when obtained, were characterised.

From the UV-Vis spectra the ε value and the energy gap were calculated and are reported in Table 3.16.

Table 3.16: UV-Vis characterisation of the commercial and synthesised compounds

Monomer	**λ_{max} (nm)**	**λ_{onset} (nm)**	**Eg,opt (eV)**	**ε (M^{-1} cm^{-1})**
Br-BT-Br	311	348	3.56	12600
Br-TPA	303	344	3.60	30000
TMS-TPA	333	367	3.38	29000
Et-TPA	306	361	3.43	19000
Br-BT-Et-TPA	329	370	3.35	37000
Et-BT-Et-TPA	339	382	3.25	37000
Tpy-Et-BT-Et-TPA	345	429	2.89	12000

High molar extinction coefficients are usually characterised by an extensive delocalisation of the HOMO that should also be well separated from the LUMO. In this case the presence of the two ethynyl groups should favour this geometry. On the other way the energy gap is a value that allow to make considerations about the electronic communication along the whole of the molecule, and as a consequence to have an idea of how efficient a compound can be in light harvesting applications.

From Table 3.16 it is possible to evaluate:

- substituting the Br atom on the TPA a red-shift of the absorption maxima occurs and this is more evident for the TMS-TPA than for Et-TPA. The latter also has a lower ε value than the other derivatives;
- the introduction of Et-TPA on the bithiophene leads to a clear red shift of the absorption maxima, and this is much more evident for Tpy-Et-BT-Et-TPA, with an energy gap of 2.89 eV. This bathochromic shift is probably due to the increase in the molecule conjugation.
- ε values are higher for all TPA derivatives, while the introduction of terpyridine leads to a decrease of this value, as already seen for the corresponding monomer with one ethynyl group Tpy-Et-BT-TPA (19000 M^{-1} cm^{-1}).

CV data of all the starting and synthesised products are reported in Table 3.17.

Table 3.17: CV data of starting and synthesised molecules in CH_2Cl_2

Monomers	**$E_{p,1}$ (V)**	**$E_{p,2}$ (V)**	**$E_{onset,1}$ (V)**	**$E_{onset,2}$ (V)**	**HOMO (eV)[a]**	**HOMO-1 (eV)[b]**
Br-BT-Br	1.76		1.47		-6.18	
Br-TPA	1.06		0.94		-5.65	
TMS-TPA	1.06		0.89		-5.60	
Et-TPA	1.20		0.94		-5.65	
Br-BT-Et-TPA	1.03	1.54	0.85	1.20	-5.56	-5.91
Et-BT-Et-TPA	1.06	1.55	0.86	1.20	-5.57	-5.95
Tpy-Et-BT-Et-TPA	0.98	1.45	0.80	1.15	-5.51	-5.86

[a]HOMO calculated from the first onset potential [b] HOMO-1 value calculated from the second peak onset potential

From the comparison with theoretical data of the series of compounds with one ethynyl group, it is possible to confirm the attribution of the first oxidation peak (relative to the HOMO) to the TPA moiety in the compounds Br-Bt-Et-TPA, Et-BT-Et-TPA and Tpy-Et-BT-Et-

TPA. For the same compounds the second anodic process (HOMO-1) is related to the bithiophene oxidation.

The presence of free electron-withdrawing ethynyl moiety on the TPA (Et-TPA) leads to an increase in the oxidation potential of the compound in respect to the brominated and sylylated analogues. The same trend is visible for Br-BT-Et-TPA and Et-BT-Et-TPA. The introduction of terpyridine lowers the oxidation potential of both the TPA and the bithiophene fragments; in this case the high conjugation of the system has a stronger influence on oxidation than the presence of electron-withdrawing ethynyl on TPA.

All the synthetic intermediates were electropolymerised but not all the monomers gave homogeneous films, as explained in the synthesis paragraph; the corresponding polymers were characterised and CV data are reported in Table 3.18.

Table 3.18: CV data of the polymer films on a Pt electrode

Polymer	E_p	E_{onset}	HOMO
Poly(Br-BT-Br)	1.43	1.34	-6.05
Poly(Br-BT-Et-TPA)	1.13	0.52	-5.23
Poly(Et-BT-Et-TPA)	1.08	0.73	-5.44
Poly(Tpy-Et-BT-Et-TPA)	1.08	0.88	-5.59

The TPA-Et introduction on the bithiophene backbone destabilises the HOMO more than the analogues compound Br-BT-TPA (paragraph 3.2.1.2) without ethynyl attached to TPA (-5.23 eV for poly(Br-BT-Et-TPA) and -5.69 eV for poly(Br-BT-TPA)) against -6.05 V for poly(Br-BT-Br)). So it can be deduced that the presence of one and then two ethynyl groups on a bithiophene backbone led to a subsequent progressive destabilisation of the polymers HOMO.

UV-Vis data are reported in Table 3.19 for the polymers deposited through chronoamperometry on ITO.

Table 3.19: UV-Vis data of the polymers deposited on ITO

Polymer	λ_{onset}	$E_{g,opt}$
Poly(Br-BT-Br)	626	1.98
Poly(Br-BT-Et-TPA)	453	2.74
Poly(Et-BT-Et-TPA)	459	2.70
Poly(tpy-Et-BT-Et-TPA	451	2.75

The values of the energy gaps are similar and they all lie between 2.70 and 2.75 eV except for Br-BT-Br. As already said, this does not imply a worsening of the conducting properties of the polymer. Usually energy gap values lower than 2 eV do not allow controlling the electronic transitions properly. A significant increase in the energy gap can be seen already in Br-Bt-Et-TPA, thus suggesting that the presence of the ethynyl fragment between the TPA and bithiophene plays a significant role in the polymer optical properties; as a matter of fact this effect on the energy gap is less pronounced in polymers where the TPA is directly bonded to bithiophene (par. 3.2.1.2), where the E_g increases but with a more gradual trend.

It is possible to say that electrochemical and optical properties of all synthesised molecules and of the corresponding electrogenerated polymers were evaluated and trials to understand the influence of the introduction of each substituent on the bithiophene backbone were done. The final product Tpy-Et-BT-Et-TPA showed a low energy gap value and relative high extinction coefficients and for these reason it can be considered as good candidate for light harvesting applications. The electro-synthesised polymers are organic chromophores with a D-π-A geometry and they can be studied as dyes for applications in lightsensitive device because of their stability for several doping and de-doping cycles and good charge transport properties.

3.2.3 Discussion on chromophores that differ for the presence of one or two ethynyl groups on the bithiophene backbone

Comparison of optical and electrochemical data of the two groups of chromophores above discussed allow evaluating the influence of the presence and the position of ethynyl groups on the properties of the synthesised monomers and corresponding polymers. In particular, comparing Br-BT-TPA and Br-BT-Et-TPA (Fig. 3.80), that differ for the ethynyl group between the bithiophene and TPA, evidences (Table 3.20) that the presence of the unsaturated acetylene group strongly influences the energy gap value of the monomer Br-BT-Et-TPA that exhibits a strong red shift in respect to Br-BT-TPA.

Tab 3.20: optical data for Br-BT-TPA and Br-BT-Et-TPA

monomer	E_g (eV)
Br-BT-TPA	3.36
Br-BT-Et-TPA	3.03

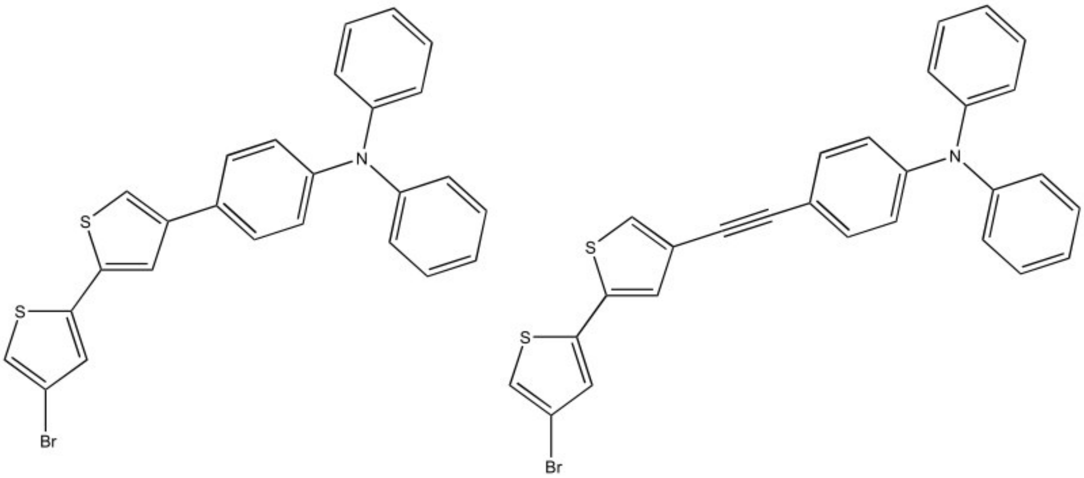

Fig. 3.80: Br-BT-TPA and Br-BT-Et-TPA

Another comparison can be made between the two monomers in Fig. 3.81. The optical and electrochemical characterisation data are reported in Table 3.21.

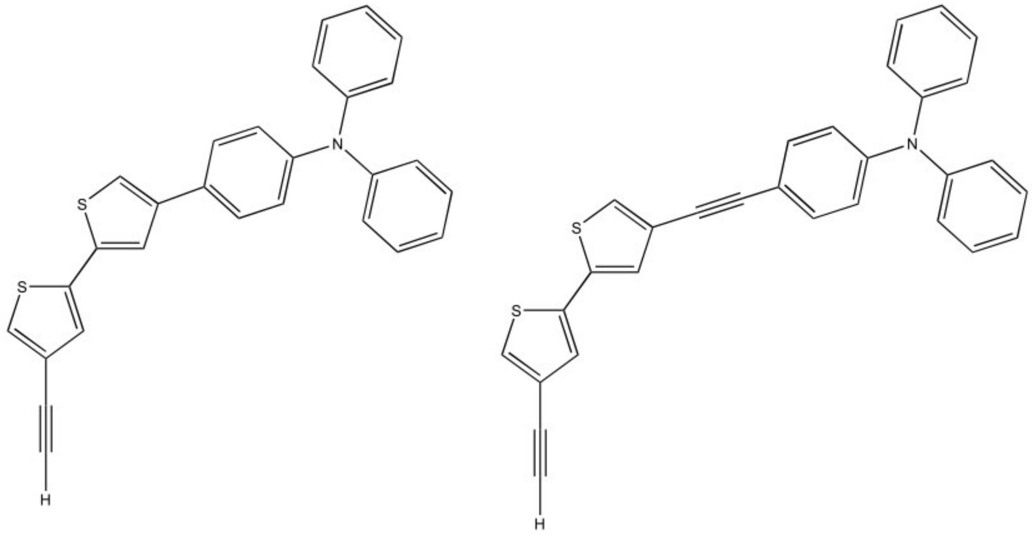

Fig 3.81: Et-BT-TPA and Et-BT-Et-TPA

Table 3.21: optical and electrochemical data for Et-BT-TPA and Et-BT-Et-TPA in CH_2Cl_2

monomer	**E_g (eV)**	**E_{p1} and E_{p2}**
Et-BT-TPA	3.35	1.02/1.55
Et-BT-Et-TPA	3.25	1.06/1.55

The same trend of the previous analogues can be appreciated: lower band gap values for the more ethynylated compound. The first oxidation potential (E_{p1}) relative to the TPA rings, as already said, is shifted to higher values for di-ethynyl derivative and this is probably due to the electronwithdrawing effect of the unsaturated substituent on the TPA electrons In this case the second oxidation potential (related to bithiophene) is not influenced by the presence of one or two unsaturated groups.

Finally, in the comparison between the two final D-π-A organic dyes Tpy-Et-BT-TPA and Tpy-Et-BT-Et-TPA (Fig. 3.82 and Table 3.22) it is possible to further appreciate the significative lowering of the energy gap value for the diethynylated monomer (2.89 eV for Tpy-Et-BT-Et-TPA vs 3.30 eV for Tpy-Et-BT-TPA). In this case the oxidation of TPA for Tpy-Et-BT-Et-TPA gives a peak at 0.98 V, and this potential is higher than that of the analogue for Tpy-Et-BT-TPA, confirming that the presence of ethynyl bonded to TPA acts as electron-acceptor. The potentials attributed to bithiophene are higher for the diethynylated molecule; this suggests that at the increase of the systems conjugation, the presence of two electrowithdrawing ethynyl groups weaken the donor power of the TPA.

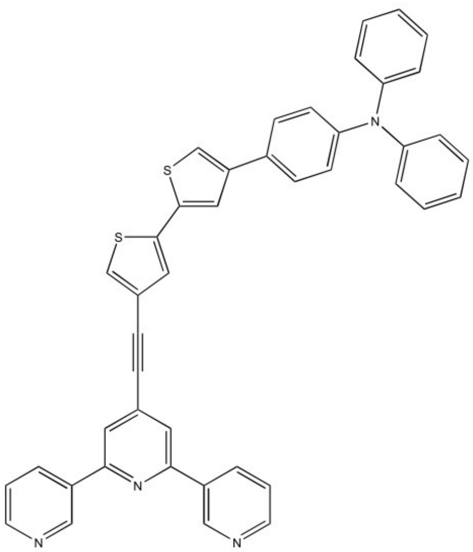

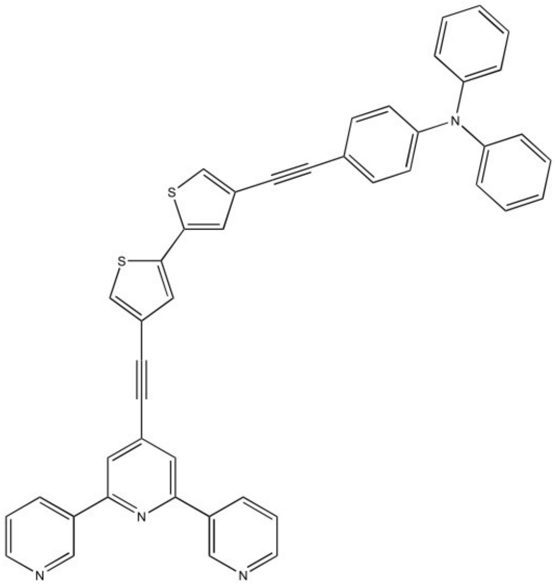

Fig. 3.82: Tpy-Et-BT-TPA and Tpy-Et-BT-Et-TPA

Table 3.22: optical and electrochemical data for Tpy-Et-BT-TPA and Tpy-Et-BT-Et-TPA in CH_2Cl_2

monomer	E_g (eV)	E_{p1}/E_{p2} (V)
Tpy-Et-BT-TPA	3.30	0.91/1.29
Tpy-Et-BT-Et-TPA	2.89	0.98/1.45

A final discussion on the analogues polymers can be done when looking at Table 3.23, where the comparisons are made with polymers bearing one or two ethynylic moieties (same line for each analogue).

Table 3.23: Optical and electrochemical data of all polymers, analogues with one or two ethynylic groups are written on the same line.

polymers	E_g (eV)	E_p	polymers	E_g (eV)	E_p
Poly(Br-BT-TPA)	2.03	1.24	**Poly(Br-BT-Et-TPA)**	2.74	1.13
Poly(Et-DT-TPA)	2.28	1.12	**Poly(Et-DT-Et-TPA)**	2.70	1.08
Poly(Tpy-Et-BT-TPA)	2.67	1.04	**Poly(Tpy-Et-BT-Et-TPA)**	2.75	1.08

The introduction of ethynyl near to the TPA leads to a rapid increase in the energy gap of the polymers; the doping potential (E_p in Table 3.23), is lower for diethynylated polymers than the monoethynylated counterparts with the exception of the terpyridine-functionalised compounds that show similar doping values.

A general increase in polymers energy gaps is observable at increasing conjugation of the monomeric unit. As already said, this is not the only parameter for a promising polymeric dye; another important factor is relative to the charge separation properties and in this case the reversibility and stability of the polymer films suggests proper charge transport.

Conclusions

The experimental work performed during this thesis was devoted to the design, synthesis and characterisation of photosensitive materials.

On one side, synthesis of mesoporous titania powders through EISA method was performed. The influence of synthetic conditions (precursors type and molar ratio, ligand addition, calcination rates and temperatures, water addition and surfactant type) on both structural (phase composition and crystallite size) and morphological (surface areas, pore distribution and size) parameters were evaluated. Experimental parameters obtained by X-Ray Powder Diffraction, N_2 Physisorption measurements and Transmission Electron Microscopy were estimated. The materials obtained were also tested as photoanodes in the water splitting reaction and the results compared to Degussa P25 (a well-known highly photoactive titania) as standard. It was possible to find relationships between the titania precursors type and molar ratio and the final phase composition of the samples. Moreover, experimental results allowed to correlate phase composition and porous structure to the photocatalytic performances of the powders: in particular, one sample showed current density values at 0V bias vs Ag/AgCl higher than the commercial P25. This finding suggested that homogeneous intra- and inter-particles pore distribution is an important parameter for high photoactivities.

On the other hand, synthesis, electrochemical and optical characterization of novel D-π-A dyes were performed. All the compounds obtained in each synthetic step were characterised in the same way, thus allowing to study the influence of the introduction of donor or acceptor fragments on a bithiophene backbone.

In the D-π-A structure here reported, TPA played the donor role. Its introduction in a bithiophene backbone leads to compounds with high molar extinction coefficients (30000-35000 $M^{-1}cm^{-1}$), thus suggesting promising light harvesting properties. Moreover, compounds showing high ε values often feature significant HOMO delocalization and proper separation from LUMO, both important features for photosensitive compounds. The presence of terpyridine as acceptor leads to a decrease in energy gap values of the chromophores and to a decrease in the ε value. Anyway, molar extinction coefficient of D-π-A chromophores was still higher than that of not functionalized bithiophene. The bithiophene group was used as spacer with the addition of one or two ethynyl moieties. The influence of the position of these unsaturated substituents was evaluated, showing that the higher conjugation offered by the diethynylated compound leads to lower energy gap values of the corresponding chromophores.

Almost all the synthesised compounds were electropolymerised. The corresponding conducting polymers, which can be regarded as polymer dyes, were characterised by cyclic voltammetry and UV-Vis spectrophotometry. All polymers exhibited doping and de-doping reversible processes for various cycles that are indicative of good charge transport through the backbone. The introduction of two ethynyl groups induces a general increase in the polymers energy gaps compared to the mono-ethynyl derivatives. The only exception is in the case of the electrogenerated polymers of the terpyridine-functionalised derivatives, where similar energy gap and doping potential values were observed. These evidences suggested that the presence of one or two unsaturated moieties tends to be less relevant when the systems possess a high delocalisation due to terpyridine presence.

The prosecution of this work will be the testing of the most photoactive titania sample together with the synthesised chromophores and the evaluation of their photocatalytic performances in DSSCs application. The possibility of coordinating a Ru metal centre to both the monomer or polymer terpyridine-functionalised derivatives should also be explored.

Aknowledgements

For Scientific collaboration aknowledgements go to:

- Dr. Maria Dolors Baró, Dr. Eva Pellicer and Dr. Jordi Sort from the Physic Department of Universitat Autònoma de Barcelona, for TEM measurements
- Dr. Agnieszka Rzeszutek and Dr. Iris Herrmann-Geppert from Helmholtz Centre Geesthacht, Institute for Materials Research, for electrochemical characterisations on titania samples
- Dr. Antonio Zucca from Department of Chemistry and Pharmacy, University of Sassari, for NMR spectra interpretation